Electronic Theses and Dissertations

Theses, Dissertations, and Major Papers

2022

Mechanical Characterization of Direct/In-line Compounded, Compression Molded Polyamide / Carbon Fibre Long Fibre Thermoplastic

Matthew Bondy
University of Windsor

Follow this and additional works at: https://scholar.uwindsor.ca/etd

Part of the Mechanical Engineering Commons

Mechanical Characterization of Direct/In-line Compounded, Compression Molded Polyamide / Carbon Fibre Long Fibre Thermoplastic

By

Matthew Bondy

A Dissertation

Submitted to the Faculty of Graduate Studies

through the Department of Mechanical, Automotive & Materials Engineering

in Partial Fulfillment of the Requirements for

the Degree of Doctor of Philosophy

at the University of Windsor

Windsor, Ontario, Canada

2022

Mechanical Characterization of Direct/In-line Compounded, Compression Molded

Polyamide / Carbon Fibre Long Fibre Thermoplastic

by

Matthew Bondy

APPROVED BY:

_____

R. Vaziri, External Examiner
University of British Columbia

_____

B. Minaker
Department of Mechanical, Automotive & Materials Engineering

_____

A. Alpas
Department of Mechanical, Automotive & Materials Engineering

_____

J. Johrendt
Department of Mechanical, Automotive & Materials Engineering

_____

W. Altenhof, Advisor
Department of Mechanical, Automotive & Materials Engineering

November 3, 2022

DECLARATION OF CO-AUTHORSHIP / PREVIOUS PUBLICATION

I.   Co-Authorship

I hereby declare that this thesis incorporates material that is result of joint research, as follows:

Chapter 3 was co-authored with Dr. Pascal Pinter and Dr. William Altenhof. Dr. Pascal Pinter completed computed tomography scans of material samples and edited the manuscript. Dr. William Altenhof provided feedback on refinement of concepts and edited the manuscript. The key ideas, primary contributions, experimental designs, mechanical testing, data analysis, and writing of the manuscript were contributed by the author.

Chapter 4 was co-authored with Dr. William Rodgers and Dr. William Altenhof. Dr. William Rodgers was directly involved in mechanical testing, provided feedback on refinement of concepts, and edited the manuscript. Dr. William Altenhof provided feedback on refinement of concepts and edited the manuscript. Dustin Reisberg made significant contributions to the mechanical testing. The key ideas, primary contributions, experimental designs, data analysis, and writing of the manuscript were contributed mainly by the author.

Chapter 5 was co-authored with Dr. William Altenhof. Dr. William Altenhof directly contributed to completion of mechanical testing, provided feedback on refinement of concepts, and edited the manuscript. The key ideas, primary contributions, experimental designs, experimental testing, data analysis, and writing of the manuscript were contributed mainly by the author.

Chapter 6 was co-authored with Dr. William Altenhof. Dr. William Altenhof directly contributed to completion of mechanical testing, provided feedback on refinement of concepts, and edited the manuscript. The key ideas, primary contributions, experimental designs, experimental testing, data analysis, and writing of the manuscript were contributed mainly by the author.

Chapter 7 was co-authored with Dr. William Altenhof, Dr. John Magliaro, and Pouya Mohammadkhani. Dr. William Altenhof directly contributed to completion of mechanical testing, provided feedback on refinement of concepts, and edited the manuscript. Dr. John Magliaro and Pouya Mohammadkhani directly contributed to completion of mechanical testing and edited the manuscript. The key ideas, primary contributions, experimental designs, experimental testing, data analysis, and writing of the manuscript were contributed mainly by the author.

I am aware of the University of Windsor Senate Policy on Authorship and I certify that I have properly acknowledged the contribution of other researchers to my thesis, and have obtained written permission from each of the co-author(s) to include the above material(s) in my thesis.

I certify that, with the above qualification, this thesis, and the research to which it refers, is the product of my own work.

II.   Previous Publication

This thesis includes 5 original papers that have been previously published/submitted for publication in peer reviewed journals, as follows:

Thesis Chapter	Publication title/full citation	Publication status
Chapter [3]	Bondy, M., P. Pinter, and W. Altenhof. "Experimental characterization and modelling of the elastic properties of direct compounded compression molded carbon fibre/polyamide 6 long fibre thermoplastic." Materials & Design 122 (2017): 184-196.	Published
Chapter [4]	Bondy, M., W. Rodgers, and W. Altenhof. "Tensile fatigue characterization of polyamide 66/carbon fiber direct/in-line compounded long fiber thermoplastic composites." Composites Part B: Engineering 173 (2019): 106984.	Published

Chapter [5]	Bondy, M., and W. Altenhof. "Low velocity impact testing of direct/inline compounded carbon fibre/polyamide-6 long fibre thermoplastic." International Journal of Impact Engineering 111 (2018): 66-76.	Published
Chapter [6]	Bondy, M., and W. Altenhof. "Experimental characterization of the mechanical properties of a carbon fibre/PA66 LFT automotive seatback under quasi-static and impact loading." International journal of crashworthiness 25.4 (2020): 401-420.	Published
Chapter [7]	Bondy, M., P. Mohammadkhani, J. Magliaro, W. Altenhof. "Elevated Strain Rate Characterization of Compression Molded Direct/In-Line Compounded Carbon Fibre/Polyamide 66 Long Fibre Thermoplastic." Materials 15.21 (2022): 1-23.	Published

I certify that I have obtained a written permission from the copyright owner(s) to include the above published material(s) in my thesis. I certify that the above material describes work completed during my registration as a graduate student at the University of Windsor.

III.   General

I declare that, to the best of my knowledge, my thesis does not infringe upon anyone's copyright nor violate any proprietary rights and that any ideas, techniques, quotations, or any other material from the work of other people included in my thesis, published or otherwise, are fully acknowledged in accordance with the standard referencing practices. Furthermore, to the extent that I have included copyrighted material that surpasses the bounds of fair dealing within the meaning of the Canada Copyright Act, I certify that I have obtained a written permission from the copyright owner(s) to include such material(s) in my thesis.

I declare that this is a true copy of my thesis, including any final revisions, as approved by my thesis committee and the Graduate Studies office, and that this thesis has not been submitted for a higher degree to any other University or Institution.

ABSTRACT

Direct compounded compression molded carbon fibre long fibre thermoplastic (LFT-D) combines the high strength and stiffness of carbon fibre with a mass production manufacturing process intended to maximize fibre length. However, this process is more commonly used in industry with glass fibre. Extensive characterization of mechanical properties, spanning fundamental tensile tests to impact characterization of standard specimens and a complex automotive component, was completed to understand the strengths and deficiencies of this novel material formulation for engineering applications: fundamental uniaxial tension (quasi-static and intermediate strain rate) and three-point bending tests, tensile stress-life fatigue characterization, ISO 6603-2 instrumented impact of standard specimens, and quasi-static/low velocity impact loading of an automotive seating component. These studies provide the data necessary to advance commercial adoption of direct compounded long carbon fibre thermoplastic.

Uniaxial tension and three-point bending characterization of 9% to 25% weight fraction compression molded carbon fibre LFT-D polyamide-6 was completed with orientations of 0°, ±45°, and 90°. A novel finding that has importance for process modelling was that uniaxial tension and flexural properties were higher in the +45° direction compared to -45° (tensile modulus: 20%, strength: 10%, flexural modulus: 8%). Correspondingly, engineering strain at failure for uniaxial tensile tests was 18% lower in the +45° direction. These observations are hypothesized to be the result of fibre orientation asymmetry in the compression molding charge due to the screw of the compounder.

Tensile fatigue characterization was carried out for 40% (by weight) carbon fiber/polyamide 66 LFT-D composites. This characterization yielded fatigue stress-life curves (23°C, dry as molded, R = 0.1, 3 Hz) for 0°, 45°, and 90° orientations with respect to flow. Peak stresses at which the samples achieved 10^6 cycles were 105 MPa for samples oriented in the flow direction, 72 MPa for samples oriented 45° to the flow direction, and 53 MPa for samples oriented 90° to flow. Poorly dispersed fibre with little to no wet-out were identified by SEM at the fracture surfaces for those specimens with fatigue properties near the stress-life lower bound. Further development of the direct compounding process is needed for carbon fibre.

Direct/in-line compounded PA6/CF long fibre thermoplastic was also characterized under low velocity impact consistent with ISO standard 6603-2. Additionally, a quasi-static variant of the ISO method was employed to assess rate sensitivity. At quasi-static loading rates, flow region specimens were notably more brittle considering the force-deflection response. However, the energy absorption did not differ significantly between charge and flow region specimens. In terms of rate sensitivity, puncture energy under low velocity impact decreased by 18% on average with respect to quasi-static loading.

Tensile specimens were extracted from an automotive seatback structure compression molded from PA66/CF. Additionally, quasi-static and low velocity impact loading of seatback components was completed. Under low velocity impact loading a local force maxima was observed for seatbacks produced with a longitudinal charge orientation. No local maxima were consistently observed for transverse charge seatbacks. In terms of rate effects: initial stiffness was 550% higher for low velocity impact with respect to quasi-static loading. Digital image correlation identified localized deformation at the hemispherical indenter for low-velocity impact indicating an inertial component to the rate sensitivity. Catastrophic failure occurred at larger deflections for low velocity impact (36% increase for longitudinal charge placement, 24% for transverse).

A study of specimen size effect for quasi-static uniaxial tension puncture test was completed for compression molded direct compounded carbon fibre LFT. No significant size effects were observed for the elastic modulus or tensile strength obtained from tensile specimens with four different gauge lengths (6.25 mm to 57 mm). The failure strain decreased by 27.5% and 29.9%, respectively, across the gauge length range for the 0°/90° directions. This material was also characterized at intermediate strain rates (10 s^{-1} to 100 s^{-1}) through uniaxial tension tests on a novel apparatus and ISO 6603-2 puncture tests. Intermediate strain rate tensile tests showed little to no strain rate sensitivity for the 0° and 90° directions. However, initial stiffness was approximately 50% higher for ISO 6603-2 impact tests compared to quasi-static puncture tests.

ACKNOWLEDGEMENTS

TABLE OF CONTENTS

LIST OF TABLES

LIST OF FIGURES

LIST OF ABBREVIATIONS

ASTM	American Society for Testing and Materials
AR	Aspect ratio
CF	Carbon fibre
CFC	Channel frequency class
CNC	Computer numerical control
CoV	Coefficient of variation
CT	Computed tomography
DIC	Digital image correlation
FE	Finite element
FLD	Fibre length distribution
FOD	Fibre orientation distribution
FPC	Fraunhofer Project Centre
FRP	Fibre reinforced polymer
GF	Glass fibre
GSC	Generalized self-consistent
HS	Heat stabilized
IAM	Institute of Applied Mechanics
IEPE	Integrated Electronics Piezo-Electric
ILC	Inline compounding
inHG	Inches of Mercury
ISO	International Organization for Standardization
KIT	Karlsruhe Institute of Technology
LFT-D	Direct compounded long fibre thermoplastic
LFT-G	Long fibre thermoplastic granule
MATLAB	Matrix Laboratory
NI	National Instruments
PA	Polyamide
PEEK	Polyether ether ketone
PP	Polypropylene

PPS	Polyphenylene sulfide
RPM	Revolutions per minute
SAE	Society of Automotive Engineers
SEM	Scanning electron microscope
SHPB	Split Hopkinson pressure bar
SMC	Sheet molding compound
STP	Standard temperature and pressure
TTL	Transistor-to-transistor logic
UTS	Ultimate tensile strength
μCT	Micro-computed tomography

NOMENCLATURE

A_f	Y-intercept of log-log S-N curve (fatigue)
A_{GSC}	Generalized self consistent micromechanics model parameter
A_{ij}	Laminate model parameters
a	Fibre aspect ratio
a_{ij}	2nd order orientation tensor
a_{ijkl}	4th order orientation tensor
α_i	Mori-Tanaka micromechanics model parameters
B_f	Slope of log-log S-N curve (fatigue)
B_{GSC}	Generalized self consistent micromechanics model parameter
B_i	Transversely isotropic stiffness tensor invariants
B_{ij}	Laminate model parameters
β_i	Mori-Tanaka micromechanics model parameters
C_{GSC}	Generalized self consistent micromechanics model parameter
c	Halpin-Tsai micromechanics model coefficient
Γ	Halpin-Tsai micromechanics model correction factor for materials with high fibre volume fractions
γ_{xy}	In-plane shear strain (laminate)
γ_{xz}	Transverse shear strain (laminate)
γ_{yz}	Transverse shear strain (laminate)
D	Halpin-Tsai micromechanics model parameter
D_{ij}	Laminate model parameters
d	Fibre diameter
d_{plug}	Diameter of epoxy plug for collecting sample to measure fibre length distribution
δ_{ij}	Unit tensor
E_{11}	Longitudinal (aligned to fibre) elastic modulus of a unidirectional fibre composite material
E_{22}	Elastic modulus of a unidirectional fibre composite material perpendicular to the fibre direction

E_{fibre}	Elastic modulus of reinforcing fibre
E_{matrix}	Elastic modulus of matrix material
E_x	Elastic modulus in x-direction (laminate)
E_y	Elastic modulus in y-direction (laminate)
E_{fx}	Flexural modulus for bending moment causing curvature κ_x (laminate)
E_{fy}	Flexural modulus for bending moment causing curvature κ_y (laminate)
ε_j	Strain tensor
ε_x	In-plane normal strain in x-direction (laminate)
ε_y	In-plane normal strain in y-direction (laminate)
ε_z	Transverse normal strain in z-direction (laminate)
F_i	Mori-Tanaka micromechanics model parameters
F_p	F-distribution parameter (fatigue)
G_{12}	Longitudinal shear modulus of unidirectional fibre composite
G_{23}	Transverse shear modulus of unidirectional fibre composite
G_{fibre}	Shear modulus of reinforcing fibre
G_{matrix}	Shear modulus of matrix material
θ	Out-of-plane angle of fibre
k	Plane strain bulk modulus of the composite
k_f	Number of samples (fatigue)
k_{fibre}	Plane strain bulk modulus of the fibre
k_{matrix}	Plane strain bulk modulus of the matrix
κ_x	Bending curvature in xz plane (laminate)
κ_y	Bending curvature in yz plane (laminate)
κ_{xy}	Twisting curvature in xy plane (laminate)
l	Fibre length
$\Lambda(l)$	Experimental fibre length distribution with sampling bias
M_x	Bending moment about the y-axis causing curvature κ_x (laminate)
M_y	Bending moment about the x-axis causing curvature κ_y (laminate)

M_{xy}	Torsional moment about the x-axis (laminate)
M_{yx}	Torsional moment about the y-axis (laminate)
$N(l)$	Fibre length distribution without bias (or with bias corrected)
N_f	Number of loading cycles (fatigue)
N_x	Normal force in the x-direction per unit length (laminate)
N_y	Normal force in the y-direction per unit length (laminate)
N_{xy}	Shear force in the xy plane per unit length (laminate)
n	Number of pixels in fibre cross section for which orientation is being computed
η_{fibre}	Generalized self consistent micromechanics model parameter
η_{matrix}	Generalized self consistent micromechanics model parameter
ϕ	In-plane angle of fibre
$\vec{p}$	Unit vector in fibre direction
p_i^k	Unit vector components for fibre k
ρ_{fibre}	Density of reinforcing fibre
ρ_{matrix}	Density of matrix material
Q_{ij}	Transversely isotropic stiffness tensor (unidirectional fibre composite)
$(Q_{ij})_m$	Stiffness tensor for lamina m (laminate)
$Q_{ij_{N(l)}}$	Transversely isotropic stiffness tensor (unidirectional fibre composite) incorporating fibre length distribution $N(l)$
Q'_{ij}	Stiffness tensor after orientation averaging
R	Halpin-Tsai micromechanics model modulus
r_e	Equivalent ellipsoidal axis ratio
r_{major}	Major radius of fibre cross section for which orientation is being computed
r_{minor}	Minor radius of fibre cross section for which orientation is being computed
S_f	Engineering stress (fatigue)

S_{ijkl}	Eshelby tensor
σ_i	Stress tensor
σ_f	Variance (fatigue)
T_x	First moment about the x axis of the fibre cross section for which orientation is being computed
T_{xx}	Second moment about the x axis of the fibre cross section for which orientation is being computed
T_{xy}	Second moment about the x and y axes of the fibre cross section for which orientation is being computed
T_y	First moment about the y axis of the fibre cross section for which orientation is being computed
T_{yy}	Second moment about the y axis of the fibre cross section for which orientation is being computed
t	Laminate thickness
τ_{xz}	Transverse shear stress (laminate)
τ_{yz}	Transverse shear stress (laminate)
ν_{fibre}	Poisson's ratio of reinforcing fibre
ν_{matrix}	Poisson's ratio of matrix material
V_{fibre}	Volume fraction of reinforcing fibre
V_{matrix}	Volume fraction of matrix material
V_{voids}	Volume fraction of voids
v_x	Velocity component of flow field in x-direction
v_y	Velocity component of flow field in y-direction
V50	Ballistic limit where 50% of projectiles do not perforate the specimen
W_{fibre}	Weight fraction of reinforcing fibre
W_{matrix}	Weight fraction of matrix material
w	Displacement in z-direction (laminate)
w_i	Value of pixel i (0 or 1 for a binarized image)
X	Base 10 logarithm of number of loading cycles (fatigue)
$\bar{X}$	Mean of the base 10 logarithm of the number of loading cycles (fatigue)

x_i	x-coordinate of pixel i
Y	Base 10 logarithm of engineering stress (fatigue)
$Y_{lower\ limit}$	Lower confidence limit of Y (fatigue)
$Y_{upper\ limit}$	Upper confidence limit of Y (fatigue)
y_i	y-coordinate of pixel i
$\psi(\theta,\phi)$	Fibre orientation distribution
z_m	z-position of innermost surface of ply m (laminate)
Ω_{max}	Maximum fibre volume fraction (from fibre packing) for Halpin-Tsai micromechanics model

CHAPTER 1

INTRODUCTION

1.1 Motivation for the Industrial use of Thermoplastic Composites

Composite materials, particularly carbon fibre reinforced composites, are optimal materials in terms of specific strength and specific stiffness (see Figure 1.1) and are therefore of interest for any application where there are economic advantages and/or societal benefits from reducing the mass of structural components. One such application is the automotive sector where a reduction in mass is beneficial for emissions and/or vehicle range. However, in the automotive sector, the finite life of the product introduces requirements for recyclability and recoverability (e.g., 85% and 95%, respectively in the European Union [1]).
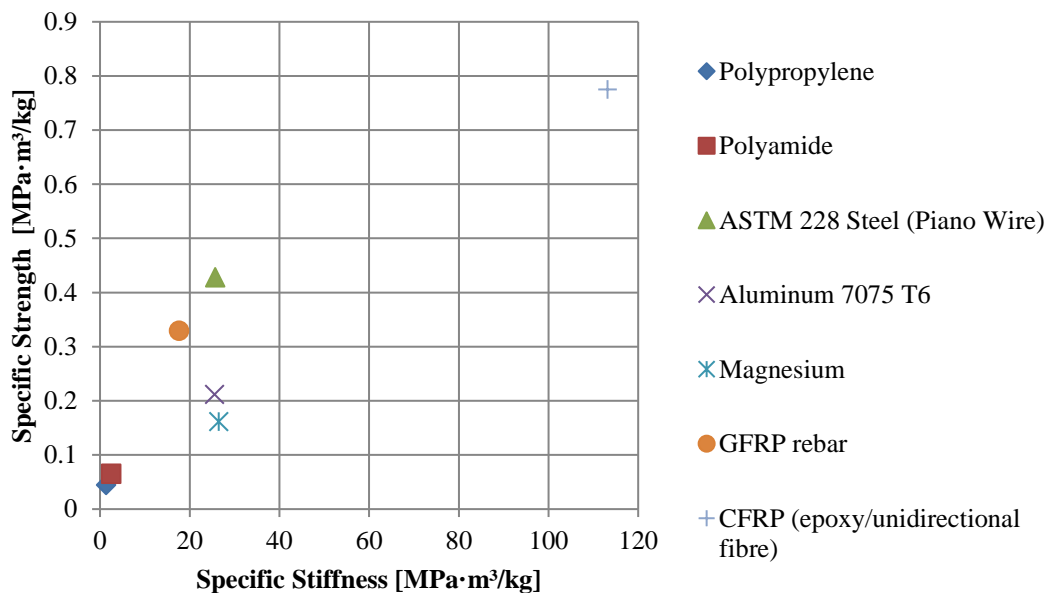
Figure 1.1: Specific stiffness and strength of various materials (data from [2])

Thermoplastic matrix composites have advantages over thermosets for recyclability. However, the higher viscosity of thermoplastics presents challenges for fibre wetout / interfacial strength [3,4]. It is particularly difficult to achieve fibre wetout with continuous woven fibre and a traditional thermoplastic matrix due to its viscosity, though it is possible to polymerize in the mold to overcome this difficulty [5]. Discontinuous (e.g.,

chopped) fibre can be utilized for mass production without significant manufacturing restrictions but short fibres reduce stiffness and significantly reduce strength as the matrix becomes a more critical structural component. For pelletized material, fibre length is limited by the pellet length to approximately 25 mm. Note that this is prior to any compounding/degradation in an extruder screw and before forming the end product (e.g., injection molding). The forming process will also result in fibre length degradation. Long fiber thermoplastics (LFTs) contain reinforcing fibers with an average aspect ratio greater than 100 (approximate fiber length of 1 mm) [3,6].

Early research on LFT materials focused on polyamide (PA) matrices [7-10]. However, commercial success has primarily been realized with polypropylene (PP) where glass fibre (GF) is the dominant reinforcement [11-13]. Global LFT consumption is approximately 200 000 tonnes annually with 80% consumed by the automotive industry and 60% of manufacturers located in the EU [14]. Direct/in-line compounding, though versatile in terms of fibre/matrix material combinations, entails high capital costs and requires highly qualified personnel to identify suitable process parameters. Capital costs are approximately €1 million; as a result the process is economical with a production rate in excess of approximately 500 000 kg annually [15].

The focus of this dissertation is a carbon fibre reinforced thermoplastic (PA6 and PA66) produced with a manufacturing process known as in-line or direct compounding. This process compounds multiple continuous fibre tows (bundles of many individual fibres) with thermoplastic immediately prior to extrusion of a charge which is placed in a mold. This charge is then formed into an industrial component (e.g., a seatback structure) through compression molding. The use of a single, large charge reduces fibre breakage at the extrusion die and in the mold. This process allows for a balanced combination of material properties and economics through maximizing fibre length/production rates and reducing cost of constituent materials through optimization of the compounding process [15].

In each chapter, details are presented for the manufacturing process parameters employed for producing the material/components upon which each set of mechanical

testing was completed. Therefore, additional necessary details on this manufacturing process are not presented in this introductory section.

1.2 Objective of the Research

The objective of this research was to comprehensively characterize the mechanical response of mass produced samples of carbon fibre reinforced LFT-D (long fibre thermoplastic, direct compounded) with a polyamide matrix. The direct compounding process has seen commercial use but mainly with glass fibre. The Fraunhofer Project Center at Western in London, Ontario modified Dieffenbacher LFT-D processing equipment to produce material and components with carbon fibre reinforcement (see the following chapters for details). No published studies on mechanical properties of carbon fibre LFT-D material were identified at the onset of this research project. Few studies are available at the time of defense of this dissertation. The main body of such research consists of the publications included in this document. Therefore, the motivation for this research was to comprehensively characterize this novel variation of carbon fibre reinforced thermoplastic. Specific objectives were as follows:

1. Complete fundamental mechanical characterization of carbon fibre / PA LFT-D material specimens with standardized specimen geometries and characterization procedures. This characterization included, but was not limited to, uniaxial tension, three-point bending, and impact testing.
2. Document process parameters for this novel manufacturing process variant in the open literature.
3. Compare mechanical properties resulting from manufacturing process variations / material compounding parameters.
4. Assess the fatigue properties of carbon fibre/PA LFT-D material specimens and evaluate fracture surfaces to understand failure mechanisms.
5. Assess strain rate sensitivity of carbon fibre/PA LFT-D material.
6. Characterize the mechanical properties of a practical industrial component fabricated with the LFT-D process from carbon fibre / PA with an assessment of impact properties and manufacturing process variations.

1.3 Structure of the Dissertation

This dissertation follows the manuscript format and consists of 8 chapters, described below. As a result of the manuscript format, there are a small number of instances where research findings and discussion can be found in more than one chapter. These instances are few in number and do not constitute a significant portion of this dissertation.

Chapter 2 presents a brief literature review of fundamental concepts generally common to the subsequent studies presented in each chapter: micromechanics, laminate theory, and flow-induced fibre orientation. Since the manuscript dissertation format is being used here, each chapter includes a brief overview focused on the specific area of research for that chapter / publication, as was originally presented in each publication.

Chapter 3 documents fundamental material characterization of carbon fibre / PA LFT-D material including tensile testing and three-point bending. Microstructure is investigated with CT scans and experimental fibre length distributions are presented. Experimental mechanical properties are compared to calculated mechanical properties from micromechanics models. This chapter is published in *Materials & Design*.

Chapter 4 discusses 0°, 45°, and 90° stress-life fatigue properties of carbon fibre / PA LFT-D material including examination of images obtained by electron microscopy of the fracture surfaces of failed specimens. This chapter is published in *Composites Part B: Engineering*.

Chapter 5 describes the impact properties of a range of carbon fibre / PA LFT-D material formulations / manufacturing process parameters following the ISO 6603-2 impact testing standard. The quasi-static mechanical properties for the material employed in this study are presented in Chapter 3. This chapter is published in *Impact Engineering*.

Chapter 6 consists of the procedure for and results from evaluating quasi-static and impact load-deflection responses and displacement contours (from DIC) for an automotive seatback compression molded from a carbon fibre / PA LFT-D material. Seatback component variants produced using two different compression molding process configurations are compared. This chapter is published in the *International Journal of Crashworthiness*.

Chapter 7 discusses intermediate strain rate tensile testing and ISO 6603-2 puncture testing (quasi-static and low velocity) of PA66/carbon fibre LFT-D material. This chapter is published in *Materials*.

Chapter 8 consists of overall conclusions, discussion, and suggestions for future work in related areas of research. Each of the chapters of the main body which are based on a publication have had any discussion of future work in the published article removed. Future work is exclusively discussed in Chapter 8.

1.4 References

1. Miller L, Soulliere K, Sawyer-Beaulieu S, et al. Challenges and alternatives to plastics recycling in the automotive sector. Waste Management and Valorization. 2017:237-266.
2. Kelly A. Composites for the 1990s. Philosophical Transactions of the Royal Society of London Series A, Mathematical and Physical Sciences. 1987;322(1567):409-423.
3. Schemme M. LFT–development status and perspectives. Reinforced Plastics. 2008;52(1):32-39.
4. Schemme M. LFT - development status and perspectives. Plastics Additives & Compounding. 2008:38-43.
5. Parton H, Verpoest I. In situ polymerization of thermoplastic composites based on cyclic oligomers. Polymer composites. 2005;26(1):60-65.
6. Thomason J. The influence of fibre length and concentration on the properties of glass fibre reinforced polypropylene: 5. Injection moulded long and short fibre PP. Composites Part A: Applied Science and Manufacturing. 2002;33(12):1641-1652.
7. Guyot H. VERTON in long fibres. Plast Mod Elastom. 1985;37(5):44-45.
8. Toll S, Aronsson C-G. Notched strength of long-and short-fibre reinforced polyamide. Composites science and technology. 1992;45(1):43-54.
9. Belbin G, Staniland P, Bhatt M, et al. Advanced Thermoplastics and their Composites [and Discussion]. Philosophical Transactions of the Royal Society of London A: Mathematical, Physical and Engineering Sciences. 1987;322(1567):451-464.
10. Bailey R, Davies M, Moore D. Processing property characteristics for long glass fibre reinforced polyamide. Composites. 1989;20(5):453-460.
11. Bartus S, Vaidya U, Ulven C. Design and development of a long fiber thermoplastic bus seat. Journal of Thermoplastic Composite Materials. 2006;19(2):131-154.
12. Noh W-J, Choi M-H, Choi C-H, et al. Development of Door Module Plate with Long-fiber-reinforced Thermoplastic Polypropylene. SAE Technical Paper; 2006.
13. Krause W, Henning F, Tröster S, et al. LFT-D—a process technology for large scale production of fiber reinforced thermoplastic components. Journal of Thermoplastic Composite Materials. 2003;16(4):289-302.
14. Markarian J. Long fibre reinforced thermoplastics continue growth in automotive. Plastics, Additives and Compounding. 2007;9(2):20-24.
15. van Hattum F, van Breugel S. LFT: the future of reinforced thermoplastics? Reinforced Plastics. 2001;45(6):42-44.

CHAPTER 2
LITERATURE REVIEW

The following chapters, prior to the final chapter with conclusions, consist of articles published in refereed journals (with some re-formatting for consistency to the other chapters and the required dissertation format). Each chapter includes a brief literature review focused on research directly relevant to the topics covered in that chapter. However, there are other fundamental previous works relevant to the research documented in this dissertation. Five topics are covered in this literature review chapter, namely, micromechanics, measuring fibre orientation, orientation tensors / orientation averaging, flow induced fibre orientation, and laminate theory.

2.1 Micromechanics

Mechanical properties of a composite are strongly dependent on volume fraction of the reinforcing fibre (Equation 2.1). However, manufacturing processes are generally limited to controlling weight fractions (Equation 2.2) of constituents (W_{fibre} and W_{matrix}). Volume fractions (V_{fibre} and V_{matrix}) can be computed as shown from weight fractions with the densities of each component (ρ_{fibre} and ρ_{matrix}). In some texts it is common to use an upper-case V for volume of each constituent and lower case for the volume fraction. However, the common use of the lower-case Greek letter Nu (ν) for Poisson's ratio can lead to confusion. The practice of using an upper-case V for volume fraction is adopted here.

An important consideration is the maximum volume fraction: packing cylindrical fibres firmly in contact in bundles leaves gaps which will either be voids or contain the matrix material. Fibres in direct contact are of course not properly wetted and so there will be no load transfer between fibres in the direct fibre-to-fibre contact regions. Additionally, only unidirectional fibre allows for this theoretical maximum fibre volume fraction (in the range of 80% to 90%) [1]. If the fibre orientation is 3D random the theoretical maximum fibre volume fraction is greatly reduced [2]. Therefore, at higher volume fractions, fibre tows may not disperse/wet-out effectively.

$$V_{fibre} + V_{matrix} + V_{voids} = 1$$

Equation 2.1

$$W_{fibre} + W_{matrix} = \rho_{fibre}V_{fibre} + \rho_{matrix}V_{matrix} = 1 \qquad \text{Equation 2.2}$$

The simplest models for determining the mechanical properties of a composite material from the mechanical properties of the constituent materials are the rule of mixtures and the inverse rule of mixtures. The rule of mixtures (Equation 2.3) is the result of assuming fibre (continuous) and matrix undergo equal deformation with load distribution through each component proportional to the stiffness of each component. E_{11} is the elastic modulus of a unidirectional fibre composite material in the fibre direction. $E_{fibre}$is the elastic modulus of the fibre and $E_{matrix}$is the elastic modulus of the matrix. The rule of mixtures also applies to computing mass properties. The inverse rule of mixtures

(Equation 2.4) is based on a load applied perpendicular to the fibre direction. It assumes the load is not divided between the fibre and matrix (i.e., fibre and matrix are in series and each carry the full load) and deformation of each component is not equal but is proportional to the compliance of each component. It should be noted that carbon fibres are not isotropic and will have a transverse modulus significantly lower than the longitudinal modulus due to their microstructure [3].

$$E_{11} = V_{fibre}E_{fibre} + V_{matrix}E_{matrix} \qquad \text{Equation 2.3}$$

$$\frac{1}{E_{22}} = \frac{V_{fibre}}{E_{fibre}} + \frac{V_{matrix}}{E_{matrix}} \qquad \text{Equation 2.4}$$

The rule of mixtures and inverse rule of mixtures are simple models that do not account for finite fibre length. The inverse rule of mixtures is particularly idealized in that it does not account for the fibre geometry (i.e., cylindrical shape). The inverse rule of mixtures underestimates the transverse elastic modulus and shear modulus (to which it can also be applied). These simple models are generally only useful for quick estimates of mechanical properties. Computing the full set of constitutive equations for a 3D state of stress requires more advanced models. The generalized self consistent model, presented in Appendix A, considers a cylindrical fibre embedded in a concentric annular ring of matrix which is then embedded in an infinite composite medium [4]. This model does not consider fibre length but is still useful for continuous fibre composites.

For discontinuous fibre composites, a model which includes the influence of fibre length is necessary. The semi-empirical modified Halpin-Tsai model is presented in Equation 2.5 through Equation 2.9 [5]. One equation is used to compute all elastic moduli (R) but with different values for the coefficient c for longitudinal/transverse and elastic/shear moduli as shown in Table 2.1. The modification from the original form includes a correction factor for materials with higher fibre content, Γ, which is a function of the fibre volume fraction and the maximum volume fraction (from fibre packing), Ω_{max} [6]. Poisson's ratio in the longitudinal direction (ν_{12}) is computed with the rule of mixtures and the plane strain bulk modulus, k, is given by Equation 2.9 [7].

Mori and Tanaka [8] developed a fully analytical model based on the misfitting inclusion principle of Eshelby [9] (see Appendix B for the Mori-Tanaka model).

$$\frac{R_{composite}}{R_{matrix}} = \frac{1 + cDV_{fibre}}{1 - D\Gamma V_{fibre}} \qquad\qquad \text{Equation 2.5}$$

$$D = \frac{\dfrac{R_{fibre}}{R_{matrix}} - 1}{\dfrac{R_{fibre}}{R_{matrix}} + c} \qquad\qquad \text{Equation 2.6}$$

$$\Gamma = 1 + \frac{1 - \Omega_{max}}{\Omega_{max}^2} V_{fibre} \qquad\qquad \text{Equation 2.7}$$

$$\nu_{12} = \nu_{fibre}V_{fibre} + \nu_{matrix}(1 - V_{fibre}) \qquad\qquad \text{Equation 2.8}$$

$$\frac{k}{k_{matrix}} = 1 + \frac{V_{fibre}}{k_{matrix}\left(\dfrac{1}{k_{fibre} - k_{matrix}} + \dfrac{1 - V_{fibre}}{k_{matrix} + G_{matrix}}\right)} \qquad\qquad \text{Equation 2.9}$$

Table 2.1: Halpin-Tsai equation coefficient values for longitudinal, transverse, and shear moduli

R (modulus)	c
E_{11}	$2\dfrac{l}{d}$
E_{22}	2.0
G_{12}	1.0
G_{23}	1.0

2.2 Measuring Fibre Orientation

A number of methodologies have been used to measure fibre orientation: optical [10] and confocal microscopy [11], micro-computed tomography [12], and acoustic microscopy [13]. Optical microscopy is the simplest method but presents a significant challenge: a single section does not provide sufficient data to determine the orientation of each fibre as there are two possible orientations for a given cross section. Either two sections are needed or the fibre orientation data that is obtained will be incomplete, though this data may still be useful. A technique originally employed in astronomy using first moments/centroids (T_x and T_y) and second moments (T_{xx}, T_{xy}, and T_{yy}) can be used to compute the orientation of each fibre [14].

For Equation 2.10 through Equation 2.19, n is the number of pixels in each fibre cross-section and w_i is the grayscale value of each pixel (or 0/1 for a binarized image). x_i and y_i are the horizontal and vertical positions of each pixel, respectively. r_{major} and r_{minor} are the major and minor radii of the fibre cross section, respectively. ϕ is the in-plane angle of the fibre and θ is the out-of-plane angle. There are two possible out-of-plane angles. Appendix C applies this methodology in MATLAB with image analysis tools which automate the identification of fibre cross sections for which orientation is computed.

$$n = \sum_{i=1}^{n} w_i \qquad\qquad \text{Equation 2.10}$$

$$T_x = \frac{\sum_{i=1}^{n} x_i w_i}{n} \qquad\qquad \text{Equation 2.11}$$

$$T_y = \frac{\sum_{i=1}^{n} y_i w_i}{n} \qquad\qquad \text{Equation 2.12}$$

$$T_{xx} = \frac{\sum_{i=1}^{n} x_i^2 w_i}{n} - T_x^2 \qquad\qquad \text{Equation 2.13}$$

$$T_{yy} = \frac{\sum_{i=1}^{n} y_i^2 w_i}{n} - T_y^2 \qquad\qquad \text{Equation 2.14}$$

11

$$T_{xy} = \frac{\sum_{i=1}^{n} x_i y_i w_i}{n} - T_x T_y \qquad\qquad \text{Equation 2.15}$$

$$r_{major} = \sqrt{2(T_{xx} + T_{yy}) + 2\left[(T_{xx} - T_{yy})^2 + 4T_{xy}^2\right]^{0.5}} \qquad\qquad \text{Equation 2.16}$$

$$r_{minor} = \sqrt{2(T_{xx} + T_{yy}) - 2\left[(T_{xx} - T_{yy})^2 + 4T_{xy}^2\right]^{0.5}} \qquad\qquad \text{Equation 2.17}$$

$$\phi = 0.5 \cdot tan^{-1}\left(\frac{2T_{xy}}{T_{xx} - T_{yy}}\right) \qquad\qquad \text{Equation 2.18}$$

$$\theta = cos^{-1}\left(\frac{r_{minor}}{r_{major}}\right) \qquad\qquad \text{Equation 2.19}$$

2.3 Orientation Tensors and Orientation Averaging

Typical high production volume manufacturing processes employed with thermoplastics are generally only possible with discontinuous fibre. In such processes, the fibre orientation is a function of flow in the mold during the forming of the component. However, even within localized regions (at a macroscopic scale) the fibre orientation is not just a single vector but a statistical distribution, $\psi(\theta, \phi)$. For efficiency, both in terms of computing fibre orientation and storing/sharing this data, a simplified representation of the fibre orientation distribution is useful. In engineering software for process simulation and for structural design, the orientation tensor (2nd order in Equation 2.18, 4th order in Equation 2.24) proposed for use with composites by Advani and Tucker [15] has been widely adopted. This tensor is computed either from the orientation distribution (converted from the spherical to Cartesian coordinate system, Equations 2.20-2.22) or can be approximated as shown in Equation 2.23 if the direction of each of N fibres ($\vec{p}$ is a unit vector in the direction of each fibre) is known (measured using micrographs, μCT data, etc.). Equation 23 assumes the data sample is unbiased.

$$p_1 = \sin(\theta) \cos(\phi) \qquad \text{Equation 2.20}$$

$$p_2 = \sin(\theta) \sin(\phi) \qquad \text{Equation 2.21}$$

$$p_3 = \cos(\theta) \qquad \text{Equation 2.22}$$

$$a_{ij} = \oint p_i p_j \psi(\vec{p}) d\vec{p} \cong \frac{1}{N} \sum_{k=1}^{N} p_i^k p_j^k \qquad \text{Equation 2.23}$$

$$a_{ijkl} = \oint p_i p_j p_k p_l \psi(\vec{p}) d\vec{p} \qquad \text{Equation 2.24}$$

The trace of the 2nd order orientation tensor must be unity (since $\vec{p}$ is a unit vector). Additionally, the tensor is symmetric. Examples of orientation tensors for simple orientation states are given in Equation 2.25 (unidirectional) and Equation 2.26 (planar random). Higher order orientation tensors can be computed and are of importance since

13

using orientation tensors to compute mechanical properties requires both the 2nd and 4th order orientation tensors. As discussed below, models of flow induced fibre orientation also require both the 2nd and 4th order tensors. If the orientations of all fibres (or a sufficient sample) are known, both the 2nd and 4th order tensors can be directly computed. However, in the case where orientation is computed with a process model, the output of most commercial software will include only the 2nd order tensors. If this output is mapped to a structural model and used to compute mechanical properties, the 4th order tensor is estimated with a closure approximation. One of the simplest closure approximations is the quadratic closure (Equation 2.27). The quadratic closure is exact for unidirectional fibre but is not exact for random fibre orientation. A number of closure approximations exist which are more accurate across a range of fibre orientation states [16,17].

$$a_{ij} = \begin{bmatrix} 1 & 0 & 0 \\ 0 & 0 & 0 \\ 0 & 0 & 0 \end{bmatrix}$$
Equation 2.25

$$a_{ij} = \begin{bmatrix} 0.5 & 0 & 0 \\ 0 & 0.5 & 0 \\ 0 & 0 & 0 \end{bmatrix}$$
Equation 2.26

$$a_{ijkl} = a_{ij} a_{kl}$$
Equation 2.27

Orientation averaging is the method by which orientation tensors are used to compute mechanical properties using micromechanics models which assume unidirectional fibre orientation. The stiffness tensor (Q_{ij}, Equations 2.29-2.34) of a transversely isotropic material (i.e., unidirectional fibre composite) is shown here as a precursor to presenting orientation averaging. For a unidirectional fibre composite: E_{11} is the longitudinal elastic modulus, G_{12} is the longitudinal shear modulus, G_{23} is the transverse shear modulus, k is the plane strain bulk modulus, and v_{12} is the longitudinal Poisson's ratio. The equations for orientation averaging are presented in Equations 2.35-2.40. δ_{ij} is the unit tensor where $\delta_{ij} = 1$ when $i = j$ and $\delta_{ij} = 0$ when $i \neq j$.

$$\sigma_i = Q_{ij}\varepsilon_j \qquad\qquad \text{Equation 2.28}$$

$$Q_{ij} = \begin{bmatrix} Q_{11} & Q_{12} & Q_{12} & 0 & 0 & 0 \\ Q_{12} & Q_{22} & Q_{23} & 0 & 0 & 0 \\ Q_{12} & Q_{23} & Q_{22} & 0 & 0 & 0 \\ 0 & 0 & 0 & \dfrac{Q_{22}-Q_{23}}{2} & 0 & 0 \\ 0 & 0 & 0 & 0 & Q_{66} & 0 \\ 0 & 0 & 0 & 0 & 0 & Q_{66} \end{bmatrix} \qquad\qquad \text{Equation 2.29}$$

$$Q_{11} = E_{11} + 4v_{12}^2 k \qquad\qquad \text{Equation 2.30}$$
$$Q_{12} = 2kv_{12} \qquad\qquad \text{Equation 2.31}$$

$$Q_{22} = G_{23} + k \qquad\qquad \text{Equation 2.32}$$

$$Q_{23} = -G_{23} + k \qquad\qquad \text{Equation 2.33}$$

$$Q_{66} = G_{12} \qquad\qquad \text{Equation 2.34}$$

$$\begin{aligned} Q'_{ijkl} = B_1 a_{ijkl} &+ B_2\left(a_{ij}\delta_{kl} + a_{kl}\delta_{ij}\right) \\ &+ B_3\left(a_{ik}\delta_{jl} + a_{il}\delta_{jk} + a_{jl}\delta_{ik} + a_{jk}\delta_{il}\right) + B_4\delta_{ij}\delta_{kl} \\ &+ B_5\left(\delta_{ik}\delta_{jl} + \delta_{il}\delta_{jk}\right) \end{aligned} \qquad \text{Equation 2.35}$$

$$B_1 = Q_{11} + Q_{22} - 2Q_{12} - 4Q_{66} \qquad\qquad \text{Equation 2.36}$$

$$B_2 = Q_{12} - Q_{23} \qquad\qquad \text{Equation 2.37}$$

$$B_3 = Q_{66} + \frac{Q_{23} - Q_{22}}{2} \qquad\qquad \text{Equation 2.38}$$

$$B_4 = Q_{23} \qquad\qquad \text{Equation 2.39}$$

$$B_5 = \frac{Q_{22} - Q_{23}}{2} \qquad\qquad \text{Equation 2.40}$$

2.4 Flow Induced Fibre Orientation

Though not of critical relevance to the content of this dissertation, another important area of prior research for discontinuous fibre composites is flow induced fibre orientation. Fibre orientation at each point in a practical industrial component will be the result of the initial fibre orientation (i.e., aligned as it passes through the gate of an injection mold or the more random initial fibre orientation of a compression molding charge) and the flow in the mold. The first models of fibre orientation associated with material flow are based on the work of Jeffery [18] who developed a model for the motion of an ellipsoid in a viscous fluid (Equation 2.41). v_x and v_y are the flow field velocity components in the x-direction and y-direction, respectively. r_e is the equivalent ellipsoidal axis ratio [19].

$$\frac{d\phi}{dt} = \frac{r_e^2}{r_e^2 + 1}\left[-sin(\phi)\,cos(\phi)\frac{\partial v_x}{\partial x} - sin^2(\phi)\frac{\partial v_x}{\partial y} + cos^2(\phi)\frac{\partial v_y}{\partial x}\right.$$
$$\left. + sin(\phi)\,cos\,(\phi)\frac{\partial v_y}{\partial y}\right]$$
$$- \frac{1}{r_e^2 + 1}\left[-sin(\phi)\,cos(\phi)\frac{\partial v_x}{\partial x} - sin^2(\phi)\frac{\partial v_y}{\partial x}\right.$$
$$\left. + cos^2(\phi)\frac{\partial v_x}{\partial y} + sin(\phi)\,cos\,(\phi)\frac{\partial v_y}{\partial y}\right]$$

Equation 2.41

This model predicts the overall trend of through thickness fibre alignment observed in many FRP components: fibre is aligned with the flow direction due to shear at the walls of the mold (the skin of the part) and is generally perpendicular to the skin in the core due to in-plane stretching of material is it exits the narrow gate and fills a section generally much wider than the gate. Figure 2.1 shows an example of skin/core/skin fibre orientation, note this is a MuCell material sample which presents a more complicated through thickness structure due to the foamed core. The model by Jeffery was adapted to apply to the orientation tensor (rather than the angle of a single fibre as in Equation 2.41) by Tucker and Folgar [20]. Improved models of flow induced fibre orientation have been developed to account for various effects, i.e. fibre interactions and the effect of fibres on viscosity [21,22].
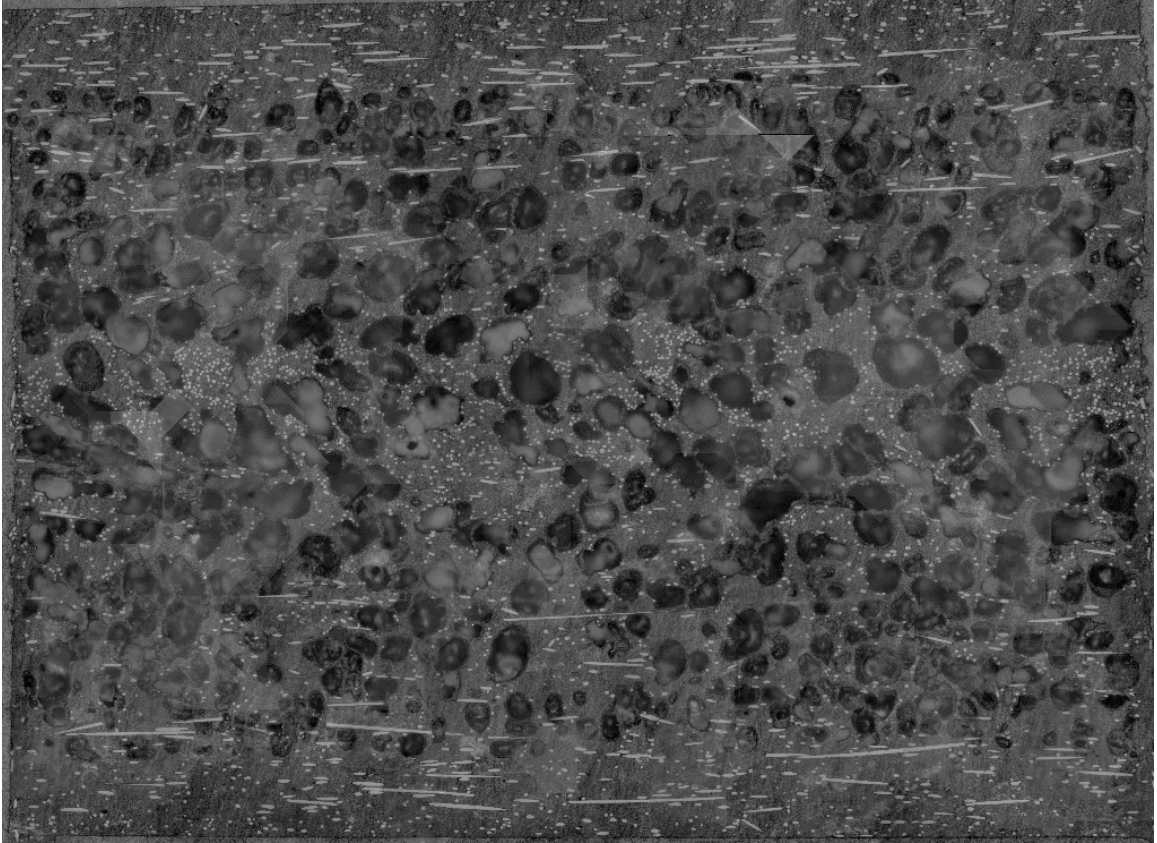
Figure 2.1: Example of skin/core/skin fibre orientation through the thickness of an injection molded FRP component

2.5 Fibre Length

For discontinuous fibre composites, fibre length can be quantified with a statistical distribution. If this statistical distribution, $N(l)$, is known, the stiffness tensor for a transversely isotropic unidirectional fibre material can be averaged as shown in Equation 2.42 prior to orientation averaging to incorporate the effect of fibre length on stiffness [23]. Note that fibre length distributions obtained experimentally, $\Lambda(l)$, should be adjusted for selection bias if the sampling region is not significantly larger than the maximum fibre length using Equation 2.43 where d_{plug} is the diameter of a plug of epoxy used to extract a sample of fibres (after removing the original matrix material, e.g., by pyrolysis) [24]. This correction assumes the fibres extracted are longer than the diameter of this extracted sample, a common technique is to burn off the original matrix and create a small 'plug' of epoxy to pull a sample of fibres.

$$Q_{ij_{N(l)}} = \frac{\int_0^\infty Q_{ij}\left(\frac{l}{d}\right) N(l)dl}{\int_0^\infty N(l)dl}$$

Equation 2.42

$$N(l) = \Lambda(l)\frac{\pi d_{plug}}{\pi d_{plug} + 4l}$$

Equation 2.43

2.6 Laminate Theory

Many composites are laminates constructed from layers/lamina of woven continuous fibre ultimately impregnated with matrix. Each layer may have a different orientation. Laminate theory is a basis for models of such structures. If the through thickness fibre orientation distribution is discretized (e.g., skin/core/skin structure), a discontinuous fibre composite can be approximated as a laminate. There are a number of assumptions for the model included here [25]:

1) The thickness of the laminate, t, is much smaller than the other overall dimensions and is uniform.
2) Displacements u, v, and w (in x, y, and z directions, respectively) are small compared to laminate thickness. In-plane displacements, u and v, are linear functions of the z-coordinate.
3) In-plane strains, ε_x, ε_y, and γ_{xy}, are small (much less than unity).
4) Transverse shear strains, γ_{xz} and γ_{yz}, are negligible.
5) Transverse normal strain, ε_z, is negligible.
6) Hooke's law applies to each lamina.
7) Transverse shear stresses, τ_{xz} and τ_{yz}, on the outer surfaces of the laminate $\left(z = \pm\frac{t}{2}\right)$ are zero.

The resulting equations (Equations 2.44 – 2.47) relate forces (N_x, N_y, and N_{xy}) and moments (M_x, M_y, and M_{xy}) per unit length to midplane strains (ε_x, ε_y, and γ_{xy}) and curvatures (κ_x, κ_y, and κ_{xy}) where $\left(Q_{ij}\right)_m$ is the lamina stiffness tensor of ply m, z_m is the position of the innermost surface of ply m. Note that M_x is not the moment about the x axis, it is the bending moment about the y axis which causes curvature κ_x. This model does not account for warping of the cross section / transverse shear deformation. Christensen [26] developed one such model by approximating displacements as nonlinear functions of the z coordinate.

$$\begin{Bmatrix} N_x \\ N_y \\ N_{xy} \\ M_x \\ M_y \\ M_{xy} \end{Bmatrix} = \begin{bmatrix} A_{11} & A_{12} & A_{16} & B_{11} & B_{12} & B_{16} \\ A_{12} & A_{22} & A_{26} & B_{12} & B_{22} & B_{26} \\ A_{16} & A_{26} & A_{66} & B_{16} & B_{26} & B_{66} \\ B_{11} & B_{12} & B_{16} & D_{11} & D_{12} & D_{16} \\ B_{12} & B_{22} & B_{26} & D_{12} & D_{22} & D_{26} \\ B_{16} & B_{26} & B_{66} & D_{16} & D_{26} & D_{66} \end{bmatrix} \begin{Bmatrix} \varepsilon_x \\ \varepsilon_y \\ \gamma_{xy} \\ \kappa_x \\ \kappa_y \\ \kappa_{xy} \end{Bmatrix} \qquad \text{Equation 2.44}$$

$$A_{ij} = \sum_{m=1}^{M} (Q_{ij})_m (z_m - z_{m-1})$$

Equation 2.45

$$B_{ij} = \frac{1}{2} \sum_{m=1}^{M} (Q_{ij})_m (z_m^2 - z_{m-1}^2)$$

Equation 2.46

$$D_{ij} = \frac{1}{3} \sum_{m=1}^{M} (Q_{ij})_m (z_m^3 - z_{m-1}^3)$$

Equation 2.47

Note that for a symmetric laminate all terms B_{ij} are 0. A symmetric laminate with no moments applied (i.e., only forces) reduces Equation 2.44 to Equation 2.48. The inverted relationship where strains are calculated from applied forces is given in Equation 2.49. The resulting effective elastic modulus for the longitudinal and transverse directions are given by Equation 2.50 and Equation 2.51, respectively.

$$\begin{Bmatrix} N_x \\ N_y \\ N_{xy} \end{Bmatrix} = \begin{bmatrix} A_{11} & A_{12} & A_{16} \\ A_{12} & A_{22} & A_{26} \\ A_{16} & A_{26} & A_{66} \end{bmatrix} \begin{Bmatrix} \varepsilon_x \\ \varepsilon_y \\ \gamma_{xy} \end{Bmatrix}$$

Equation 2.48

$$\begin{Bmatrix} \varepsilon_x \\ \varepsilon_y \\ \gamma_{xy} \end{Bmatrix} = \begin{bmatrix} A'_{11} & A'_{12} & A'_{16} \\ A'_{12} & A'_{22} & A'_{26} \\ A'_{16} & A'_{26} & A'_{66} \end{bmatrix} \begin{Bmatrix} N_x \\ N_y \\ N_{xy} \end{Bmatrix}$$

Equation 2.49

$$E_x = \frac{\sigma_x}{\varepsilon_x} = \frac{N_x/t}{A'_{11}N_x} = \frac{1}{tA'_{11}}$$

Equation 2.50

$$E_y = \frac{\sigma_y}{\varepsilon_y} = \frac{N_y/t}{A'_{22}N_y} = \frac{1}{tA'_{22}}$$

Equation 2.51

Similarly, for a symmetric laminate with no forces applied (i.e., only moments) Equation 2.44 reduces to Equation 2.52. The inverted relationship between curvatures and moments is given by Equation 2.53. The resulting flexural modulus for the x-direction is given by Equation 2.54 (Equation 2.55 is the flexural modulus for the y-direction).

$$\begin{Bmatrix} M_x \\ M_y \\ M_{xy} \end{Bmatrix} = \begin{bmatrix} D_{11} & D_{12} & D_{16} \\ D_{12} & D_{22} & D_{26} \\ D_{16} & D_{26} & D_{66} \end{bmatrix} \begin{Bmatrix} \kappa_x \\ \kappa_y \\ \kappa_{xy} \end{Bmatrix}$$
Equation 2.52

$$\begin{Bmatrix} \kappa_x \\ \kappa_y \\ \kappa_{xy} \end{Bmatrix} = \begin{bmatrix} D'_{11} & D'_{12} & D'_{16} \\ D'_{12} & D'_{22} & D'_{26} \\ D'_{16} & D'_{26} & D'_{66} \end{bmatrix} \begin{Bmatrix} M_x \\ M_y \\ M_{xy} \end{Bmatrix}$$
Equation 2.53

$$E_{fx} = \frac{12}{t^3 D'_{11}}$$
Equation 2.54

$$E_{fy} = \frac{12}{t^3 D'_{22}}$$
Equation 2.55

Through-thickness changes in material properties can result in a difference between the elastic modulus under a tensile or compressive force and the flexural modulus under a bending moment. The flexural modulus increases as the outermost plies are stiffer in the stressed direction. Comparing the flexural modulus and elastic modulus provides insight into the through thickness structure. This analysis applies not only to laminates but to discontinuous fibre materials with a through thickness change in fibre orientation due to the manufacturing process.

2.7 References

1. Gibson RF. Principles of composite material mechanics. Vol. 218. CRC press; 2012.
2. Evans K, Gibson A. Prediction of the maximum packing fraction achievable in randomly oriented short-fibre composites. Composites science and technology. 1986;25(2):149-162.
3. Tane M, Okuda H, Tanaka F. Nanocomposite microstructures dominating anisotropic elastic modulus in carbon fibers. Acta Materialia. 2019;166:75-84.
4. Christensen R, Lo K. Solutions for effective shear properties in three phase sphere and cylinder models. Journal of the Mechanics and Physics of Solids. 1979;27(4):315-330.
5. Halpin J, Kardos J. The Halpin-Tsai equations: a review. Polymer Engineering & Science. 1976;16(5):344-352.
6. Nielsen LE. Generalized equation for the elastic moduli of composite materials. Journal of Applied Physics. 1970;41(11):4626-4627.
7. Christensen RM. A critical evaluation for a class of micro-mechanics models. Journal of the Mechanics and Physics of Solids. 1990;38(3):379-404.
8. Mori T, Tanaka K. Average stress in matrix and average elastic energy of materials with misfitting inclusions. Acta metallurgica. 1973;21(5):571-574.
9. Eshelby JD, editor The determination of the elastic field of an ellipsoidal inclusion, and related problems. Proc. R. Soc. Lond. A; 1957: The Royal Society.
10. Fakirov S, Fakirova C. Direct determination of the orientation of short glass fibers in an injection-molded poly (ethylene terephthalate) system. Polymer composites. 1985;6(1):41-46.
11. Thomason J, Knoester A. Application of confocal scanning optical microscopy to the study of fibre-reinforced polymer composites. Journal of materials science letters. 1990;9(3):258-262.
12. Pinter P, Dietrich S, Bertram B, et al. Comparison and error estimation of 3D fibre orientation analysis of computed tomography image data for fibre reinforced composites. NDT & E International. 2018;95:26-35.
13. Lisy F, Hiltner A, Baer E, et al. Application of scanning acoustic microscopy to polymeric materials. Journal of applied polymer science. 1994;52(2):329-352.
14. Stobie R. Analysis of astronomical images using moments. Journal of the British Interplanetary Society. 1980;33:323-326.
15. Advani S, Tucker C. The use of tensors to describe and predict fiber orientation in short fiber composites. Journal of Rheology (1978-present). 1987;31(8):751-784.
16. Advani SG, Tucker III CL. Closure approximations for three-dimensional structure tensors. Journal of Rheology. 1990;34(3):367-386.
17. Cintra Jr JS, Tucker III CL. Orthotropic closure approximations for flow-induced fiber orientation. Journal of Rheology (1978-present). 1995;39(6):1095-1122.
18. Jeffery GB. The motion of ellipsoidal particles immersed in a viscous fluid. Proceedings of the Royal Society of London Series A, Containing papers of a mathematical and physical character. 1922;102(715):161-179.
19. Harris J, Pittman J. Equivalent ellipsoidal axis ratios of slender rod-like particles. Journal of Colloid and Interface Science. 1975;50(2):280-282.

20. Folgar F, Tucker III CL. Orientation behavior of fibers in concentrated suspensions. Journal of reinforced plastics and composites. 1984;3(2):98-119.
21. Phelps JH, Tucker III CL. An anisotropic rotary diffusion model for fiber orientation in short-and long-fiber thermoplastics. Journal of Non-Newtonian Fluid Mechanics. 2009;156(3):165-176.
22. Wang J, O'Gara JF, Tucker III CL. An objective model for slow orientation kinetics in concentrated fiber suspensions: Theory and rheological evidence. Journal of Rheology. 2008;52(5):1179-1200.
23. Nguyen B, Bapanapalli S, Holbery J, et al. Fiber length and orientation in long-fiber injection-molded thermoplastics—Part I: Modeling of microstructure and elastic properties. Journal of Composite Materials. 2008;42(10):1003-1029.
24. Kunc V, Frame BJ, Nguyen BN, et al. Fiber length distribution measurement for long glass and carbon fiber reinforced injection molded thermoplastics. Research Gate. 2007.
25. Whitney JM. Structural analysis of laminated anisotropic plates. Routledge; 2018.
26. Christensen RM. Mechanics of composite materials. Courier Corporation; 2012.

CHAPTER 3

EXPERIMENTAL CHARACTERIZATION AND MODELLING OF THE
ELASTIC PROPERTIES OF DIRECT COMPOUNDED COMPRESSION
MOLDED CARBON FIBRE/POLYAMIDE 6 LONG FIBRE THERMOPLASTIC

3.1 Introduction

Tensile stress-strain data is one of the most fundamental property sets for mechanical engineers evaluating materials for an application. This chapter is therefore the logical starting point for this dissertation in terms of the body of work completed, comprising a study evaluating eight PA6/carbon fibre LFT-D process configurations with fibre content between 9 and 25%. The material/process configurations were selected by collaborators producing the material at the Fraunhofer Project Centre in London, Ontario. In addition to tensile tests, three-point bending tests were completed to assess the effect on mechanical properties of the through-thickness fibre orientation. Furthermore, the fibre orientation and fibre length distributions were directly characterized, and micromechanics models were evaluated to compare the predicted mechanical properties using these distributions to experimental tensile and three-point bending test data.

Long fibre thermoplastics (LFTs) contain fibres with an average aspect ratio greater than 100 (approximate fibre length of 1-2 mm) [1,2]. These materials have a number of advantages over other FRPs. Several mass production systems exist and have been in use in the automotive industry for many years [3]. One variation, LFT-D with direct/inline compounding (ILC), can yield fibre lengths approximately an order of magnitude larger than from pellets. Tensile strength and fatigue characteristics are lower than a similar continuous fibre material but technologies exist for automated addition of localized continuous fibre reinforcement to discontinuous fibre parts [4]. Direct compounding also permits the use of any polymer/fibre/additive combination in any proportion permitted by the fibre orientation state in the compounding extruder. However, this flexibility in terms of material formulation comes at the cost of requiring personnel with the necessary expertise.

A large number of recent publications document research on long fibre thermoplastics. Teixeira et al. [5] optimized an injection molding process in terms of barrel temperature, injection speed, and screw speed to maximize flexural strength and surface quality (the latter in terms of roughness, gloss, and qualitative assessment by three experts). Flexural strength was strongly influenced by barrel temperature and screw speed. Surface quality was a function of barrel temperature and injection speed. An analysis of the microstructure found that the increase in flexural strength was a result of a change in through thickness fibre orientation such that increased fibre alignment occurred in the skin region. Luo et al. [6] mechanically characterized injection molded long carbon fibre / polyamide 6 prepared from novel aligned fibre core / unreinforced thermoplastic shell pellets. Additionally, the sizing treatment from the fibre supplier was removed and a different treatment was applied in a bath where the concentration was optimized. Increased sizing concentration improved the fibre distribution, melt flow rate, and mechanical properties up to 22%. Higher concentrations formed a thick layer of sizing material which negatively affected the mechanical properties of the fibre/matrix interface.

Few publications exist documenting mechanical properties of direct or in-line compounded materials. McLeod et al. [7] compared direct compounded injection and compression molded polypropylene/glass fibre. Significantly longer fibres were observed in the compression molding charge with respect to locations within the molded part and the nozzle of the injection molding machine where fibre length was significantly degraded. Poorer fibre dispersion was noted for compression molded material with fibre rich/depleted zones. Flexural modulus was similar for compression and injection molded specimens. However, flexural yield strength was significantly higher for specimens extracted from compression molded parts.

Rohan et al. [8] studied the effect of processing parameters including fibre loading, plastificate placement, and screw speed on the mechanical characteristics of carbon/PA6 LFT-D material. The authors note that short fibres play a critical role in material performance, particularly for flexure, and hypothesize that this is associated with fibre bundling (poor tow dispersion). Additional observations include increasing alignment of fibre in the flow direction and anisotropy of mechanical characteristics with distance from

25

the charge/plastificate and negligible variation in fibre content within the compression molded panel. Zhang and Johrendt [9] employed an artificial neural network to model the sensitivity of mechanical properties to process parameters including barrel temperatures, screw speeds, motor torques, and throughput (mass flow rate). Experimental data for six different fibre weight fractions ranging from 25 to 50% were collected and used to train a feed-forward back propagation network where there were 4 outputs: Young's modulus and tensile strength for 0° and 90°. Process parameters associated with the fibre-matrix compounding extruder were found to have greater influence on mechanical properties than the polymer/additives extruder.

Modelling of long fibre thermoplastics shares many similarities with the modelling process for short fibre materials. Local fibre orientation is often described with the orientation tensor proposed by Advani and Tucker [10]. Note that the fibre orientation distribution can be expected to vary in every direction including through the thickness. Commercial process modelling software is often limited to output of the 2nd order tensor. However, orientation averaging [11] to obtain mechanical characteristics by weighted averaging of unidirectional mechanical characteristics also requires the 4th order orientation tensor.

A number of closure approximations exist to estimate the 4th order tensor from the 2nd order tensor [10,12]. A number of micromechanics models exist for unidirectional fibre composite elasticity including: rule of mixtures (and its inverse), the Halpin-Tsai equations [13], the generalized self-consistent (GSC) model, and the Mori-Tanaka model [7]. The latter was developed using the Eshelby method [8] for generating the stiffness tensor of an inclusion in a matrix.

A number of publications exist for limited experimental characterization and modelling of LFT materials. Garesci and Fliegener [9] reviewed the state of the art for this modelling process for the elastic response and validated their results with a limited number of non-destructive tensile tests. This study used μCT data to obtain the fibre orientation distribution (in the form of the 2nd and 4th order tensors). Planar fibre and a symmetric orientation distribution were assumed. Fibre length distribution was obtained through image analysis after matrix burn off. The Halpin-Tsai equations were employed to obtain

the stiffness tensor for a unidirectional material. Nguyen et al. [11] documented their efforts to model the elastic properties of polypropylene with glass fibre for specimens extracted from two geometries: a centre gated disk and a rectangular ISO plaque. A process modelling code developed at the University of Illinois Urbana-Champaign, ORIENT, was used to model the fibre orientation distribution as a function of flow within the mold and was validated with optical microscopy. Readers interested in ORIENT can refer to [14]. The authors note the importance of high-quality fibre orientation and length data for model accuracy.

Buck et al. [15] studied compression molded PP/GF with direct/in-line compounding. Fibre orientation was numerically predicted with Autodesk Moldflow® [16] and validated with μCT data. Finite element structural models of dynamic mechanical analysis in the form of three-point bending tests were developed and compared with experimental results. The authors employed the generalized self-consistent (GSC) micromechanics model which does not allow for including the influence of fibre length on elastic properties. Consequently, no data on the fibre length distribution is presented. Structural finite element models agree well with experiments in the flow region in the 0° direction (axis of loading aligned with flow direction). Accuracy for models of specimens loaded in the 45° and 90° directions is limited. In the charge region, models do not accurately predict material characteristics with percent error as high as 47%. However, fibre orientation within/between charges/plastificates (also referred to as unfinished product) may not be sufficiently repeatable to allow for accurate predictions of mechanical properties in this region.

3.1.1 Motivation

A moderate number of publications exist on experimental characterization and modelling of long fibre thermoplastics. However, data on compression molded material with carbon fibre reinforcement produced with direct compounding is particularly scarce. Modelling of these materials, while not presenting significant additional technical challenges with respect to glass fibre or injection molded materials, has not been documented extensively in the literature. The study by Buck et al. [15] employed an older version of Moldflow which was limited to a global fibre orientation state in the charge and only permitted the

27

diagonal of the 2nd order tensor to be specified. Newer releases of this software permit the full 2nd order tensor to be input by the user. The publication by Buck et al. [15] also includes limited material characterization in terms of the number of specimens and their orientations. As presented in this chapter, more thorough material characterization permits a better understanding of the critical parameters for both the process and structural models.

3.2 Methodology

3.2.1 Specimen Preparation

Carbon fibre/PA6 LFT-D material was manufactured by the Fraunhofer Project Centre in London, Ontario on a Dieffenbacher LFT-D-ILC manufacturing line. A schematic is provided in Figure 3.1. A Motan granule dosing system (1 – see Figure 3.1) feeds a Leistritz ZSE-60HP-28D co-rotating twin screw extruder (2). This extruder feeds molten polymer via a film die to a ZSG Leistritz ZSG-75 P-17D (3) co-rotating twin screw extruder (L/D = 17, 75 mm diameter). 100 mm by 370 mm charges exit this extruder and travel along a heated conveyor (4) and are manually placed in a 46 cm by 46 cm mold installed in a Dieffenbacher DCP-U 2500/2200 (5) press.

(a)   (b)
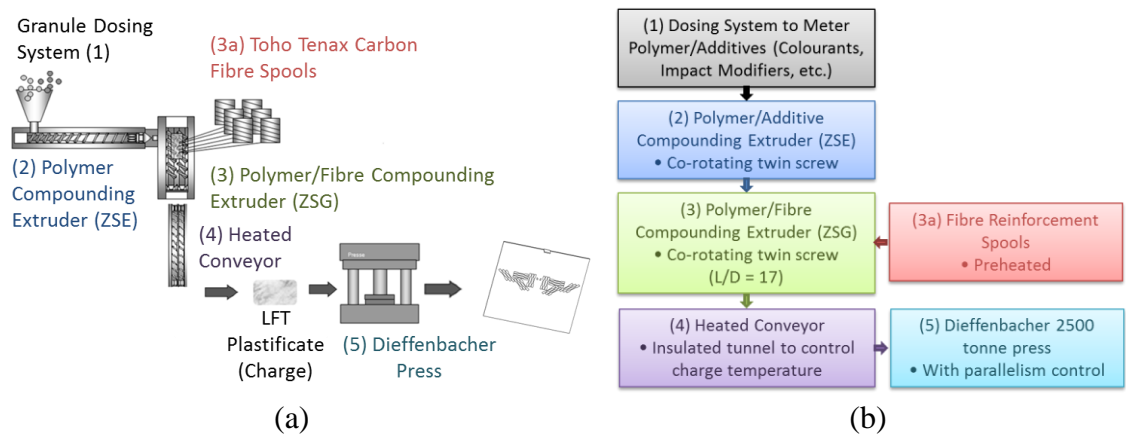
Figure 3.1: (a) Schematic and (b) Flowchart of Dieffenbacher LFT-D line at the Fraunhofer Project Centre [8]

Approximately seven 458 mm by 458 mm by 2.7 mm square plaques were provided for each of eight process configurations documented in Table 3.1. For process configurations 2 and 3, percent differences with respect to process configuration V1 are included in this table for reference. Material with fibre (Toho Tenax HTR40 F22 1550tex, 24k tow count) weight contents of 9, 12, 18, and 25% were produced. Note that this is a fibre with epoxy sizing. Subsequent research has employed carbon fibre with sizing intended for the selected matrix material. The matrix was BASF 8202 heat stabilized (HS) polyamide 6. Charge placement was asymmetric as shown in Figure 3.2 (a) with a mold coverage of approximately 14%. The formed part in the area of the mold which is covered by the charge is the 'Charge region'. The formed part in the area of the mold into which

the charge flows as the press closes is the 'Flow region'. Charge mass was defined in the manufacturing process control software to be 755 grams with approximate dimensions of 130 mm by 350 mm by 30 mm. Note that a solid rectangular prism of these dimensions would overfill the tool. A considerable amount of air is entrapped within the charge as shown in the image from computed tomography (CT) in Figure 3.3. The density of PA6/CF is approximately 1170 kg/m^3 (9% fibre weight fraction) to 1247 kg/m^3 (25%) using densities from constituent material datasheets. The mass of a solid charge without entrapped air would range from approximately 1600 to 1700 grams. The press force was 5000 kN with the speed-distance profile given in Table 3.2. The mold temperature was 120ºC and the cooling time was 30 seconds.

Table 3.1: LFT-D process/material configurations V1-V8

Trial #	Fiber weight %	Roving number	Throughput (kg/h)	Charge mass (g)	Cycle time (sec)	Fibre compounding extruder speed (rpm)	Fibre compounding extruder volume fill (%)
V1	12	23	118	755	23	61	33
V2	12	23	160 (35.6%)	755	17 (-26.1%)	83 (36.1%)	33
V3	12	35 (52.2%)	181 (53.4%)	755	15 (-34.8%)	62	50 (51.5%)
V4	18	35	118	755	23	60	32
V5	18	35	160	755	17	82	32
V6	9	17	118	755	23	62	33
V7	9	17	160	755	17	84	33
V8	25	31	109	755	25	87	20

Table 3.2: Speed-distance press profile for compression molding of material/process configurations V1-V8

Speed (mm/s)	Distance (mm)
75	50
35	35
15	15
10	0
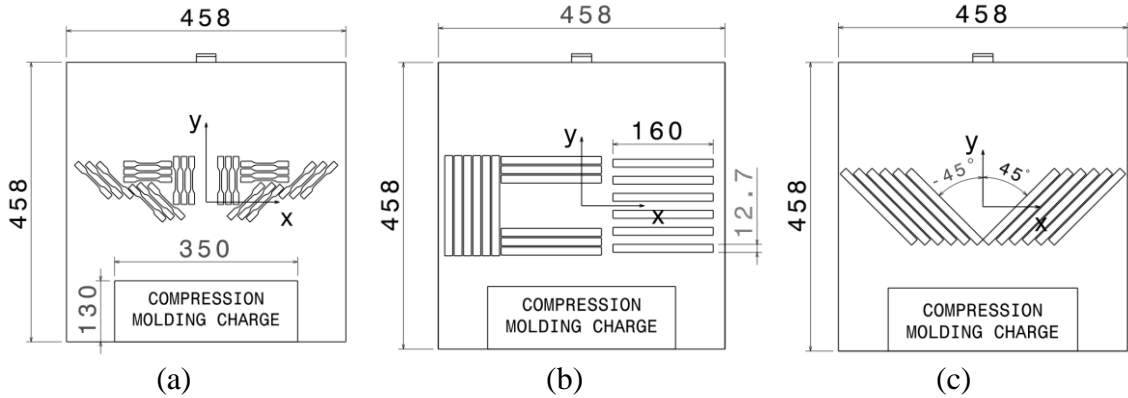
Figure 3.2: Fundamental characterization of material/process configurations V1-V8:
(a) Tensile specimen and charge configuration, (b) Flexure specimen layout (0° & 90°),
(c) Flexure specimen layout (±45°)

(a)   (b)
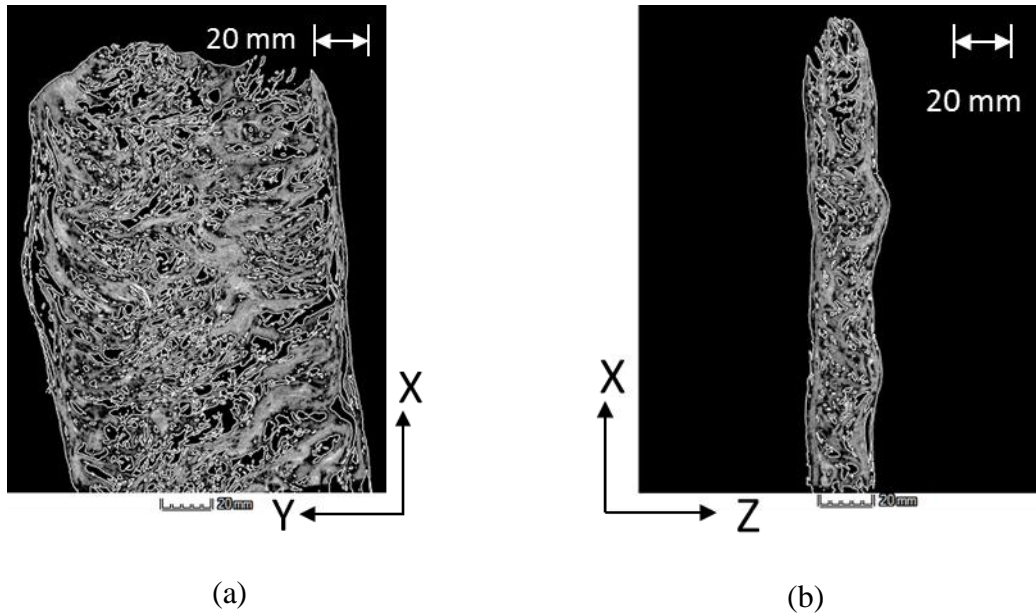
Figure 3.3: Computed tomography of a compression molding charge showing a
significant volume fraction of entrapped air: (a) top view, (b) side view

Six 0º and six 90º ASTM D638 [17] type I specimens were extracted from both the charge and flow regions of a plaque from process configuration V3 to assess the repeatability of mechanical properties within these regions. All specimens were extracted by water jet at a pressure of 345 MPa with a nozzle diameter of 0.076 mm. For all process configurations, six 0º, six 90º, six +45º, and six -45º tensile (ASTM D638 Type V specimen geometry, as shown in Figure 3.4) and flexure (ASTM D790 [18], 40:1 span to depth ratio, see Figure 3.2 for specimen dimensions) specimens were extracted from the flow region

31

immediately adjacent to the charge region for all process parameter configurations as shown in Figure 3.2. The 0° and 90° specimen layout includes extra 90° specimens as the result of an error by the water jet service provider. The original layout included only +45° specimens in the centre of the plaque. However, the parts were not cut using the provided layout. The 90° specimens in the centre of the plaque were used to characterize dried specimens for flexural modulus.
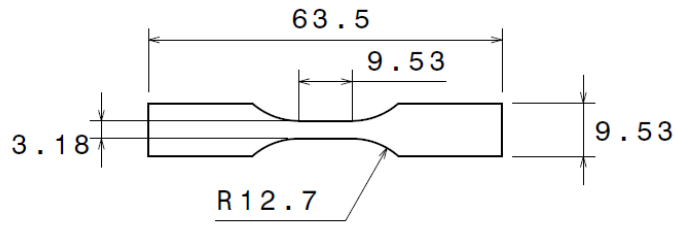
Figure 3.4: ASTM D638 Type V Specimen Geometry

3.2.2 Specimen Conditioning

Specimens were conditioned at room temperature (25℃) and approximately 30% relative humidity until saturated (material was stored under such conditions for approximately 3 years). A set of 90° flexural specimens (6 specimens for each process configuration) were dried at 80° C in a GCA Corporation Model 10 vacuum oven (20 inHg). Full sets of tensile specimens were dried for process configurations 6 and 8 (minimum and maximum fibre content). A limited amount of material did not allow for full mechanical characterization of both dried and conditioned specimens. Since stiffness and strength decrease with moisture content, practical minimum values for these properties at room temperature were acquired by characterizing conditioned specimens. For specimens of the same fibre content, moisture content, expressed as a percentage of specimen mass, was fairly consistent suggesting the moisture level in the specimens had reached equilibrium. Data on moisture content is provided in Figure 3.5. Moisture content decreased 0.034% per 1% increase in fibre content (weight fraction). An unfilled material would therefore have a stable moisture content of approximately 2.4%. This is consistent with data from the resin supplier for maximum moisture absorption under the given conditions [19].
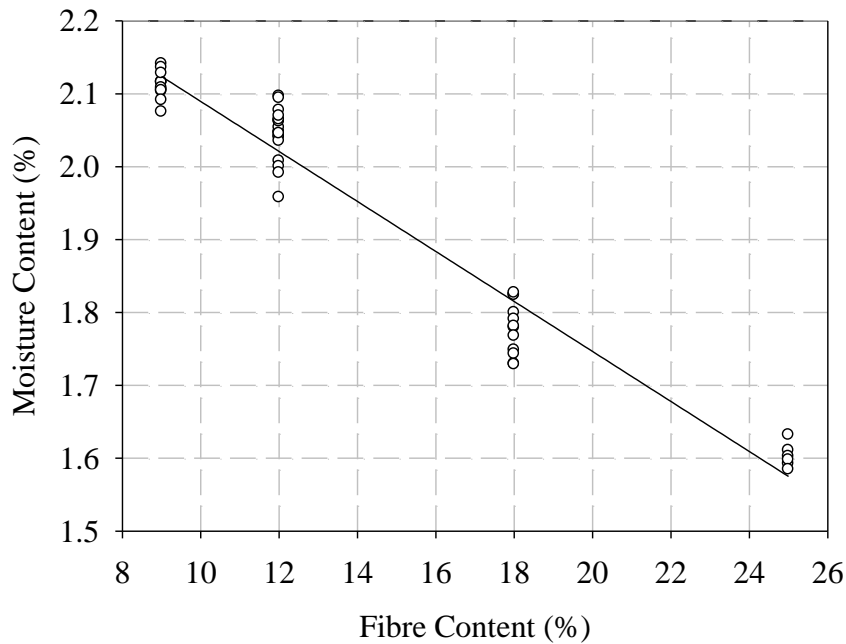
Figure 3.5: Moisture content as a function of fibre content for LFT-D material with fibre content ranging from 9% to 25%

3.2.3 Mechanical Characterization

Tensile tests were completed on an MTS EM40 Criterion electromechanical load frame with a 50 kN load cell consistent with ASTM standard D638 [17] with engineering strain rates of 0.1 min^{-1} and 0.15 min^{-1} for type I and type V specimens respectively. Three-point bending (flexure) tests were completed on the same load frame with an MTS Model 642.10B fixture consistent with ASTM standard D790 [18] (engineering strain rate of 0.01 min^{-1}). The data acquisition rate for both tensile and three-point bending tests was 100 Hz.

3.2.4 μCT Measurements of Fibre Orientation

Micro-computed tomography data was acquired by the Institute of Applied Mechanics (IAM) at the Karlsruhe Institute of Technology (KIT). Scans were carried out using an YXLON precision computed tomography system containing an open micro-focus X-ray transmission tube with tungsten target and a 2048 pixel by 2048 pixel flat panel detector from Perkin Elmer. Acceleration voltage and tube current were set to 90 kV and 0.02 mA respectively. The raw volume images with a size of 2048^3 voxels were reconstructed from 3000 projections acquired with an integration time of one second. Image resolution was

3.5 µm/voxel. Specimen location and geometry are shown in Figure 3.6 (a). Coordinates for the two specimens are (-11, -50) and (11, 50) [mm], see Figure 3.2 for coordinate system. Specimens were extracted by water jet from one plaque from process configuration V2. Fibre orientation at each voxel was computed using the structure tensor [20] with the open source software Composight [21]. Data from Composight was post-processed in MATLAB® to extract fibre orientation from voxels where high contrast indicated the presence of fibre. Second and fourth order orientation tensors were computed in MATLAB® using data from only these voxels. As a concomitant method, one CT data set was post-processed with VG Studio® to obtain the 2nd order orientation tensor.

3.2.5 Fibre Length Characterization

Fibre length characterization was completed by an industrial partner. Specimens for fibre length characterization were extracted from the flow and charge regions of process configurations 6 and 8 (minimum and maximum fibre weight fractions; 9% and 25%, respectively). Locations (-100, -70) and (-100, -222) [mm] within the compression molded plaque are shown in Figure 3.6 (b). Fibres were recovered by placing the specimens in an oven at 550°C for 30 minutes. An entangled mass of fibre was removed with forceps, placed in a petri dish with soap/water, and gently agitated. Several drops of the resulting fibre suspension were placed on a glass slide. Images were then captured with a Nikon DS-Fi1 camera and a Zeiss Axiophot transmitted light microscope. Image-Pro Plus v5.1 was employed to measure a minimum of 1000 fibre lengths for each sample.
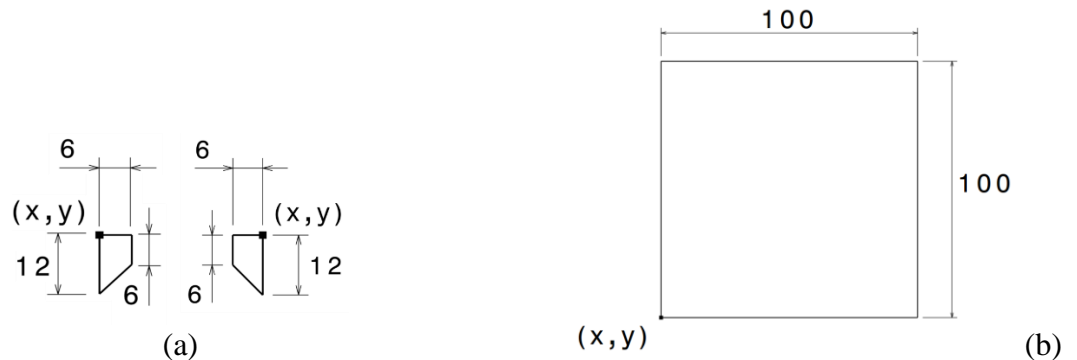
Figure 3.6: Fibre orientation and length distribution characterization: (a) CT specimen location and geometry (mm), (b) fibre length distribution specimen geometry and location (mm)

3.3 Results and Discussion

3.3.1 Uniaxial Tension

Within the charge region, there is significant overlap of measurements of elastic modulus and Poisson's ratio in the 0° and 90° directions as shown in Figure 3.7. Elastic modulus was measured through linear regression of the stress-strain response (at least 30 data points, the number of data points was selected to maximize R^2). Poisson's ratio was calculated consistent to Annex A3 of ASTM D638 [17]. In the flow region, 0° and 90° characteristics are much more distinct. Material characteristics within the charge region may not be accurately predicted with a deterministic approach if the fibre orientation within a charge is not repeatable from one charge to the next. This charge region may be of critical importance when considering applications for this material. However, a more comprehensive study of repeatability and/or the range of mechanical properties to be expected in the charge region is warranted but was not possible due to limited material. Based upon this observation, limited availability of material, and observations by other researchers [15], tensile tests were only completed for the flow region for all process configurations. The following chapters include ISO 6603-2 instrumented impact tests of both flow and charge region specimens. This method of characterization was found to be relatively insensitive to the variation in fibre orientation.
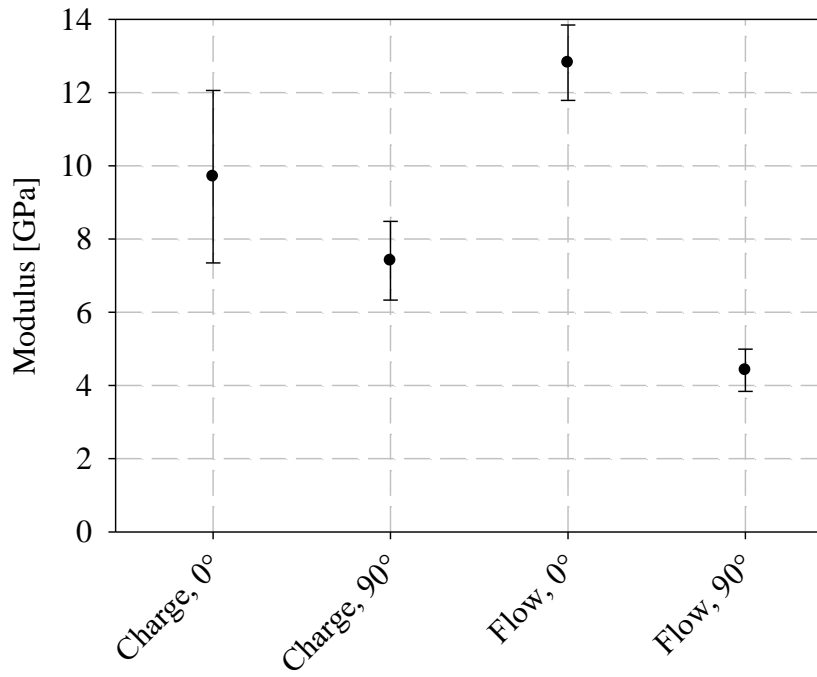
(a)
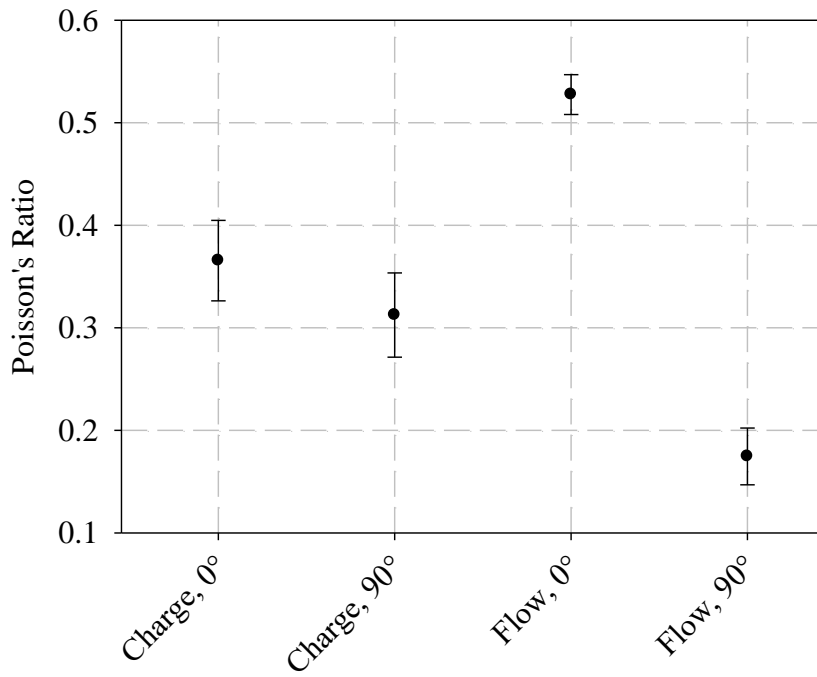
(b)

Figure 3.7: (a) Elastic modulus and (b) Poisson's ratio, 0° & 90°, flow and charge regions

Elastic modulus for the 0° and 90° directions for specimens extracted from the flow region are given in Figure 3.8 (a). Refer to Table 3.1 for the labels on the horizontal axis. A change in the fibre orientation distribution occurred with flow such that the distribution shifted from an approximately random planar state to highly anisotropic with significant alignment of fibre in the flow direction. An increase in 0° tensile elastic modulus of approximately 800 MPa per 1% fibre weight fraction was observed for the range of fibre content studied. Average 0° and 90° stress-strain responses are given in Figure 3.9. Elastic modulus for the +45° and -45° directions are presented in Figure 3.8 (b). Significant variation within each process condition and specimen orientation was observed regardless of moisture content. Further investigation of specimen locations within the flow region may be prudent to understand if more consistent data can be acquired. No trends in terms of modulus versus cycle time or throughput were noted. It was, however, observed that stiffness was consistently higher in the +45° direction compared to -45°. It is hypothesized that this is the result of fibre orientation asymmetry in the compression molding charge. Other researchers have noted a helical pattern in the fibre when studying LFT-D charges with glass fibre by computed tomography [7]. This is likely associated with the pitch of the fibre/resin compounding twin screw extruder. The Fraunhofer Project Centre may currently, or in the future, have multiple sets of screws for this extruder allowing for an investigation of this phenomenon.

Tensile strength for the eight process configurations studied are shown in Figure 3.11. In the 0° direction, an approximate increase of 7 MPa per 1% fibre weight fraction was observed. Significant variation in mechanical properties in the +/-45° directions was again observed. In addition to the increased elastic modulus (20% increase), strength was, on average, 10% higher in the +45° direction with respect to the -45° direction. This +/-45° asymmetry has a number of implications for further investigations. In developing a process model, the initial fibre orientation for the charge region should be such that this asymmetry in the fibre orientation state in the flow region is captured. Additionally, for mechanical properties (i.e., in a structural finite element model) a global orthotropic material model should not be used if the fibre orientation distribution is asymmetric. A fully anisotropic material model may be necessary.
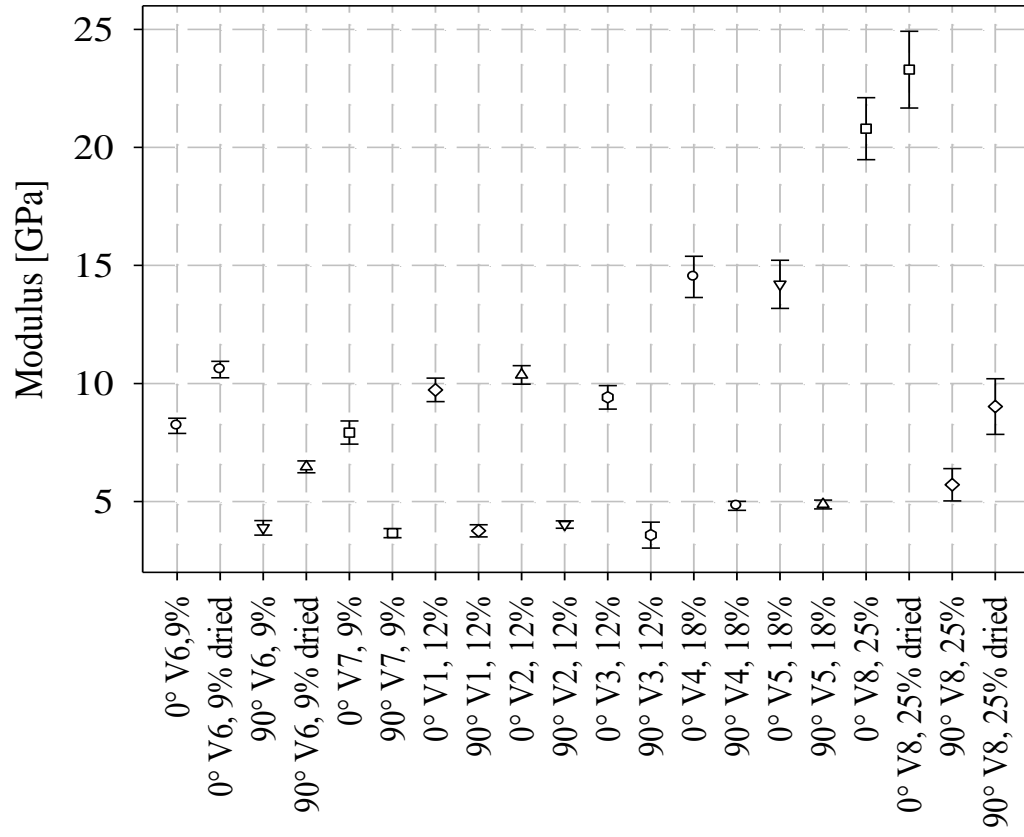
(a)
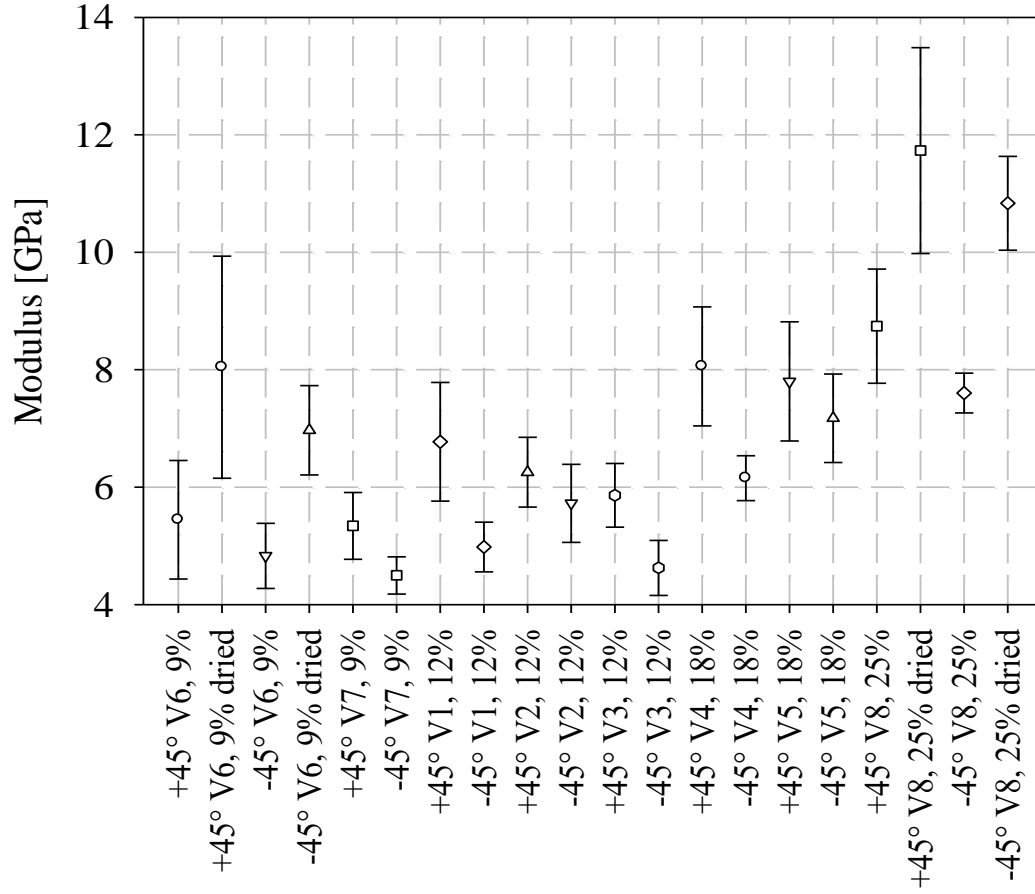
(b)

Figure 3.8: Elastic modulus for process/material configurations V1-V8:
(a) 0° & 90°, (b) +45° & -45°
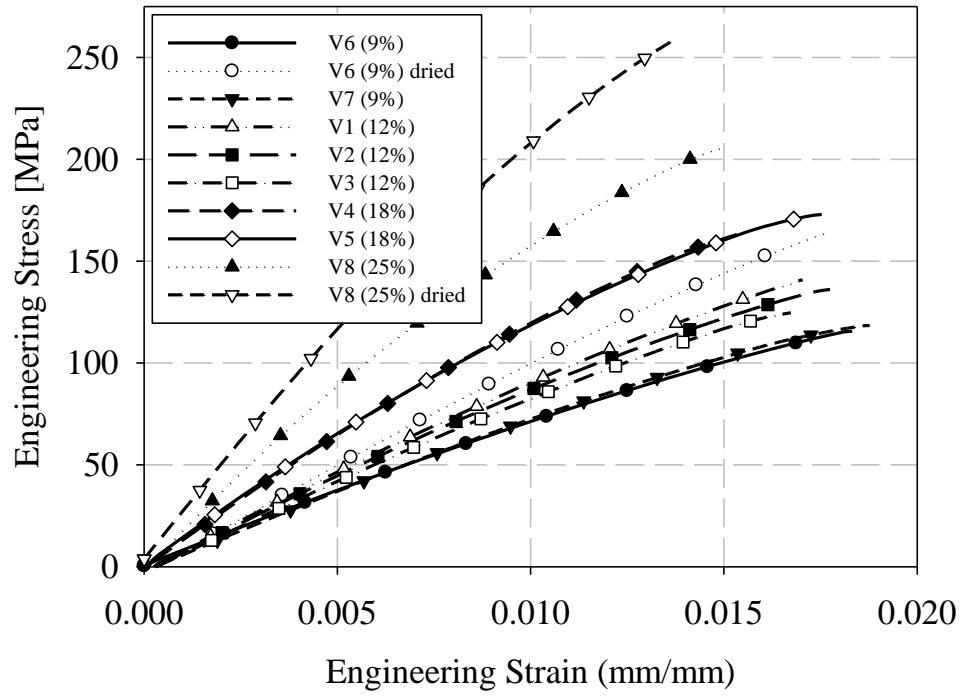
(a)
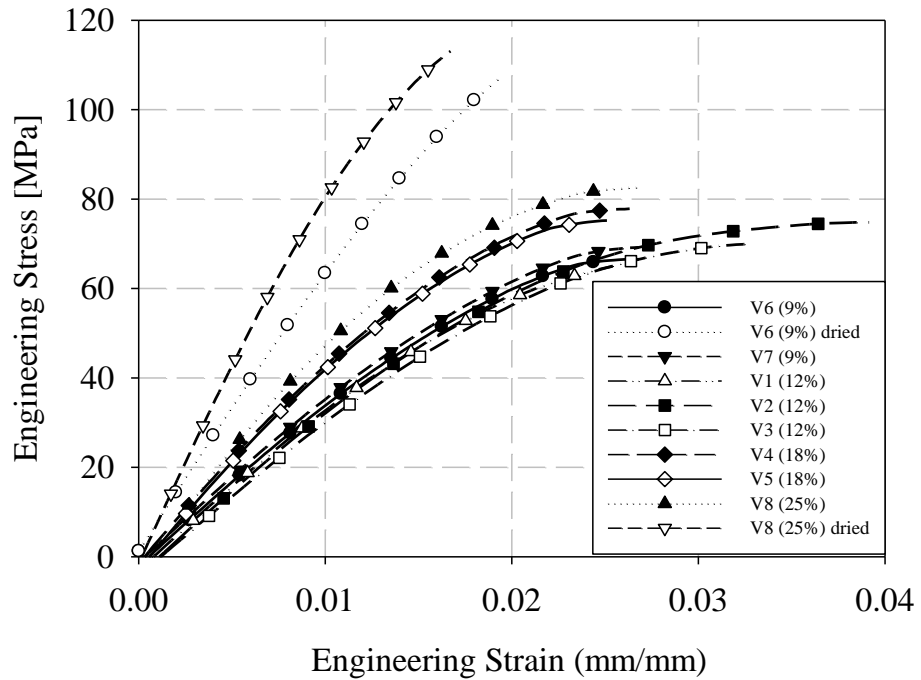
(b)

Figure 3.9: Average tensile stress-strain responses for process/material configurations
V1-V8: (a) 0° and (b) 90°
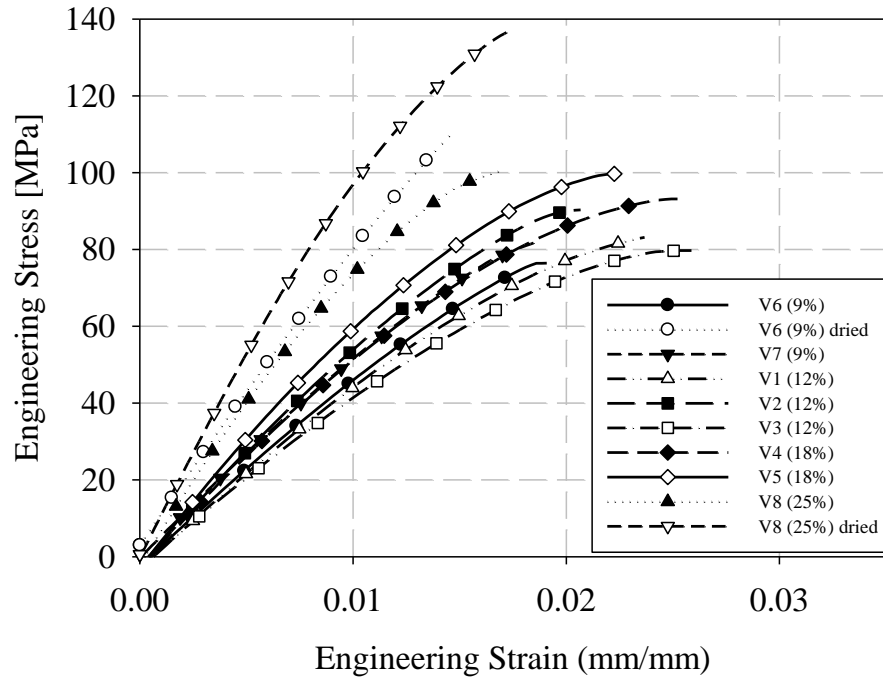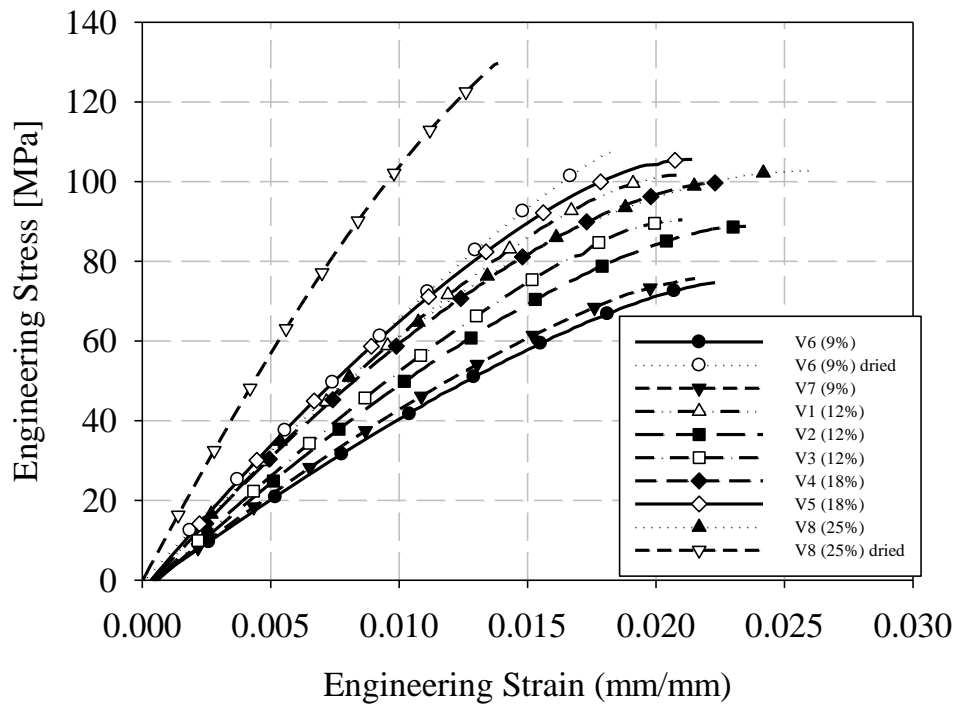
Figure 3.10: Average tensile stress-strain responses for process/material configurations
V1-V8: (a) +45° and (b) -45°

41

Engineering strain at failure is presented in Figure 3.12. In the 0° direction, where failure is primarily a function of the low strain to failure of the carbon fibre, strain to failure for the LFT specimens is relatively consistent for each process configuration. Significant scatter in the 90°, +45°, and -45° directions introduces challenges for identifying any meaningful trends. Strain to failure is, on average, 18% lower in the +45° direction with respect to the -45° direction further reinforcing previously presented evidence of FOD asymmetry which may be associated with the initial fibre orientation in the charge/plastificate. Drying the specimens has a significant effect on the strain at failure measurement.
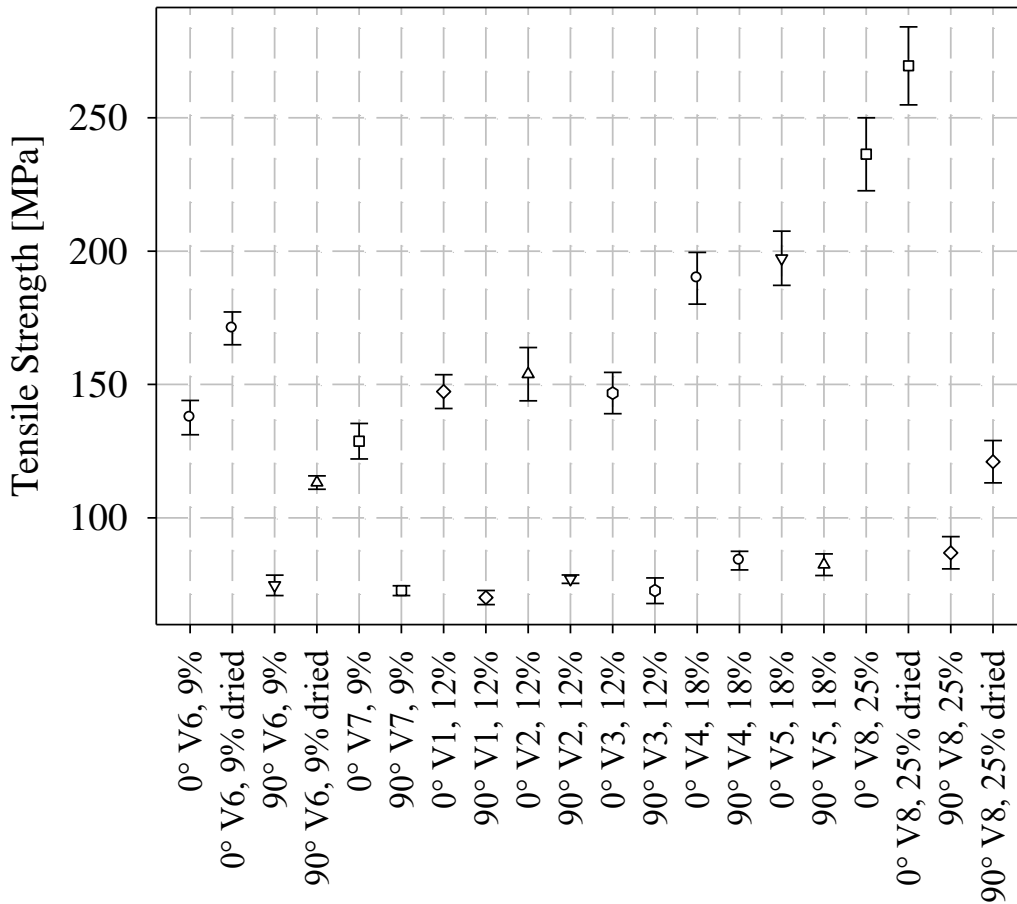
(a)
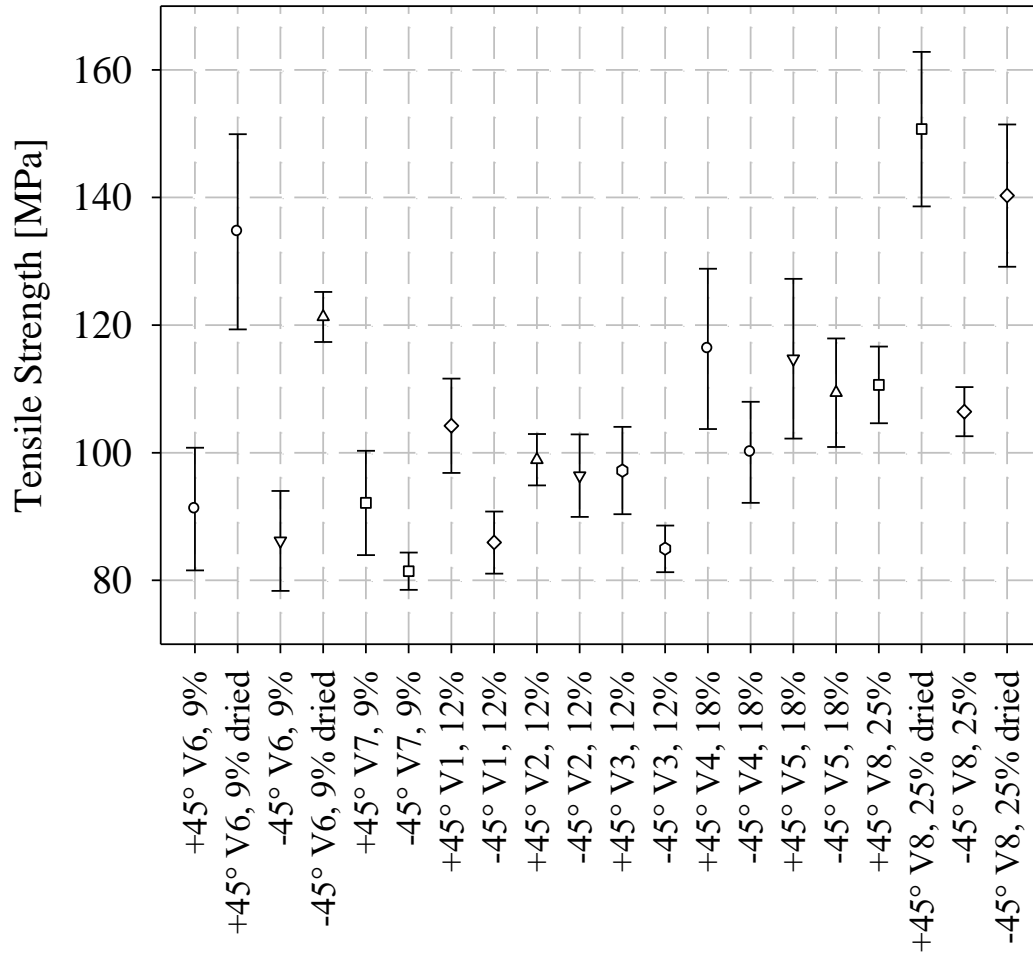
(b)

Figure 3.11: Tensile strength for process/material configurations V1-V8:
(a) 0° & 90°, (b) +45° & -45°

(a)

44
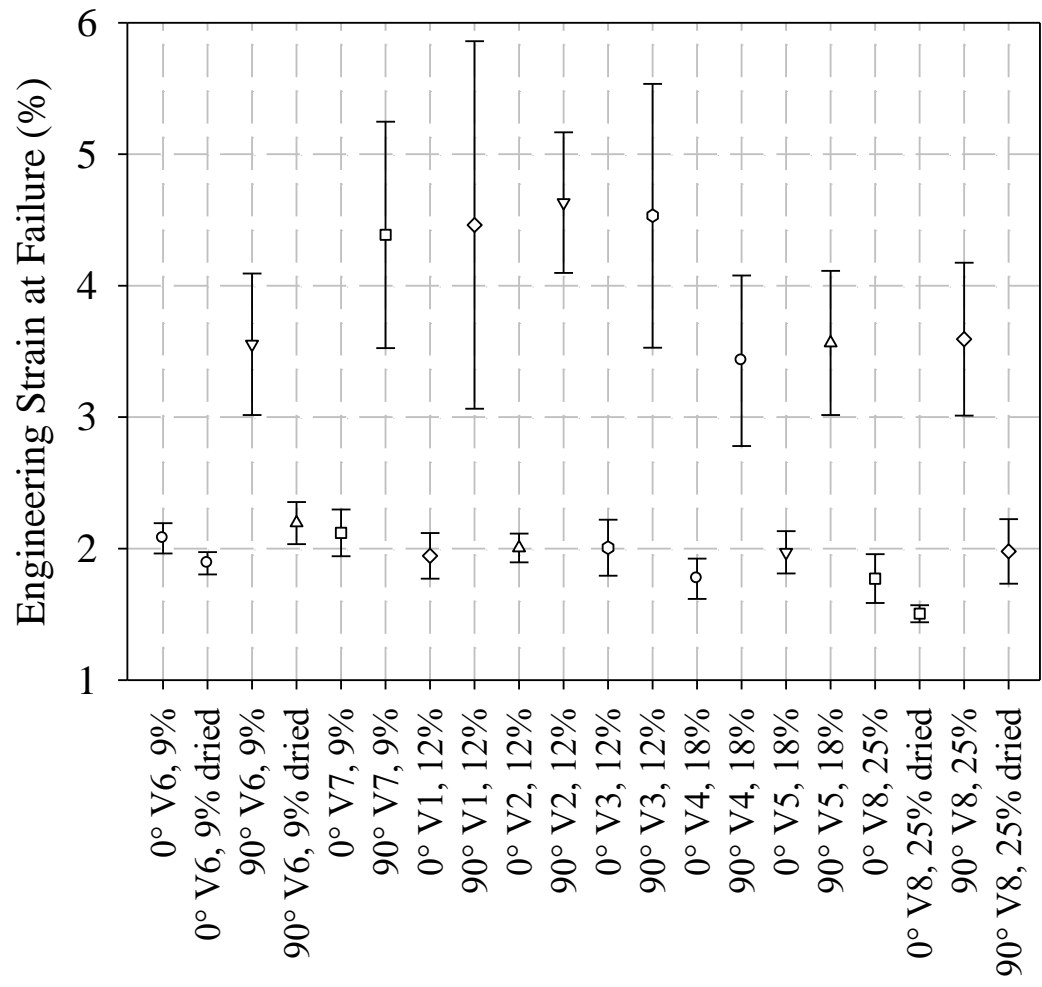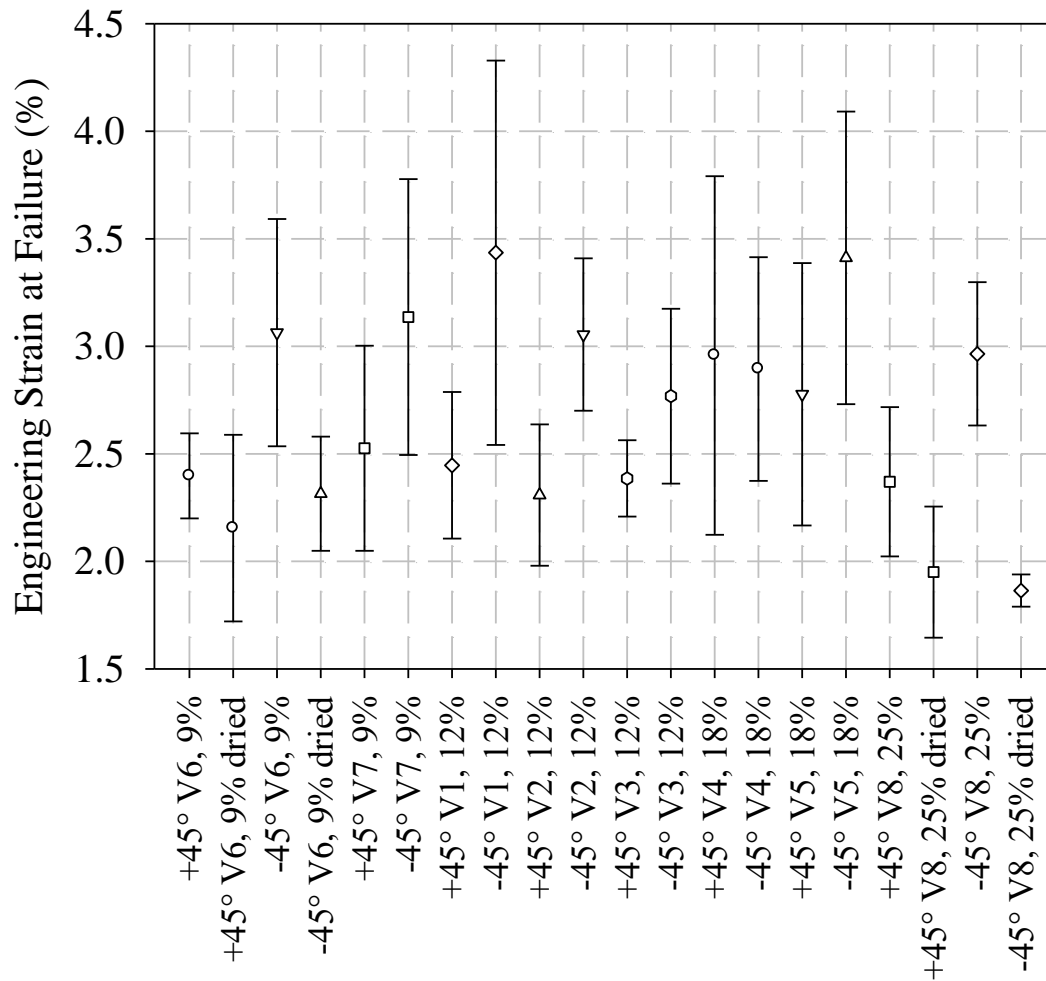
(b)

Figure 3.12: Engineering strain at failure for process/material configurations V1-V8:
(a) 0° & 90°, (b) +45° & -45°

3.3.2 Flexural Modulus

Flexural modulus for 0°, 90°, and +/-45° specimens are presented in Figure 3.13. The greater degree of consistency between specimens of the same orientation suggests that the larger specimen cross section of the ASTM D790 [18] specimens may have reduced the effect of poor fibre dispersion on mechanical properties. An approximate increase of 340 MPa per 1% fibre weight fraction was observed for the 0° direction. A possible trend of increased stiffness (8%) in the +45° direction compared to the -45° direction is again noted providing additional evidence of a difference between these two directions. Flexural strength and strain at failure are not included here as the available fixture did not permit sufficient deflection even for relatively brittle dried specimens since, as per ASTM

standard D790 [18], the recommended span to thickness ratio of 40 was selected based upon observations of significant anisotropy in tensile characteristics. A further study with digital image correlation (DIC) may be warranted to minimize specimen length and permit measurements of flexural strength and engineering strain at failure.

(a)
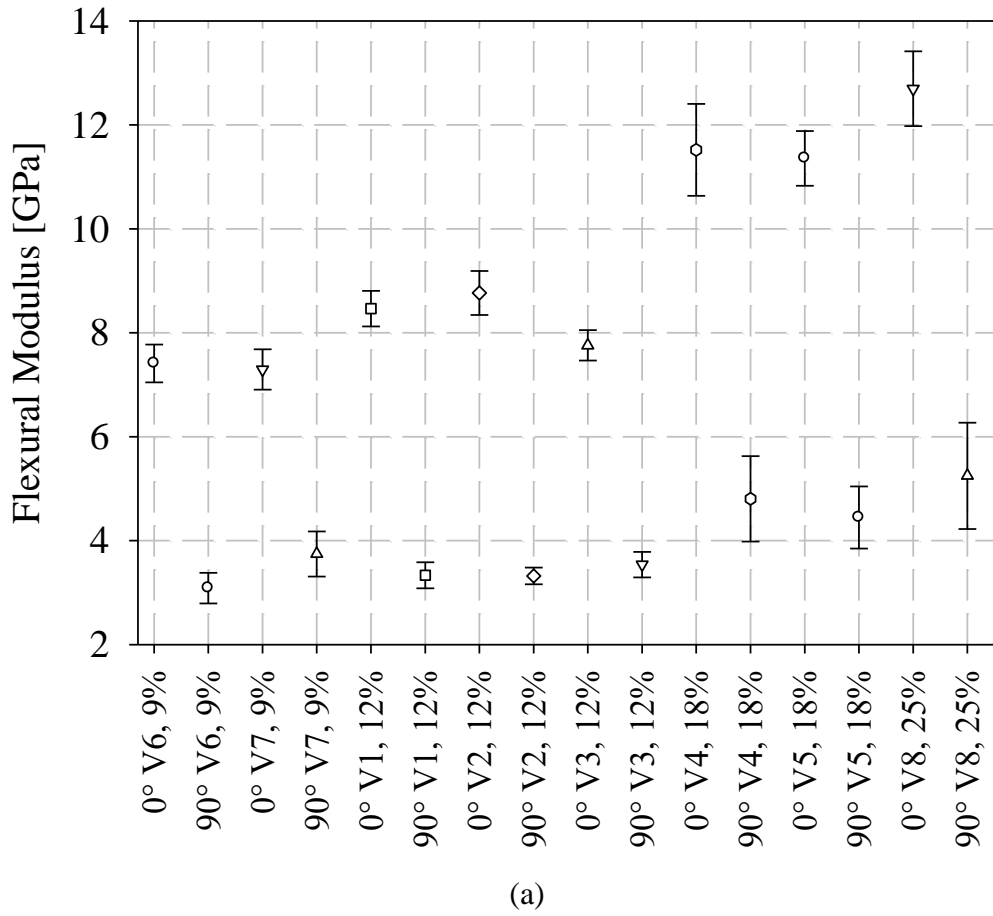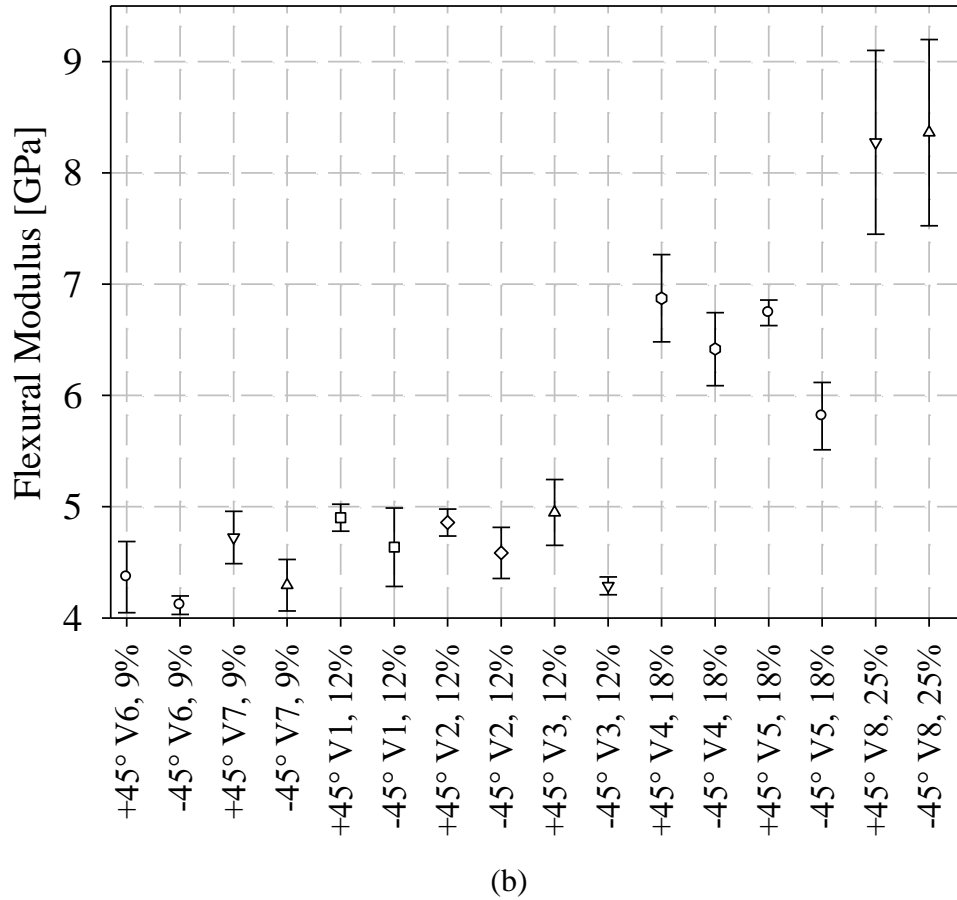
(b)

Figure 3.13: Flexural modulus for process/material configurations V1-V8:
(a) 0°& 90° directions and (b) +/-45° directions

Flexural modulus for 90° dried and STP conditioned specimens is presented in Figure 3.14 (a). Mechanical properties in this direction are mainly determined from the mechanical characteristics of the polyamide 6 matrix which are a strong function of moisture content. Averaging the data for all 8 process configurations, flexural modulus increased 36.0% (coefficient of variation: 0.038) after drying. Flexural and tensile moduli for the 0° direction are presented for comparison in Figure 3.14 (b). The tensile modulus is consistently higher (24% on average) indicating that there is either variation in fibre content or orientation through the thickness. If fibre orientation changes through the thickness (and fibre content is approximately constant), less alignment of the fibre with the length of the specimen (for 0° specimens) near the outer surfaces is expected. A possible trend of increased ratio of tensile to bending stiffness with increasing fibre content was observed.

A polymer rich (or fibre deficient) surface layer may exist and could also contribute to or be entirely responsible for the observed decrease in stiffness under bending. However, this is also a potential trend of increasing disparity between tensile and flexural moduli as fibre content increases but there is limited data to quantify such a trend. Additional data for higher fibre content material would be valuable in developing a better understanding of this phenomenon.
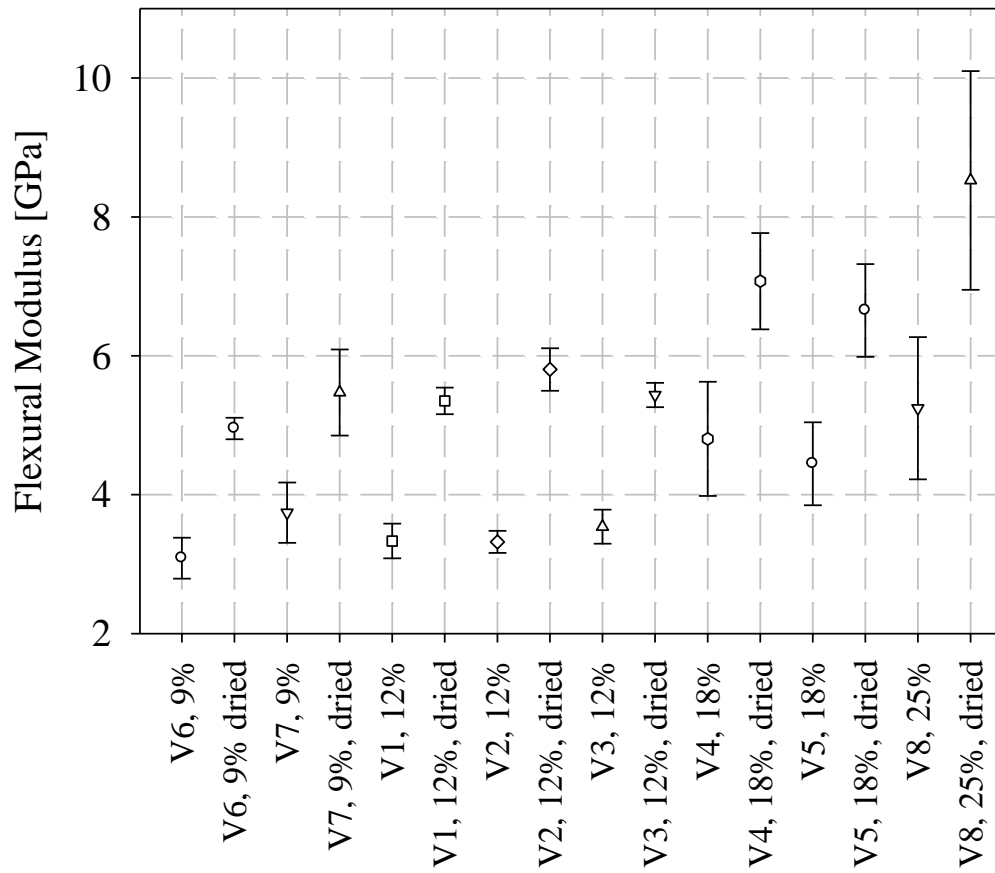
(a)
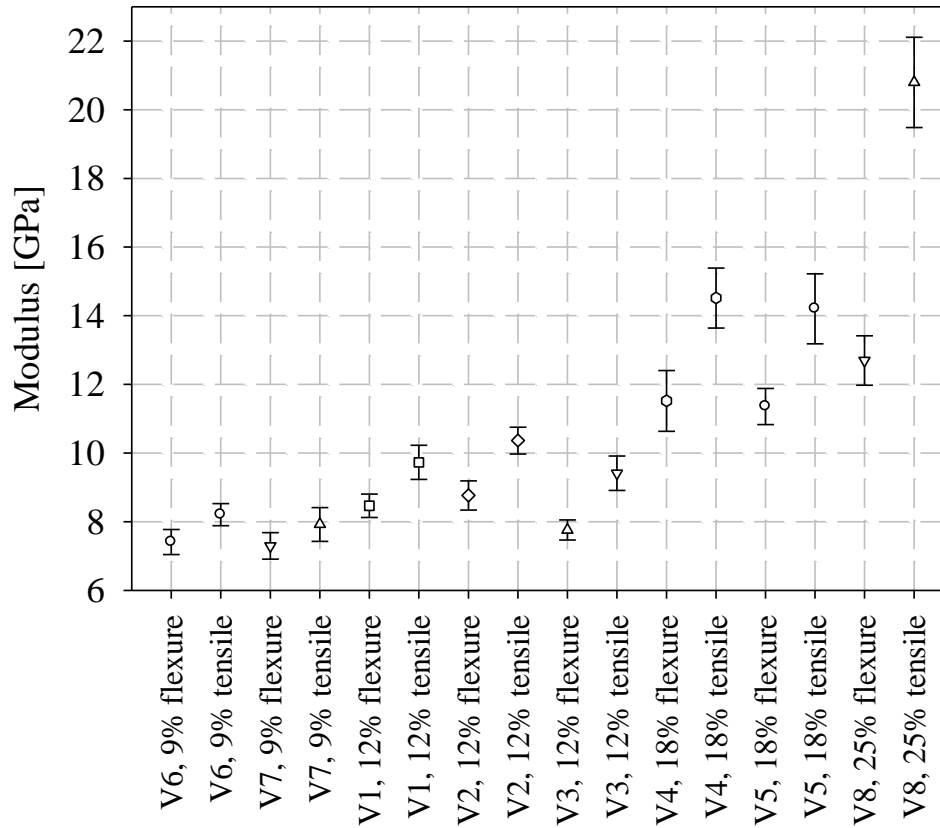
(b)

Figure 3.14: Material/process configurations V1-V8: (a) Flexural modulus: 90° dried and conditioned, (b) Flexural versus tensile modulus (0°)

3.3.3 µCT Measurements of Fibre Orientation

Second order orientation tensors for the flow region for process configuration V2 from VG Studio® and Composight/MATLAB® are presented in Table 3.3. The 4th order tensor was also computed in MATLAB® but is not currently available as an output of VG Studio. For brevity it is not presented here. The 2nd order orientation tensor diagonal is fairly consistent between VG Studio and Composight/MATLAB® (~3% error for a_{11} and a_{22}). However, the off-diagonal terms, which can capture the +45°/-45° asymmetry, and terms associated with the component of orientation in the thickness direction vary considerably between commercial and open-source software. The fibre orientation distribution, with the approximation of planar fibre, is shown in Figure 3.15. Three probability distributions, generated from orientation tensors, are superimposed on the histogram of the in-plane angle (histogram generated from the raw orientation output of Composight). All forms of the

49

fibre orientation distribution clearly support the observations of increased stiffness/strength in the +45° direction.

The ability to compute the 4th (and higher) order tensor(s) with Composight is clearly of significant value. VG Studio® is not alone in only outputting the 2nd order tensor; process modelling software including Moldflow® and Moldex® do not make higher order tensors available as standard outputs. A paper presented at CANCOM 2017 investigated the use of closure approximations, a necessary approach with orientation data from VG Studio® and process modelling software. VG Studio® could (and may do so in the future) compute the 4th order tensor from CT data. However, process modelling software will use a closure approximation. It may be of benefit to engineers developing structural finite element (FE) models to extract the 4th order tensor that must be computed by the process modelling software. Different software packages implement unique closure approximations, some are certain to be more accurate than others. Some of these closure approximations are not sufficiently documented to be easily implemented by third parties.

Table 3.3: Flow region orientation tensors from VG Studio and Composight/MATLAB for LFT-D material/process configuration V2

Orientation tensor component	VG Studio	Composight/MATLAB
a_{11}	0.6487	0.6295
a_{12}	0.037	0.0281
a_{13}	-0.001	0.0187
a_{22}	0.3058	0.3134
a_{23}	0.0087	0.0078
a_{33}	0.0456	0.0570
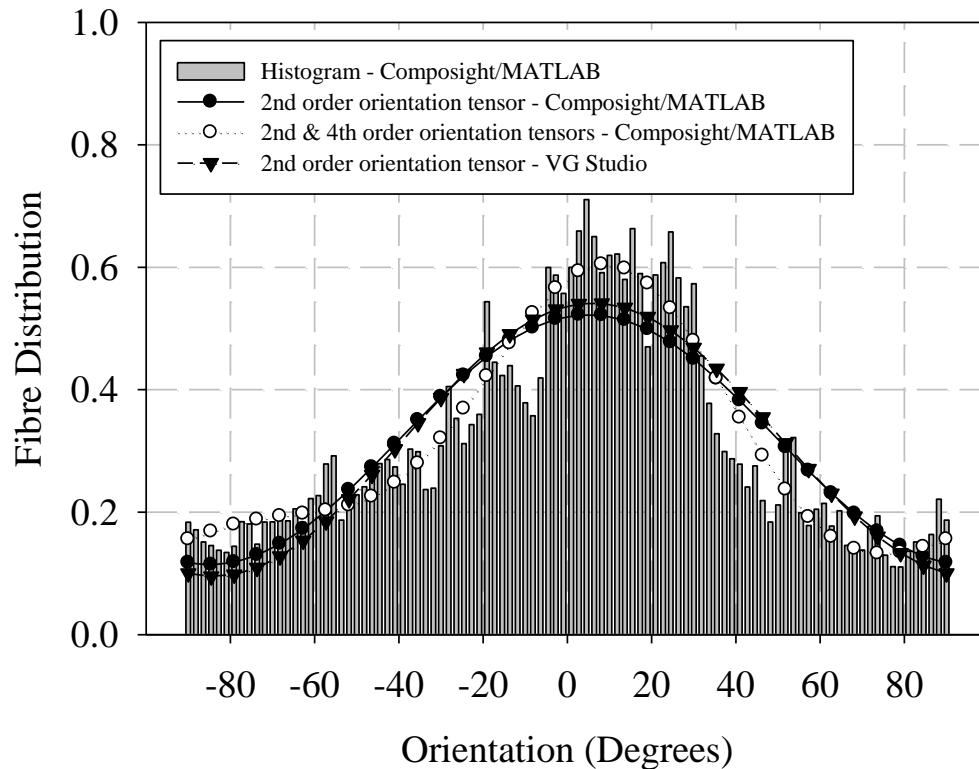
Figure 3.15: Planar fibre orientation distribution for LFT-D material/process V2

As noted in the analysis of the flexural modulus, a change in fibre orientation through the specimen thickness could explain the observation of a lower magnitude with respect to the tensile modulus. The diagonal of the 2nd order orientation tensor plotted as a function of location through the specimen thickness in Figure 3.16. The through thickness direction was divided into 6 layers as this would be the approximate level of discretization of a finite element model. A small but still significant change in fibre orientation through the thickness was observed. Fibre is increasingly aligned with the flow direction moving away from the surface. This is consistent with the observation that the tensile modulus is larger than the flexural modulus.

51
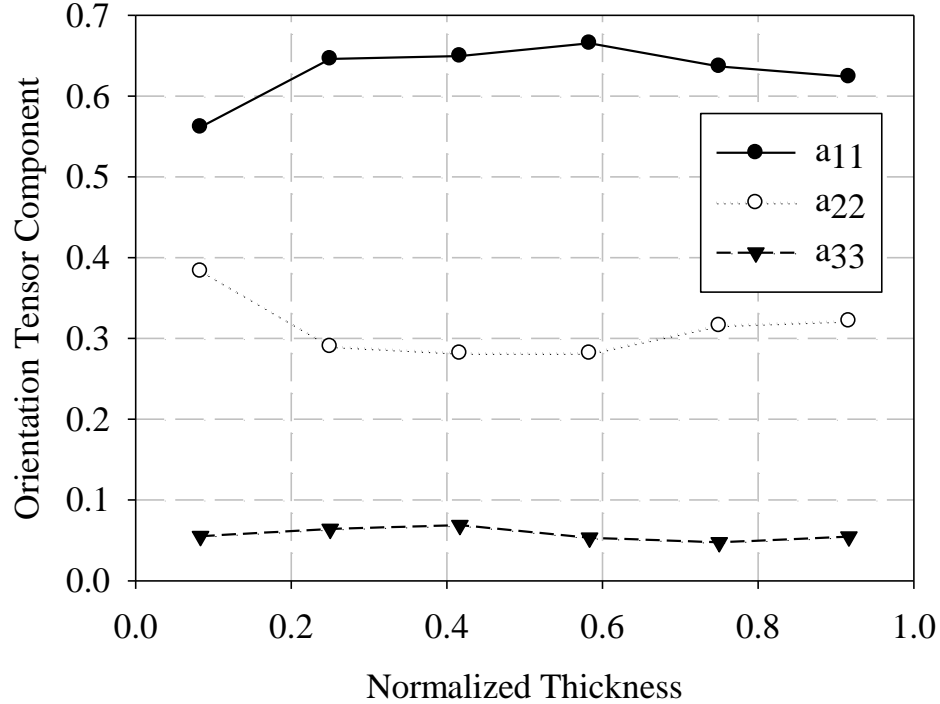
Figure 3.16: Orientation tensor diagonal plotted as a function of through-thickness location for material/process V2

3.3.4 Fibre Length Characterization

Statistics on fibre length are presented in Table 3.4. Mean fibre length was approximately 32% lower with 25% fibre weight fraction with respect to mean fibre length in 9% fibre content material. Maximum fibre volume fraction is limited by fibre aspect ratio. For a given fibre orientation state (i.e., planar random, unidirectional, or 3D random), a maximum volume fraction is a function of fibre aspect ratio [22]. Planar random or 3D random orientation states may approximate the fibre orientation state in the fibre-polymer compounding extruder. Fibre lengths are approximately consistent with these limits as shown in Table 3.4, though it is clear that a 3D random fibre orientation state is not a suitable approximation for the conditions in the extruder which limit maximum fibre length. Longer fibres may be associated with poor fibre dispersion since the effective fibre aspect ratio, accounting for the diameter of the bundle, may be quite low. Dispersing such fibre bundles after separating the fibre from the matrix is challenging and resulted in degradation of fibre length. However, leaving the bundle intact may be worth considering

if the bundle diameter (and correspondingly the aspect ratio) can be measured. Novel μCT measurements of fibre length [23,24], though challenging for carbon fibre due to the small diameter and low contrast, may be promising techniques for further investigations of this direct compounding phenomenon.

Note that mean fibre lengths in the range of 200 to 400 μm result in average aspect ratios ranging from 28 to 57. As noted in the literature review, an LFT material is expected to have fibres with an aspect ratio (AR) of approximately 100. This, combined with micromechanics modelling presented in this manuscript, strongly suggest that this fibre length distribution data is skewed to exclude longer fibres. This investigation was performed by an industrial partner and limited details on the methodology are available, critical details on sampling error or 'edge effects' (introducing artificially short fibres by extracting a specimen from a larger part) are not available. The personnel who completed the fibre length characterization noted that some long fibres could not be dispersed and were discarded. Quantitative details on for example, the mass fraction of discarded fibres was not provided.

Table 3.4: Carbon fibre length statistics for LFT-D materials/processes V6 & V8

	Fibre Length Measurements (μm)				Theoretical Maximum Fibre Length (μm)	
	Minimum	Maximum	Mean	Std. Dev.	3D Random	Planar Random
V6.6 (9%) charge region	20.39	5368.20	379.87	399.09	839.1	3596.1
V6.6 (9%) flow region	20.39	2673.70	360.65	359.66		
V8.5 (25%) charge region	24.00	3576.20	254.23	293.32	283.4	1214.7
V8.5 (25%) flow region	24.00	4569.80	248.51	287.62		

Fibre Length (microns)

(a)

Fibre Length (microns)
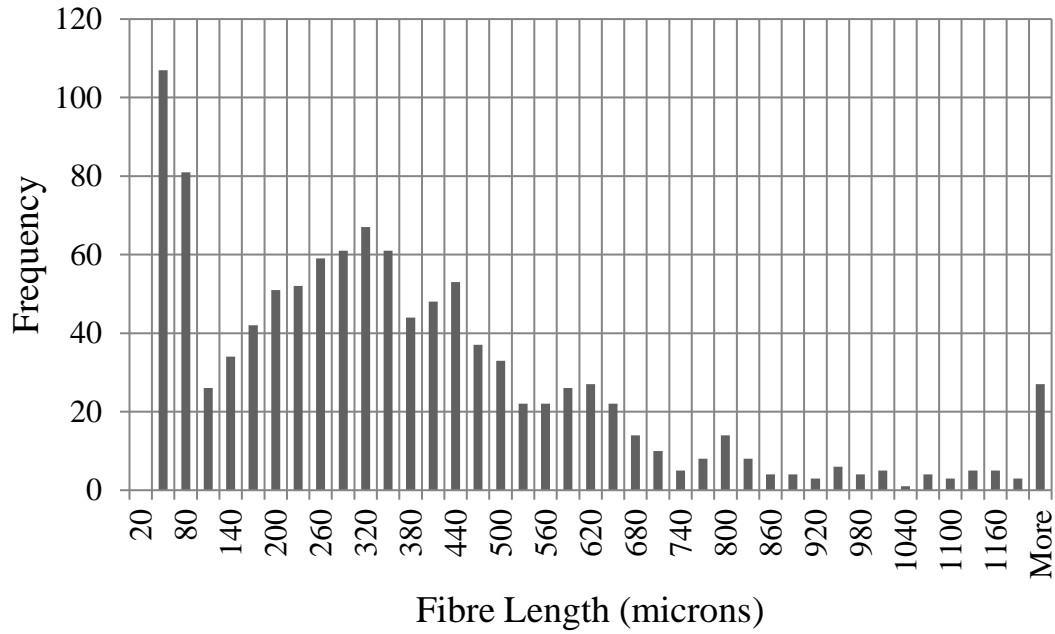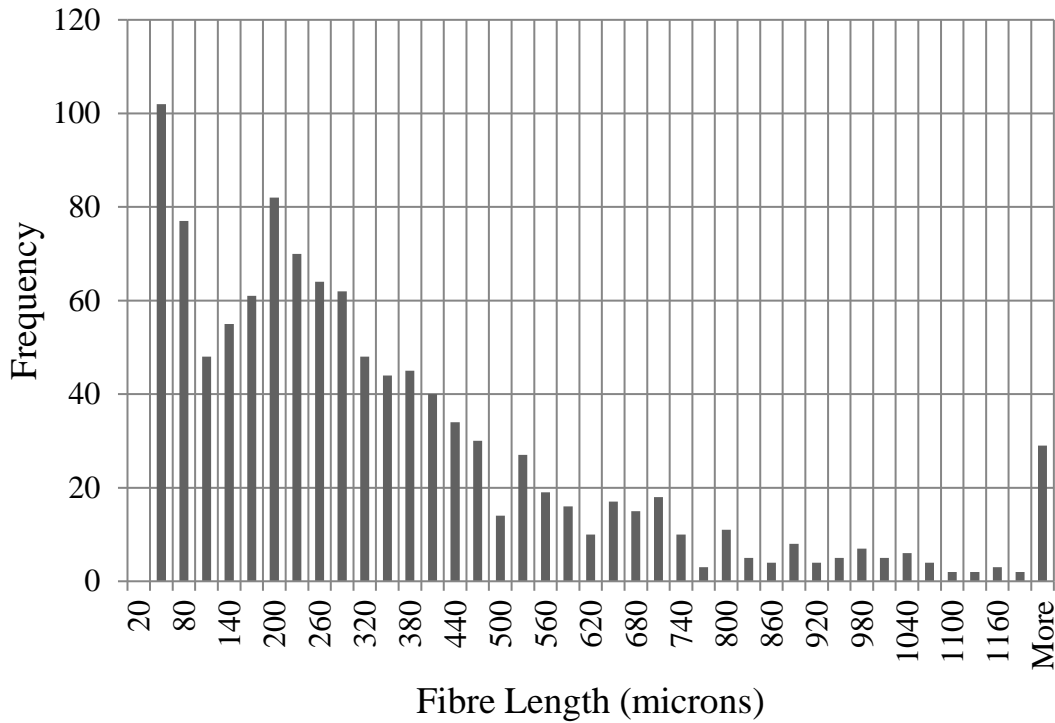
(b)

Figure 3.17: (a) Charge and (b) flow region fibre length distributions for LFT-D process/material configuration V6 (9% fibre weight fraction)

The histograms in Figure 3.17 and Figure 3.18 may provide some evidence of fibre breakage as a result of flow within the mold since longer fibres are observed in the charge region. Alternatively, it may be that shorter fibres had a greater tendency to be transported and longer fibres remained in the charge region. Additionally, experimental error cannot be ruled out. However, the part geometry for this study is very simple and may minimize in-mold fibre length degradation. There may even be evidence in these plots of increased fibre length in the flow region. However, this may be associated with difficulty in separating fibre bundles containing long fibres. Such bundles may have been reduced in number and/or easier to separate for flow region fibre length specimens. Comparing the low and high fibre content material, the distributions shift from a more uniform fibre length to a distribution with a greater decrease in the fraction of fibres with increased length. It would be interesting to extract fibre length specimens from compression molding charges as was completed (for glass fibre) by Mcleod et al. [7] to evaluate fibre length degradation associated with compression molding.
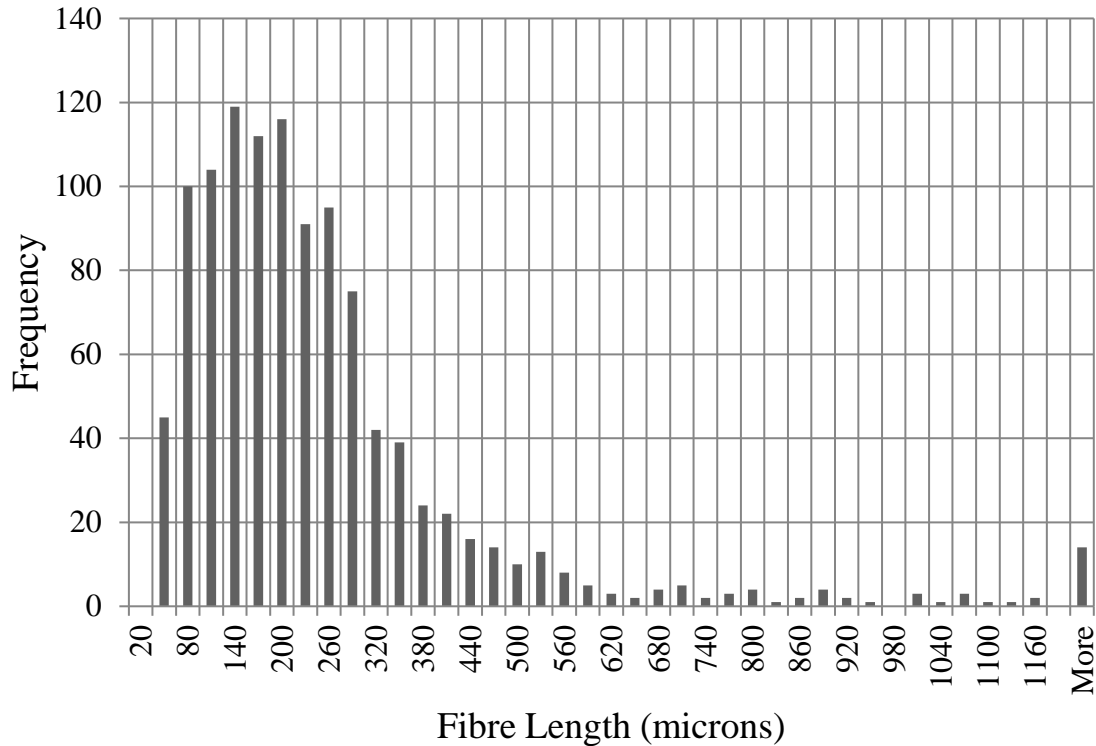
(a)
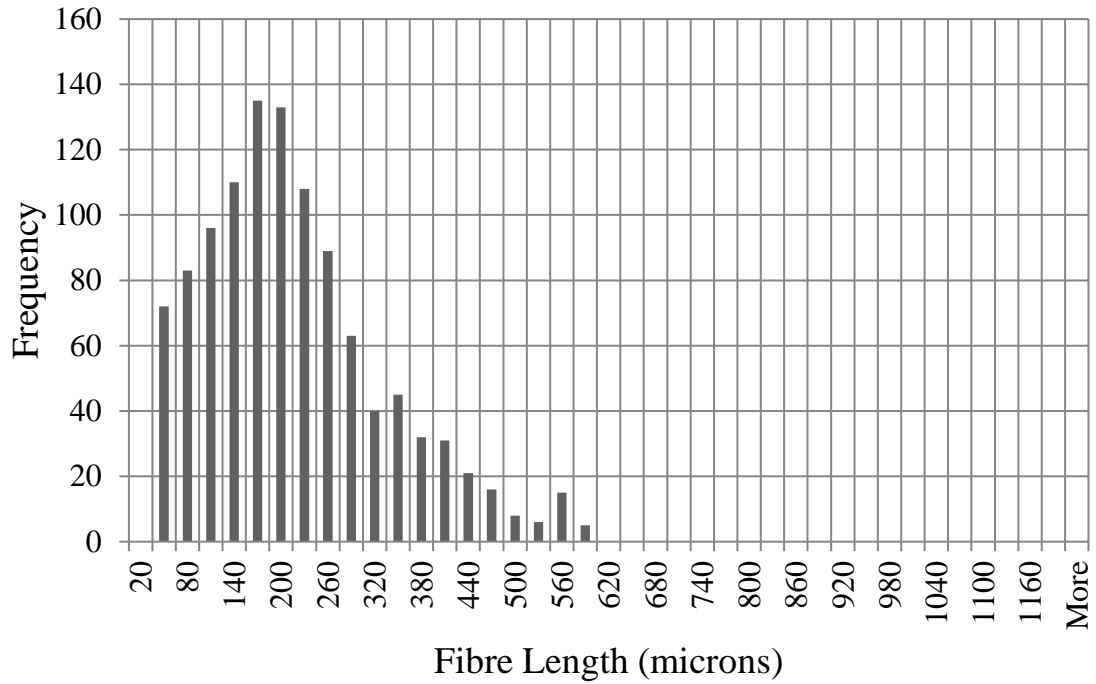
(b)

Figure 3.18: (a) Charge and (b) flow region fibre length distributions for LFT-D process/material configuration V8 (25% fibre weight fraction)

3.3.5 Comparison of Modulus Measurements to Micromechanics Models

Mechanical properties of the matrix and fibre combined with the CT measurements of fibre orientation permit the elastic modulus to be estimated using micromechanics models and orientation averaging. Note that the fibre orientation state in the flow region of process configuration V2 is assumed to be valid for all other process configurations. The fibre length distribution was invoked for the Halpin-Tsai and Mori-Tanaka micromechanical models. A comparison of theoretical predictions of 0°, 90°, +45°, and -45° moduli with respect to average experimental measurements are presented in Table 3.6, Table 3.7, Table 3.8, and Table 3.9. The MATLAB code for this analysis is available in Appendix D and at mathworks.com/matlabcentral/fileexchange/58020. The mechanical properties of the constituent materials are given in Table 3.5. Elastic modulus for the conditioned matrix was estimated from the inverse rule of mixtures, a micromechanics model noted for its poor accuracy, and linear regression of the experimental 90° tensile modulus with respect to fibre volume fraction.

Table 3.5: Mechanical properties of fibre and matrix for micromechanics modelling

Mechanical Property	Value
Elastic modulus of PA6 (dried)	2.70 GPa [19]
Elastic modulus of PA6 (conditioned)	2.50 GPa
Poisson's ratio of PA6	0.39 [25]
Density of PA6	1.13 g/cc [19]
Elastic modulus of carbon fibre (longitudinal)	240 GPa [26]
Poisson's ratio of carbon fibre	0.2 [27]
Density of carbon fibre	1.81 g/cc [26]

The generalized self-consistent (GSC) model provides an upper bound on modulus since it does not consider fibre length. For the GSC model, the effectiveness of each process configuration is computed as the ratio of actual modulus to the prediction of the GSC model expressed as a percentage. The use of such a metric, and the focus on modulus, was selected for simplicity and based upon feedback from industry where meeting stiffness requirements may be the deciding factor for material selection [8]. This effectiveness is in the range of 90-100% in the flow direction (0°), though there is certain to be error introduced by the previously noted assumption of the validity of using the fibre orientation from process configuration V2 for all other process configurations. For ±45° and 90°, the effectiveness is much lower (60-70%).

Table 3.6: Comparison of average experimental and theoretical predictions of 0° elastic modulus

	Process Configuration							
	V1 (12%)	**V2 (12%)**	**V3 (12%)**	**V4 (18%)**	**V5 (18%)**	**V6 (9%)**	**V7 (9%)**	**V8 (25%)**
Experimental [GPa] (CoV)	9.73 (5.11%)	10.36 (3.77%)	9.41 (5.32%)	14.51 (6.02%)	14.20 (7.19%)	8.21 (3.90%)	7.92 (6.21%)	20.79 (6.32%)
GSC [GPa] (Effectiveness)	10.91 (89.2%)	10.91 (95.0%)	10.91 (86.3%)	15.42 (94.2%)	15.42 (94.2%)	8.74 (93.9%)	8.74 (93.9%)	20.98 (99.1%)
Halpin-Tsai, Experimental FLD [GPa] (% Error)	6.60 (-32.2%)	6.60 (-36.4%)	6.60 (-29.9%)	9.30 (-36.0%)	9.30 (-34.5%)	5.45 (-33.6%)	5.45 (-31.2%)	13.61 (-34.6%)
Halpin-Tsai, AR=100 [GPa] (% Error)	8.63 (-11.3%)	8.63 (-16.7%)	8.63 (-8.29%)	12.38 (-14.7%)	12.38 (-12.8%)	6.96 (-15.1%)	6.96 (-12.1%)	17.85 (-14.1%)
Mori-Tanaka, Experimental FLD [GPa] (% Error)	7.62 (-21.7%)	7.62 (-26.5%)	7.62 (-19.0%)	10.47 (-27.9%)	10.47 (-26.3%)	6.27 (-23.6%)	6.27 (-20.8%)	14.09 (-32.3%)
Mori-Tanaka AR=100 [GPa] (% Error)	10.20 (4.88%)	10.20 (-1.55%)	10.20 (8.41%)	14.38 (-0.96%)	14.38 (1.23%)	8.20 (-0.05%)	8.20 (3.56%)	19.57 (-5.90%)

As shown in Figure 3.19, the Halpin-Tsai model predicts a much larger aspect ratio to maximize modulus than the Mori-Tanaka model. For either micromechanics model, the slope for any curve is roughly equal for the same fibre aspect ratio and micromechanics model. Therefore, expressing the instantaneous slope as a percent increase in modulus indicates that as the orientation approaches 90°, there is a greater dependence on fibre aspect ratio to maximize modulus. There is also the possibility that the FLD and FOD are coupled. Perhaps future CT inspection technologies will permit an investigation of this possible coupling (or tedious investigations by microscopy). In any case, increasing the fibre length might be of great benefit for the LFT-D manufacturing process since the mechanical properties are highly anisotropic. Properties perpendicular to the flow direction may present a particular challenge in finding an industrial component well suited to this material.
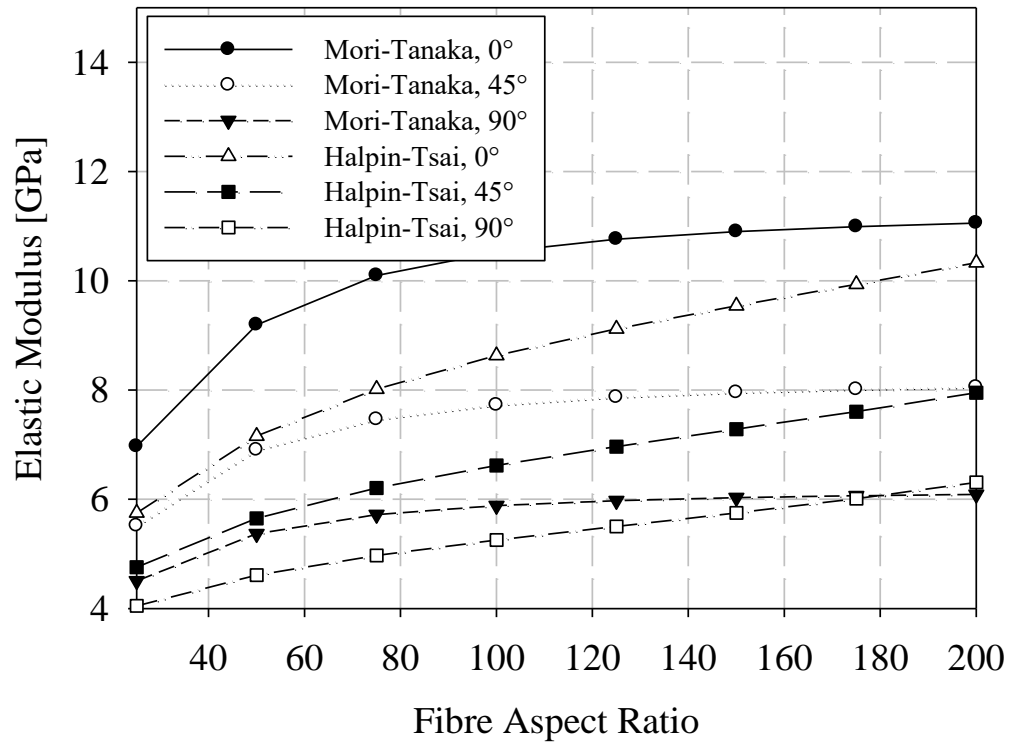
Figure 3.19: Modulus as a function of fibre aspect ratio for the fibre orientation distribution of section 3.3 (12% fibre weight fraction)

Table 3.7: Comparison of average experimental and theoretical predictions of 90° elastic modulus

	Process Configuration							
	V1 (12%)	V2 (12%)	V3 (12%)	V4 (18%)	V5 (18%)	V6 (9%)	V7 (9%)	V8 (25%)
Experimental [GPa] (CoV)	3.76 (6.92%)	4.02 (3.90%)	3.57 (15.4%)	4.82 (3.94%)	4.87 (3.78%)	3.88 (8.01%)	3.66 (5.28%)	5.71 (12.0%)
GSC [GPa] (Effectiveness)	6.032 (62.3%)	6.03 (66.7%)	6.03 (59.2%)	7.91 (60.9%)	7.91 (60.9%)	5.13 (75.7%)	5.13 (75.7%)	10.24 (55.8%)
Halpin-Tsai, Experimental FLD [GPa] (% Error)	4.46 (18.7%)	4.46 (10.9%)	4.46 (24.8%)	5.81 (20.5%)	5.81 (19.2%)	3.90 (0.54%)	3.90 (6.78%)	8.09 (41.6%)
Halpin-Tsai, AR=100 [GPa] (% Error)	5.25 (39.8%)	5.25 (30.6%)	5.25 (47.0%)	7.00 (45.4%)	7.00 (43.7%)	4.50 (15.8%)	4.50 (23.0%)	9.72 (70.3%)
Mori-Tanaka, Experimental FLD [GPa] (% Error)	4.76 (26.6%)	4.76 (18.3%)	4.76 (33.1%)	6.00 (24.5%)	6.00 (23.1%)	4.17 (7.42%)	4.17 (14.1%)	7.58 (32.8%)
Mori-Tanaka, AR=100 [GPa] (% Error)	5.76 (53.2%)	5.76 (43.2%)	5.76 (61.1%)	7.50 (55.7%)	7.50 (54.0%)	4.92 (26.7%)	4.92 (34.6%)	9.69 (69.7%)

As noted in the results/discussion of the fibre length distribution data, there is evidence that the fibre length data documented in this study are not accurate and skewed to exclude longer fibres. Given this concern, for each micromechanics model and orientation, two fibre length distributions are used: 1) the closest experimental data set or 2) a fibre aspect ratio of 100, as would be expected for an LFT material. In the 0° direction, for either micromechanics model, the percent error is reduced from over 20% to less than 10% comparing the experimental fibre length distribution to the expected aspect ratio of approximately 100. However, in the 90° direction, the experimental fibre length distribution yields more accurate results (though the accuracy is still poor). In the +45° direction, the Halpin-Tsai model with a fibre aspect ratio of 100 may be more accurate

than the same model with experimental data. However, this result is reversed for the Mori-Tanaka model. In the -45° direction, the experimental fibre length distribution is generally more accurate than the assumption of a fibre aspect ratio of 100.

There are multiple considerations in assessing these results. The micromechanics models employed assume both the fibre and matrix are isotropic materials. Carbon fibre has been noted to exhibit significant anisotropy [27], the ratio of longitudinal modulus to transverse modulus can be more than 10. Digimat® offers the option of an anisotropic fibre model. An intermediate effective fibre modulus, though the formula to estimate this value is unknown, may be an acceptable approach allowing for the use of micromechanics models based upon isotropic constituents.

Table 3.8: Comparison of average experimental and theoretical predictions of +45° elastic modulus

	Process Configuration							
	V1 (12%)	V2 (12%)	V3 (12%)	V4 (18%)	V5 (18%)	V6 (9%)	V7 (9%)	V8 (25%)
Experimental [GPa] (CoV)	6.77 (14.9%)	6.26 (9.48%)	5.86 (9.24%)	8.06 (12.6%)	7.80 (13.0%)	5.44 (18.5%)	5.34 (10.6%)	8.74 (11.1%)
GSC [GPa] (Effectiveness)	7.96 (85.1%)	7.96 (78.6%)	7.96 (73.7%)	10.82 (74.4%)	10.82 (72.1%)	6.57 (82.8%)	6.57 (81.2%)	14.36 (60.9%)
Halpin-Tsai, Experimental FLD [GPa] (% Error)	5.34 (-21.1%)	5.34 (-14.6%)	5.34 (-8.85%)	7.23 (-10.2%)	7.23 (-7.29%)	4.549 (-16.4%)	4.55 (-14.8%)	10.34 (18.2%)
Halpin-Tsai, AR=100 [GPa] (% Error)	6.62 (-2.29%)	6.62 (5.80%)	6.62 (12.9%)	9.15 (13.6%)	9.15 (17.3%)	5.50 (1.12%)	5.50 (3.07%)	12.96 (48.3%)
Mori-Tanaka, Experimental FLD [GPa] (% Error)	5.92 (-12.5%)	5.92 (-5.31%)	5.92 (1.04%)	7.78 (-3.36%)	7.78 (-0.21%)	5.04 (-7.46%)	5.04 (-5.67%)	10.15 (16.1%)
Mori-Tanaka, AR=100 [GPa] (% Error)	7.52 (11.1%)	7.52 (20.3%)	7.52 (28.4%)	10.19 (26.4%)	10.19 (30.6%)	6.24 (14.7%)	6.24 (16.9%)	13.50 (54.4%)

Table 3.9: Comparison of average experimental and theoretical predictions of -45° elastic modulus

Process Configuration								
	V1 (12%)	V2 (12%)	V3 (12%)	V4 (18%)	V5 (18%)	V6 (9%)	V7 (9%)	V8 (25%)
Experimental [GPa] (CoV)	4.98 (8.51%)	5.73 (11.6%)	4.63 (10.1%)	6.15 (6.21%)	7.18 (10.5%)	4.83 (11.5%)	4.50 (7.06%)	7.60 (4.46%)
GSC [GPa] (Effectiveness)	7.34 (67.9%)	7.34 (78.0%)	7.34 (63.1%)	9.92 (62.1%)	9.92 (72.4%)	6.10 (79.2%)	6.10 (73.8%)	13.10 (58.0%)
Halpin-Tsai, Experimental FLD [GPa] (% Error)	5.03 (1.02%)	5.03 (-12.1%)	5.03 (8.75%)	6.75 (9.67%)	6.75 (-5.94%)	4.32 (-10.6%)	4.32 (-4.02%)	9.59 (26.2%)
Halpin-Tsai, AR=100 [GPa] (% Error)	6.16 (23.6%)	6.16 (7.58%)	6.16 (33.1%)	8.45 (37.3%)	8.45 (17.8%)	5.16 (6.77%)	5.16 (14.7%)	11.93 (56.9%)
Mori-Tanaka, Experimental FLD [GPa] (% Error)	5.53 (10.9%)	5.53 (-3.48%)	5.53 (19.4%)	7.20 (17.0%)	7.20 (0.33%)	4.74 (-1.97%)	4.74 (5.29%)	9.33 (22.7%)
Mori-Tanaka, AR=100 [GPa] (% Error)	6.95 (39.5%)	6.95 (21.4%)	6.95 (50.2%)	9.34 (51.8%)	9.34 (30.2%)	5.80 (20.1%)	5.80 (29.0%)	12.33 (62.2%)

3.4 Conclusions

Characterization of 9% to 25% weight fraction compression molded carbon fibre LFT-D polyamide-6 was completed including uniaxial tension and three-point bending tests with specimen orientations of 0°, ±45°, and 90°. Fibre orientation was quantified through μCT scans and the fibre length distribution was studied by an industrial partner. The findings are summarized as follows:

1. Tensile stiffness/strength and flexural stiffness were consistently higher in the +45° direction with respect to -45° (tensile modulus: 20%, tensile strength: 10%, flexural modulus: 8%). Correspondingly, engineering strain at failure for uniaxial tensile tests was 18% lower, on average, in the +45° direction.

2. The +45°/-45° asymmetry may be associated with the design of the fibre/thermoplastic compounding extruder (ZSG) of the Dieffenbacher LFT-D line. Engineers developing compression molding process models for this process should consider the capabilities of their models to capture this asymmetry through initial conditions for fibre orientation in the charge/plastificate. In a future trial, a simple test consisting of rotating the charges 180 degrees may be considered.

3. Significant anisotropy in mechanical characteristics, such that at 90° the properties are approximately those of the unreinforced matrix [19], may present challenges for selecting this material for an industrial application.

4. Fibre length, even with direct compounding, is only sufficient to effectively maximize modulus in the 0° direction ('effectiveness' of approximately 90%). Fibre lengths much larger than observed with injection molding with LFT pellets were not observed, though fibre length measurement is an area in which standardized procedures for long fibre materials must be developed and adhered to by the laboratories performing such analyses. Much longer fibres than were measured for this material are required for optimal stiffness in the ±45° and 90° directions and strength/impact properties.

3.5 References

1. Thomason J. The influence of fibre length and concentration on the properties of glass fibre reinforced polypropylene: 5. Injection moulded long and short fibre PP. Composites Part A: Applied Science and Manufacturing. 2002;33(12):1641-1652.
2. Schemme M. LFT–development status and perspectives. Reinforced Plastics. 2008;52(1):32-39.
3. Krause W, Henning F, Tröster S, et al. LFT-D—a process technology for large scale production of fiber reinforced thermoplastic components. Journal of Thermoplastic Composite Materials. 2003;16(4):289-302.
4. Brümmer M, Henning F, Krause W. Long-Fiber Reinforced Thermoplastics Tailored for Structural Performance. SPE ACCE. 2005.
5. Teixeira D, Giovanela M, Gonella L, et al. Influence of injection molding on the flexural strength and surface quality of long glass fiber-reinforced polyamide 6.6 composites. Materials & Design. 2015;85:695-706.
6. Luo H, Xiong G, Ma C, et al. Preparation and performance of long carbon fiber reinforced polyamide 6 composites injection-molded from core/shell structured pellets. Materials & Design. 2014;64:294-300.
7. McLeod M, Baril E, Hetu J, et al., editors. Morphological and Mechanical Comparison of Injection and Compression Moulding In-Line Compounding of Direct Long Fibre Thermoplastics. SPE Automotive Composites; 2010; Troy, MI: SPE.
8. Rohan K, McDonough T, Ugresic V, et al. Mechanical Study of Direct Long Fiber Thermoplastic Carbon/Polyamide 6 and its Relations to Processing Parameters. University of Western Ontario/Zoltek Corporation; 2015. p. 1-24.
9. Zhang X, Johrendt J. Using Neural Networks to Examine the Sensitivity of Composite Material Mechanical Properties to Processing Parameters. SAE International Journal of Materials and Manufacturing. 2016;9(2016-01-0499):737-745.
10. Advani S, Tucker C. The use of tensors to describe and predict fiber orientation in short fiber composites. Journal of Rheology (1978-present). 1987;31(8):751-784.
11. Nguyen B, Bapanapalli S, Holbery J, et al. Fiber length and orientation in long-fiber injection-molded thermoplastics—Part I: Modeling of microstructure and elastic properties. Journal of Composite Materials. 2008;42(10):1003-1029.
12. Cintra Jr JS, Tucker III CL. Orthotropic closure approximations for flow-induced fiber orientation. Journal of Rheology (1978-present). 1995;39(6):1095-1122.
13. Halpin J, Kardos J. The Halpin-Tsai equations: a review. Polymer Engineering & Science. 1976;16(5):344-352.
14. Bay RS, Tucker CL. Fiber orientation in simple injection moldings. Part I: Theory and numerical methods. Polymer composites. 1992;13(4):317-331.
15. Buck F, Brylka B, Müller V, et al., editors. Coupling of mold flow simulations with two-scale structural mechanical simulations for long fiber reinforced thermoplastics. Materials Science Forum; 2015: Trans Tech Publ.
16. Autodesk Moldflow. Autodesk; 2017.
17. International A. D638. Standard Test Method for Tensile Properties of Plastics. West Conshohocken, PA: ASTM International.

18. International A. D790. Standard Test Methods for Flexural Properties of Unreinforced and Reinforced Plastics and Electrical Insulating Materials. West Conshohocken, PA: ASTM International.

19. Product Information: Ultramid 8202 HS Polyamide 6 [Internet]. Available from: http://iwww.plasticsportal.com/products/dspdf.php?type=iso&param=Ultramid+8 202+HS.

20. Pinter P, Dietrich S, Weidenmann K, editors. Algorithms for the Determination of Orientation Tensors from Three Dimensional uCT Images with Various Microstructures. ICCM 2015; 2015; Copenhagen, Denmark.

21. Bertram B, Pinter P. Composight. 0.2.0 R314. Sourceforge; 2016.

22. Evans K, Gibson A. Prediction of the maximum packing fraction achievable in randomly oriented short-fibre composites. Composites science and technology. 1986;25(2):149-162.

23. Pinter P, Bertram B, Weidenmann K, editors. A Novel Method for the Determination of Fibre Length Distributions from μCT-data. 6th Conference on Industrial Computed Tomography; 2016; Wels, Austria.

24. Salaberger D, Kannappan K, Kastner J, et al. Evaluation of computed tomography data from fibre reinforced polymers to determine fibre length distribution. International Polymer Processing. 2011;26(3):283-291.

25. Professional Plastics. Mechanical Properties of Plastic Materials [[09/16/2016]. Available from: http://www.professionalplastics.com/professionalplastics/MechanicalPropertiesof Plastics.pdf

26. Toho Tenax America. Test Report - Tenax-A HTR40 F22 24K 1550TEX. 2013. p. 1.

27. Gibson RF. Principles of composite material mechanics. Vol. 218. CRC press; 2012.

CHAPTER 4

TENSILE FATIGUE CHARACTERIZATION OF POLYAMIDE 66/CARBON
FIBRE DIRECT/IN-LINE COMPOUNDED LONG FIBRE THERMOPLASTIC
COMPOSITES

4.1 Introduction

The previous chapter presents a comprehensive study of fundamental mechanical properties of carbon fibre/polyamide LFT-D material from uniaxial tension and three-point bending tests. This data was accompanied by characterization of fibre orientation and fibre length distributions. For the purposes of considering this material for engineering applications, the data in the previous chapter provides solid foundations but is likely insufficient. One particular deficiency is for applications with many cycles of a low load. As shown in the previous chapter, the fundamental elastic properties can be estimated with some accuracy from analytical models. This is not the case for fatigue properties. Since this material is produced by the uncommon direct compounding/compression molding process, which has also been modified to allow the use of carbon fibres, a study of fatigue properties through experimental testing is of critical importance.

Mechanical properties under quasi-static and impact loading for carbon fiber LFT-D are documented in a limited number of publications [1-5]. However, studies in the open literature of fatigue behavior for direct compounded long fiber thermoplastics or long carbon fiber reinforced thermoplastics are especially few in number. Goel et al. [6] have published detailed fatigue characterization of chopped long E-glass fiber and polypropylene composites (20% volume fraction). The study included analyses of longitudinal and transverse direction hysteresis (with respect to flow direction), specimen temperature, frequency, and fracture surfaces. Tension-tension fatigue tests were completed using a stress ratio of 0.2 at three frequencies: 10, 15, and 20 Hz. Peak stress ranged from 13 MPa to 35 MPa. In terms of failure mechanisms, fiber pull out, fiber fracture, and matrix fracture were all observed. Hysteretic heating decreased the modulus through matrix softening during evaluation. Correspondingly, at a given stress level, the number of cycles to failure decreased as frequency increased.

Grove and Kim [7] assessed the fatigue performance of short and long glass fiber reinforced thermoplastics (polypropylene, polyamide, and polyphthalamide) under tension-

tension ($R \approx 0$) and flexural loading ($R = -1$). The frequency for cyclical loading was 10 Hz for tension-tension and 30 Hz for flexural loading. For these materials the quasi-static tensile strength, Izod impact strength and flexural strength were noted to increase significantly with fiber length. For tension-tension fatigue and low cycle counts (under 1000 cycles) long fiber materials exhibited an increased strength over their short fiber counterparts but this advantage was not observed for high cycle fatigue (1000 to 1 million cycles). For the flexural fatigue tests, increased fiber length enhanced the fatigue life across the full spectrum of stress levels and cycles to failure.

Nguyen et al. [8] applied a fatigue damage model for discontinuous fiber composites [9] to long fiber (glass, 50% weight fraction) reinforced polyamide 66. The fatigue damage model correlates a reduction in modulus and strength with the microcrack volume fraction. Mechanical characterization was completed for injection molded specimens with the load applied in the flow direction. Specimens were dried prior to fatigue testing but were exposed to unspecified laboratory conditions for the duration of the tests. The stress ratio used for these tests (R) was 0.1 and the frequency for cyclical loading was 3 Hz. Three stress levels were considered: 30%, 40%, and 50% of the ultimate tensile strength (UTS). At 30% of the UTS, failure did not occur before one million cycles. The damage model accurately predicted a flow direction modulus reduction with increasing cycle count. The authors demonstrated that the model's predictions for stress/life agreed with experimental findings but the study includes very limited experimental data for this comparison (only two stress levels: 40% and 50% of UTS).

Wyzgoski and Novak [10] compared injection molded short and long fiber (glass, carbon, and aramid) reinforced polyamide 66 in terms of fatigue crack propagation rates. Long fibers enhanced fatigue performance by reducing the rates of crack propagation. In addition, the strain energy release rate models for short fiber materials were found to be applicable to the corresponding long fiber materials. Therefore, the improved fatigue performance observed with long fibers was correlated with the increase in modulus, which decreased the strain energy at a given peak stress. Studying the fracture surfaces, no significant differences between short and long carbon or between short and long glass reinforcing materials were observed. The dominant fracture mechanism for all reinforcements was matrix fracture.

However, for long aramid fibers, extensive fiber deformation and splitting were observed. Additionally, the authors molded plaques with an increased thickness and extracted skin and core specimens which were separately evaluated to obtain crack propagation rates. Poor fiber dispersion was noted for the cores of thick plaques resulting in poor fatigue performance for both core samples and full thickness (skin/core/skin) specimens.

4.1.1 Motivation

The motivation for the current study is the scarcity of mechanical data, particularly fatigue data, for direct/inline compounded long carbon fiber reinforced thermoplastic composites. For many practical industrial/commercial applications, data on fatigue performance is of critical importance if such materials are to be considered for implementation. Information concerning direct compounded carbon fiber LFT is especially uncommon in the literature. During the course of this study, no reliable sources for fatigue data on this particular type of composite have been identified. Even basic mechanical characteristics, for example, tensile strength, are only found in a limited number of studies. Additional data published in the open literature, particularly fatigue data, may aid engineers considering this process variant for applications requiring a composite with intermediate mechanical characteristics between that of short/discontinuous reinforcements and continuous fiber reinforcements. This study also contains a significant quantity of data on the direct compounding and compression molding process configuration.

4.2 Methodology

4.2.1 Specimen Preparation

The direct/inline compounded long fiber thermoplastic (LFT-D) specimens for this study were fabricated at the Fraunhofer Project Centre (FPC) research facility in London, Ontario using a commercially capable Dieffenbacher LFT-D manufacturing line. Modifications to the apparatus were made for the use of carbon fiber including simplifying the feed zone to remove sharp metallic edges and the ability to feed the carbon fiber roving directly from center pull bobbins. A schematic drawing and a flowchart for this manufacturing process is provided in Figure 4.1 (a) and (b), respectively. A Motan granule dosing system (item (1) within Figure 4.1) fed (2) a Leistritz ZSE-60HP-28D co-rotating twin screw extruder at 290°C and 67.3 RPM. This extruder introduced molten polymer via a waterfall die (basically a fully open film die) to (3) a ZSG Leistritz ZSG-75 P-17D co-rotating twin screw extruder (L/D = 17, 75 mm diameter) at 290°C and 36.1 RPM.

Charges (approximately 160 mm by 400 mm with a thickness of approximately 40 mm, 60 kg/h) exited this extruder, travelled along a heated conveyor (4) at 270°C and were manually placed in a 460 mm by 460 mm flat plaque tool installed in a Dieffenbacher DCP-U 2500/2200 press (5). The press was then closed with a speed profile of 800 mm/s until 30 mm from fully closed, 80 mm/s until 5 mm from fully closed and finally 20 mm/s to fully closed. This fast closing speed allowed the most flow from the various charges. Once fully closed the press was held closed for 40 seconds to allow the polymer to solidify. The polymer was Ultramid® A3W polyamide 66 provided by BASF. The carbon fiber was Panex 35-62 (1% sizing, 50K tow count, 29 rovings) sourced from Zoltek. The target fiber content was 40% by weight. Tool temperature set points and measurements are given in Table 4.1. Mid-run the tool temperature set points were revised in an attempt to achieve the desired tool temperatures (set points).

Table 4.1: Tool temperature set points and measurements for LFT-D fatigue specimen material preparation

Cavity	Core	Notes
135°C	140°C	Set point at beginning of trial
110°C	112°C	Initial surface temperature readings
119°C	127°C	Surface temperature after 25 charges
120°C	126°C	Surface temperature after 50 charges
120°C	128°C	Surface temperature after 75 charges
145°C	150°C	Revised set point mid-run
124°C	126°C	Post set point revision initial surface temperature readings
130°C	136°C	Surface temperature after end of trials

The sample geometry was a modified version of the specimen called out in standard GMW16970 [11] scaled such that the standard's 10 mm gauge width was increased to 25 mm. This non-standard specimen geometry was developed to minimize the effect of the specimen geometry on the fiber length distribution in the gauge region of the sample. The specimen layouts are shown in Figure 4.2 for both quasi-static and fatigue characterization. Average specimen thickness was 3.02 mm. Fibre length distribution for a lower fibre content PA6 LFT-D material was previously investigated and published in [1]. Mean fibre length was approximately 0.3 mm with the longest measured fibres over 1 mm in length. However, as noted in [1], there were challenges in separating the longest fibres for individual measurement as they were not effectively dispersed in the ZSG extruder and

remained bundled in the compression molded part. Quasi-static mechanical characterization of samples excised from plaques that were molded at the same time and under the same conditions as the plaques used for fatigue evaluations was completed at the Research & Development facility at General Motors (Warren, Michigan). Fatigue specimens were extracted from eight plaques. An additional tensile test for validation purposes was completed on one 0° specimen leaving twenty-three 0° specimens for fatigue characterization. Twenty-four fatigue tests were completed for the 45° and 90° sample orientation specimens. To ensure dry as molded conditions, all specimens were dried at 80°C in a vacuum oven for a minimum of five days with mass measurements once per day to confirm that all moisture had been removed. Specimens were subsequently sealed in aluminum pouches to preserve the samples in a dry state.

(a)   (b)
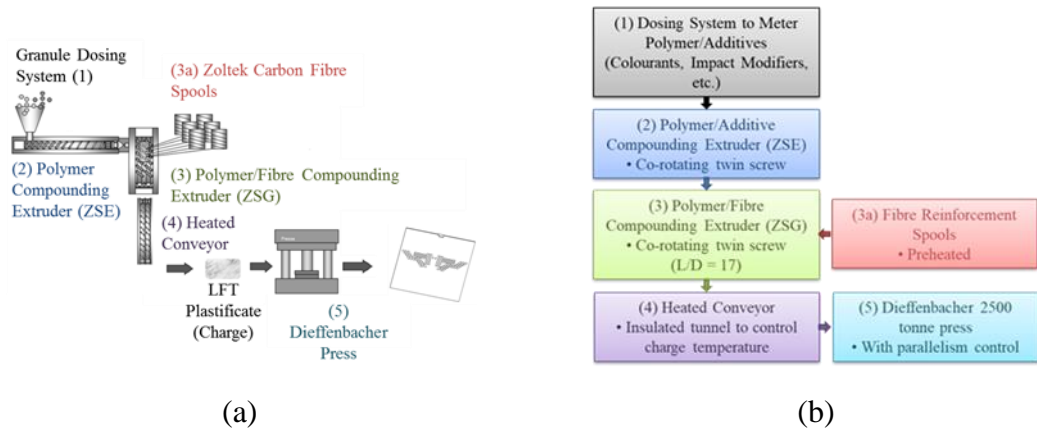
Figure 4.1: (a) Schematic and (b) Flowchart of Dieffenbacher LFT-D line at the Fraunhofer Project Center located at Western Ontario University

4.2.2 Stress-Life Fatigue Characterization

Fatigue characterization was completed on either an MTS Landmark 370.10 servohydraulic load frame with a 100 kN load cell or an MTS 858 tabletop servohydraulic load frame with a 25 kN load cell. Both load frames were controlled by a single Flex Test 60 controller connected to a personal computer. The cyclic loading frequency was 3 Hz with a stress ratio (R) of 0.1. Specimens (dimensions given in Figure 4.3) were extracted from molded plaques at orientations of 0°, 45°, and 90° with respect to the flow direction (as shown in Figure 2(b)). Given the duration of a test of one million cycles (up to four days), fatigue tests were completed without removing the specimens from the

aluminum pouches. This ensured that the specimen remained in a dry state during the test, thereby eliminating the confounding factor of water absorption. The pouch length was significantly greater than the specimen allowing an accordion-like geometry such that the load was transmitted through the specimen. The grip regions of the samples were visually assessed post-test to ensure minimal slippage. All tests were load controlled.

For 45° and 90° directions, the modulus was measured during post fatigue testing for runout specimens on electromechanical MTS load frames with a mechanical extensometer. Post runout testing for 0° specimens was completed on the servohydraulic fatigue frames with the collected data being limited to load and displacement. For select 45° and 90° direction specimens, an additional 1000 cycles were completed at the University of Windsor on an electromechanical load frame with a data acquisition rate of 100 Hz. Peak stress (maximum stress during a fatigue cycle) and R-value were identical to those used for the initial 10^6 cycles completed on the servohydraulic frame. Instrumentation included a mechanical extensometer. The frequency was reduced to be within the capabilities of the electromechanical load frame (0.3 Hz). The number of specimens for any post-fatigue characterization was the number of specimens in each direction that achieved 10^6 cycles without failure (three specimens in the 0° direction, four samples in the 45° direction, and four samples in the 90° direction).
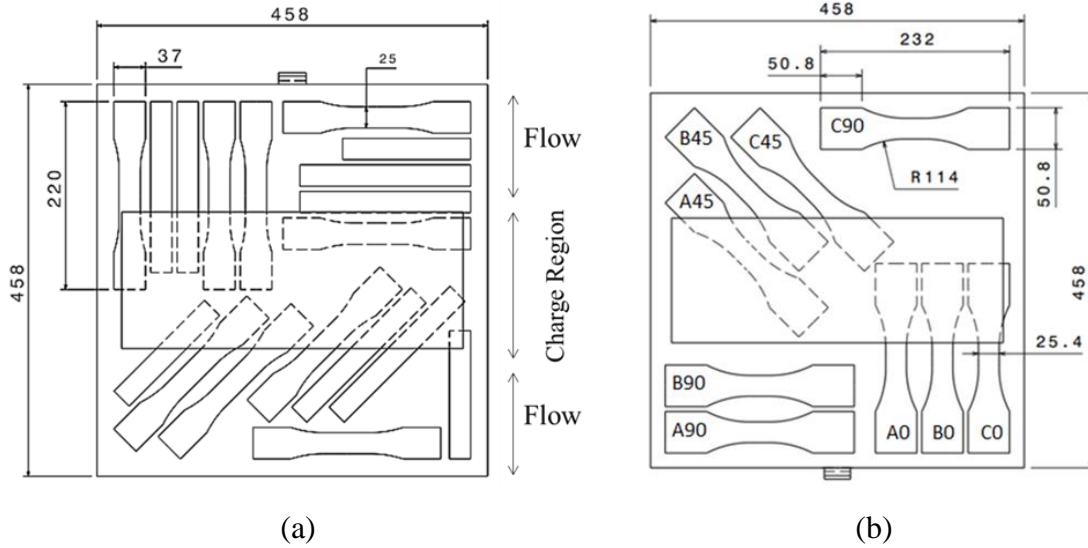
Figure 4.2: PA66/40% carbon fibre LFT-D (a) Quasi-static specimen layout and (b) Fatigue specimen layout (all dimensions in mm)
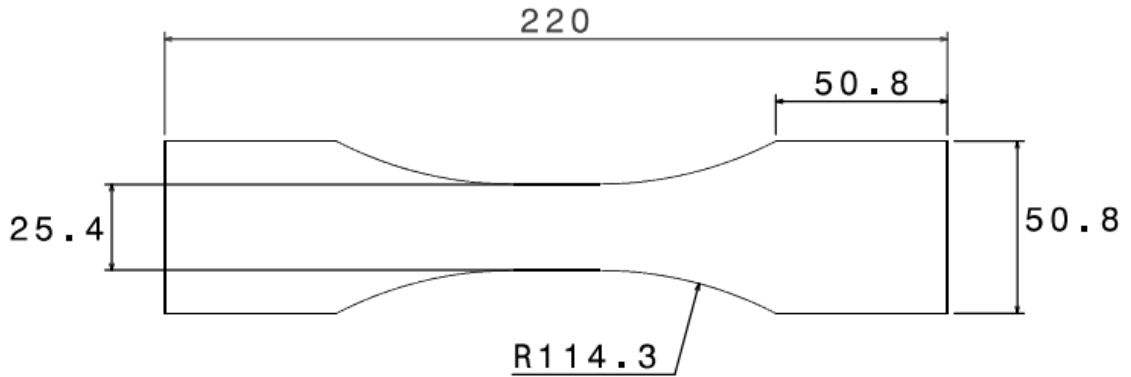
Figure 4.3: GMW16970 scaled fatigue specimen

4.2.3 Scanning Electron Microscopy of Fracture Surfaces

Fracture surfaces were analyzed by scanning electron microscopy (SEM). The apparatus was an environmental Scanning Electron Microscope (SEM) equipped with an FEI Quanta 200 field emission gun located at the Great Lakes Institute for Environmental Research. Images were acquired in low vacuum mode, thereby eliminating the need for carbon or gold specimen coatings. The electron beam voltage was 15 kV with a spot size of 3.9. The

spot size setting and electron beam voltage determine the approximate diameter of the electron beam at the sample surface. For the settings employed in this study (noted above) the electron beam diameter was approximately 3 nm. Images were generally acquired using a backscatter electron (atomic mass) detector.

4.3 Results & Discussion

4.3.1 Fatigue of 0° Orientation Specimens

Initial quasi-static tensile tests were completed for twenty-four 0° specimens. Chord modulus, computed by linear regression of engineering stress-strain data for 0.1% to 0.3% strain [12]; strain to failure; and tensile strength for the 0° direction are presented in Figure 4.4, Figure 4.5, and Figure 4.6, respectively. In each case, the histogram is compared to a normal distribution generated from the mean and standard deviation of each data set. Assessing the statistical distribution for the tensile strength aided in identifying the appropriate load/stress levels for the fatigue characterization. Normality of the experimental results was assessed with the Shapiro-Wilk normality test [13]. Normal distributions cannot be rejected (at p = 0.05) for any of these three primary mechanical parameters. However, comparing the histogram to the calculated normal distribution, the actual measurements appear to be somewhat skewed to the low end of the distribution. Clearly, not enough evaluations were performed to perfectly map out the distribution. Load or peak stress targets for the fatigue measurements were estimated by subtracting integer multiples of the standard deviation from the mean tensile strength.

Figure 4.4: PA66/40% carbon fibre LFT-D chord modulus measured in the 0° orientation

Figure 4.5: PA66/40% carbon fibre LFT-D strain to failure measured in the 0°
orientation

Results from eight of the twenty-three 0° orientation fatigue specimens were discarded due to failure outside of the gauge region. The fatigue life curve, with upper and lower bounds, for the remaining 0° specimens is shown in Figure 4.7. The 95% confidence band was generated consistent with ASTM E739-10 [14]. A power law relationship between peak stress and cycles to failure was assumed (Equations 1 to 3). The stress-life relationships, including upper and lower bounds, for the 0° specimens from linear regression are given by Equations 4.1 to 4.5 with the variable parameter values provided in Table 4.2. Generally, for the fatigue specimens the independent variable (as shown in the equations) was selected to be the number of cycles to failure. This is not consistent with ASTM E739 [14] standard but was necessary to obtain a curve that fits the data with acceptable accuracy. These parameters and equations allow this material to be assessed for use in applications where either a required number of cycles or a maximum uniaxial stress are known and maximum stress or cycles to failure, respectively, are to be calculated. Significant limitations are imposed on such analyses by the anisotropy of the material.

Runout specimens (specimens cyclically loaded to 1 million cycles without failure) were not included in the analyses for linear regression or upper/lower limits. Runout specimens were subsequently loaded at a quasi-static rate to failure to assess their retained strength following fatigue evaluation. The tensile strengths after 1 million cycles for 0° specimens (run-out) are also shown in Figure 4.7. These residual strengths averaged 226 ± 7 MPa (three run-out specimen) and were higher than the mean quasi-static tensile strength value for the 0° samples of 203 ± 25 MPa, although the deviation ranges do overlap. The small number of run-out specimens must be highlighted given the resulting high uncertainty for the runout tensile strength standard deviation.
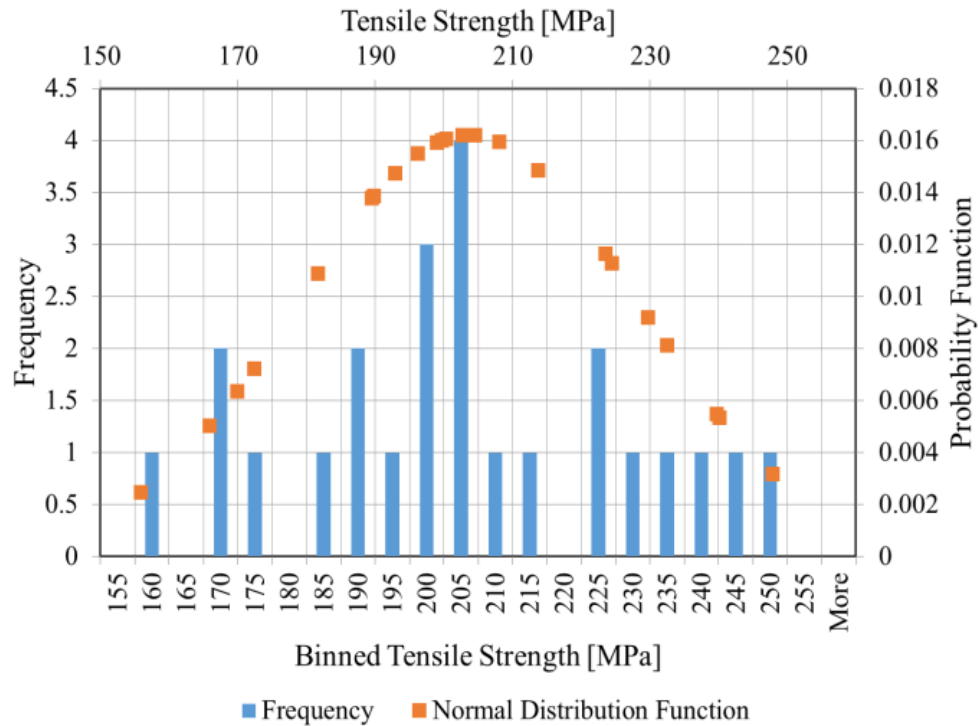
Figure 4.6: PA66/40% carbon fibre LFT-D tensile strength measured in the 0° orientation
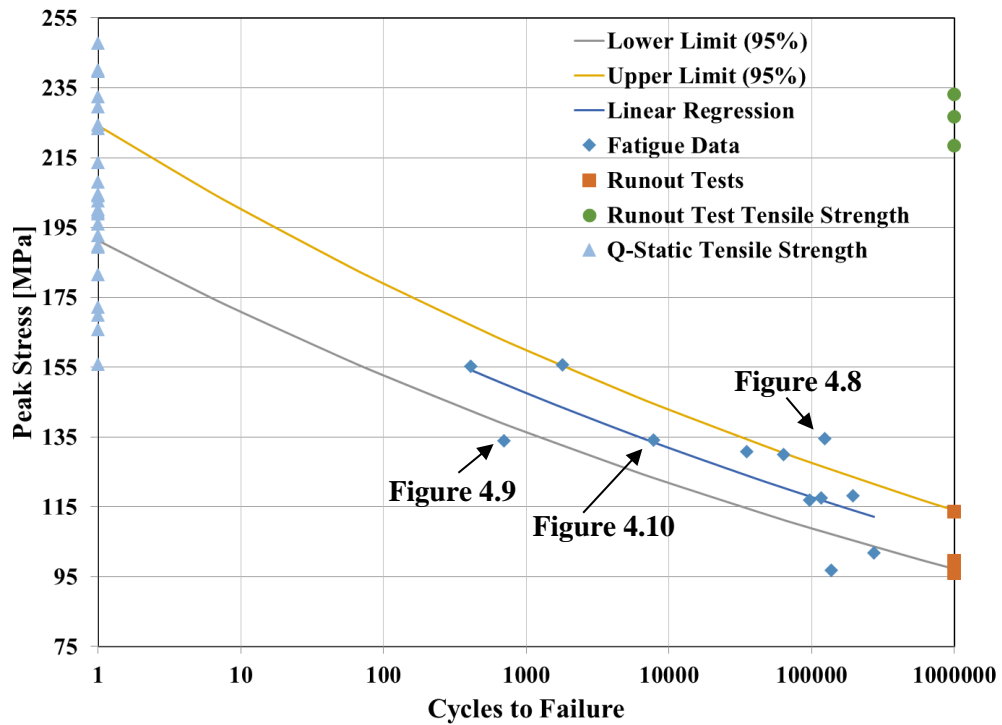
Figure 4.7: PA66/40% carbon fibre LFT-D fatigue stress-life curves for 0° specimens

The 0-degree peak stress (from line of best fit) for the runout samples is 105 MPa with lower and upper bounds of 97 MPa and 114 MPa, respectively. This stress value for the runout samples is approximately 52% of the initial average quasi-static tensile stress. Given the unique attributes of this study in terms of fiber content, molding process, direct-compounding, matrix selection, and fatigue testing methodology, finding a suitable data set for direct comparison is challenging. Properties of unreinforced PA66 provide a lower bound. For reference, the fatigue life for a stress ratio of R = -1 for unreinforced PA66 at 10^6 cycles is approximately 35 MPa [15]. Therefore, the measured average value for runout stress at 105 MPa is approximately a 200% increase with respect to that reported for unreinforced PA66. It is worth noting that the 90° direction is best suited for comparison with this lower bound. For further comparison, one data set was identified for an injection molded 40% long carbon fiber reinforced PA66. In this study, the fatigue results were expressed as a percentage of material strength for injection molded test bars characterized for fatigue using a stress ratio of -1 (fully reversing tension-compression test method). The

peak stress that resulted in the sample lasting 1 million cycles was approximately 115 MPa [16]. An earlier study of injection molded PA66 with 40% carbon fiber observed an essentially identical peak stress at 1 million cycles for tensile-tensile fatigue with a stress ratio of 0.1 [17]. Both of these studies show similar peak stresses for runout as we measured in this study.

$$Y = A_f - B_f \cdot X \qquad\qquad \text{Equation 4.1}$$

$$Y = \log(S_f) \qquad\qquad \text{Equation 4.2}$$

$$X = \log(N_f) \qquad\qquad \text{Equation 4.3}$$

$$Y_{upper\ limit} = A_f - B_f \cdot X + \sqrt{2F_p}\,\sigma_f \left[\frac{1}{k_f} + \frac{(X - \bar{X})^2}{\sum_{i=1}^{k_f}(X_i - \bar{X})^2} \right]^{0.5} \qquad \text{Equation 4.4}$$

$$Y_{lower\ limit} = A_f - B_f \cdot X - \sqrt{2F_p}\,\sigma_f \left[\frac{1}{k_f} + \frac{(X - \bar{X})^2}{\sum_{i=1}^{k_f}(X_i - \bar{X})^2} \right]^{0.5} \qquad \text{Equation 4.5}$$

Table 4.2: Parameters for stress-life equations for PA66/40% carbon fibre LFT-D 0° specimens

Parameter	Value	Description
A_f	2.316	y-intercept of log-log S-N curve
B_f	0.0489	Slope of log-log S-N curve
F_p	4.1028	F-distribution parameter [14]
σ_f	0.0418	Variance
k_f	12	Number of samples
$\bar{X}$	4.413	Mean log(N)
$\sum_{i=1}^{k}(X_i - \bar{X})^2$	11.045	Sum of squares: each measurement less the mean.

Three specimens were selected from the samples evaluated in the 0° orientation for SEM investigation of the fracture surfaces. These included: one specimen from above the 95th percentile upper bound with a relatively high cycle count, one specimen with a relatively low cycle count that was below the 95th percentile lower bound, and one specimen essentially on the line of linear regression. The three specimens that were chosen had all been evaluated at similar stress levels. Therefore, it is believed that the difference in the performance of the specimens was likely to be due to microstructural differences. The specimen shown in Figure 4.8, evaluated with a peak stress of 135 MPa, performed above the 95th percentile upper limit with failure occurring at approximately 123,000 cycles. In the first micrograph (low magnification, Figure 4.8(a)) a fiber bundle is observed in the lower left corner of the sample. Since the bundle is lying mostly in the fracture plane, it is oriented not in the 0° direction, but somewhere closer to 90°. This type of orientation is not unusual as flow forces are all that is aligning the fibers in the compression molding process. This orientation primarily loads the matrix. The high magnification figure (Figure 4.8(c)) shows that though the fiber bundle is not oriented in the desired direction, the fibers appear to be separated from each other and wetted with solidified resin. This clearly improved the performance of this particular bundle. Other fibers in the same micrograph are aligned with the direction of force and appear to have broken rather than pulled out of the matrix.
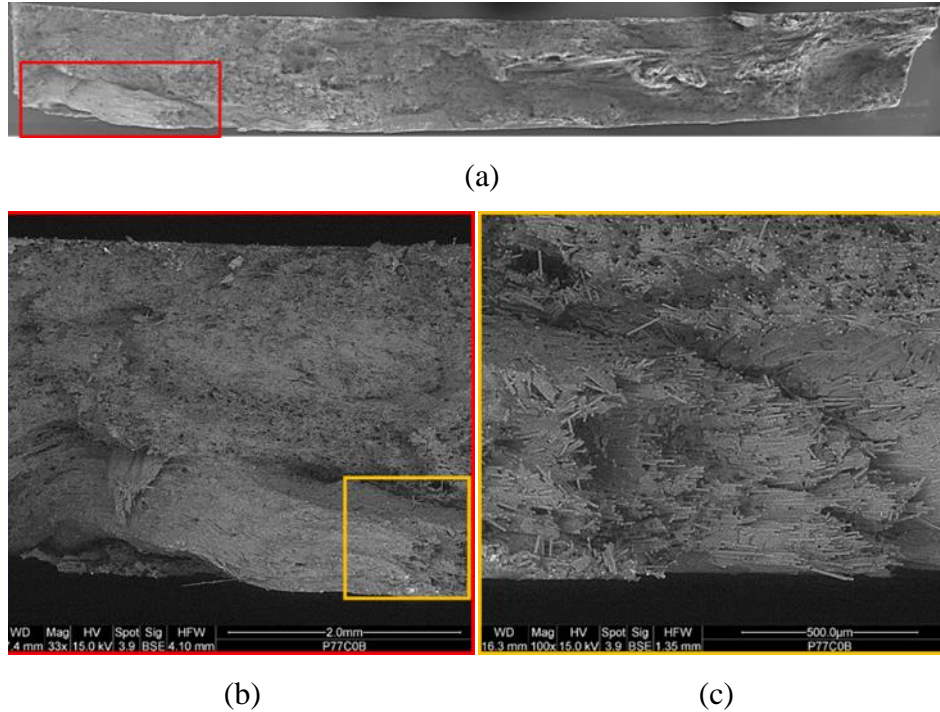
Figure 4.8: 0° specimen P77C0 fracture surface, 123,000 cycles at 135 MPa peak stress: (a) stitched images of full fracture surface, (b) fiber bundle highlighted in red, (c) end of fiber bundle highlighted in yellow

The 0° specimen in Figure 4.9, evaluated at a stress of 134 MPa, performed below the 95th percentile lower bound curve, failing at approximately 700 cycles. A large bundle of fiber was present in the core of the specimen that was aligned perpendicular to the loading axis (Figure 4.9(b)). Figure 4.9(c) shows typical failure surfaces for both the highlighted bundle and a region with a more commonly observed failure surface/microstructure. In the bundle, the fibers appear to be reasonably well surrounded by resin. However, due to the orientation, the failure is matrix dominated (fiber/matrix debonding) in this area. This results in relatively long segments of the fiber with little resin attached. Away from the bundle, fiber breakage/pullout is observed as the primary failure mode. In this latter region, fiber is generally aligned in the flow direction (parallel to the loading axis, perpendicular to the plane of the image/fracture surface).
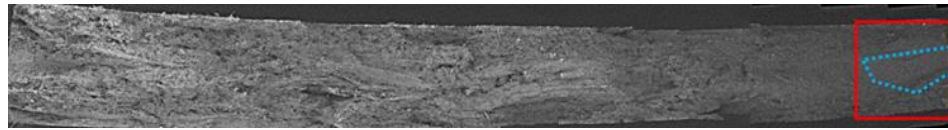
(a)
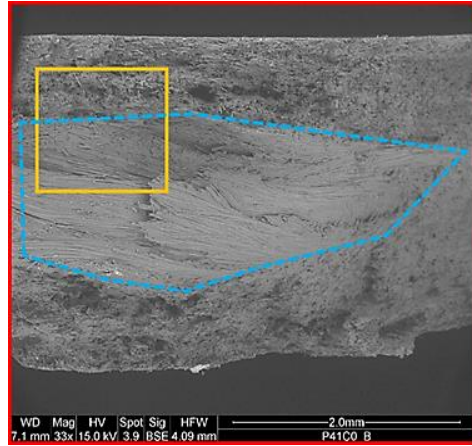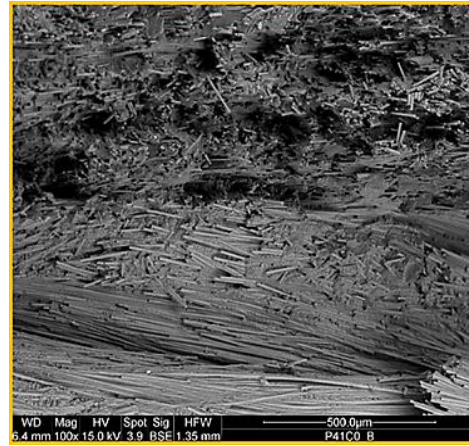
(b)   (c)

Figure 4.9: 0° specimen P41C0 fracture surface, 700 cycles at peak stress of 134 MPa: (a) full fracture surface, (b) large defect, (c) typical fracture surface at defect periphery (defect outlined, dashed blue)

The specimen shown in Figure 4.10 represents the line of best fit shown in Figure 4.7, lasting 7800 cycles at a peak stress of 134 MPa. Two defects were observed on the fracture surface for this specimen: both consisted of poorly dispersed fiber with poor fiber wet-out. The first defect shown in Figure 4.10 consists of fiber that may be somewhat aligned parallel to the loading direction. However, this fiber aligned to the loading direction was not able to transfer load to the surrounding structure. Fiber failure without pullout of fibers that were not appropriately wetted with resin is hypothesized as the cause since no sign of polymer matrix bonded to the fiber is observed on either side (Figure 4.10 (b) and (c)) of the fracture surface. The possibility exists that a void was present at the end of a fibre bundle.

The image in Figure 4.10 (b) is interesting. Examining the figure closely shows fibers in what appears to be a helical fiber structure embedded in the matrix. The sample failed in this area due to matrix failure. It is difficult to learn from the images why the fibers surrounding this structure appear to be in somewhat of a net. It is possible that this structure

83

is what remains of a fiber bundle that was not completely wetted. As the sample failed, the fibers that were not wetted with resin scattered over the fracture surface or were lost when the sample was removed from the test. This is the best evidence observed during this study that not all the fibers in the tows are completely wetted. A separate, smaller defect in specimen P45A0, shown in Figure 4.10 (d), consists of a fiber bundle perpendicular to the loading direction with poor wet-out as indicated by the well over two-millimeter length of the fibers that show no evidence of polymer adhering to their surface. This creates a large inherent flaw in the middle of the fatigue sample.

Summarizing the 0° orientation specimens it is clear that a key factor in the performance of these specimens was the presence or absence of poorly dispersed or wet-out fibers. Poorly dispersed fibers perpendicular to the loading direction allow for matrix dominated failure leading to early fatigue failure. Fibers that are not wetted by the resin are unable to support or transfer loads to adjacent fibers and therefore lead to particularly poor fatigue performance. Though not shown here in terms of SEM images, the runout samples, although fractured in post-fatigue tensile tests, showed that good fiber wetting and distribution can be achieved with this process.

(a)   (b)

(c)   (d)
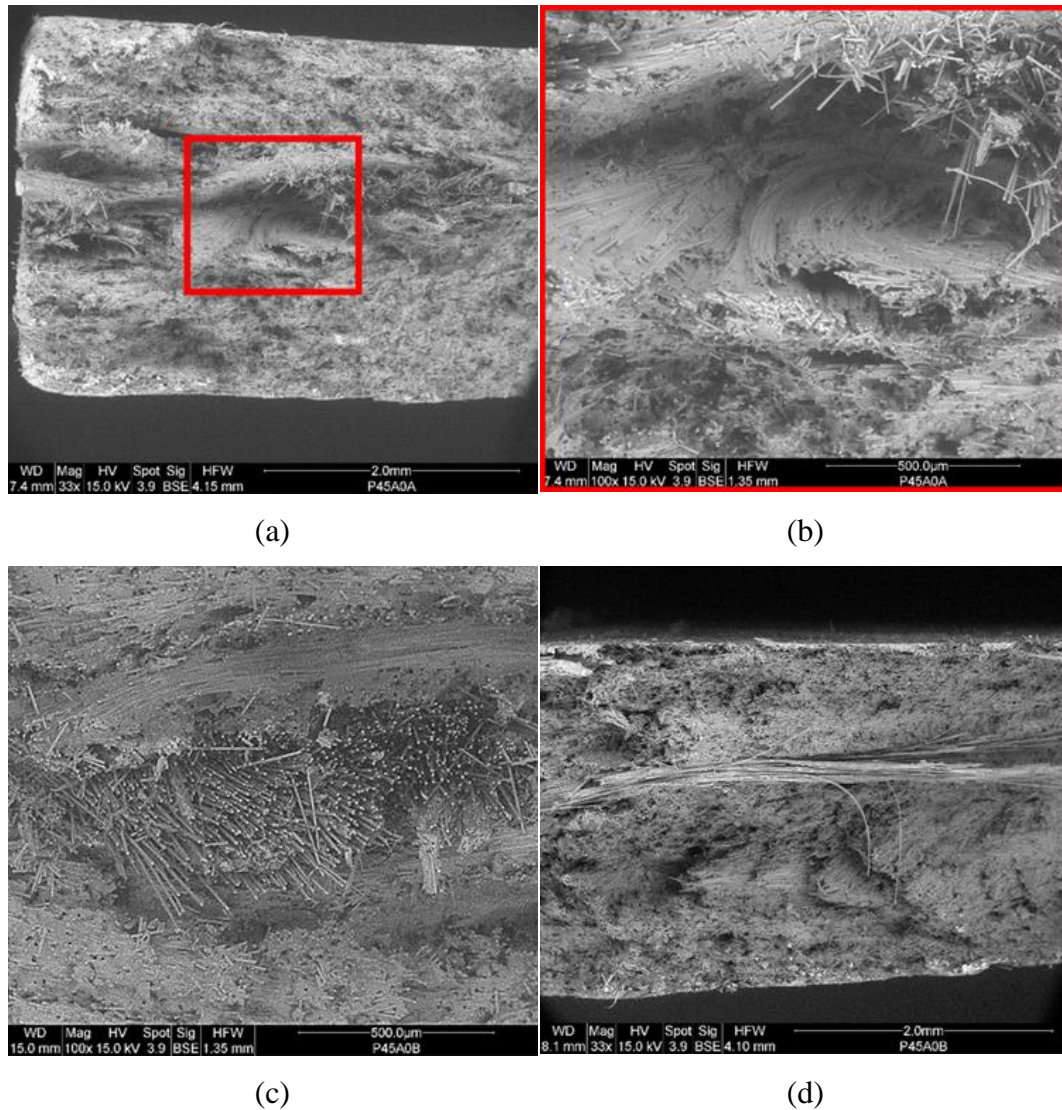
Figure 4.10: 0° fatigue specimen P45A0 fracture surface, 7800 cycles at a peak stress of 134 MPa: (a) defect observed from fracture surface A at low magnification such that its scale can be compared to the thickness of the specimen, (b) higher magnification image of this defect, (c) higher magnification image of this defect from fracture surface B, (d) a separate defect visible on fracture surface B

4.3.2 Fatigue of 45° Orientation Specimens

Initially twenty-two quasi-static tensile tests were completed for the 45° direction. Chord modulus, strain to failure, and tensile strength distributions are shown in Figure 4.11 to Figure 4.13, respectively. Once again, although the distributions appear slightly skewed, normality cannot be rejected ($p = 0.05$) for any of these three parameters. The selection of peak stresses used during the fatigue characterization was consistent with the procedure

noted for the 0° direction (i.e., subtraction of integer multiples of the tensile strength's standard deviation from the mean).
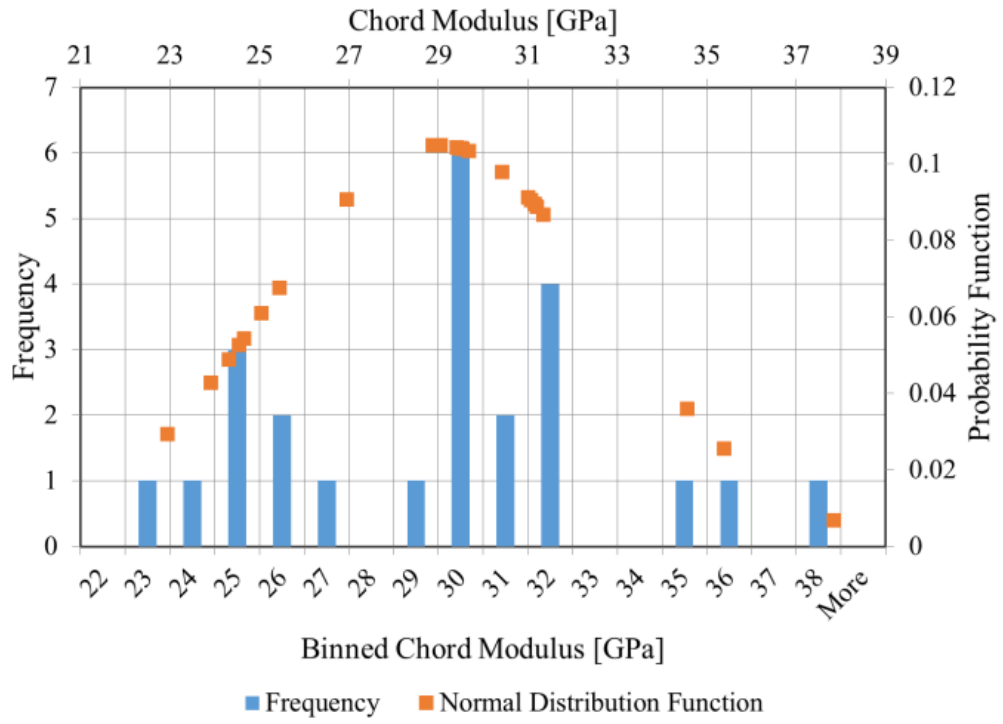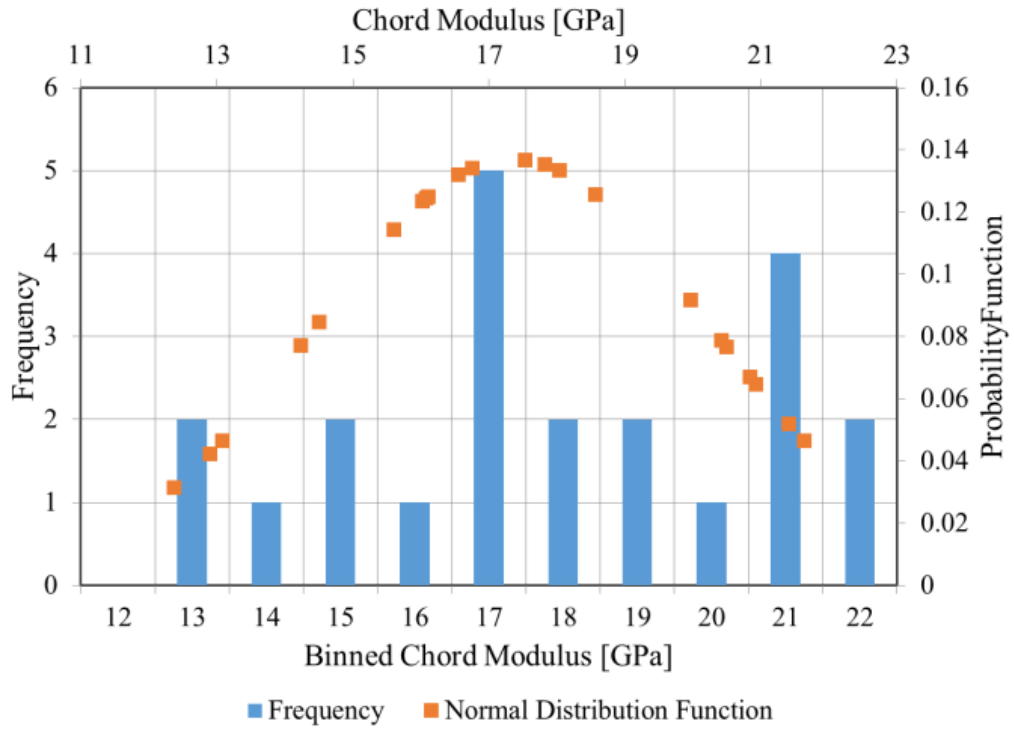

Figure 4.11: PA66/40% carbon fibre LFT-D chord modulus measured in the 45° orientation

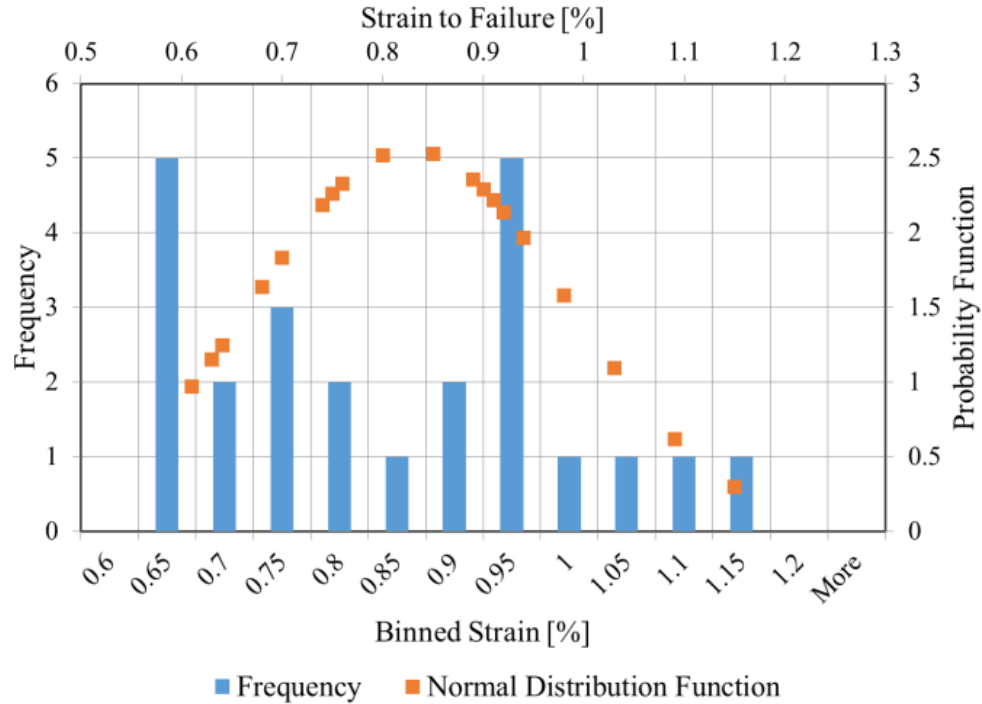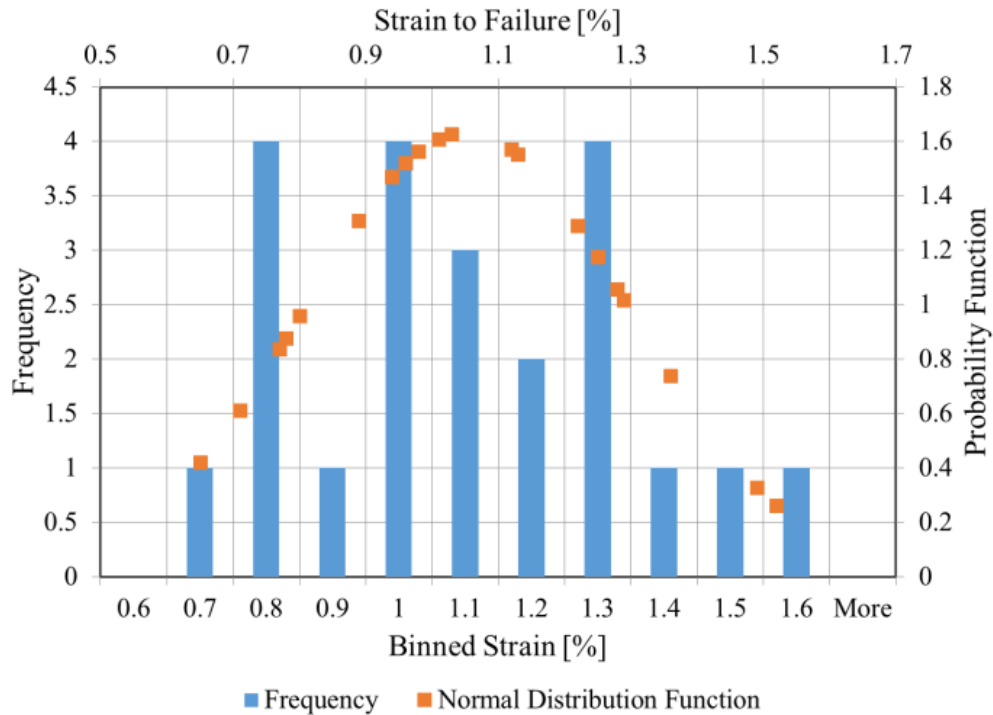Figure 4.12: PA66/40% carbon fibre LFT-D strain to failure measured in the 45°
orientation

Nine of the twenty-four fatigue specimens oriented at 45° to the flow direction broke
far outside of the gauge region and were not considered for further analysis. The fatigue
life data for the 45° specimens are shown in Figure 4.14. Parameters for the line of best fit
and upper and lower bounds (95%) for 45° specimens are given in Table 4.3. Consistent
with the procedure for the 0° direction, the number of cycles to failure was selected as the
independent variable to obtain the line of best fit. The approach taken here yields a better
fit since there is significant variability in the cycles to failure for a given stress level and
direction. The line of best fit is much closer to the horizontal than to the vertical,
extrapolating to a minimum experimental stress level can predict a very large cycle count.
Therefore, minimizing error in terms of cycles to failure for such data generally results in
very large error magnitudes for data points at the lower and upper limits of stress and a low
coefficient of determination.

From the figure, the peak stress (line of best fit) at 10^6 cycles was 72 MPa (lower and
upper bounds: 65 MPa and 80 MPa, respectively). For comparison, the mean quasi-static

tensile strength for the 45° direction was 140 ± 21 MPa. Therefore, the runout specimens occurred at approximately 51% of the initial tensile strength. This value is quite similar to the value observed with the samples oriented at 0° to the flow direction. Also, at 10^6 cycles, the mean peak stress to failure is approximately 130% greater than that of unreinforced PA66. Since this value is closer to the value for the unreinforced material than the value for the 0° oriented samples, it does show that when the fibres are oriented at an angle to the loading direction, the failures become progressively more matrix dominated. However, a direct comparison of fatigue behavior of these high fibre content materials to an unreinforced PA66 from a different supplier employing a different fatigue characterization methodology is not really possible due to the large differences in modulus and stress at failure imparted by the carbon fibre.
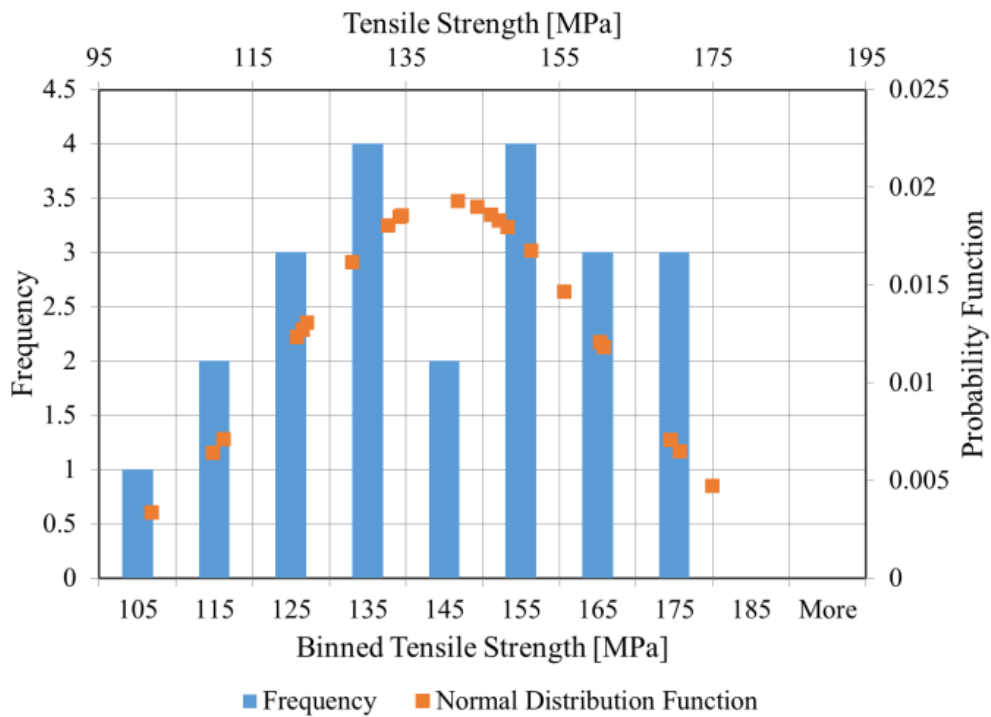
Figure 4.13: PA66/40% carbon fibre LFT-D tensile strength measured in the 45° orientation
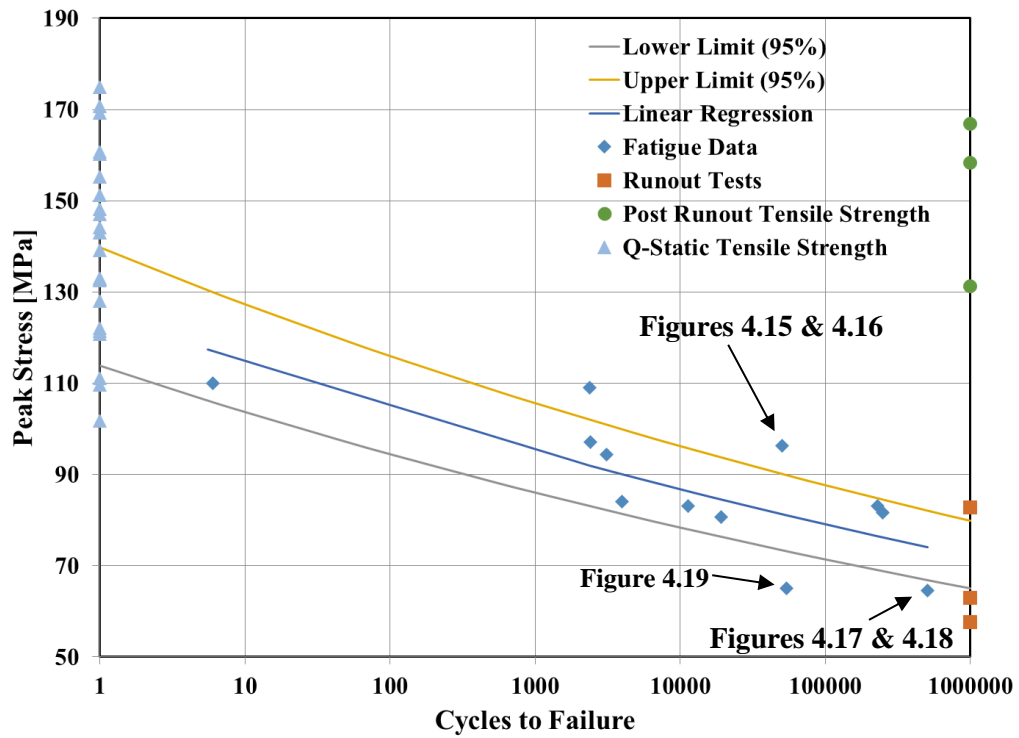
Figure 4.14: PA66/40% carbon fibre LFT-D fatigue stress-life curves for 45° specimens

Table 4.3: Parameters for stress-life equations for PA66/40% carbon fibre LFT-D 45° fatigue specimens

Parameter	Value
A_f	2.100
B_f	0.0403
F_p	4.1028
σ_f	0.0539
k_f	12
$\bar{X}$	4.067
$\sum_{i=1}^{k}(X_i - \bar{X})^2$	19.576

Samples chosen for SEM examination were again representing samples that performed better than the 95% upper confidence limit or more poorly than the lower 95% confidence limit. The fracture surface shown in Figure 4.15 was acquired from a specimen loaded to a peak stress of 96 MPa that reached 50,000 cycles prior to failure. The fatigue life of this specimen is above the upper confidence limit as shown in Figure 4.14. It contained one defect at the fracture surface, shown at a higher magnification in Figure 4.16. Although the fibers in this area indicate that there were issues with the fiber wet-out by the polymer for this particular fiber bundle, it appears that there has been significant deformation of the wetted part of this bundle. This shows that even with a wetting issue, some bundles can contribute to the fatigue resistance of the composite.
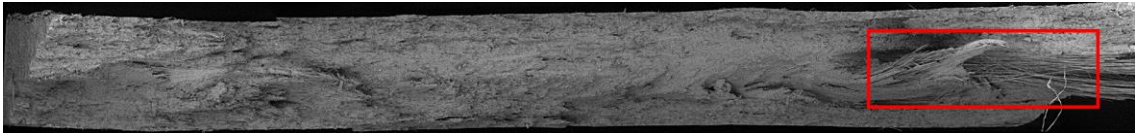
Figure 4.15: Fracture surface for 45° fatigue specimen P41B45, 50,000 cycles at a peak stress of 96 MPa
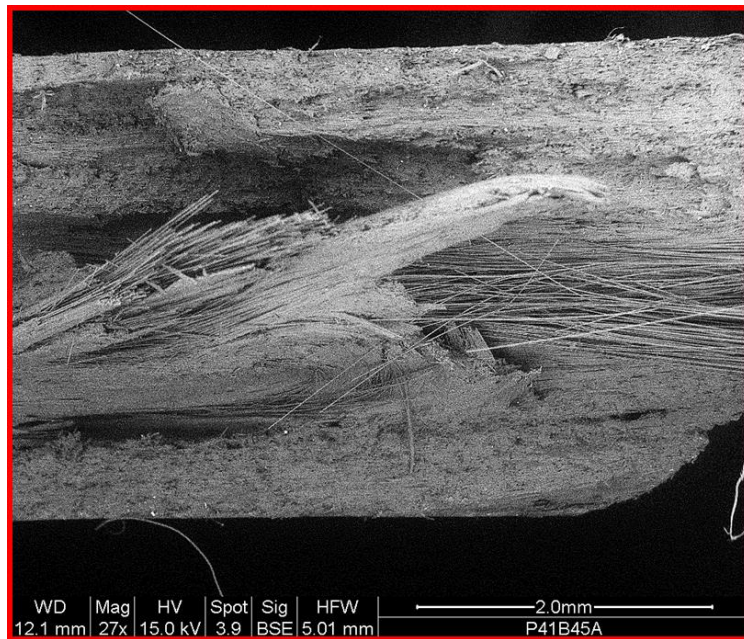
Figure 4.16: Defect highlighted in Figure 4.15, specimen P41B45

The fracture surface shown in Figure 4.17 is from a specimen that performed below the lower confidence limit as shown in Figure 4.14. This specimen failed after 508,000 cycles with a peak stress of 65 MPa. It contains only one identifiable defect at the fracture surface, shown enlarged in Figure 4.18. This defect again seems to be a lack of wetting of a fiber bundle by the thermoplastic resin. This sample also seems to have a number of fibers in nearly a 90° orientation to the fracture surface, which would also lead to lower performance in this particular sample.
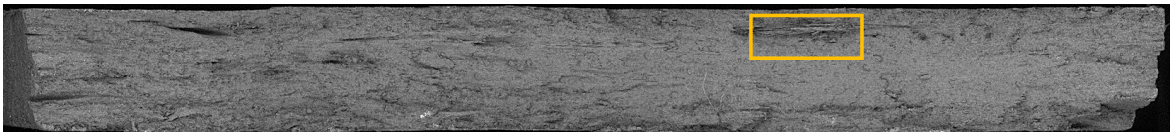
Figure 4.17: Fracture surface for 45° specimen P41C45 at a peak stress of 65 MPa for 508,000 cycles
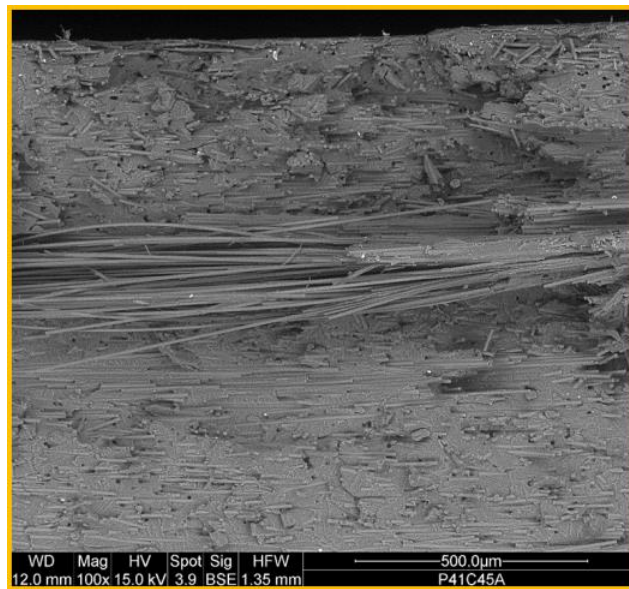
Figure 4.18: Defect highlighted in Figure 4.17, specimen P41C45

The fracture surface for a different 45° specimen evaluated at the same peak stress of 65 MPa, but with failure occurring at 53,000 cycles, is shown in Figure 4.19. The fatigue life of this specimen is well below the lower confidence limit determined from the data. Multiple large defects with very poor fiber wet-out were observed to cover the majority of the failure surface. Comparison of the fracture surfaces in Figure 4.17 and Figure 4.19 provides evidence that the fatigue life for the materials in this study may be determined by the presence and scale of manufacturing defects. As previously noted, further efforts to improve quality control for the direct/in-line compounding process are very much warranted.
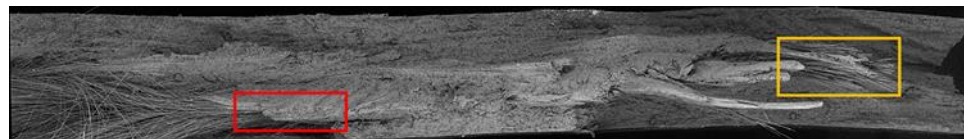
(a)
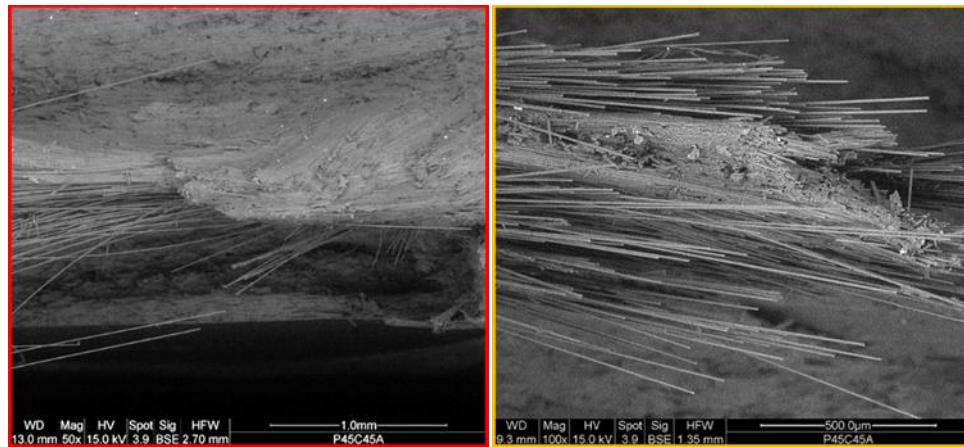
(b)   (c)

Figure 4.19: 45° fatigue specimen P45C45 fracture surface, 53,000 cycles at 65 MPa: (a) full fracture surface, (b) transition to poor wetout for a large bundle of dry fiber, (c) smaller bundle of dry fiber

In an additional evaluation, the elastic modulus was measured for 1000 additional cycles for the runout specimens (four 45° specimens) using an MTS electromechanical load frame in order to better understand the damage accumulation/failure mechanisms and obtain data necessary to apply damage models [8]. For most specimens, the modulus held

relatively constant over these 1000 cycles. For a 45° specimen with a peak stress of 83 MPa, a crack was found (after 1000 additional cycles on an electromechanical frame) to have propagated partially through the gauge section (Figure 4.20). However, this crack did not continue to propagate to cause catastrophic failure in a post runout tensile test (failure occurred in the gauge to grip transition region). Measurements of modulus during the 1000 post runout additional fatigue cycles suggest this fracture initiated at approximately 700 cycles and propagated until it was apparently arrested at about 810 cycles, as indicated in Figure 4.21. For this particular sample, modulus measurements during loading are shown. Modulus measurements determined from the unloading curve are slightly but not significantly lower (less than 0.1%).

Modulus measurements on another 45° specimen, loaded to a peak stress of 63 MPa, show two interesting phenomena (Figure 4.22). A gradual modulus reduction over the 1000 cycles suggest this specimen has cracks that are propagating during the evaluation and that it is possible that the sample would fail with a limited number of additional loading cycles. Comparing the change in modulus versus loading cycle, this slope is 216% higher for P33A45 versus the average loading cycle-modulus slope for all post-runout tested specimens. This modulus reduction may be useful for damage model calibration [14]. Furthermore, this sample exhibited a 1.0% difference between the loading and unloading moduli. This difference indicates increased energy loss per cycle than was observed with other specimens that exhibited much lower differences between loading and unloading moduli (average of 0.2%; the 1.0% difference of specimen P33A45 is approximately 4 standard deviations above the mean for these post-runout tested samples). This energy dissipation may be associated with damage accumulation but the mechanism for damage propagation is expected to differ from specimen P21B45 since there is no significant difference between loading and unloading moduli for specimen P21B45 between 700 – 810 cycles where crack propagation is hypothesized to occur. However, the possibility exists that this specimen is an outlier.

Figure 4.20: 45° fatigue sample P21B45 loaded to a peak stress of 83 MPa, arrested fatigue crack propagation
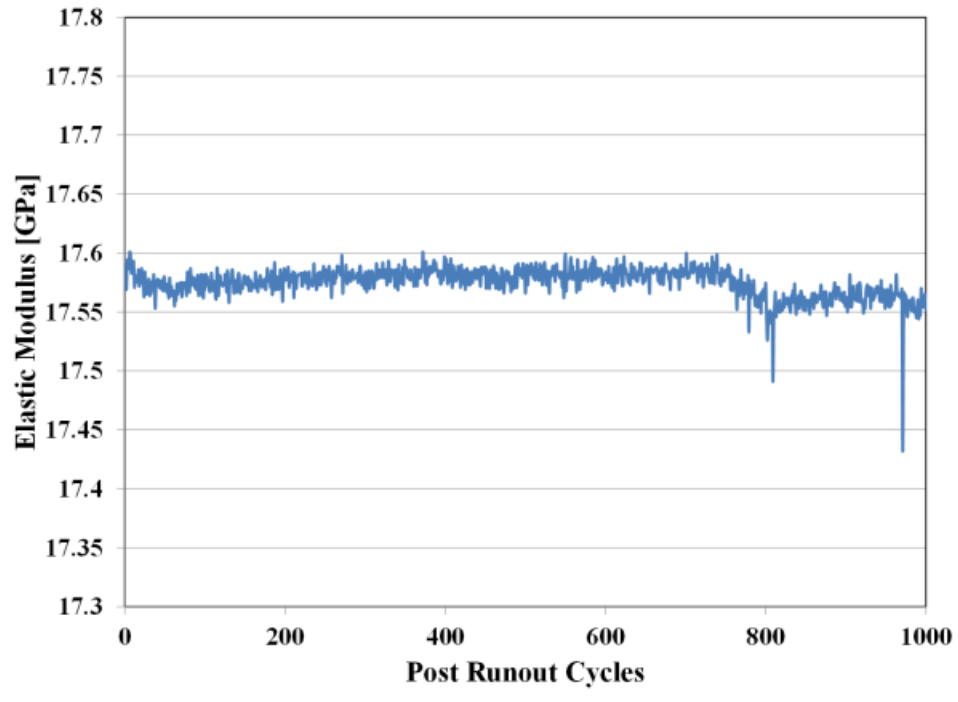
Figure 4.21: Post runout modulus measurements for 45° sample P21B45 loaded to a peak stress of 83 MPa
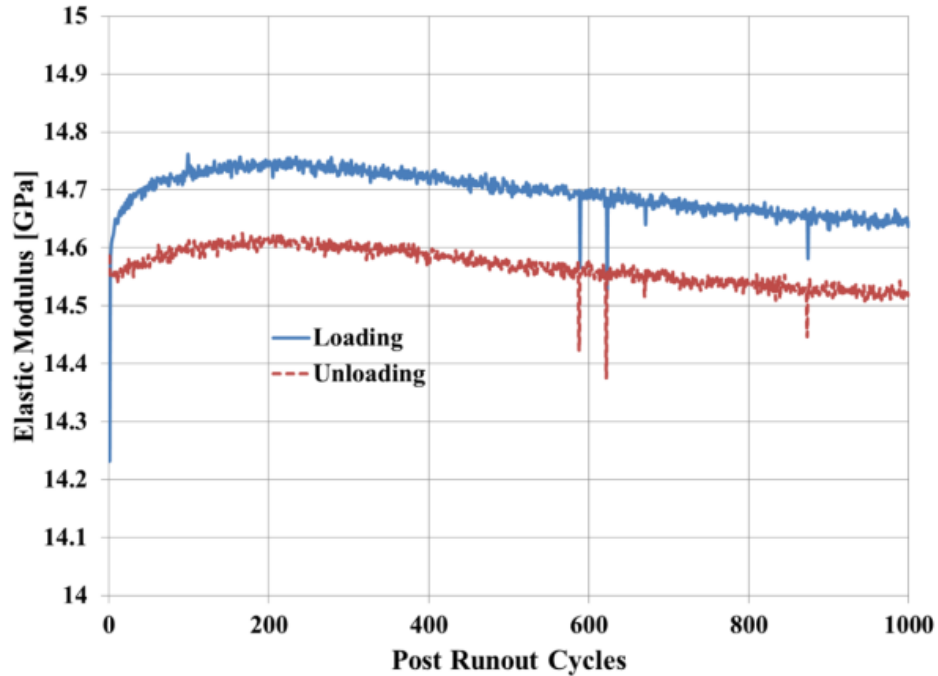
Figure 4.22: Post runout modulus measurements for 45° sample with a peak stress of 63 MPa (P33A45)

4.3.3 Fatigue of 90° Orientation Specimens

For the 90° direction, twenty-four initial quasi-static tensile tests were conducted to determine chord modulus, strain to failure, and tensile strength, the results of which are shown in Figure 4.23 to Figure 4.25, respectively. A normal distribution is not rejected for tensile strength. Therefore, the process for selecting peak stress levels for fatigue characterization was unchanged from the previous orientations. Further post-fatigue testing mechanical evaluation included 1000 additional cycles on an electromechanical load frame and quasi-static displacement controlled loading to failure.
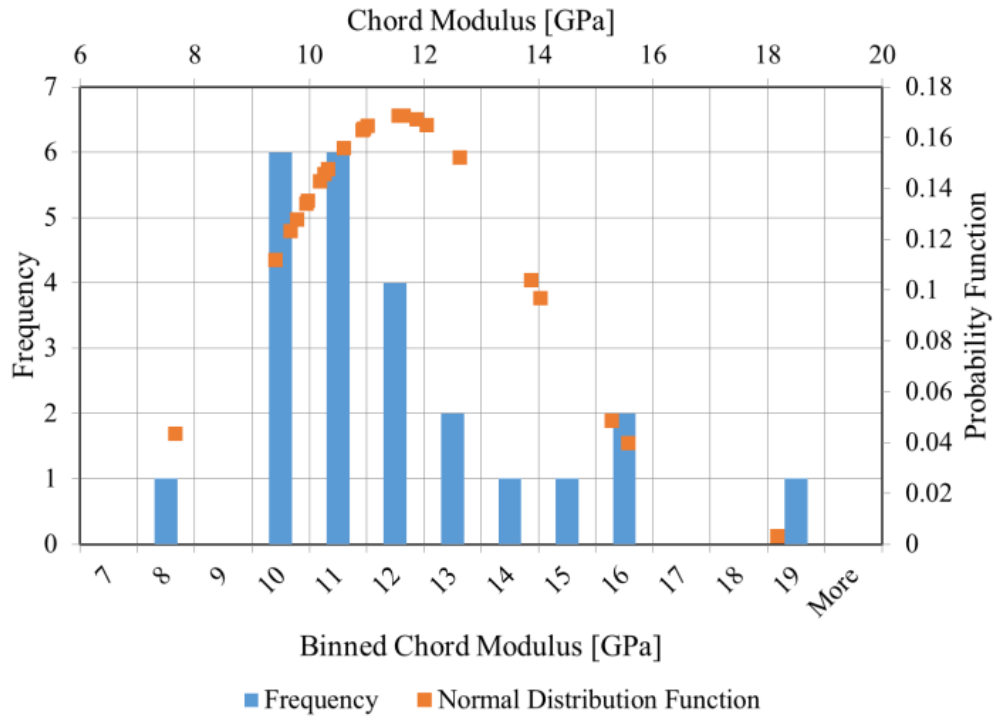
Figure 4.23: PA66/40% carbon fibre LFT-D chord modulus measured in the 90°
orientation
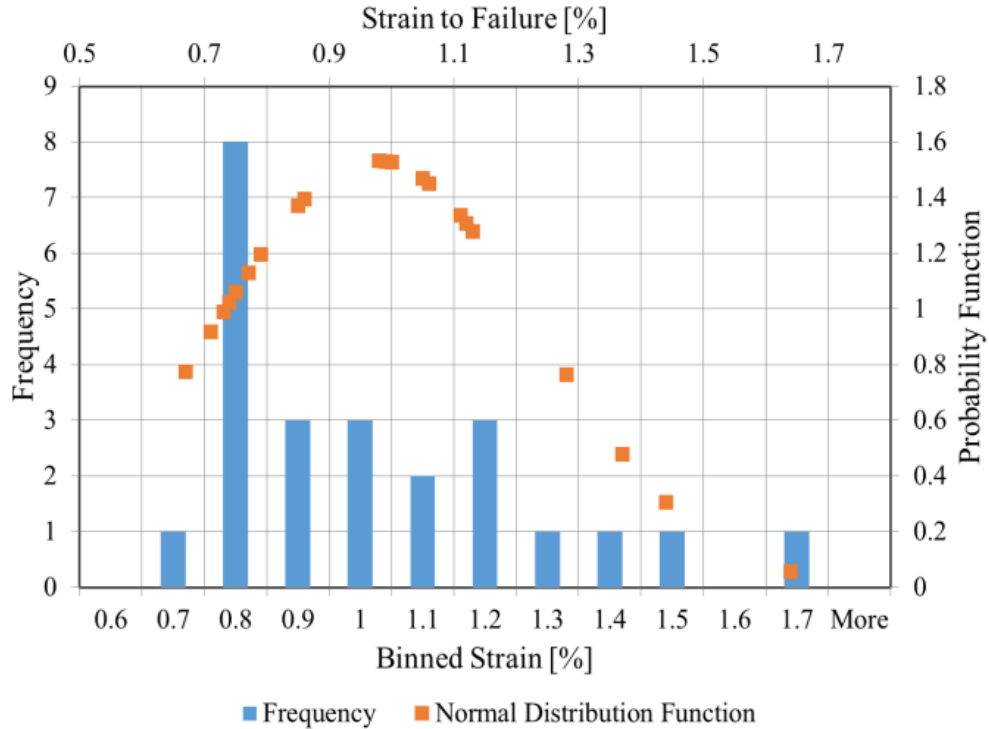
Figure 4.24: PA66/40% carbon fibre LFT-D strain to failure measured in the 90°
orientation

Ten of twenty-four 90° fatigue specimens failed outside of the gauge region and were not considered for further analysis. Of the remaining specimens, four reached one million cycles without failure (runout). The fatigue life prediction curves, upper/lower confidence limits, initial tensile strengths, and post-runout tensile strengths for the 90° specimens are shown in Figure 4.26. Parameters for the line of best fit and upper and lower bounds (95%) for 90° specimens are given in Table 4.4. Consistent with the procedure for the previous samples, the number of cycles to failure was selected as the independent variable to obtain a better line of best fit.

The initial mean quasi-static tensile strength for samples in this orientation is 93 ± 15 MPa. Peak stress at 10^6 cycles is 51 ± 5 MPa (55% of the quasi-static tensile strength) with lower and upper bounds of 39 MPa and 72 MPa, respectively. Peak stress at 10^6 cycles is approximately 46% higher than unreinforced PA66 (51 MPa versus 35 MPa). The reader will note that as the orientation with respect to the flow direction becomes larger, the runout peak stress gets closer to the unfilled PA66 value. This shows that at

these higher orientations with respect to flow, the matrix is becoming more dominant in the fatigue response.
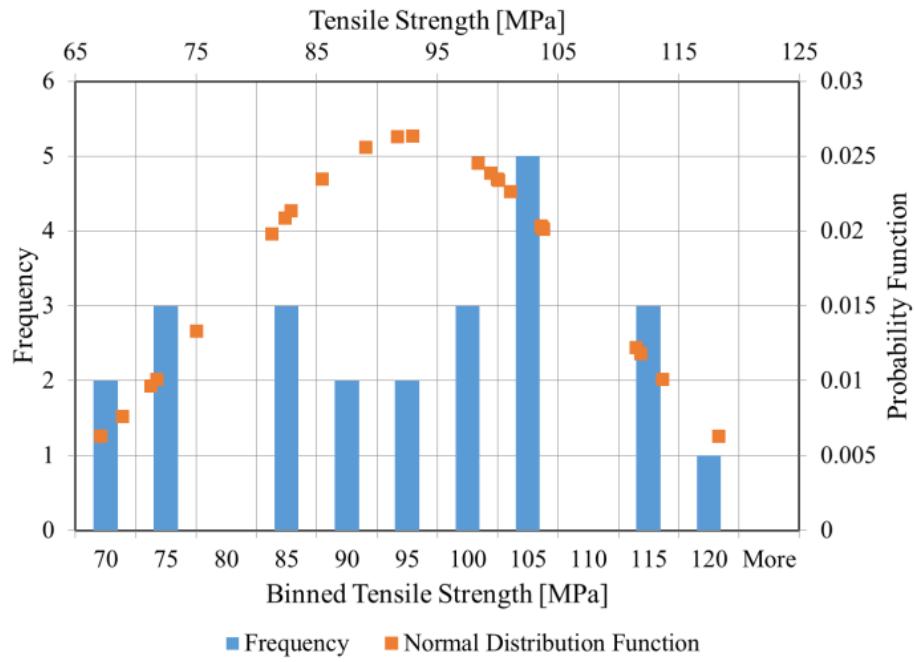
Figure 4.25: PA66/40% carbon fibre LFT-D tensile strength measured in the 90° orientation
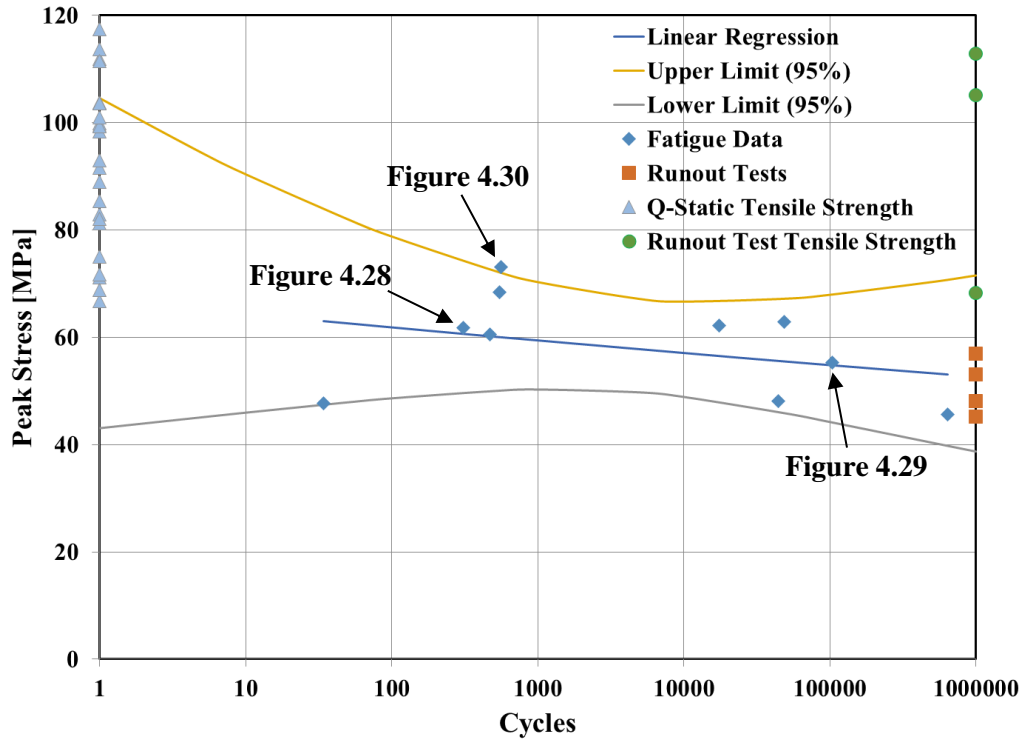
Figure 4.26: PA66/40% carbon fibre LFT-D fatigue stress-life curves for the 90°
specimens

Table 4.4: Parameters for stress-life equations for PA66/40% carbon fibre LFT-D 90°
fatigue specimens

Parameter	Value
A_f	1.827
B_f	0.0176
F_p	4.459
σ_f	0.0691
k_f	10
$\bar{X}$	3.657
$\sum_{i=1}^{k}(X_i - \bar{X})^2$	17.358

A photograph of a specimen on the lower confidence limit of the fatigue performance envelope (P18A90) is shown in Figure 26. This figure clearly shows that this specimen possessed particularly poor fiber wet-out in the gauge region and as a result, failed in only 34 cycles at a peak stress of 48 MPa. Fortunately, samples such as this were not common; however, such specimens are particularly undesirable and very clearly demonstrate the need for ongoing research and further development of this material and manufacturing process.

Figure 4.27: 90° specimen P18A90, failure after 34 cycles with a peak stress of 48 MPa

Fracture surfaces for two specimens with 90° orientations that exhibited fatigue life consistent with the line of best fit are shown in Figures 27 and 28. The peak stress applied to the specimen in Figure 27 was 62 MPa, and fatigue failure occurred after 309 cycles. Two distinct regions with poor fiber dispersion/wet-out were identified. In fact, there were many areas on the fracture surface of this specimen where poor fiber wetting or failure at the ends of fiber bundles were observed. The highlighted areas are particularly poor. For the specimen shown in Figure 28, the peak stress applied to the specimen was 55 MPa with failure occurring after 103,000 cycles. No defects which could be detected at the levels of magnification employed in this study were found on the fracture surface for this specimen. Figure 28 shows the complete fracture surface as well as higher magnification images for locations spread evenly (approximately) across the cross section. For the small proportion of fiber nominally in the normal direction (to the fracture surface), fiber pullout is present. However, the majority of the fibers are approximately in the plane of the fracture surface image as is expected for a sample in this orientation and indicates that the fatigue life for this sample orientation is matrix dominated.
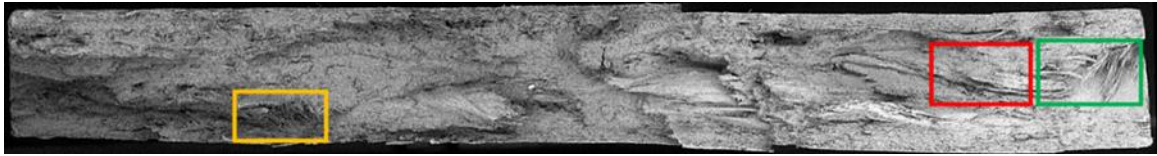
(a)
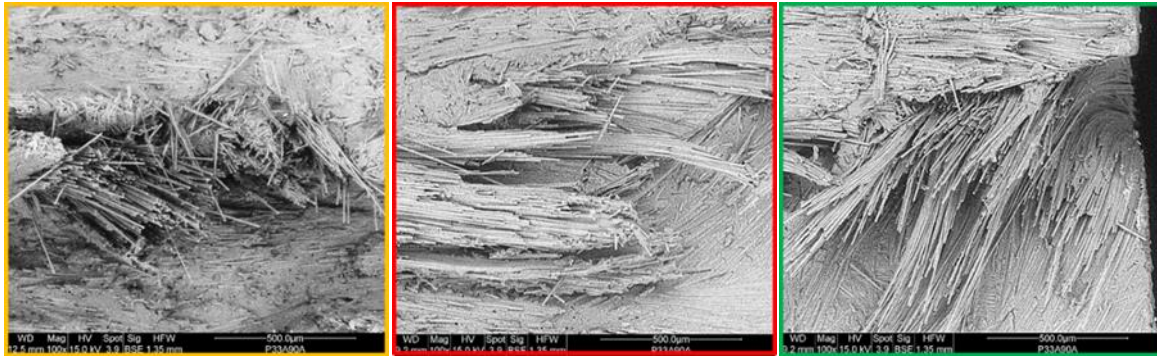
(b)

(c)

(d)

Figure 4.28: 90° fatigue specimen P33A90, peak stress of 62 MPa, failure at 309 cycles: (a) full fracture surface, (b) high magnification view of dry fiber bundle, (c) poorly dispersed fiber bundle with fiber wet-out, (d) fiber bundle with some wet-out

(a)

(b)   (c)   (d)
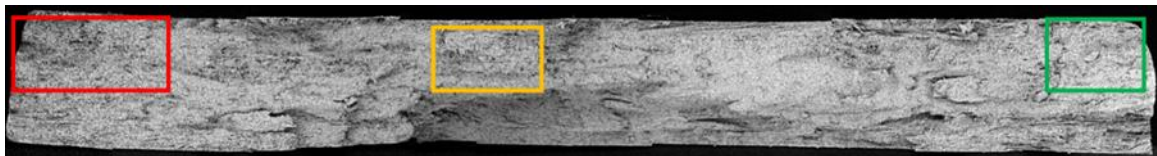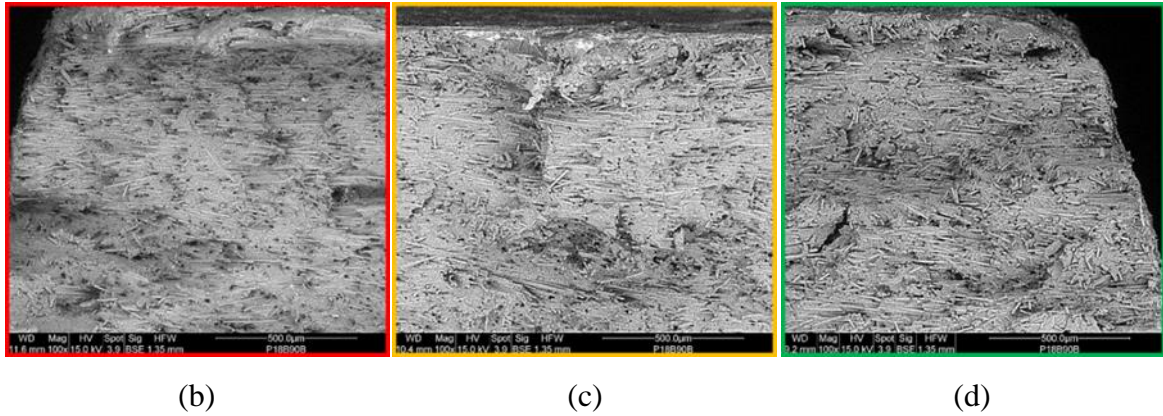
Figure 4.29: Fracture surface of 90° fatigue specimen P18B90, peak stress of 55 MPa. Failed at 103,000 cycles: (a) full fracture surface fracture surface, (b) higher magnification view of top left corner, (c) mid-span, (d) top right corner
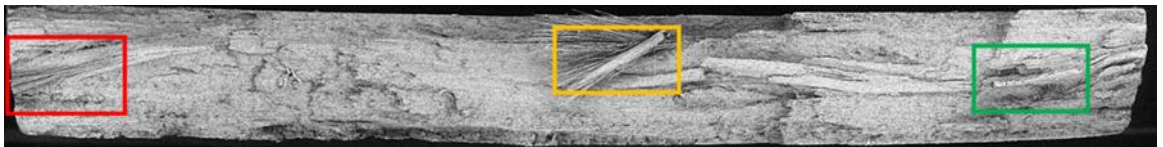
(a)

(b)   (c)   (d)

Figure 4.30: Fracture surface of 90° fatigue specimen P41B90, peak stress of 73 MPa, failure occurred at 558 cycles: (a) full fracture surface, (b) dry, poorly dispersed fiber perpendicular to the axis on which load was applied, (c) dry, poorly dispersed fiber perpendicular to the axis on which load was applied & a broken bundle of fiber with wet-out, (d) embedded bundle of dry fiber parallel to the axis on which load was applied

The 90° fatigue specimen shown in Figure 29 was selected for post-test visual analysis since its response is slightly above the upper confidence limit shown in Figure 25. This specimen failed at 558 cycles at a peak stress of 73 MPa. Several defects exhibiting poor

fiber wetting and dispersion were identified at the fracture surface. Though the fatigue life response is above the upper bound, the number of cycles to failure is quite low. It is unclear why the specimen performed so well with respect to the upper confidence limit. The results from this particular specimen emphasize the need for further work in the area of optimization of the LFT-D process to improve fiber wet-out and dispersion.

4.4 Conclusions

Tensile fatigue characterization of compression molded direct/in-line compounded carbon fiber/polyamide 66 (40% fiber weight fraction) was completed in this investigation. Fatigue life prediction curves for a stress ratio of 0.1 were developed for samples oriented at 0°, 45°, and 90° with respect to the flow direction. Selected fatigue fracture surfaces from each group of samples (orientations) were inspected using a scanning electron microscope. This study can serve as a baseline for the performance of LFT-D prepared carbon fiber reinforced materials. Key results include:

1. For the 0° fiber orientation samples, the peak stress at 10^6 cycles (from the line of best fit) was 105 MPa (52% of the initial mean quasi-static tensile strength for samples in this orientation). Lower and upper limits (95% confidence) were 97 MPa and 114 MPa, respectively.

2. The peak stress at 10^6 cycles for specimens oriented 45° to the flow direction was 72 MPa (line of best fit) with lower and upper confidence limits of 65 MPa and 80 MPa, respectively. This peak stress at runout was 51% of the initial mean 45° quasi-static tensile strength.

3. Peak stress at 10^6 cycles for the samples oriented at 90° to the flow direction was 51 MPa (line of best fit) with lower and upper confidence limits of 39 MPa and 72 MPa, respectively. This peak stress is 55% of the mean initial quasi-static 90° tensile strength (coefficient of variation: 16%).

4. Fatigue evaluations carried out with compression molded direct/in-line compounded (LFT-D) 40% w/w carbon fiber reinforced polyamide 6,6 exhibited a reasonable fit to a typical power law response with respect to the relationship between peak stress and the number of cycles to failure. Regardless of specimen orientation, the runout stress was approximately 50% of the mean quasi-static tensile stress for samples in the same orientation. Therefore, the fatigue performance was typical for a tension-tension fatigue evaluation at a stress ratio of 0.1.

5. The peak stress at runout (10^6 cycles) was approximately 200%, 130%, and 45% higher than unreinforced PA66 for samples oriented at 0°, 45°, and 90° directions

with respect to flow, respectively. One key aspect of the approximate nature of these values is the use of PA66 data from the open literature.

6. Given the number of defects observed on the fracture surfaces and the conclusion noted above, it appears that improvements to minimize processing defects would shift the peak stress versus number of cycles curve to higher stresses. This would improve the utility of these materials in potential structural applications.

7. The majority of the defects noted were due to poor wetting of fibers in bundles that were not appropriately dispersed. This points to the need for further investigations into LFT-D processing.

4.5 References

1.   Bondy M, Pinter, P., Altenhof, W. Experimental Characterization and Modelling of the Elastic Properties of Direct Compounded Compression Molded Carbon Fibre/Polyamide 6 Long Fibre Thermoplastic. Submitted to Materials & Design. 2016 12/16/2016:1-25.
2.   Zhang X, Johrendt J. Using Neural Networks to Examine the Sensitivity of Composite Material Mechanical Properties to Processing Parameters. SAE International Journal of Materials and Manufacturing. 2016;9(2016-01-0499):737-745.
3.   Bondy M, Altenhof W. Low velocity impact testing of direct/inline compounded carbon fibre/polyamide-6 long fibre thermoplastic. International Journal of Impact Engineering. 2018;111:66-76.
4.   Rohan K, McDonough T, Ugresic V, et al. Mechanical Study of Direct Long Fiber Thermoplastic Carbon/Polyamide 6 and its Relations to Processing Parameters. University of Western Ontario/Zoltek Corporation; 2015. p. 1-24.
5.   Yan X, Cao S. Structure and interfacial shear strength of polypropylene-glass fiber/carbon fiber hybrid composites fabricated by direct fiber feeding injection molding. Composite Structures. 2018;185:362-372.
6.   Goel A, Chawla K, Vaidya U, et al. Characterization of fatigue behavior of long fiber reinforced thermoplastic (LFT) composites. Materials characterization. 2009;60(6):537-544.
7.   Grove D, Kim H. Fatigue behavior of long and short glass reinforced thermoplastics. SAE transactions. 1995:450-456.
8.   Nguyen B, Kunc V, Bapanapalli S. Modeling Fatigue Damage in Long-Fiber Thermoplastics. Fatigue of Composite Materials. 2013;3:103.
9.   Nguyen BN, Tucker BJ, Khaleel MA. A Multiscale Modeling Approach to Fatigue Damage in Discontinuous Fiber Polymer Composites. Pacific Northwest National Lab.(PNNL), Richland, WA (United States); 2005.
10.   Wyzgoski M, Novak G. Fatigue fracture of long fiber reinforced nylon 66. Polymer composites. 1995;16(1):38-51.
11.   General Motors. Guidelines for Conducting Axial Load-Controlled Fatigue Testing of Neat, Filled, and Short-Fiber Reinforced Thermoplastic Polymeric Materials. General Motors.
12.   International A. D3039. Standard test method for tensile properties of polymer matrix composite materials. West Conshohocken, PA: American Society of Testing and Materials.
13.   Shapiro SS, Wilk MB. An analysis of variance test for normality (complete samples). Biometrika. 1965;52(3/4):591-611.
14.   International A. E739. Standard Practice for Statistical Analysis of Linear or Linearized stress–life (S–N) and strain–life (ϵ–N) fatigue data. West Conshohocken, PA: American Society of Testing and Materials.
15.   DuPont. DuPont Minlon and Zytel nylon resins Design Information - Module II. 2018.
16.   PlastiComp. Expanding the Performance Envelope for Long Fiber Thermoplastic Composites with Unidrectional Tape Inserts. Winona, MN2018.

17.	Mandell JF, Huang D, McGarry F. Fatigue of glass and carbon fiber reinforced engineering thermoplastics. Polymer Composites. 1981;2(3):137-144.

CHAPTER 5

LOW VELOCITY IMPACT TESTING OF DIRECT/INLINE COMPOUNDED
CARBON FIBRE/POLYAMIDE-6 LONG FIBRE THERMOPLASTIC

5.1 Introduction

The previous chapters have covered fundamental mechanical properties of carbon fibre LFT-D including elastic properties; fibre orientation and fibre length distributions; and stress-life fatigue characteristics. Impact performance is another material characteristic which will be critical for many engineering applications. Furthermore, the evaluation of fatigue performance revealed many defects (e.g., poor wet-out/fibre dispersion), some of which were of a large size relative to the material specimen. Such defects may be severely detrimental to impact performance. In this chapter a study of the impact performance of eight carbon fibre LFT-D formulations is presented.

A much larger knowledgebase is available in the open literature for mechanical properties of glass fibre LFT materials compared to carbon fibre. While some conclusions from such research may be applicable, the relatively low stiffness of glass fibre with respect to its strength may yield reduced material performance in terms of impact with respect to carbon fibre (CF) reinforcement. Thomason [1] investigated the impact performance of dry-as-molded and boiling water conditioned injection molded glass fibre (10, 14, and 17 μm diameter; 10-50% by weight) and PA 66. The product of fibre aspect ratio and volume fraction indicated a random fibre orientation during melt processing limited the fibre length in the molded part. Notched and un-notched specimens were characterized; notched specimen impact characteristics were effectively independent of fibre diameter. Un-notched specimen impact performance was not strongly influenced by fibre length.

Bartus and Vaidya [2] subjected compression molded LFT-G (granule) PP & GF specimens to blunt object intermediate velocity (40 – 140 m/s) impact to obtain a critical velocity where 50% of projectiles do not perforate the specimen (similar to the V_{50} ballistic limit but applied to low velocity impact). One critical conclusion was that the material did not exhibit significant rate sensitivity under the conditions of the study. Another finding applicable to the current work is the strong indication of fibre orientation influencing impact characteristics.

In a rare investigation of direct compounded long fibre thermoplastic materials, Zhang et al. [3] of the National Research Council of Canada characterized the mechanical properties of both compression and injection molded PP/GF and PA/GF materials (4 different configurations) under low velocity impact. A significant decrease in stiffness was observed at +85°C with respect to room temperature. However, the force-deflection responses prior to maximum load were minimally affected by temperature in the range of -40°C to 0°C. With a PP matrix, injection molded parts were observed to have lower maximum loads with respect to compression molded parts. In terms of damage/failure mechanisms, PP was minimally affected by temperature. Less damage was observed for PA/GF at higher temperatures.

Rate sensitivity has directly been assessed with servohydraulic testing machines and uniaxial tensile tests. Schossig et al. [4] completed tensile tests on glass reinforced thermoplastics at strain rates of 0.007 s^{-1} and 174 s^{-1}. Positive strain rate sensitivity, consistent with the literature was observed. Two sets of parameters for the G'sell-Jonas model [5] were identified (a transition from isothermal to adiabatic behaviour occurs). However, anisotropy (which can be significant for compression molded LFT materials) is not considered. Weeks and Sun [6] assessed the rate dependence of mechanical properties of AS4 CF/PEEK thermoplastic. Tests were conducted on balanced angle ply specimens with orientations of 0°, 15°, 30°, 45°, and 60° with a servohydraulic testing machine (strain rates between 10^{-5} and 0.1 s^{-1}) and a split Hopkinson pressure bar (SHPB) (100 to 1000 s^{-1}). Two rate dependent constitutive models were developed.

5.1.1 Motivation

The open literature includes few, if any, studies of the mechanical properties of compression molded, direct compounded carbon fibre reinforced thermoplastic. Impact data is particularly scarce. The current study is a first step in developing a better understanding of the influence of process configuration and material formulation on impact properties for this type of material through the use of an industry standard test. While Charpy impact may be the more popular method for assessing impact properties, there are concerns that for longer fibre lengths the small size of a Charpy specimen may introduce a dependence of mechanical properties on specimen size. Therefore, the ISO 6603-2 [7]

puncture test was selected rather than a unique apparatus (i.e., Bartus et al.) which would introduce challenges in comparisons with data in the literature.

5.2 Methodology

5.2.1 Specimen Preparation

Carbon fibre/PA6 material was manufactured by the Fraunhofer Project Centre in London, Ontario on a Dieffenbacher LFT-D manufacturing line. Approximately seven 458 mm by 458 mm by ~ 2.7 mm square plaques were provided for each of eight process configurations which are documented in Table 5.2. Material with fibre weight contents (Toho Tenax HTR40 F22 1550tex, 24k tow count) of 9, 12, 18, and 25% were produced. Note that this is a fibre with epoxy sizing. Subsequent research has employed carbon fibre intended for the selected matrix material. The matrix was BASF 8202 heat stabilized (HS) polyamide 6. Charge placement was asymmetric as shown in Figure 5.1 (a) with a mold coverage of approximately 14%. Charge mass was defined in the manufacturing process control software to be 755 grams with approximate dimensions of 100 mm by 300 mm by 20 mm. The press force was 5000 kN with the speed-distance profile shown in Table 3.2. The mold temperature was 120ºC and the cooling time was 30 seconds.

Table 5.1: Speed-distance profile for compression molding of process/material configurations V1-V8

Speed (mm/s)	Distance (mm)
75	50
35	35
15	15
10	0

The specimens were conditioned at room temperature and an approximate relative humidity of 30%. Details in moisture absorption can be found in [8]. Specimens were extracted by water jet at DYDD Systems in Oldcastle, Ontario at a pressure of 345 MPa with a nozzle diameter of 0.076 mm. Six 140 mm by 140 mm ISO 6603-2 [7] impact specimens were extracted from each plaque as shown in Figure 5.1 (a): three from the flow region and three from the charge region. Four plaques from each process configuration were prepared to obtain 12 specimens from each region for each process configuration: 6 for quasi-static characterization and 6 for low velocity impact.

Table 5.2: LFT-D Material/process configurations V1-V8

Trial #	Fiber weight %	Roving number	Throughput (kg/h)	Charge mass (g)	Cycle time (sec)	Fibre compounding extruder speed (rpm)	Fibre compounding extruder volume fill (%)
V1	12	23	118	755	23	61	33
V2	12	23	160	755	17	83	33
V3	12	35	181	755	15	62	50
V4	18	35	118	755	23	60	32
V5	18	35	160	755	17	82	32
V6	9	17	118	755	23	62	33
V7	9	17	160	755	17	84	33
V8	25	31	109	755	25	87	20

5.2.2 Quasi-static Characterization

Uniaxial tensile and flexure (three point bending) testing for this material are documented in Chapter 3 [8]. To study this material under a more complex stress state and indirectly assess rate sensitivity (by comparison with low velocity impact), quasi-static loading with a hemispherical indenter was completed consistent with the geometry in the ISO 6603-2 [7] instrumented impact standard. In contrast to tensile tests the puncture test subjects the region of the specimen inside the clamping ring to a complex 2D stress state (a combination of biaxial tension and flexure). Additionally, there is a localized 3D stress state where the specimen contacts the indenter. A fixture was constructed compatible with an MTS Criterion Model 45 electromechanical load frame equipped with a 150 kN load cell. The striker was lubricated with PC Waylube 68 (viscosity of 69.7 cSt at 40°C; ISO 6603-1 [9] recommended range: 10 – 10000 cSt) for both quasi-static and impact tests. Images for observing damage/fracture propagation were acquired with an MTS Advantage video extensometer (Allied Vision Mantra 1.3 MP camera with a frame rate of 2 fps). The loading rate was 2.6 cm per minute (1% of the nominal low velocity impact speed of 4.4 m/s) to a deflection of 25 mm.

Flow Region Specimens (3)

Charge Region Specimens (3)

Compression Molding
Charge
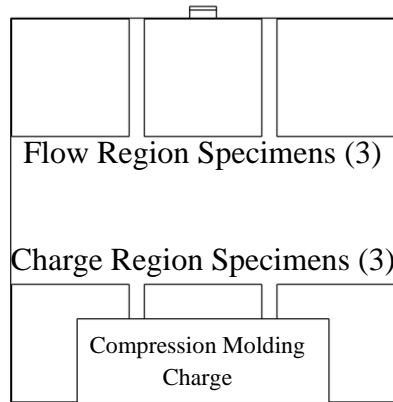
Figure 5.1: ISO 6603-2 specimen layout and charge placement

5.2.3 Low Velocity Impact

Low velocity impact testing was completed consistent with the ISO 6603-2 [7] standard on a custom drop tower equipped with suitable fixtures. Specimen deflection was measured with an Acuity 300 mm (30 mm/V sensitivity) laser displacement transducer acquiring the drop tower crosshead position. The laser displacement transducer data was acquired with a National Instruments (NI) 9205 16-bit analog input module in a CompactDAQ chassis. The average impact speed was 4.46 m/s with a coefficient of variation of 1.86% (ISO 6603-2 [7] requirement: 4.4 ± 0.1 m/s). The relatively large mass of the drop tower carriage (approximately 60 kg) resulted in a negligible change in carriage velocity resulting from the energy absorption by the specimen (< 3% of the kinetic energy of the carriage). Incorporated into the hemispherical 20 mm diameter striker was a Dytran Model 1050V5 integrated electronic piezoelectric (IEPE) load cell (sensitivity of 5 mV/lbf). Load cell data was acquired with an NI 9233 IEPE module. The sampling rate for all data was 50 kHz.

5.2.4 Data Post-processing

Force-deflection data was post-processed in MATLAB® R2014a. Force-time data from low velocity impact testing was filtered with a 4 pole Butterworth filter (2 pole with forward and reverse passes) with a channel frequency class (CFC) of 1000 (1650 Hz cutoff) consistent with SAE standard J211 [10]. Energy was computed by integrating the force-deflection response, consistent with the ISO 6603-2 [7] standard (the external forces

applied to the specimen are limited to the indenter and the clamping ring, since there is no displacement at the clamping ring the only work done to the specimen is by the indenter), with the trapezoid method; the CFC of the filter was selected from the suitable options in Table 1 of SAE standard J211 [10] such that the puncture energy was not affected. Quasi-static force-time data was not filtered.

5.3 Results and Discussion

5.3.1 Quasi-static Puncture Tests

Force-deflection responses for all 6 flow specimens and 6 charge specimens of process configuration V1 are shown in Figure 5.4 (a) and (b) respectively. Flow region specimens were more brittle. This can be observed in the force-deflection responses for one specimen from each location (charge and flow) presented in Figure 5.2. The nomenclature PX.Y SZ identifies the material/process configuration (1-8), X, and which plaque (at least two were needed), Y. The specimen number (1-6), Z, is also given. For example, P1.2 S3 indicates material/process configuration 1 and the specimen (3 of 6) was extracted from the 2nd plaque molded with that configuration. Additionally, catastrophic failure, resulting from circumferential fractures, can be observed in images of flow region specimen deformation (Figure 5.5). For charge region specimens under quasi-static loading only radial fracture is observed (Figure 5.3).

(a)
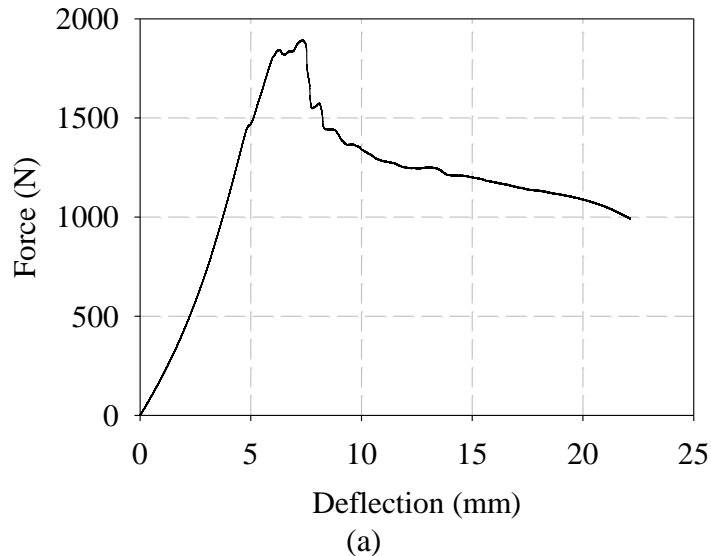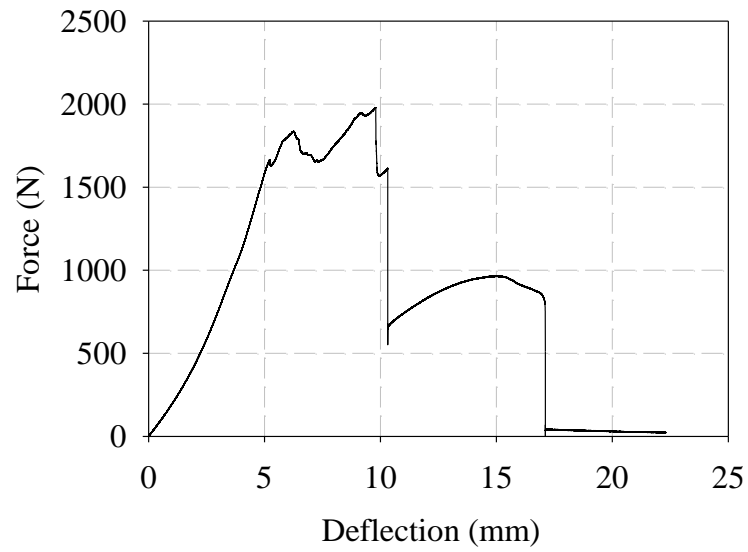
(b)

Figure 5.2: Force-deflection responses for (a) charge (P1.1 S1) and (b) flow region (P1.1 S4) quasi-static specimens
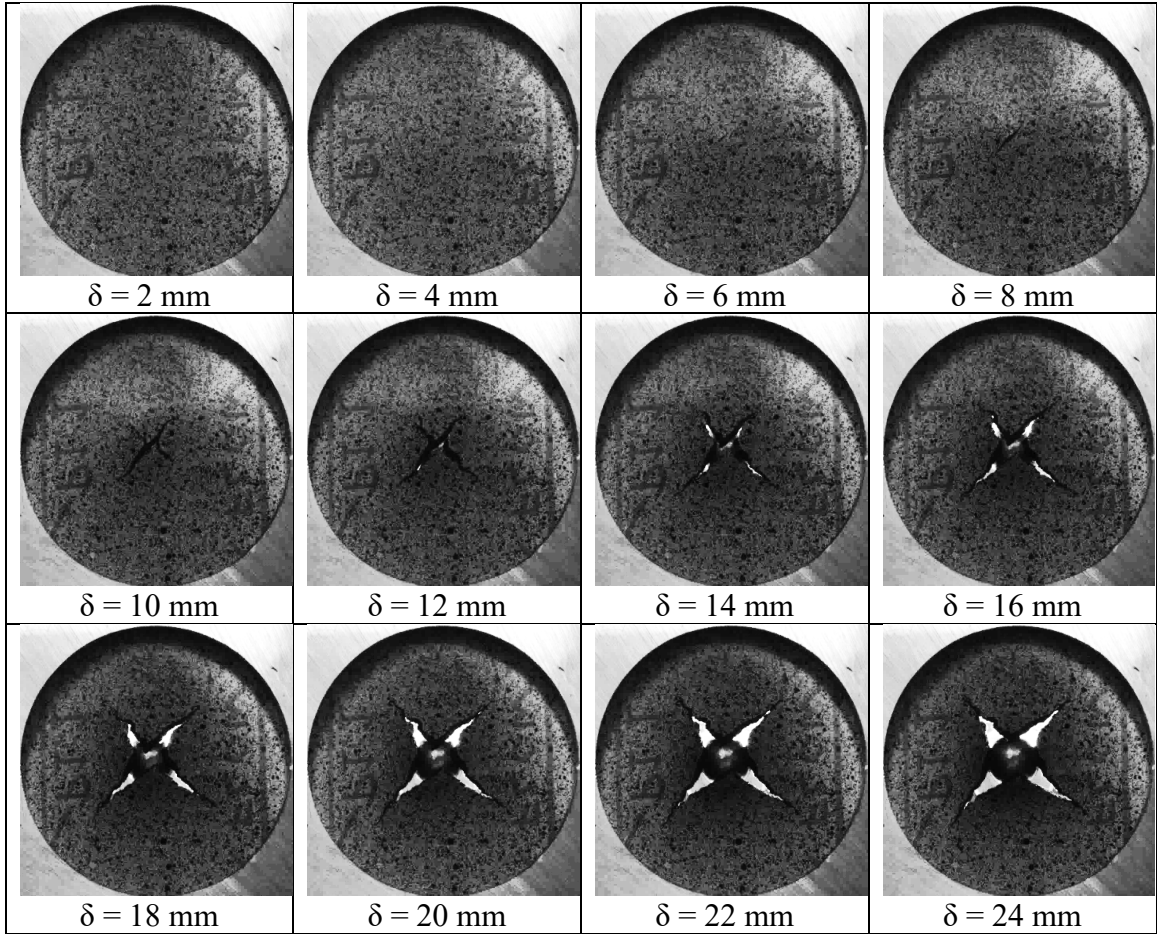
Figure 5.3: Images of deformation/failure mechanisms for specimen P1.1 S1 (charge region)
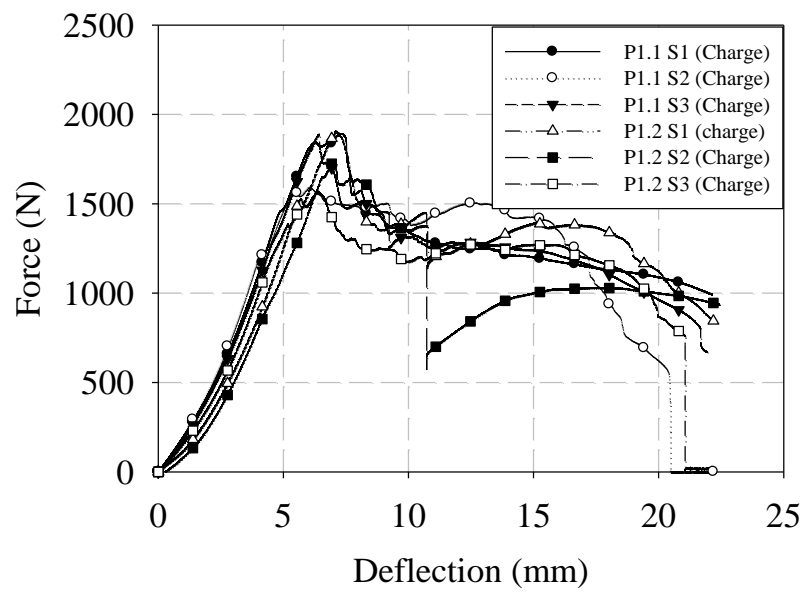
(a)
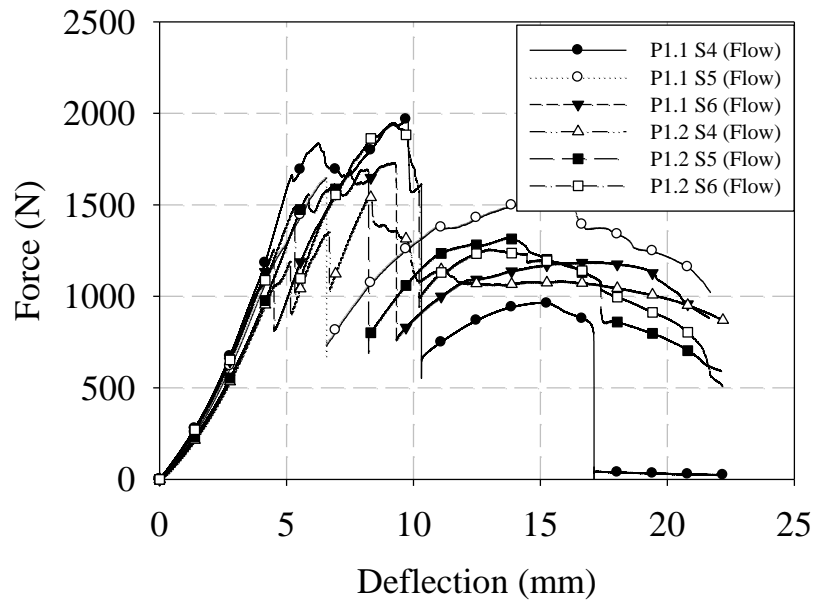
(b)

Figure 5.4: (a) Charge and (b) flow region specimen force-deflection quasi-static responses for material/process configuration V1
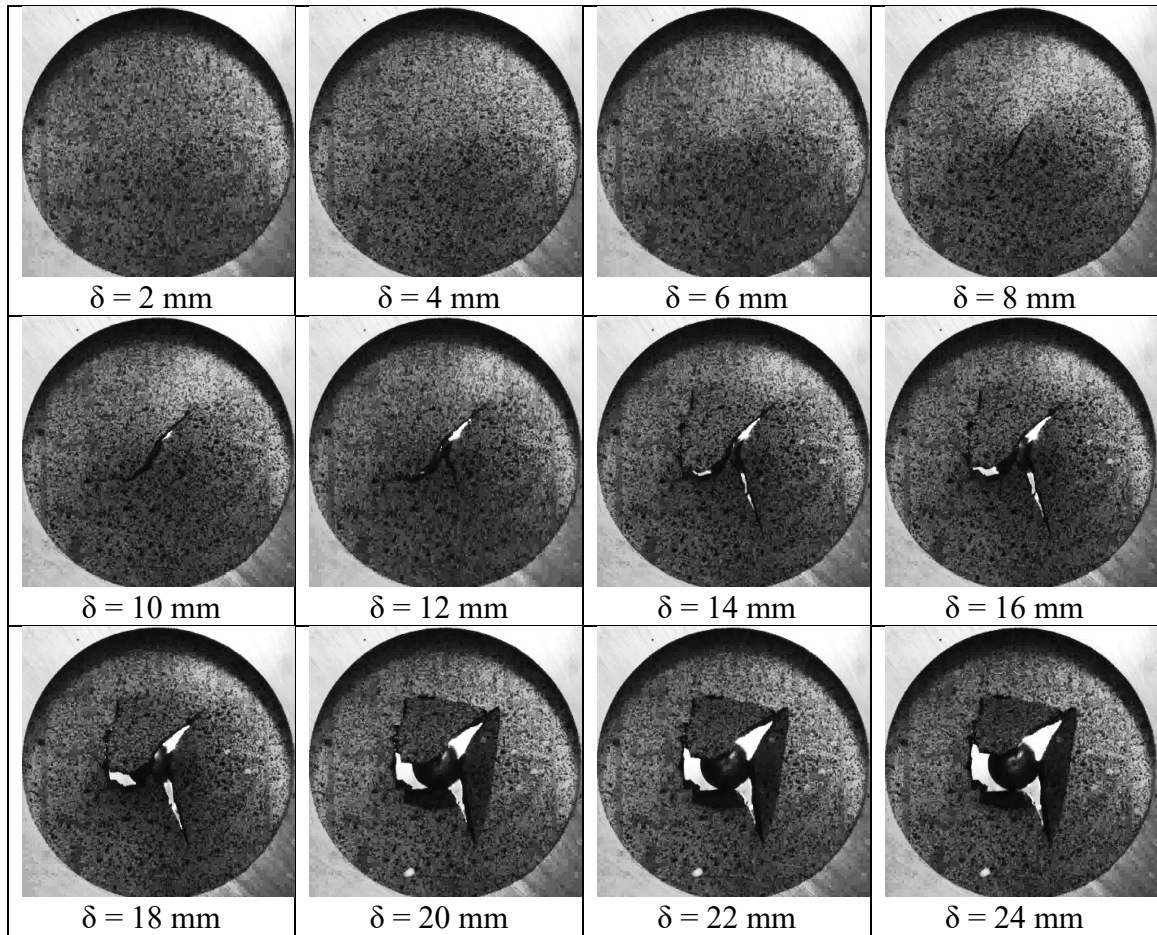
Figure 5.5: Images of deformation/failure mechanisms for specimen P1.1 S4
(flow region)

Total energy absorbed versus deflection responses for process configuration V1 are shown in Figure 5.6. Since these responses show some evidence of repeatability, average responses for each process configuration (V1 through V8) and specimen location (flow and charge regions) are plotted in Figure 5.7. Minimal differences in energy absorbed between flow and charge regions were observed for fibre contents less than 25%. For 9% and 18% fibre content specimens, energy absorbed is consistent regardless of other process parameters. For the 12% fibre content process configurations, V1 absorbs more energy than V2 and V3 for both specimen locations. Further investigation of process configuration V1 may be warranted.

(a)

(b)
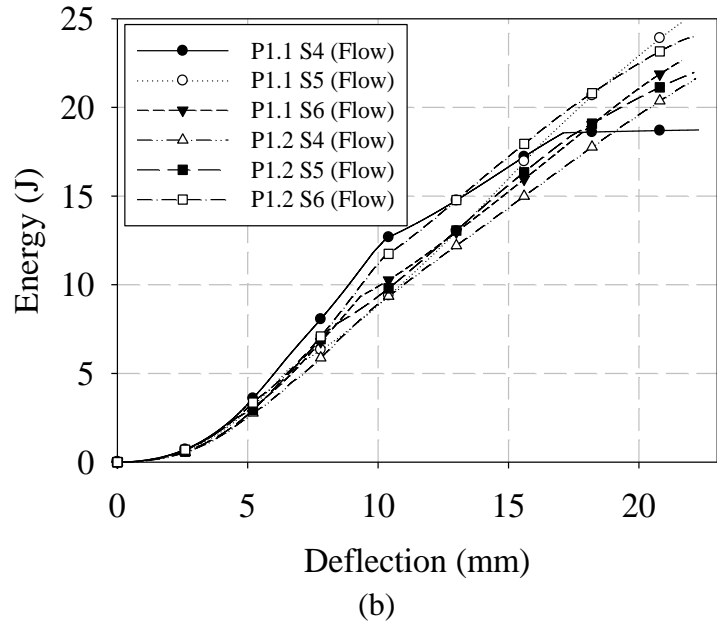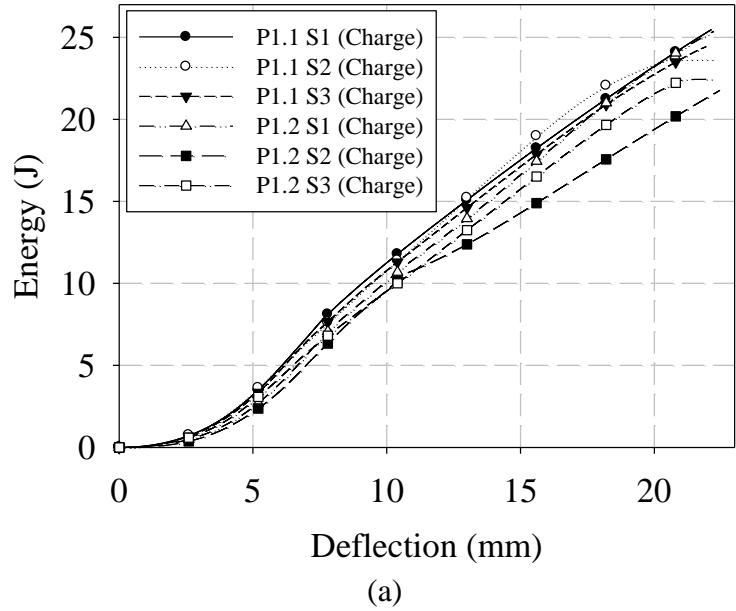
Figure 5.6: (a) Charge and (b) flow region energy-deflection responses (quasi-static) for material/process configuration V1
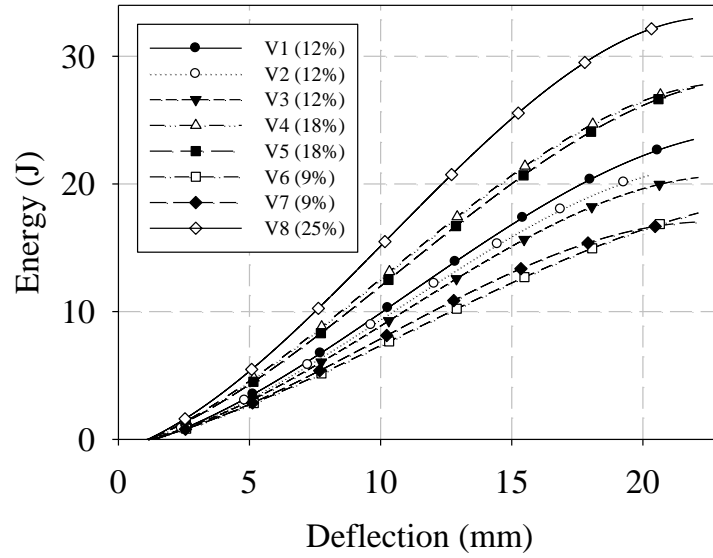
(a)
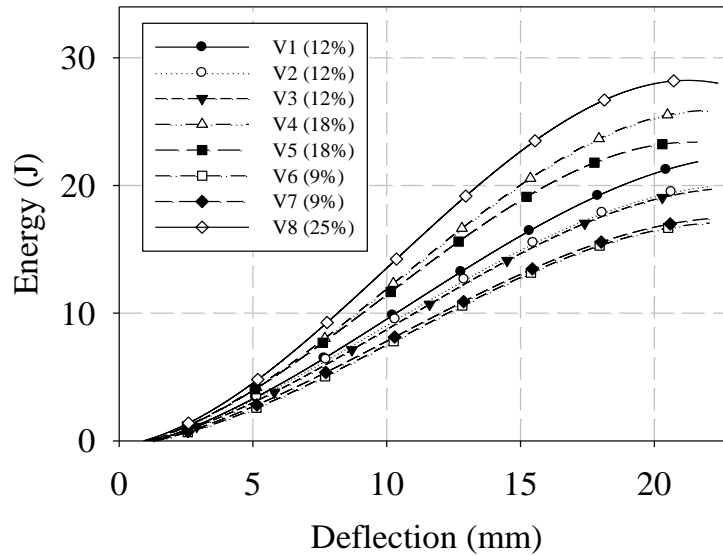
(b)

Figure 5.7: (a) Charge and (b) flow region average energy-deflection responses for material/process configurations V1-V8

Puncture energy, as per the ISO 6603-2 standard [7], is the energy absorbed when force drops below half of the maximum force. However, for quasi-static loading the material is much more ductile and for some tests the force does not, subsequent to the maximum, drop below half of the peak force. Therefore, the average puncture displacement

from low velocity impact, rounded to the nearest millimeter, was used to find the quasi-static puncture energy (12 mm) (Figure 5.8). This has the added advantage of improving consistency for a given process configuration and specimen location. No significant trend in terms of puncture energy versus specimen location was noted. Puncture energy increased approximately 0.50 J per 1% increase in fibre weight fraction.

For a small fraction of specimens, the maximum load occurs at a deflection much larger than that at which fracture initiates. Two example force-deflection responses for process configuration V6 are shown in Figure 5.9. For specimen P6.1 S1 the maximum load occurs just after fracture initiates (the maximum load is the local maxima associated with the onset of fracture). For specimen P6.1 S3 the maximum load occurs at a significantly larger deflection than that at which fracture initiates (at a local maxima, not the global maximum). Maximum force increased approximately 50 N per 1% increase in fibre weight content.
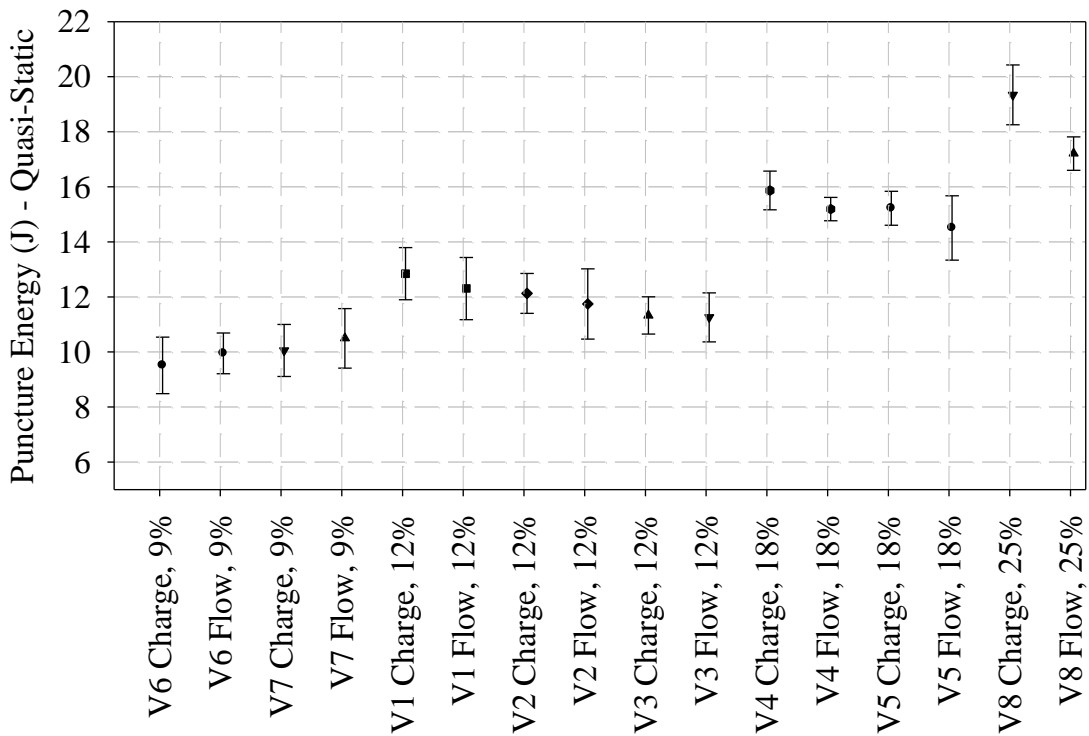
Figure 5.8: Quasi-static (modified) puncture energy for flow and charge region specimens, material/process configurations V1-V8
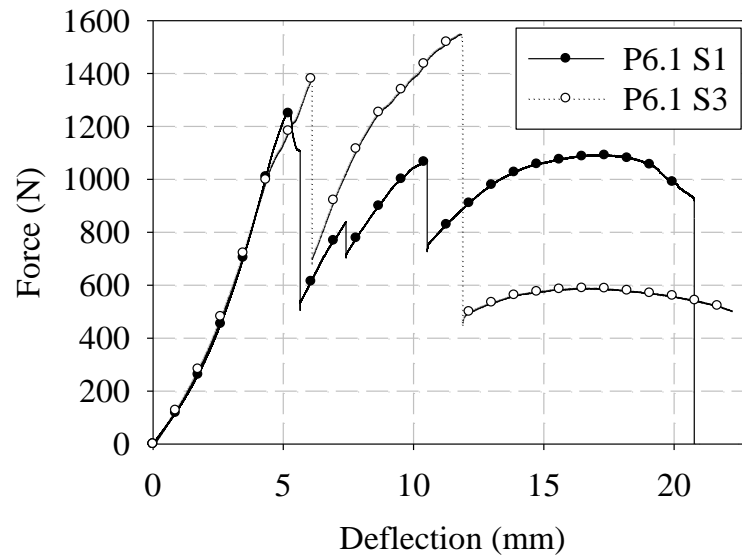
Figure 5.9: Example force-deflection responses for material/process configuration V6, quasi-static

5.3.2 ISO 6603-2 Instrumented Impact

Filtered and unfiltered force-deflection responses for a low velocity impact charge region specimen from process configuration V1 are shown in Figure 5.10. Significant high frequency content is present. Filtered force-deflection responses for two charge and two flow region specimens for process configuration V1 are shown in Figure 5.11 (a) and (b) respectively. These two specimens for each specimen location were selected to include the lowest and highest deflections when catastrophic failure occurs (~ 30% difference). All individual force-deflection responses for process configuration V1 are provided in Appendix E. High speed imagery is shown in Figure 5.12. Catastrophic failure occurs at a deflection of approximately 14 mm in the form of circumferential fractures which form fragments as they connect the radial fractures initiated at smaller deflections.
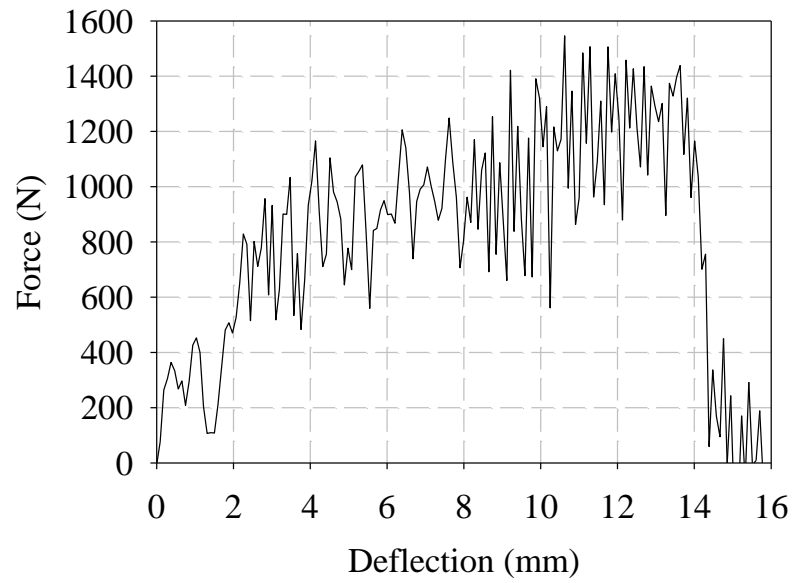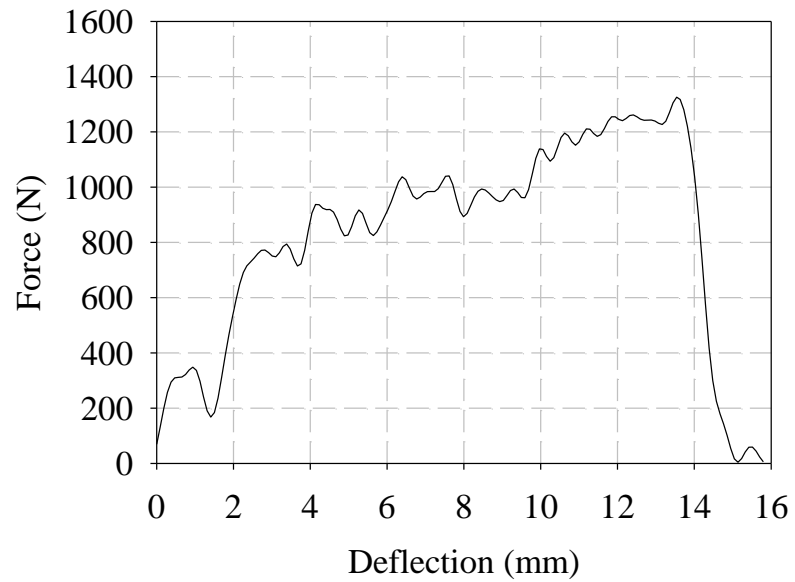
Figure 5.10: (a) Unfiltered and (b) filtered force-deflection, charge region impact, P1.3 S1

124
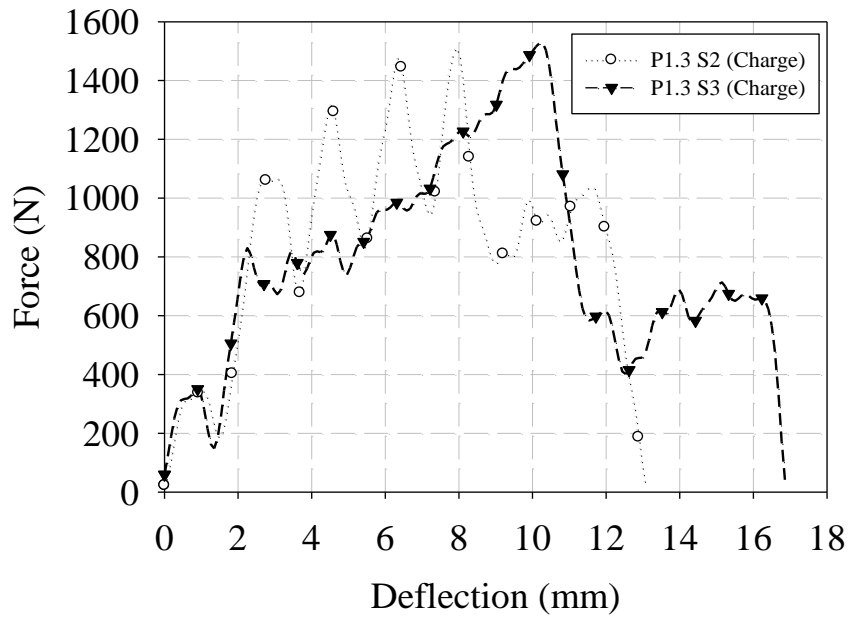
(a)
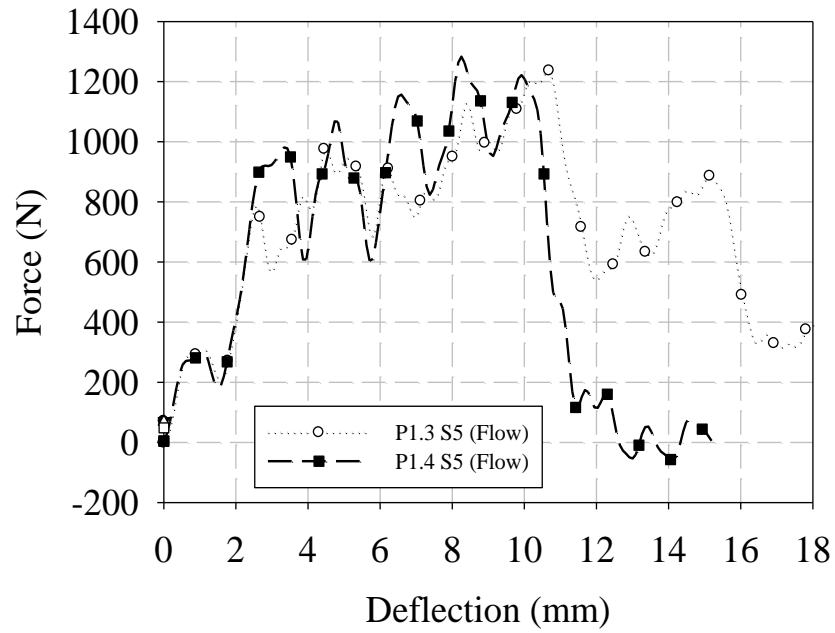
(b)

Figure 5.11: Filtered force-deflection responses for (a) charge and (b) flow region impact specimens for process configuration V1

δ = 2 mm	δ = 4 mm	δ = 6 mm	δ = 8 mm
Time = 0.45 ms	Time = 0.91 ms	Time = 1.37 ms	Time = 1.82 ms
δ = 10 mm	δ = 12 mm	δ = 14 mm	δ = 16 mm
Time = 2.27 ms	Time = 2.73 ms	Time = 3.18 ms	Time = 3.64 ms
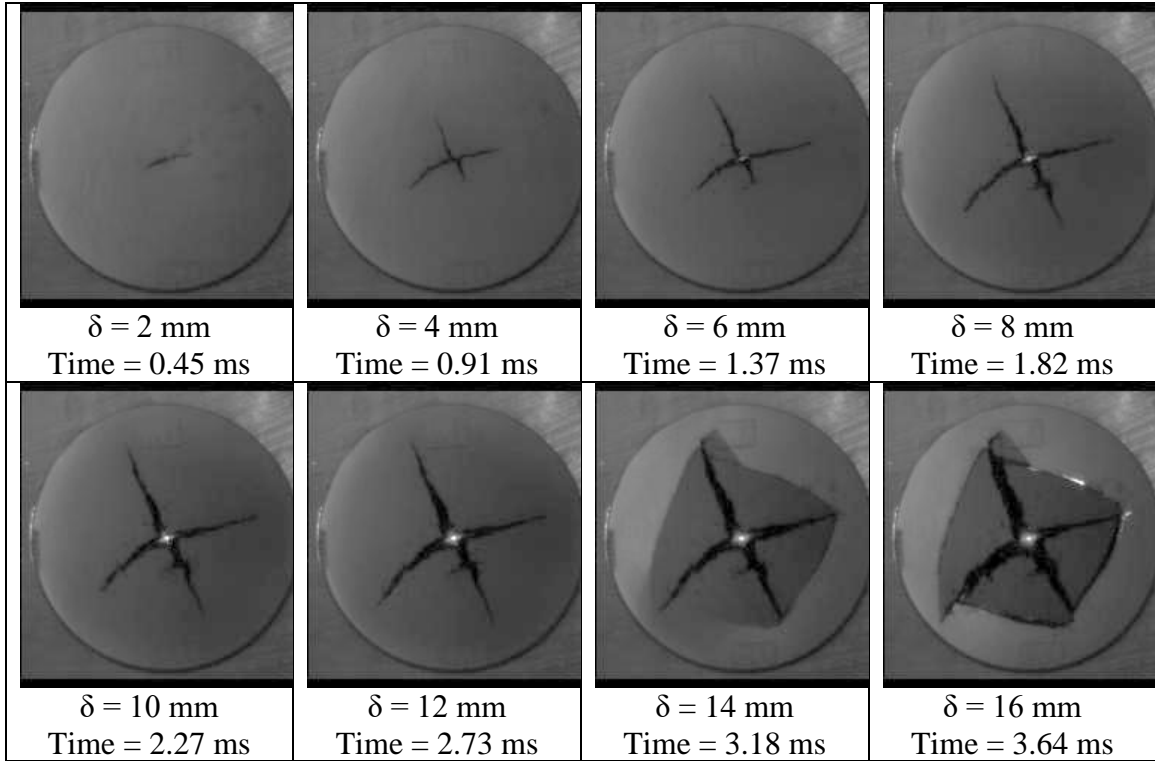
Figure 5.12: High speed imagery for specimen P1.3 S1 (charge region)

Energy versus deflection responses are shown in Figure 5.13 for charge and flow region specimens of process configuration V1. Since these results are reproducible, average energy responses for each process configuration and specimen location were computed and are shown in Figure 5.14. A clear trend of increasing energy absorption with increased fibre content is apparent. It is also clear that for a given fibre content, the charge region specimens absorb more energy for a given deflection. The charge region has been shown to be closer to planar isotropic while the flow region is highly anisotropic [8]. It is proposed that failure is more easily initiated in the flow region in the crossflow direction since a smaller fraction of fibres are aligned in this direction thereby decreasing the damage resistance. Modelling is a logical next step in better understanding this phenomenon.
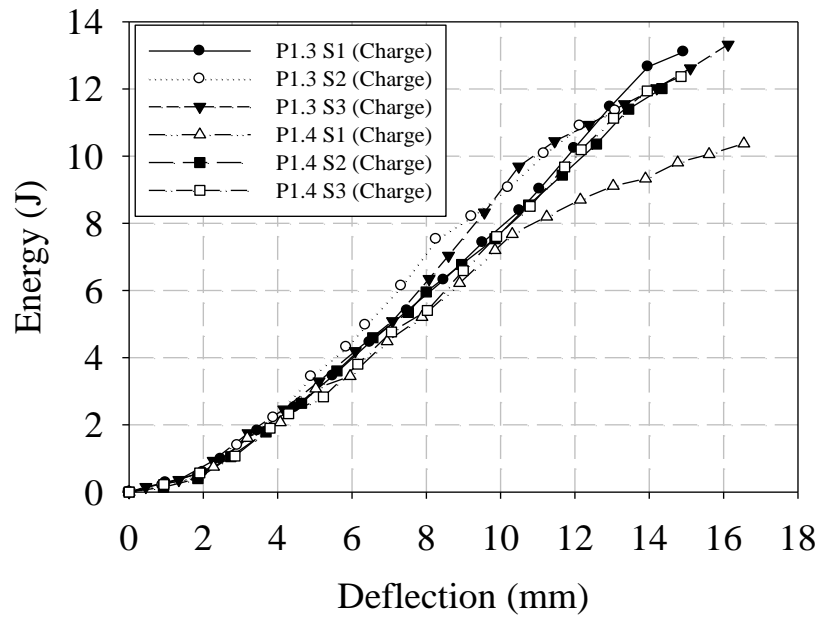
(a)
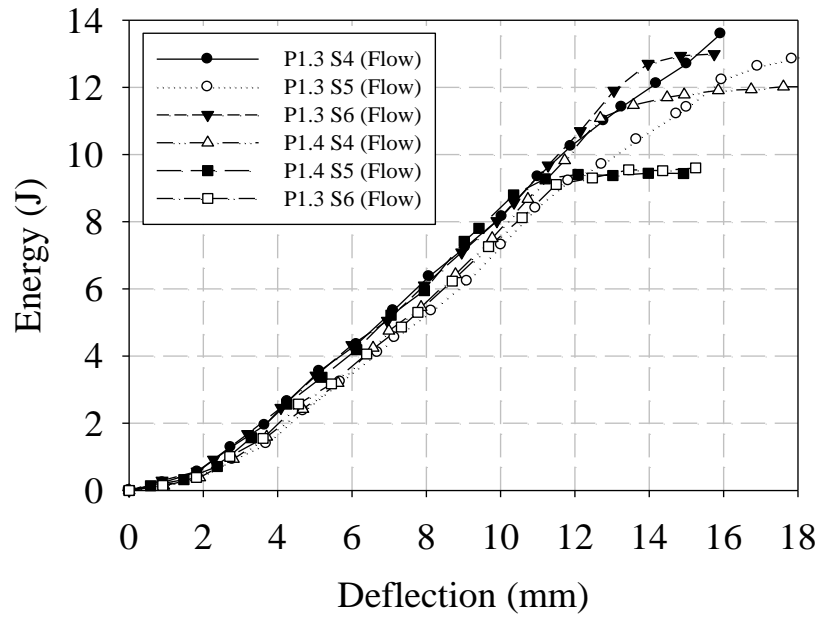
(b)

Figure 5.13: Energy-deflection impact responses, material/process configuration V1: (a) charge and (b) flow regions
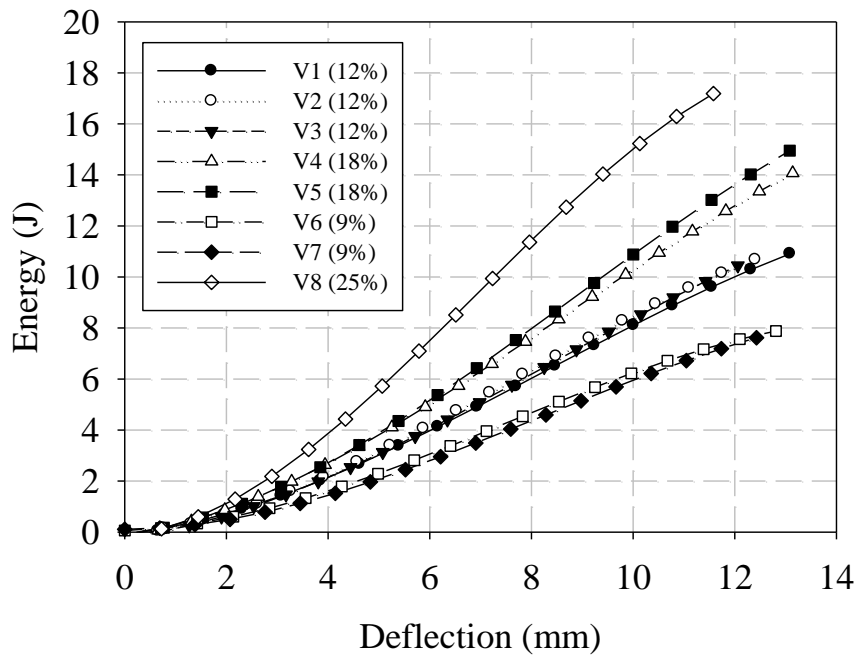
(a)
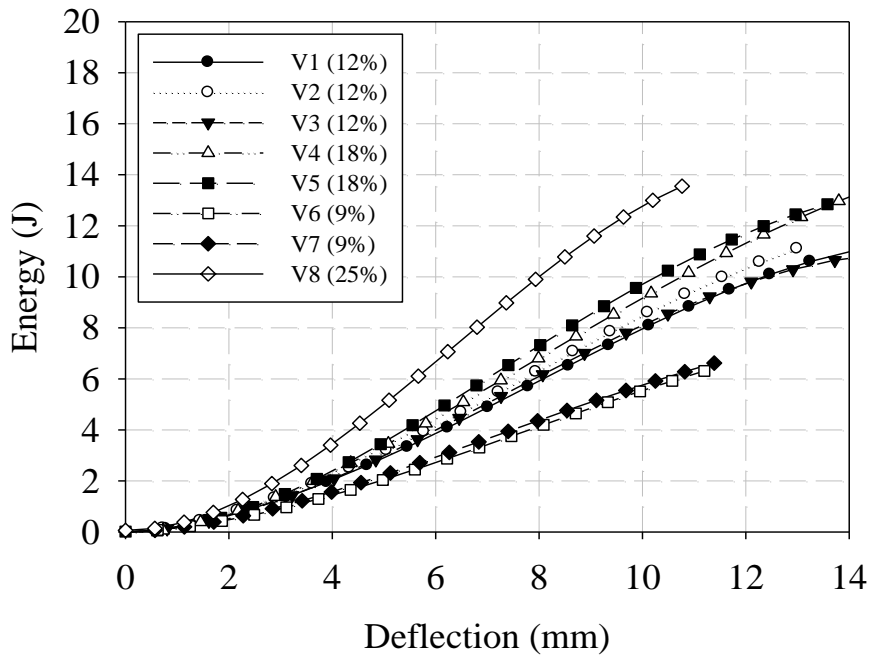
(b)

Figure 5.14: Average energy-deflection impact responses for material/process configurations V1-V8: (a) charge and (b) flow regions

Puncture energy is defined in the ISO 6603-2 standard [7] as the energy at the point in time (or deflection) when the force drops below half of the maximum force observed during the test. Puncture energy is given Figure 5.15 for all specimen configurations for impact loading. Consistent with the average energy-deflection responses, puncture energy increases with fibre content and is higher (average of +15%) in the charge region. Puncture energy increases approximately 0.61 J per 1% increase in fibre weight fraction for charge region specimens. The corresponding value for the flow region is 0.43 J. Maximum force (unfiltered) is presented in Figure 5.16. Consistent with the finding for puncture energy, maximum force is, on average, 9.6% higher in the charge region. Maximum force increases approximately 76 N per 1% increase in fibre weight fraction in the charge region and 60 N in the flow region. Zhang et al. studied compression molded PP/GF (40% weight fraction) and PA/GF (30%). They observed maximum forces at room temperature of approximately 3000 N for PP/GF and 3200 N for PA/GF. These are higher fibre weight fractions but carbon fibre has a stiffness approximately three times that of glass fibre. Strength can be similar for these two reinforcement materials. However, specimen thickness was approximately 85% higher for the study Zhang et al.
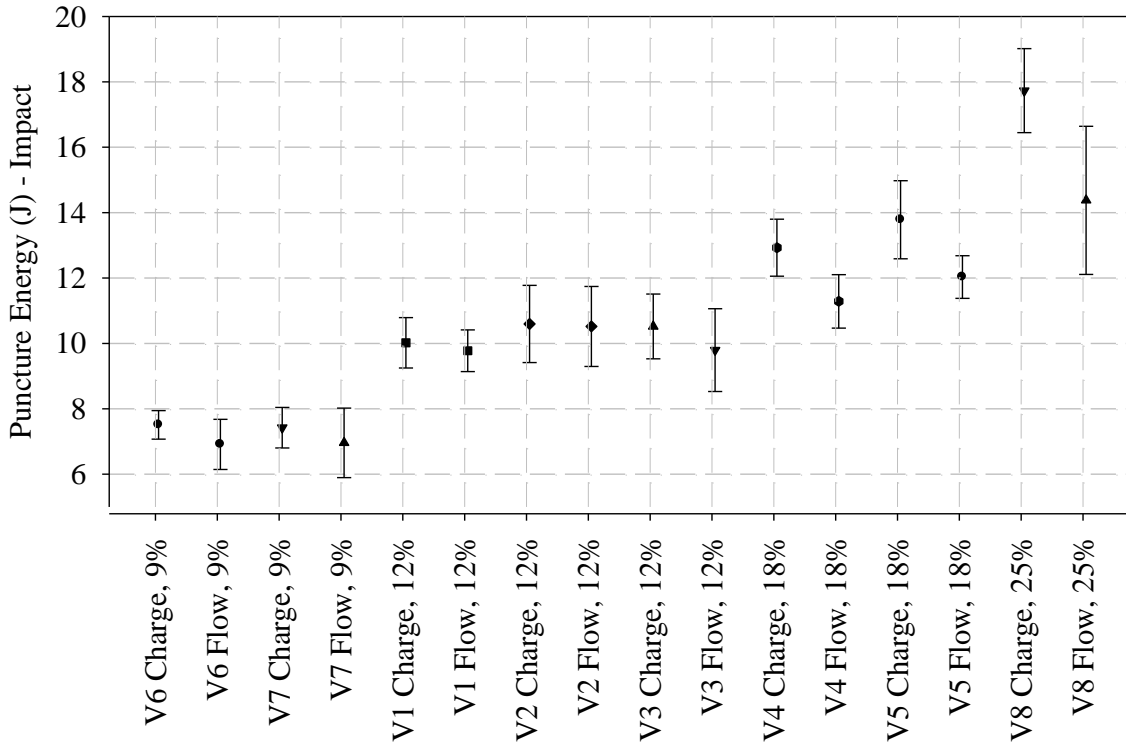
Figure 5.15: Puncture energy for charge and flow region, material/process configurations V1-V8
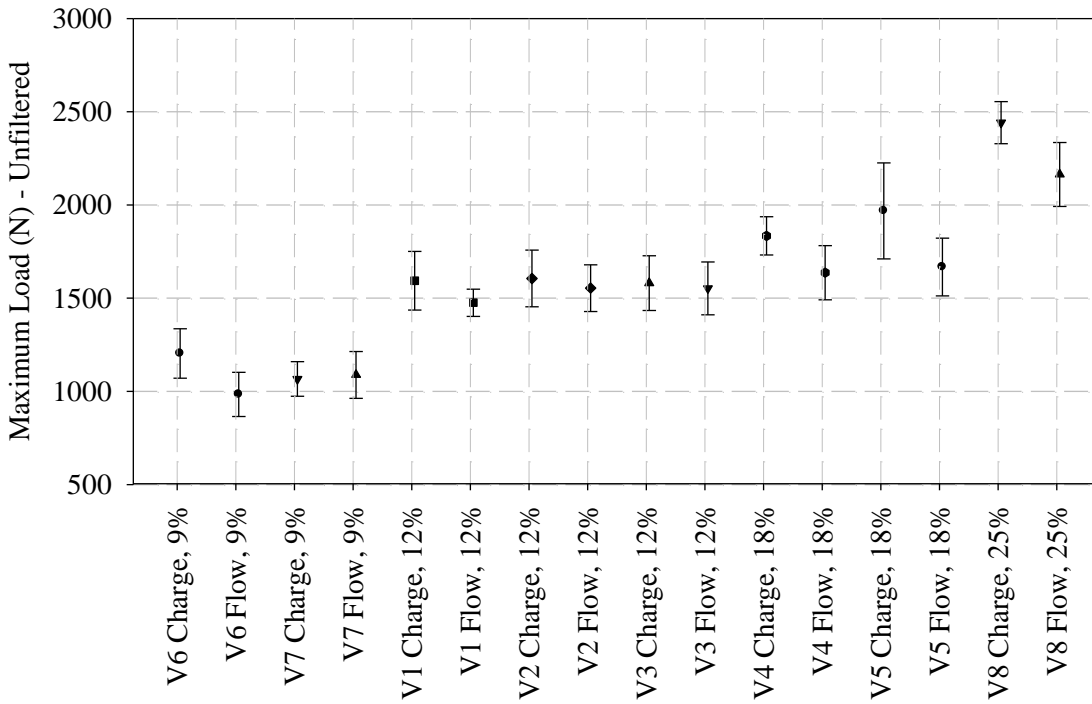
Figure 5.16: Maximum force (impact) for charge and flow region, material/process configurations V1-V8

5.3.3 Rate Sensitivity

Adjusted puncture energy (deflection of 12 mm) for both quasi-static and low velocity impact loading conditions is presented in Figure 5.17. This sole side-by-side comparison of quasi-static versus low velocity impact results is presented as it includes the adjusted puncture energy (up to a deflection of 12 mm) for low velocity impact. For the data in Figure 5.15 (a), puncture energy is computed consistent with the ISO 6603-2 standard [7] such that the force-deflection response is integrated to a deflection associated with the load dropping below half of the peak load. Puncture energy increases an average of 18% for quasi-static loading with respect to low velocity impact.
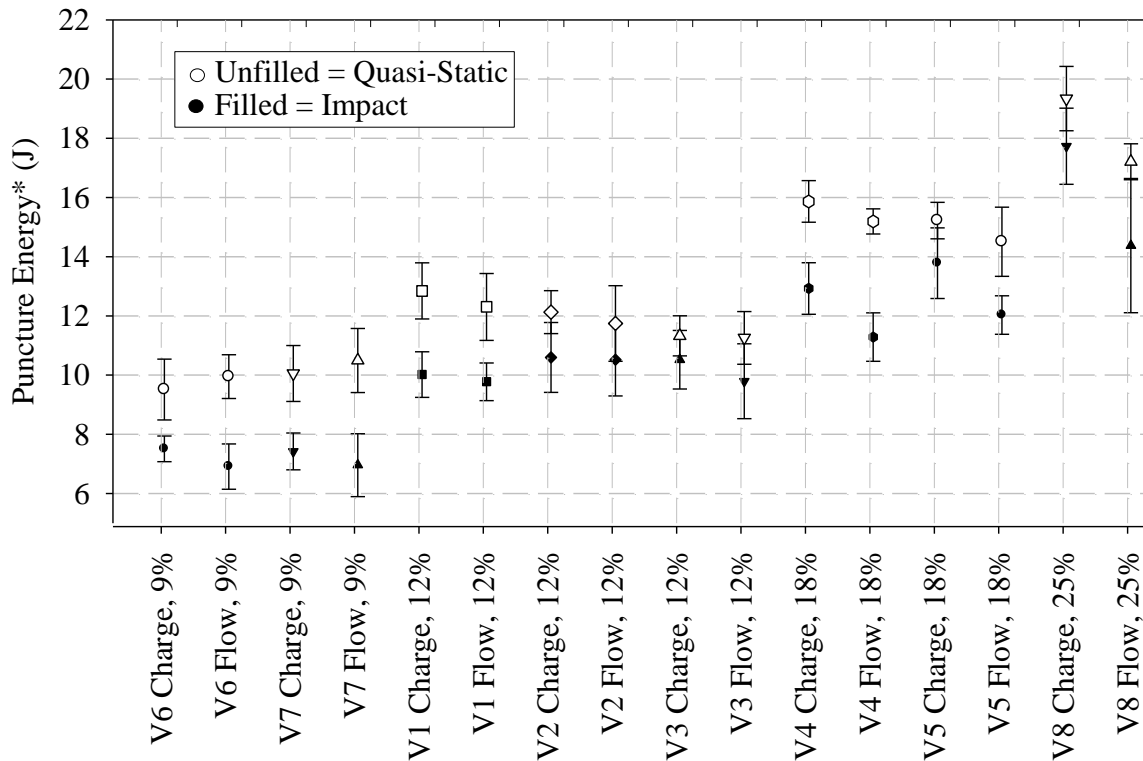
Figure 5.17: Adjusted puncture energy for quasi-static versus low velocity impact, charge and flow region, material/process configurations V1-V8

Images from quasi-static (Figure 5.3 and Figure 5.5) and low velocity impact tests (Figure 5.12) show that the onset of fracture observable from the tensile surface of the specimen occurs at a much lower deflection under impact (approximately 2 mm for impact versus approximately 8 mm for quasi-static loading). Additionally, catastrophic failure (in

the form of fragment formation as circumferential fractures connect radial cracks), which may not occur at all for quasi-static loading (to the deflection limit of this study) occur at smaller displacements under impact loading (approximately 20 mm for quasi-static loading and 14 mm for low velocity impact).

5.4 Conclusions

A key advantage of the direct compounding process is the ability to employ any desired fibre weight fraction within the limits imposed by fibre packing arrangements. Direct/in-line compounded PA6/CF long fibre thermoplastic was characterized under low velocity impact consistent with ISO standard 6603-2 [7]. Additionally, a quasi-static variant of the ISO method was employed to indirectly assess rate sensitivity. The key findings are as follows:

1. At quasi-static loading rates, flow region specimens were notably more brittle considering the force-deflection response and images capturing specimen deformation. However, the quasi-static energy absorption did not differ significantly between charge and flow region specimens.

2. In terms of mechanical properties as a function of fibre content, puncture energy increased an average of 0.5 J per 1% increase in fibre weight fraction. Maximum force increased approximately 50 N per 1% increase in fibre weight fraction.

3. Under low velocity impact, consistent trends in terms of puncture energy and maximum force between charge and flow region specimens were noted. Puncture energy increased 0.6 J and 0.4 J per 1% fibre weight fraction for charge and flow region specimens respectively. Maximum force increased 75 N and 60 N per 1% increase in fibre weight fraction for charge and flow region specimens.

4. In terms of rate sensitivity, puncture energy under low velocity impact decreased by 18% on average with respect to quasi-static loading.

5. Images of specimen deformation show that the onset of fracture occurs at much lower deformations for impact loading for the same specimen location and process configuration (2 mm for impact, 8 mm for quasi-static loading for charge region specimens from process V1).

6. Catastrophic specimen failure (the formation of large fragments as circumferential fractures connect radial cracks) also occurs at smaller displacements for low velocity impact tests (14 mm versus 20 mm). However, catastrophic failure of the specimen, while consistently observed for impact tests, may not occur at all within the deflection limit of the quasi-static testing.

5.5 References

1.   Thomason J. The influence of fibre length, diameter and concentration on the impact performance of long glass-fibre reinforced polyamide 6, 6. Composites Part A: applied science and manufacturing. 2009;40(2):114-124.
2.   Bartus S, Vaidya U. Performance of long fiber reinforced thermoplastics subjected to transverse intermediate velocity blunt object impact. Composite structures. 2005;67(3):263-277.
3.   Zhang Y JA, Guan J, Simard B. Low-speed Impact Characterization of Two Types of Fiber Reinforced Polymer Composites. 2015 Aerospace Structural Impact Dynamics International Conference; Seville, Spain2015. p. 1-25.
4.   Schoßig M, Bierögel C, Grellmann W, et al. Mechanical behavior of glass-fiber reinforced thermoplastic materials under high strain rates. Polymer Testing. 2008;27(7):893-900.
5.   G'sell C, Jonas J. Determination of the plastic behaviour of solid polymers at constant true strain rate. Journal of materials science. 1979;14(3):583-591.
6.   Weeks C, Sun C. Modeling non-linear rate-dependent behavior in fiber-reinforced composites. Composites Science and Technology. 1998;58(3-4):603-611.
7.   ISO. 6603–2-2000 Determination of Puncture Impact Behavior of Rigid Plastics - Part 2: Instrumented Puncture.
8.   Bondy M, Pinter, P., Altenhof, W. Experimental Characterization and Modelling of the Elastic Properties of Direct Compounded Compression Molded Carbon Fibre/Polyamide 6 Long Fibre Thermoplastic. Submitted to Materials & Design. 2016 12/16/2016:1-25.
9.   ISO. 6603-1-2000: Determination of Puncture Impact Behavior of Rigid Plastics – Part 1: Non-instrumented Impact Testing.
10.   SAE. J211-1 Instrumentation for Impact Test—Part 1—Electronic Instrumentation. Warrendale, PA: SAE.

CHAPTER 6

EXPERIMENTAL CHARACTERIZATION OF THE MECHANICAL PROPERTIES OF A CARBON FIBRE/PA66 LFT SEATBACK UNDER QUASI-STATIC AND IMPACT LOADING

6.1 Introduction

The previous chapter evaluated PA66/carbon fibre LFT-D under impact loading and assessed rate sensitivity. This was done with an ISO standard methodology (ISO 6603-2) [1]using a standard specimen (140 mm by 140 mm square plate). The simple geometry of this specimen is a significant limitation as most, if not almost all, practical engineering applications will have much more complex shapes. It is unknown if the findings of a study based on such a simple geometry hold true for engineering applications. Therefore, a similar impact characterization methodology was completed on an automotive seatback structure with a complex geometry.

A much larger body of knowledge is available In the open literature for LFT materials with glass fibre reinforcement than carbon fibre (the reinforcement for the current study). However, the relatively low stiffness of glass fibre with respect to its strength is expected to result in reduced mechanical characteristics with respect to carbon fibre (CF). Thomason [2] assessed the impact characteristics of boiling water conditioned and dry-as-molded injection molded PA66 and glass fibre (10, 14, and 17 μm diameters; 10-50% by weight). The fibre aspect ratio and volume fraction indicated a random fibre orientation in the barrel of the injection molding press limiting the final fibre length. This limitation on fibre length may still apply with direct/inline compounding. Notched and un-notched specimens were characterized by Thomason; un-notched specimen impact performance was not significantly influenced by fibre length. Notched specimen impact characteristics were independent of fibre diameter.

Bartus and Vaidya [3] subjected compression molded LFT-G (granule) PP & GF specimens to blunt object intermediate velocity (40 – 140 m/s) impact to obtain a critical velocity where 50% of projectiles do not perforate the specimen (equivalent V50 ballistic limit, applied to impact at low velocity). One critical conclusion was that the material did not exhibit significant rate sensitivity under the conditions of the study. Another finding

applicable to the current work is the correlation between fibre orientation and impact properties. However, the findings of Bartus and Vaidya have limited applicability to the current study considering the different matrix and reinforcement and the use of granules incorporating chopped fibre.

Zhang et al. [4] of the National Research Council of Canada assessed the mechanical properties of injection and compression molded PA/GF and PP/GF materials through low velocity impact. A decrease in stiffness was observed at +85°C with respect to room temperature. However, the force-deflection responses prior to maximum load were minimally affected by temperature in the range of -40°C to 0°C. With a PP matrix, injection molded parts were observed to have lower maximum loads with respect to compression molded parts. In terms of damage/failure mechanisms, PP was minimally affected by temperature. Less damage was observed for PA/GF at higher temperatures. This is a particularly relevant investigation in terms of manufacturing process and thermoplastic matrix selection. However, in all cases considered, the material studied includes the more commercially common glass fibre reinforcement type.

Composites for crashworthiness applications have been studied extensively, a few examples are highlighted here. NASA and the US Army developed and tested under impact a composite fuselage for light aircraft and helicopters [21]. Chirwa et al. proposed the use of needleloom felt synthetic fibre textile reinforced composite panels for automotive body/chassis side structures to effectively manage front, side, and diagonal impacts [22]. Pillai et al. investigated the use of square carbon fibre reinforced polymer tubes for vehicle rockers (sills) with the objective of minimizing mass while maintaining the crash performance possible with traditional materials/structures [23]. These three studies, and many of the crashworthiness investigations in the open literature, focus on continuous reinforcements which are associated with significant manufacturing challenges (draping/weave distortion, resin impregnation, poor recyclability, etc.). Such materials may only be suitable for low production volume vehicles. LFT materials, particularly the direct/inline compounded variant, are more suitable for high volume production.

A small number of publications exist in the open literature on applications employing LFT materials in practical engineering applications. Researchers at the

University of Alabama (Birmingham) re-designed a battery compartment access door for a public transportation vehicle to be compression molded with a 40% weight fraction glass fibre/polypropylene LFT [5]. The original component consisted of a stamped sheet metal/welded tube steel assembly. The design process consisted of simulations of the compression molding process to obtain data on fibre orientation, validation of fibre orientation models by μCT, finite element modelling of the LFT component, and experimental validation of the mechanical response of the model. The finite element model accurately predicted the stiffness of the physical part under quasi-static loading. The mass of the part was reduced by 60%.

Bartus et al. [6] developed a glass fibre/polypropylene LFT bus seat to replace an SMC/steel frame assembly to meet the requirements of SAE standard J826 [7]. A process model was developed in CadPress-Thermoplastic and a structural FE element was created from its output in ANSYS. Prototype parts were molded and evaluated against the requirements of the SAE standard. With respect to the SMC/steel frame seat, weight was reduced by 40%. The prediction for total cost reduction including manufacturing capital costs, painting, and raw material was 18%. Ning et al. [8] designed a carbon fibre polyphenylene sulfide (PPS) LFT insert to stiffen the ballistic shell of a helmet for military applications. A process model was not developed and the structural finite element model developed in the design phase assumed isotropic material properties. A small weight savings was obtained (5%) with respect to an existing combat helmet.

Vaidya et al. [9] developed a glass fibre/polyamide 6,6 LFT tailcone for a US Army artillery training round. The current aluminum tailcone and two LFT designs were evaluated with finite element models and experimental testing (field testing at a military proving ground) with high-speed photography. Material degradation from thermal loading was estimated through finite element modelling to affect an equally thin layer (0.8 mm) for both LFT and aluminum tailcones. Finite element models of the first LFT design predicted failure with the Tsai-Wu criterion [10]. High speed photography provided evidence of a failure mode consistent with the predictions of the model. A second/revised LFT design was developed and tested successfully. Cost savings of 70% were projected.

6.1.1 Motivation

These three practical/industry applications of LFT materials are limited to traditional granules in which the fibre can be no longer than the pultruded pellet. Additionally, none of these applications incorporate carbon fibre LFT materials. Manufacturing process parameters, while present in a limited form, are not extensively documented. These studies represent important milestones in efforts to deploy LFT materials in commercial applications. However, it is evident that several shortcomings in the open literature exist specific to LFT materials/components, namely, (1) limited data in the open literature on mechanical properties of carbon fibre LFT exists, especially direct/inline compounded LFT (LFT-D), particularly under impact/elevated strain rates, (2) limited data is available in the open literature on LFT-D process set points for an industrial application, (3) the number of publications on practical engineering applications for LFT materials is low with none identified for carbon fibre/PA66 LFT or LFT-D, and finally, (4) a lack of rigorous experimental testing and observations on practical/industrial composite structures, to assess the assumption of isotropy/homogeneity, exists.

6.2 Methodology

6.2.1 Specimen Preparation

The direct/inline compounded LFT seatback specimens for this study were fabricated at
the Fraunhofer Project Centre (FPC) research facility in London, Ontario. The
Dieffenbacher LFT-D manufacturing line employed for this study is more commonly used
in applications with glass fibre. Preliminary modifications to the apparatus have been made
for the use of carbon. A schematic and flowchart for this manufacturing process are
provided in Figure 6.1 (a) and (b), respectively. The seatback is shown as part of the
lightweight seat assembly (arrow indicated dark green component) in Figure 6.1 (b). A
Motan granule dosing system (item (1) within Figure 6.1) fed (2) a Leistritz ZSE-60HP-
28D co-rotating twin screw extruder at 107 RPM. This extruder introduced molten polymer
via a film die to (3) a Leistritz ZSG-75 P-17D co-rotating twin screw extruder (L/D = 17,
75 mm diameter, 56 RPM). Charges (approximately 100 mm by 900 mm with a thickness
of approximately 26 mm) exit this extruder and travelled along a heated conveyor (4)
having a temperature set point of 290°C and were manually placed in a mold installed in a
Dieffenbacher DCP-U 2500/2200 press (5). Tool set points and approximate actual
temperatures are given in Table 6.1. Press opening/closing speed and force profiles are
given in Table 6.2. The polymer was BASF A3W polyamide 66. Carbon fibre was sourced
from Zoltek (Panex 35-62, 30 rovings). Fibre content was 40% by weight. Charges were
placed longitudinally for half of the molded seatbacks and transverse for the remaining
molded parts, with both directions illustrated in Figure 6.2 (a). Throughput for the LFT-D
line for this trial was 160 kg per hour.
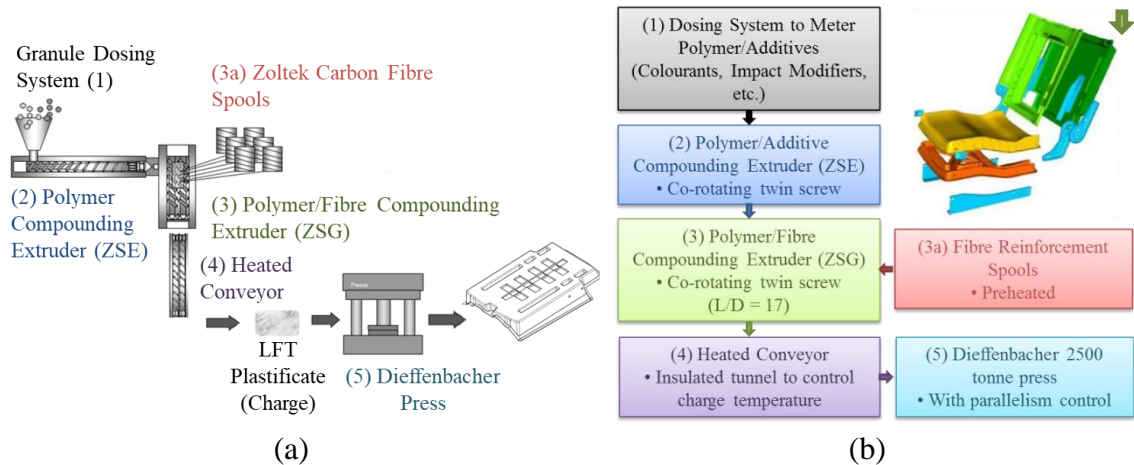
Figure 6.1: (a) Schematic and (b) Flowchart of Dieffenbacher LFT-D line at the Western FPC [11] and complete lightweight seat assembly

Table 6.1: Tool set points and actual temperatures for automotive seatback compression mold

Upper Tool Set Point	**170°C**
Upper Tool Actual	Approximately 150°C
Lower Tool Set Point	**170°C**
Lower Tool Actual	Approximately 150°C

Table 6.2: Press opening/closing speed & force profiles for automotive seatback compression molding

Speed Profile Closing		Force Profile		Speed Profile Opening	
Position [mm]	Speed [mm/s]	Time [s]	Force [kN]	Position [mm]	Speed [mm/s]
30	80	0	5000	0	2
10	80	60	5000	30	50
0	5	61	0		

Tensile specimens were extracted by CNC milling from the locations shown in Figure 6.2 (b). For both the longitudinal and transverse charge placements tensile specimens were extracted with 0° and 90° orientations from regions denoted as the top and side of the part. Six tensile tests were completed for each location, specimen orientation, and charge orientation for a total of 48 tensile tests. Tensile specimen locations were repeatable for specimens extracted from the sides of the seatback since 12 specimens were extracted and only 6 were tested (allowing for 50% to be discarded due to damage from

the extraction process). Specimen IDs are shown in Figure 6.2 (b). For the top surface of the part the number of tensile specimens extracted only allowed a small number to be discarded. An example of the specimen numbering is shown in Figure 6.10. Tensile tests were conducted on an electromechanical MTS Criterion EM40 load frame with a 50 kN load cell and a 25 mm mechanical extensometer. These tests were displacement controlled with a crosshead speed of 0.25 mm/min. No specimens (tensile, full seatbacks) were dried to remove absorbed moisture from storage at room temperature. This would normally be done to aid inter-laboratory comparisons; however, the full part is large and an oven of sufficient size was not available.

(a)   (b)
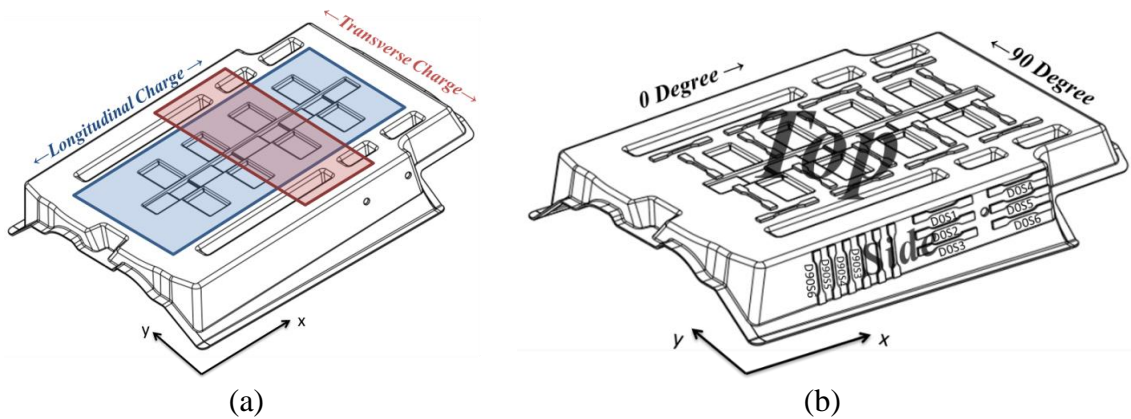
Figure 6.2: Automotive seatback (a) Charge orientations (b) Tensile specimen locations

Note the coordinate axis definitions for the x and y axes. The z-axis direction, which will be referenced throughout this manuscript, is determined by the direction of a resulting vector from the cross product of a vector along the x-axis and y-axis (i.e. $\vec{z} = \vec{x} \times \vec{y}$).

(a)   (b)
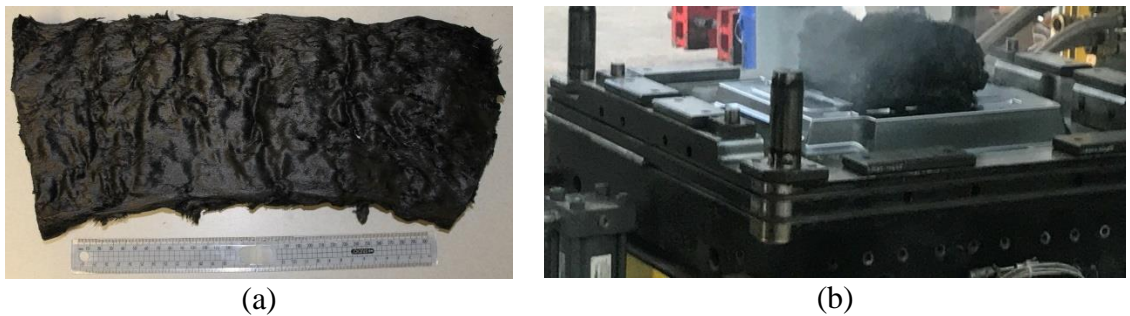
Figure 6.3: Automotive seatback compression molding charge: (a) Photograph of a solidified charge (b) Transverse charge placement on core of tool

6.2.2 Quasi-static Characterization

Quasi-static mechanical characterization of the seatback was completed on an MTS Criterion electromechanical load frame with a 150 kN load cell (see Figure 6.4). A custom fixture consisted of a Blanchard ground plate with approximate dimensions of 600 mm by 600 mm by 25 mm to support the specimen and a 20 mm diameter hemispherical indenter mounted to the crosshead. Deflection was measured from crosshead displacement. Additionally, the displacement and strain fields were captured with two Point Grey Grasshopper GRAS-50S5M cameras and Correlated Solutions VIC 3D Digital Image Correlation (DIC) software. Synchronization of the DIC system to the load frame was accomplished by transistor-to-transistor logic (TTL) signals from the load frame to a National Instruments USB-6221BNC data acquisition device which activated/deactivated the DIC system at the beginning/end of the prescribed crosshead displacement.
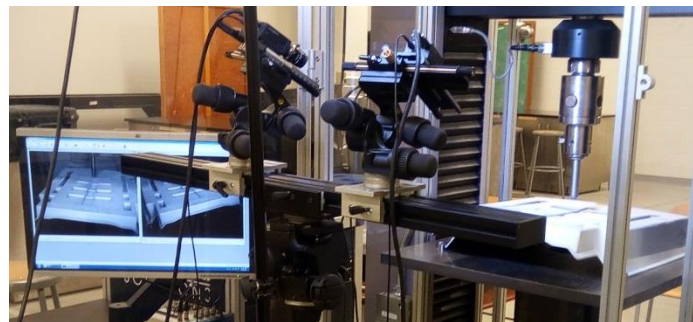
Figure 6.4: Quasi-static mechanical characterization (puncture) apparatus for automotive seatback

6.2.3 Low Velocity Impact

Low velocity impact testing of the seatback was completed on a custom-built drop tower with a drop height of approximately 1.5 m (Figure 6.5). The designation 'low velocity' is consistent to [24] and not in disagreement with a more established definition of 'high velocity' by Abrate [25] where the ratio of impactor velocity to wave speed is greater than the strain to failure. The methodology was based upon the ISO standard 6603-2 [1]. The mean impact velocity was 4.4 m/s (standard deviation: 0.09 m/s). The carriage mass was approximately 60 kg resulting in a pre-impact kinetic energy of 570 J. Energy absorption by the seatback during the puncture event was an order of magnitude lower where no significant decrease in crosshead velocity was expected or observed. The kinetic energy of

the crosshead was ultimately dissipated by crushing the part with a flat plate after the puncture event was complete.

Load was acquired from a Dytran 1050V6 IEPE load cell (incorporated into the 20 mm diameter hemispherical indenter) connected to a National Instruments 9250 analog input module in a CompactDAQ chassis. Displacement of the crosshead was measured with a 300 mm range Acuity laser displacement transducer connected to a 9205 National Instruments analog input module. Displacement and strain fields were acquired with Correlated Solutions digital image correlation (DIC) software and two Photron SA4 Fastcam highspeed cameras triggered with a TTL signal from a custom LabVIEW program through a National Instruments 9401 digital input/output module. The frame rate was 10 000 fps with a shutter speed of 1/10000 seconds. The cameras were each equipped with a Nikon 60 mm lens with adjustable focus and aperture.
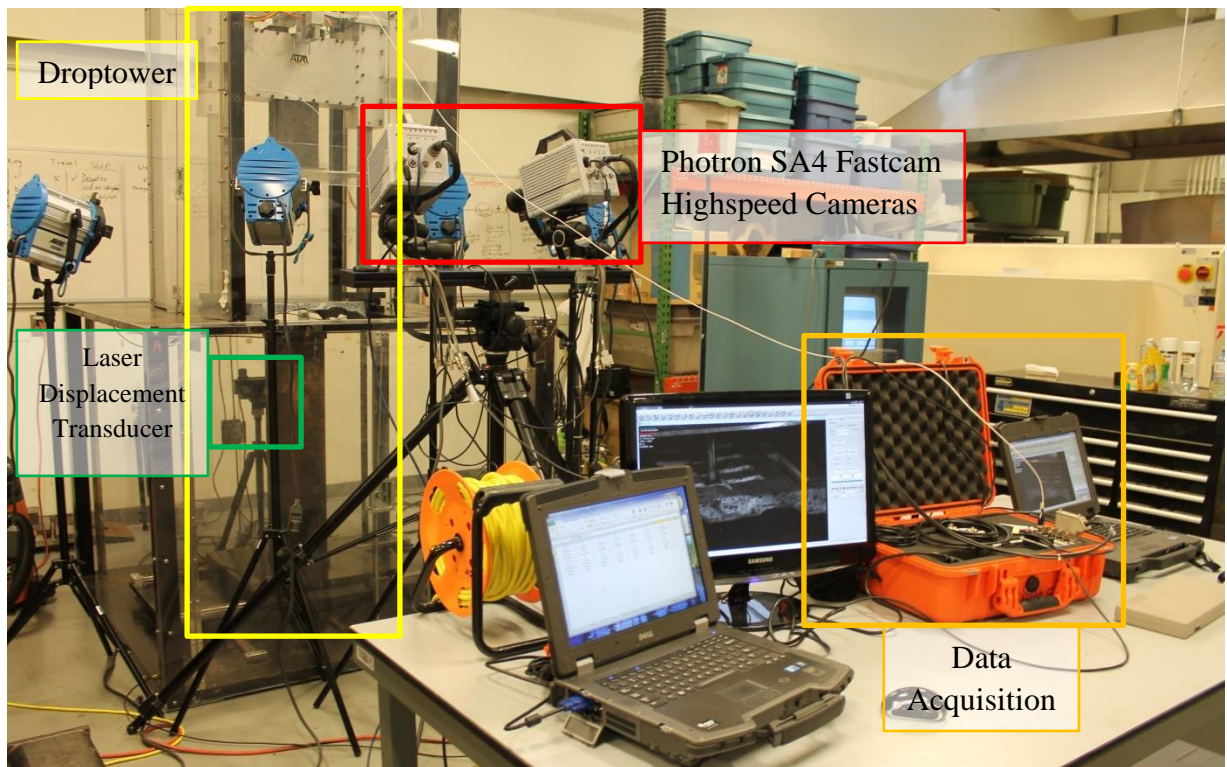
Figure 6.5: Impact testing apparatus for automotive seatback mechanical characterization

6.3 Results and Discussion

6.3.1 Tensile Data

Tensile data for the longitudinal charge seatback specimens are shown in Figure 6.6 and Figure 6.7. Engineering stress/strain responses for all specimens typically exhibit a linear to a minor degree of non-linear response without the identification of any yield strength. Significant variation in all mechanical properties was observed for a given specimen location and orientation. The top surface of the part corresponds with the surface of the tool on which the compression molding charge is placed. At this location there will be limited flow induced fibre alignment during the molding process. At the surface of the part, the fibre orientation will essentially be determined by the fibre orientation at the surface of the charge. For reference, a charge is shown in Figure 6.3. Fibre orientation within the charge is not well approximated as unidirectional at a macroscopic level [12]. However, properties of the charge and the charge region of any LFT material have not been documented extensively in the open literature. This is despite the clear demonstration with this part that the majority of a component manufactured with this process may effectively have charge region properties. Elastic modulus and tensile strength vary considerably, however, this is not unexpected for charge region specimens [12].

A summary of all tensile data is presented in Table 6.3. Variation within each group of specimens is quantified with the coefficient of variation (CoV). For the tensile specimens extracted from longitudinal charge seatbacks only the 0-degree specimens extracted from the side of the part have a coefficient of variation (15.6%) that is comparable to coefficients of variation in a study of flat molded panels with more defined charge and flow regions [12]. Modulus does not change significantly between the 0- and 90-degree directions (14.0 and 15.9 GPa, respectively with coefficients of variation of 56% and 36%) for specimens extracted from the top of longitudinal seatbacks. The specimens extracted from the sides of the seatback have a more significant difference between their elastic moduli (9.79 and 21.6 GPa) and lower coefficients of variation (15.6% and 23.0%).
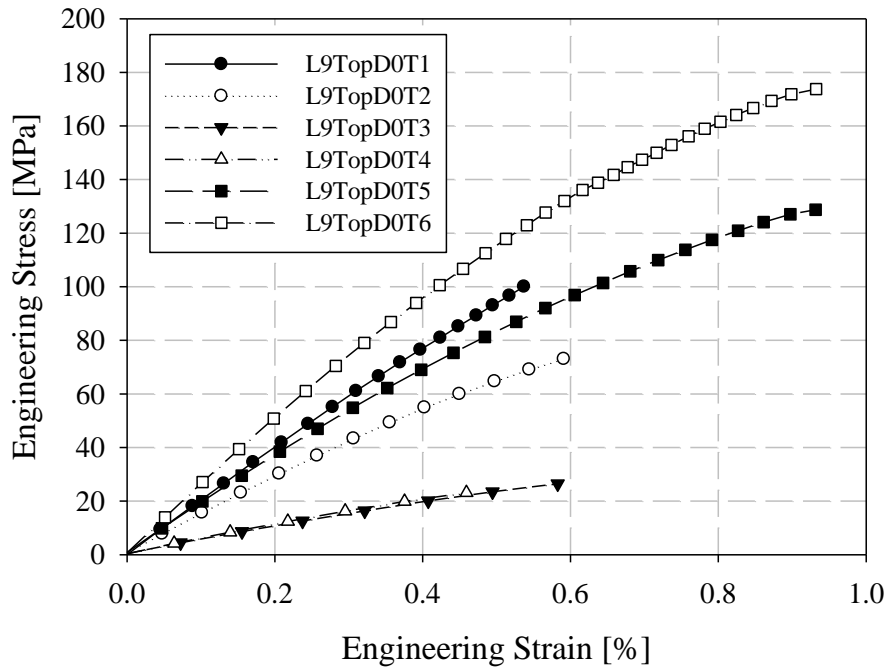
(a)
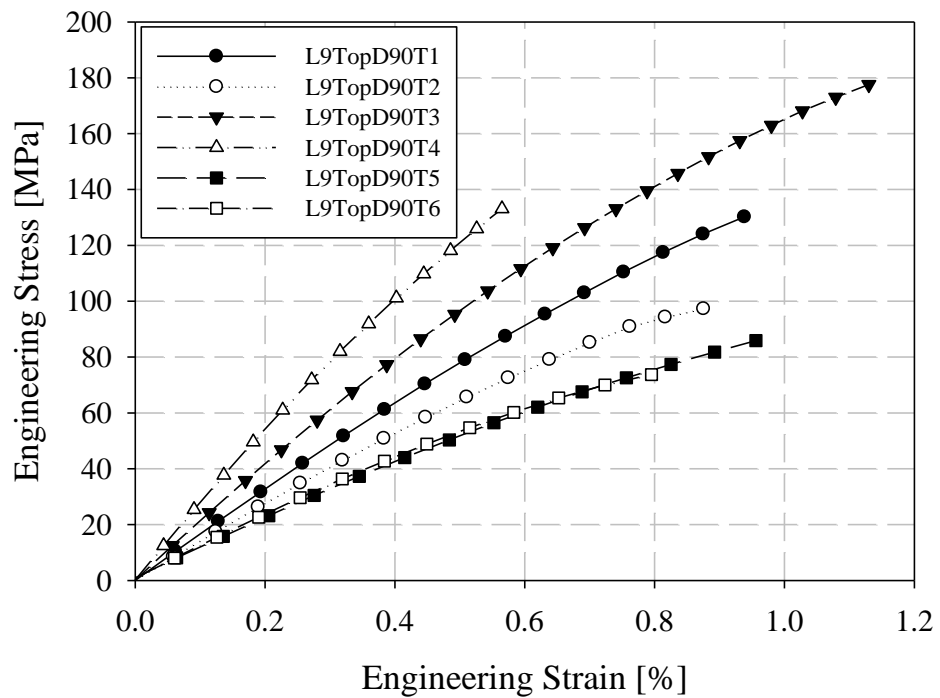
(b)

Figure 6.6: Tensile data for specimens extracted from the top of longitudinal charge automotive seatbacks: (a) 0-degree, (b) 90-degree

(a)

(b)
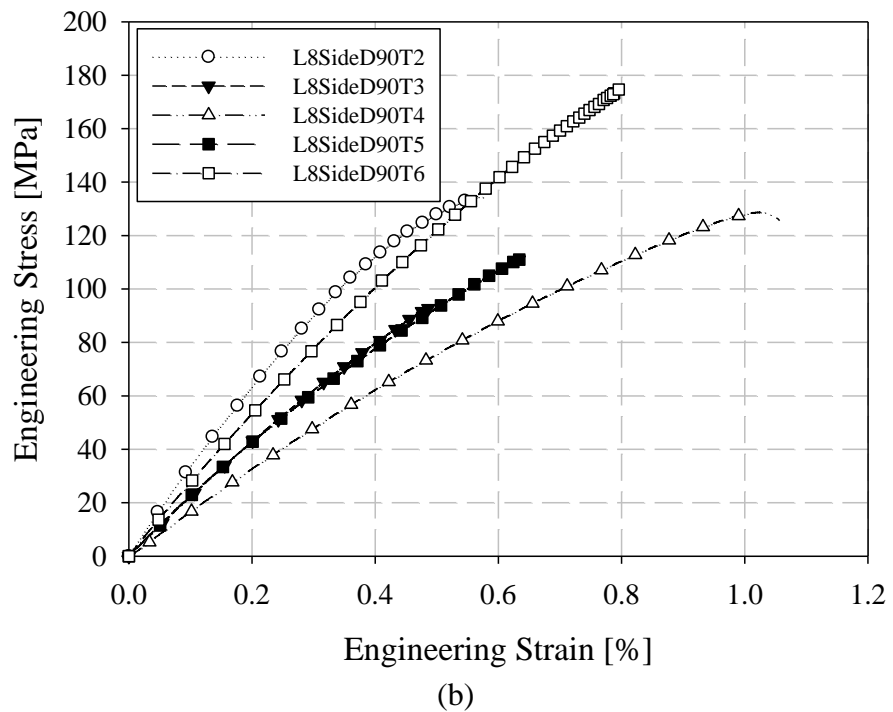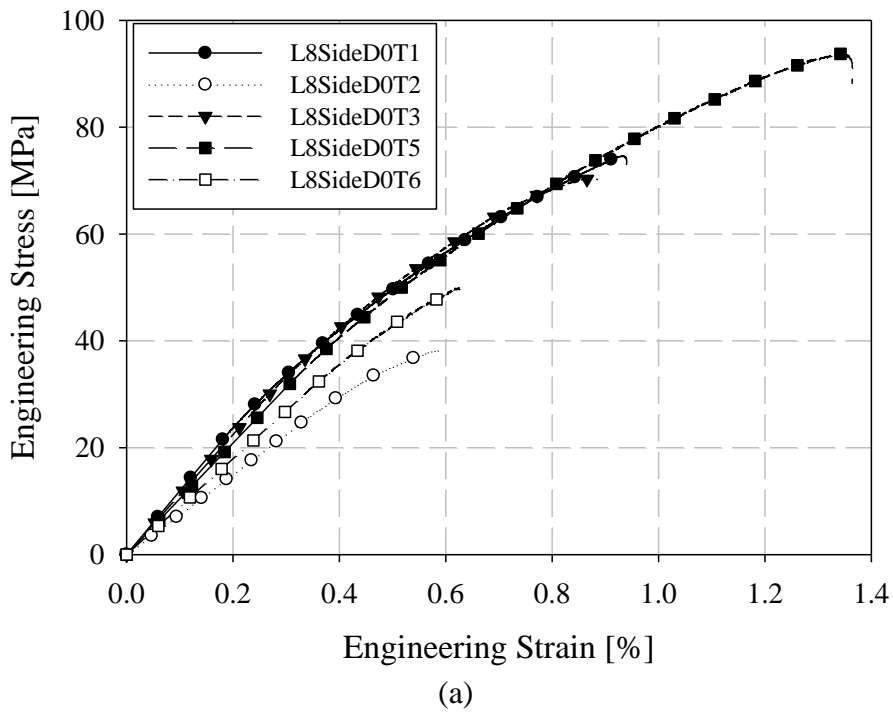
Figure 6.7: Tensile data for specimens extracted from the side of longitudinal charge automotive seatbacks: (a) 0-degrees, (b) 90-degrees

Tensile data for the transverse charge seatback specimens are shown in Figure 6.8 and Figure 6.9. A summary of all tensile data is provided in Table 6.3. In a similar fashion as previous, the stress/strain response for these specimens also exhibit linear with a minor degree of non-linear behaviour. A comparison specimens from the top of the seatback (charge region) and side of the seatback (flow region) provide limited evidence supporting the hypothesis that the side of the part may have a fibre orientation state with a more significant dependence on flow of material during the compression molding process. Elastic moduli are similar for 0- and 90-degree directions for both the top (15.8 and 12.7 GPa, respectively) and side of the part (7.11 and 11.3 GPa) and the coefficients of variation are fairly large (as high as 44.5% for 90-degree specimens extracted from the top surface).

The specimen group T11TopD90 is particularly interesting as it can be divided into two sets of three specimens with a degree of consistency not expected for mechanical properties given the anisotropy and inhomogeneity of a charge and the high mold coverage for this application. These six specimens were extracted such that there are two groups separated in the longitudinal direction by as much as 300 mm (the length of the full seatback is approximately 500 mm). The top surface of transverse charge seatback T11 after extracting tensile specimens is shown in Figure 6.10. Variation in strain to failure for all specimen location/orientation groups is hypothesized to be affected (i.e., a reduction in consistency) by the combination of the small size of the tensile specimen and the method of extraction (CNC milling). The coefficient of variation for tensile strength reaches extreme values as high as 65.5% for 0-degree specimens extracted from the top of longitudinal charge parts.
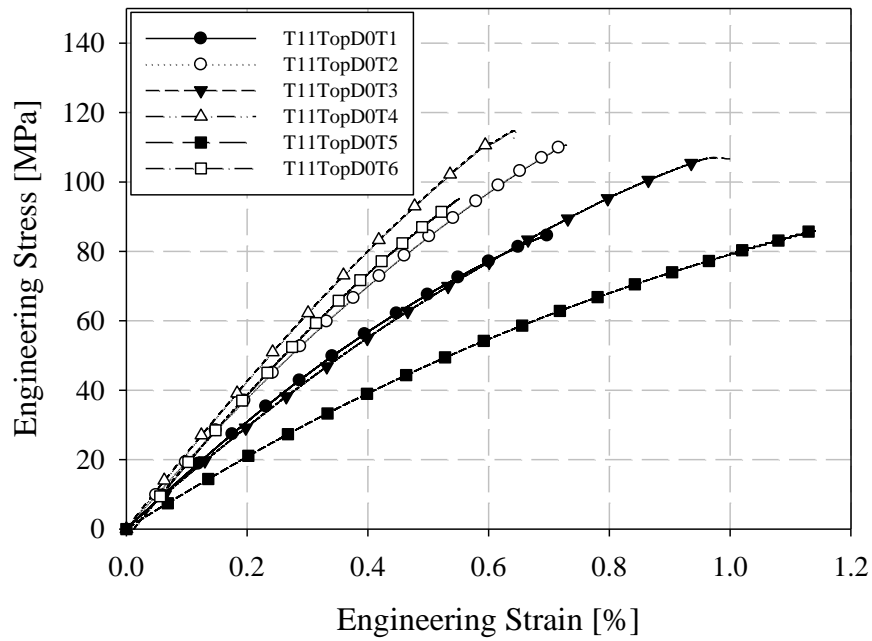
(a)
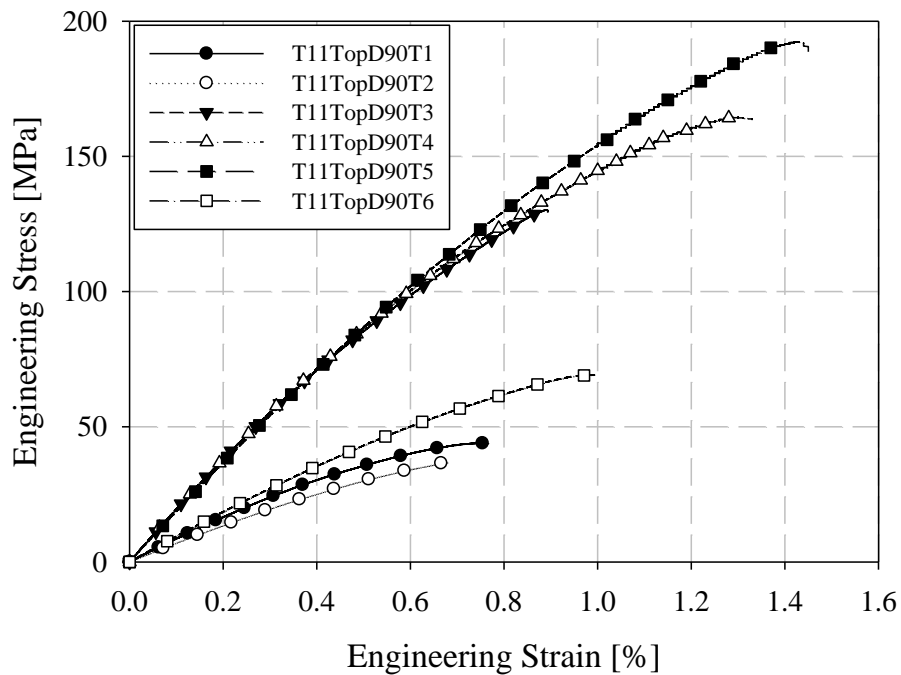
(b)

Figure 6.8: Tensile data for specimens extracted from the top of transverse charge automotive seatbacks: (a) 0-degrees, (b) 90-degrees
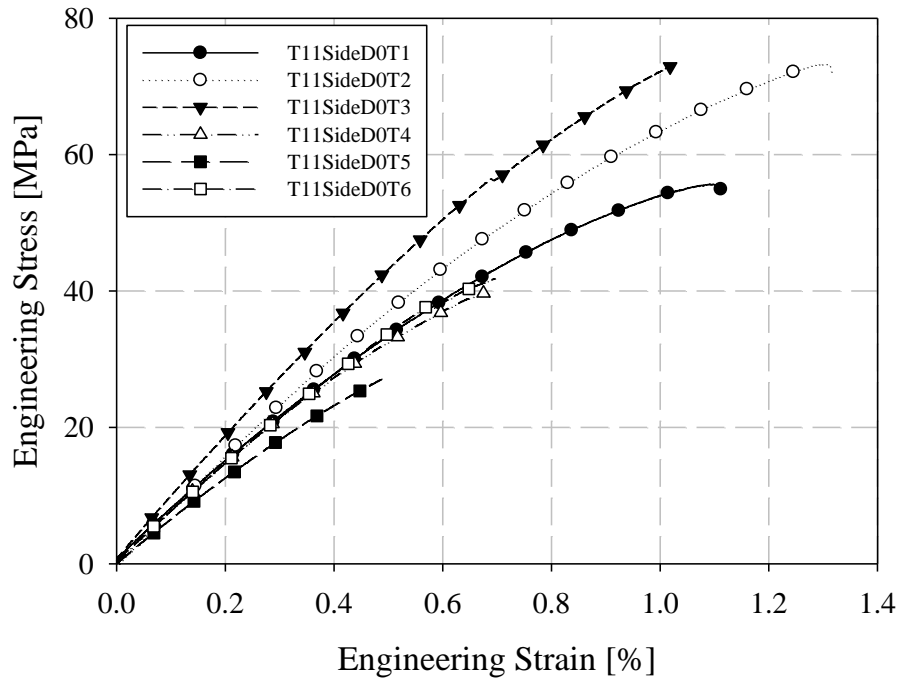
(a)
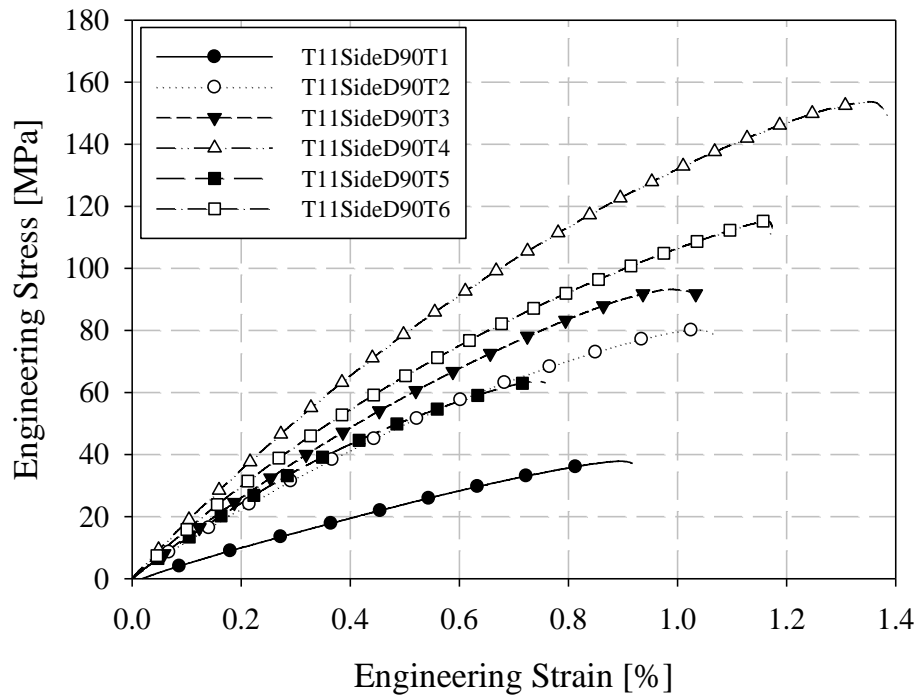
(b)

Figure 6.9: Tensile data for specimens extracted from the side of transverse charge automotive seatbacks: (a) 0-degrees, (b) 90-degrees
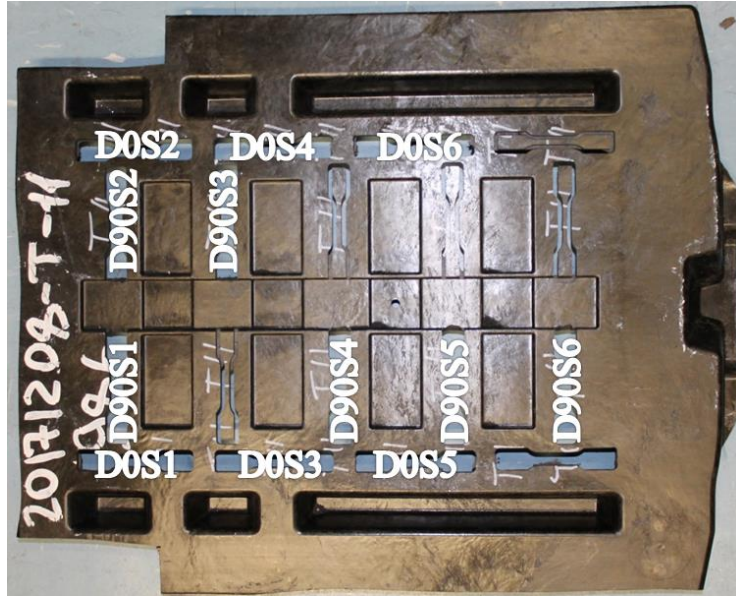
Figure 6.10: Tensile specimen locations for transverse charge automotive seatback T11

Table 6.3: Automotive seatback tensile data summary

	Chord Modulus [GPa] (CoV)	Tensile Strength [MPa] (CoV)	Failure Strain [%] (CoV)
L9 Top D0	14.0 (55.5%)	88.8 (65.5%)	0.704 (28.1%)
L9 Top D90	15.9 (36.0%)	118 (33.0%)	0.903 (22.2%)
L8 Side D0	9.79 (15.6%)	65.4 (33.2%)	0.882 (35.2%)
L8 Side D90	21.6 (23.0%)	129 (23.8%)	0.715 (31.0%)
T11 Top D0	15.8 (24.6%)	99.8 (12.9%)	0.795 (28.5%)
T11 Top D90	12.7 (44.5%)	106.0 (61.6%)	1.02 (30.3%)
T11 Side D0	7.11 (13.9%)	51.8 (36.6%)	0.887 (35.1%)
T11 Side D90	11.3 (33.5%)	90.5 (44.6%)	1.06 (20.3%)

6.3.2 Quasi-Static Loading of Seatbacks

Quasi-static force-deflection responses for longitudinal and transverse charge seatbacks are shown in Figure 6.11. Initial stiffness, typically identified by the force-deflection response within the first 10 mm deflection (longitudinal: 196 N/mm and transverse: 210 N/mm),

peak loads (2419 N and 2366 N), and energy absorbed (30.4 J and 27.2 J), do not differ significantly between charge orientations. The longitudinal specimens include one force-deflection response for which the onset of failure occurred much earlier, in terms of displacement, than all other specimens. However, an alternative load path through the structure without significant propagation of this initial failure resulted in an essentially identical stiffness while the material was primarily undergoing elastic deformation (up to approximately 10 mm deflection). This specimen may be an outlier or suggests that the longitudinal charge orientation may be more prone to defects. However, the number of specimens available/tests completed limits any confidence in either identifying this result as an outlier or making firm conclusions regarding any dependence of the onset of failure on charge orientation. Energy-deflection responses are shown in Figure 6.12. Summaries of puncture characteristics for quasi-static loading are presented in Table 6.4 and Table 6.5.

(a)
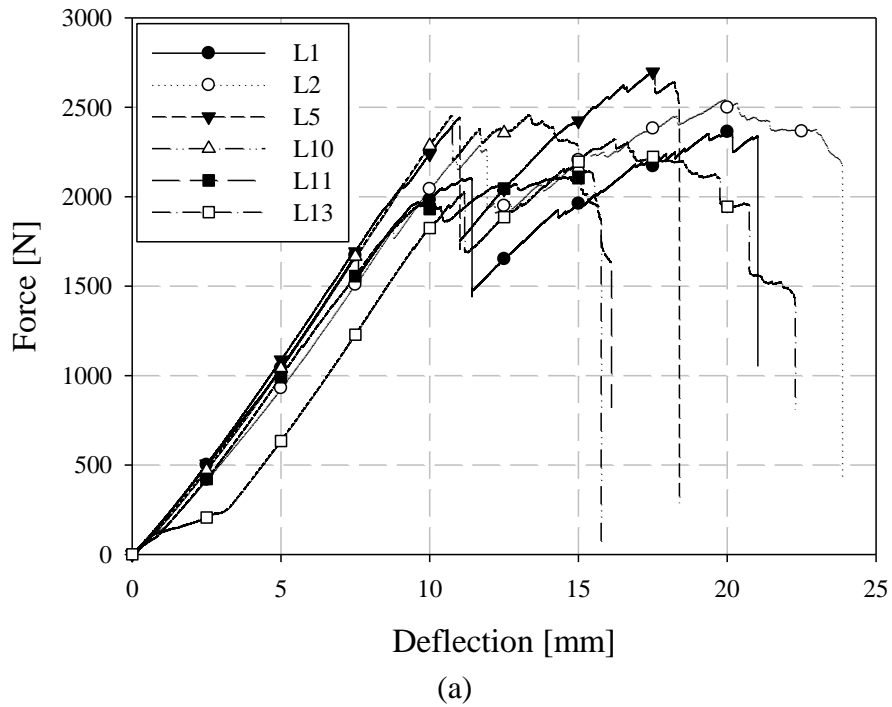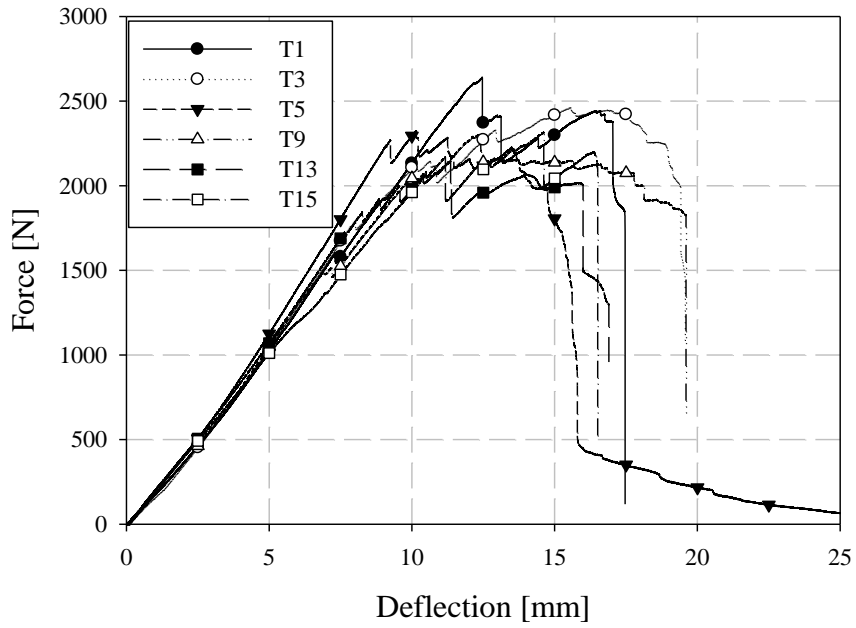
(b)

Figure 6.11: Automotive seatback hemispherical indenter quasi-static force-deflection responses: (a) longitudinal charge, (b) transverse charge
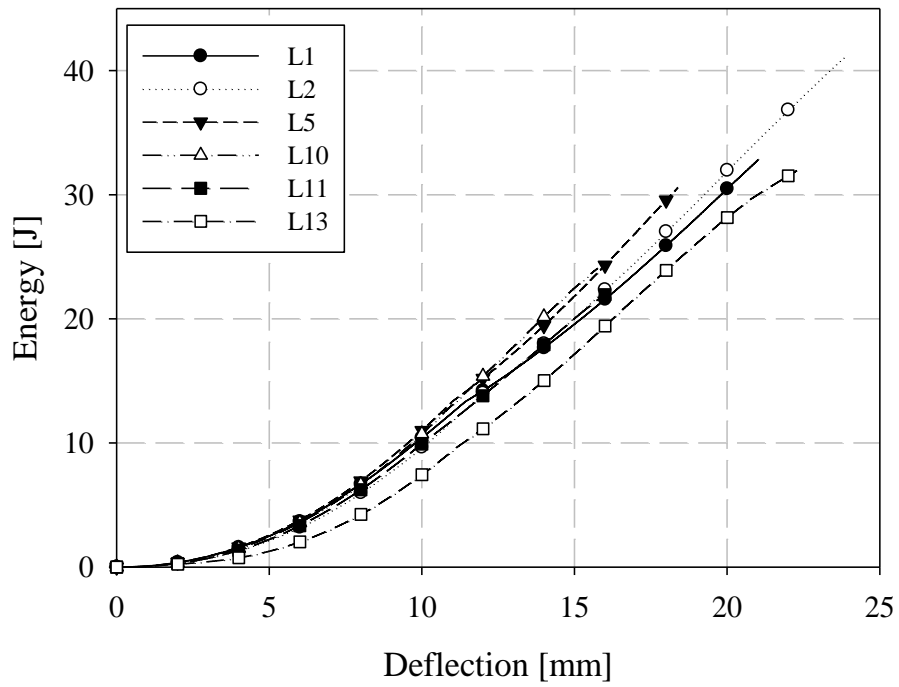
(a)
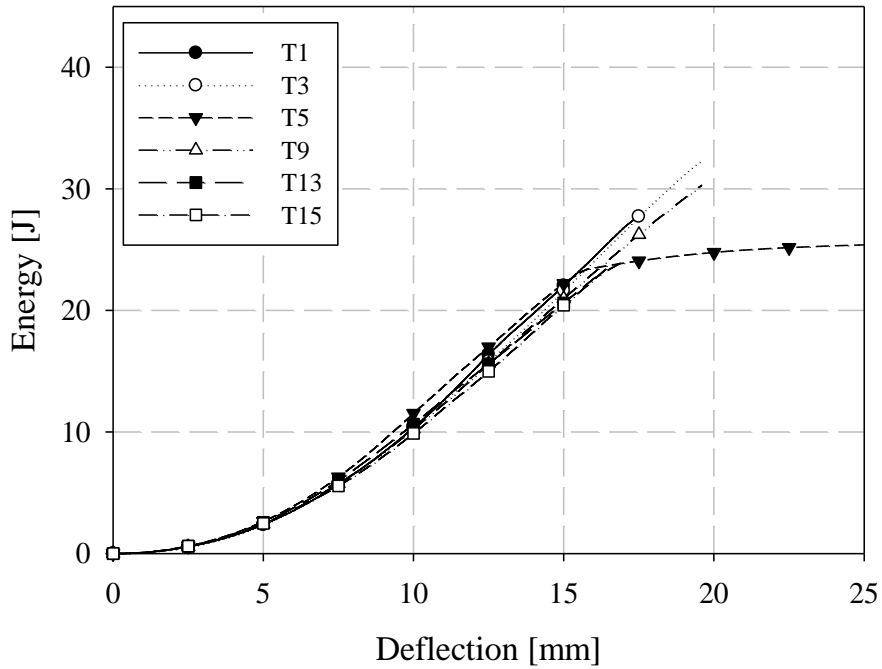
(b)

Figure 6.12: Automotive seatback hemispherical indenter energy-deflection responses for (a) longitudinal and (b) transverse charge specimens

Table 6.4: Summary of quasi-static puncture characteristics of longitudinal charge automotive seatbacks

	Stiffness [N/mm]	Maximum Force [N]	Deflection at Maximum Force [mm]	Energy [J]	Deflection Fracture Onset [mm]	Deflection Catastrophic Failure [mm]
L1	210.3	2368	20.02	32.85	11.4	21
L2	189.6	2544	19.93	41.14	11.7	23.8
L5	217.8	2708	17.56	30.58	10.7	18.4
L10	210.7	2458	13.32	24.06	10.8	15.8
L11	203.3	2113	14.22	22.12	9.7	16.1
L13	143.5	2325	16.24	31.94	11.1	20.7
Average	195.9 (14.0%)	2419 (8.4%)	16.88 (16.7%)	30.44 (22.4%)	10.9 (6.4%)	19.3 (16.1%)

Table 6.5: Summary of quasi-static puncture characteristics of transverse charge automotive seatbacks

	Stiffness [N/mm]	Maximum Force [N]	Deflection at Maximum Force [mm]	Energy [J]	Deflection Fracture Onset [mm]	Deflection Catastrophic Failure [mm]
T1	203.0	2640	12.46	27.70	12.5	17.4
T3	209.4	2467	15.56	32.24	10.6	19.4
T5	219.3	2326	10.15	25.39	9.2	15.8
T9	207.9	2302	12.33	30.30	12.1	19.6
T13	215.9	2146	11.36	23.89	11.4	16
T15	204.0	2317	14.61	23.62	11	16.5
Average	209.9 (3.1%)	2366 (7.1%)	12.74 (15.8%)	27.19 (13.0%)	11.1 (10.6%)	17.4 (9.6%)

Two longitudinal charge specimens are compared in terms of load-deflection responses in Figure 6.13 and z-deflection contour plots in Figure 6.14. Specimen selection was determined by camera location in all instances, not from features of the load-deflection or energy-deflection responses. The camera location at which the field of view covered the largest fraction of the specimen was selected. In the case of longitudinal charge seatback quasi-static testing results, specimen L13 was not considered for more detailed evaluation herein given the potential for identification as an outlier. The selection of z-deflection for contour plots was based upon the relative magnitude for deflection with respect to the x and y directions (deflection components are an order of magnitude smaller in the x direction and two orders of magnitude in the y direction). As crosshead displacement increases, the deformation becomes less localized for specimen L10. The earlier onset of failure with specimen L1 could be accompanied by strain energy release which may be observed (considering the contour plots) in this specimen comparison through reduced z-deflection away from the indenter.
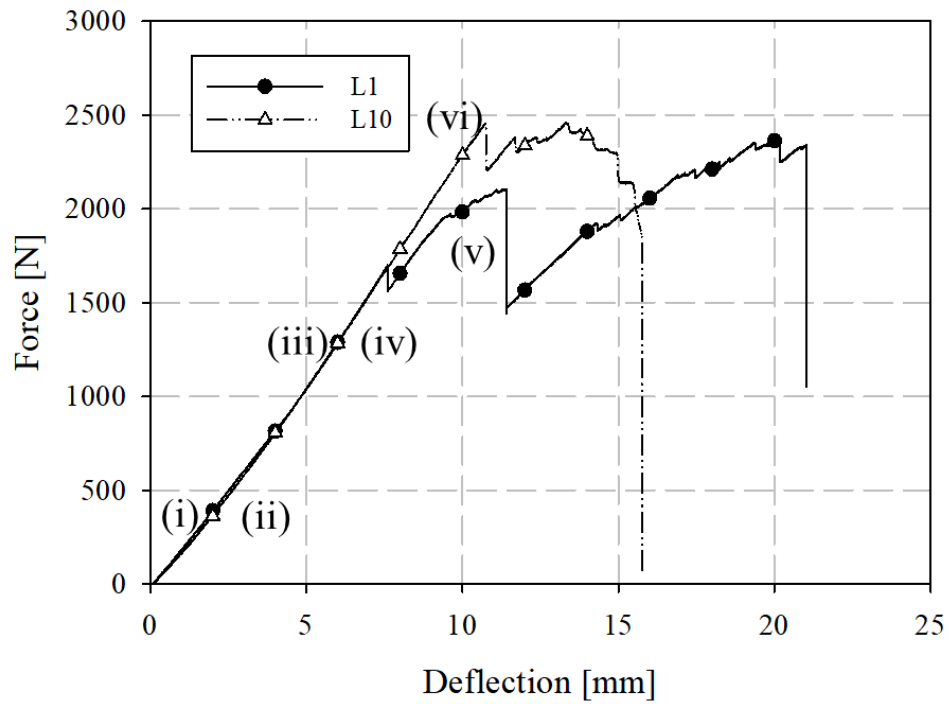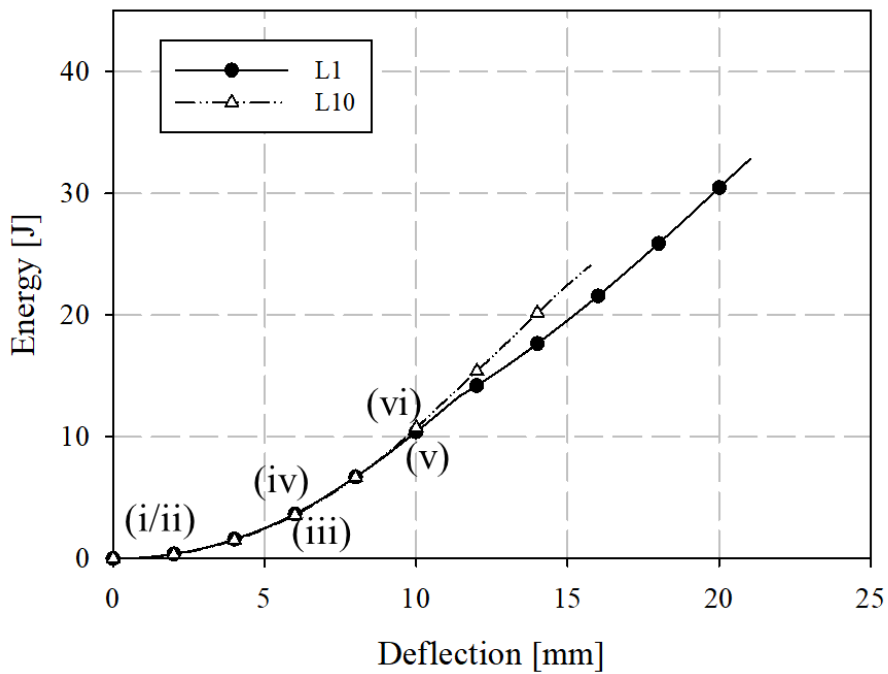
Figure 6.13: (a) Force-deflection and (b) energy-deflection responses for longitudinal charge quasi-static automotive seatback specimens annotated for DIC contour plots in Figure 6.14

(i) L1, 2 mm deflection   (ii) L10, 2 mm deflection

(iii) L1, 6 mm deflection   (iv) L10, 6 mm deflection

(v) L1, 10 mm deflection   (vi) L10, 10 mm deflection
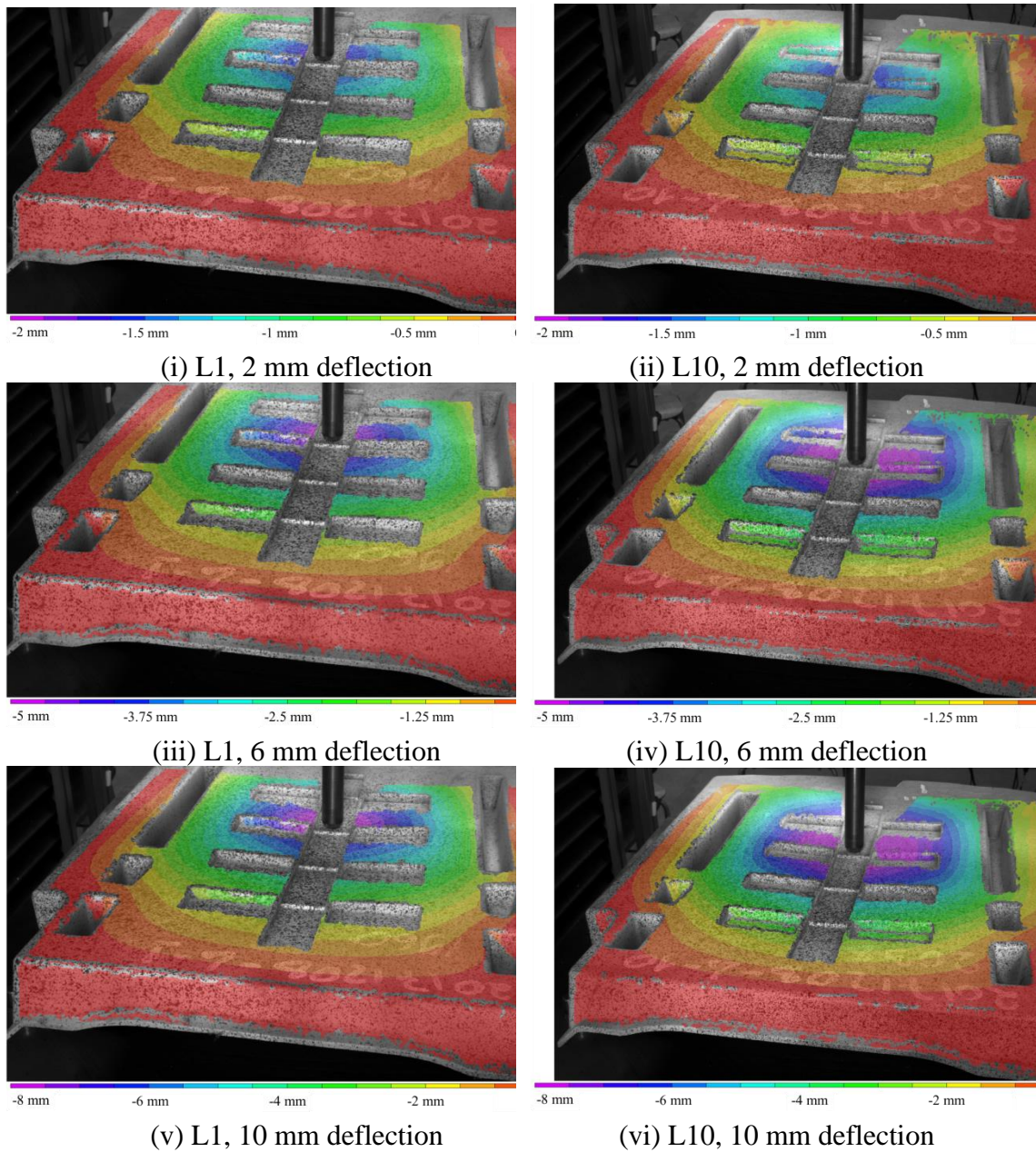
Figure 6.14: Comparison of longitudinal charge automotive seatbacks L1 & L10, z-deflection, quasi-static loading

Similarly, for transverse charge specimens quasi-static force-deflection/energy-deflection and z-deflection contour plots are compared in Figure 6.15 and Figure 6.16, respectively. Specimen selection was limited by the small number of specimens and apparatus configurations to these two specimens to obtain the most complete displacement

field measurements. There is a more distinct difference between the force-deflection responses of these two transverse charge components at deflections less than 6 mm with respect to the pair of longitudinal charge specimens. A reduced level of z-deflection across the full specimen is observed for specimen T3 with respect to specimen T5. This provides further evidence that the earlier onset of failure in one specimen (T3) may reduce strain energy and overall deflection.

(a)

(b)
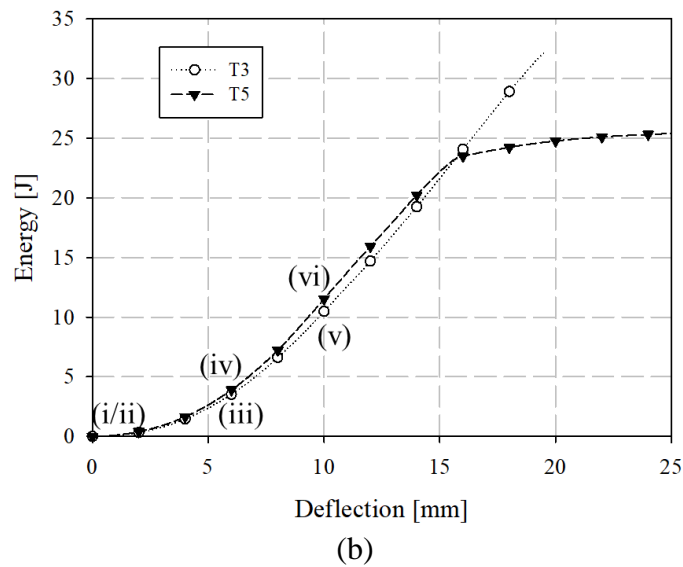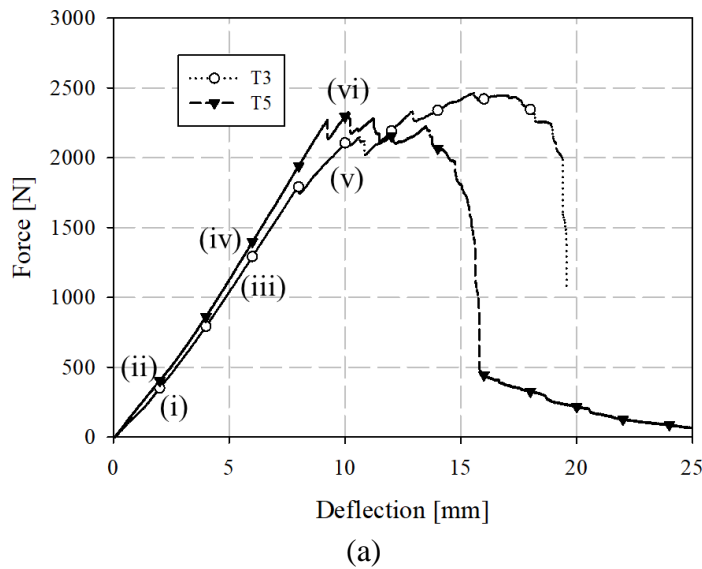
Figure 6.15: (a) Force-deflection and (b) energy-deflection responses for transverse charge automotive seatback specimens T3 and T5

(i) T3, 2 mm crosshead displacement   (ii) T5, 2 mm crosshead displacement

(iii) T3, 6 mm crosshead displacement   (iv) T5, 6 mm crosshead displacement

(v) T3, 10 mm crosshead displacement   (vi) T5, 10 mm crosshead displacement
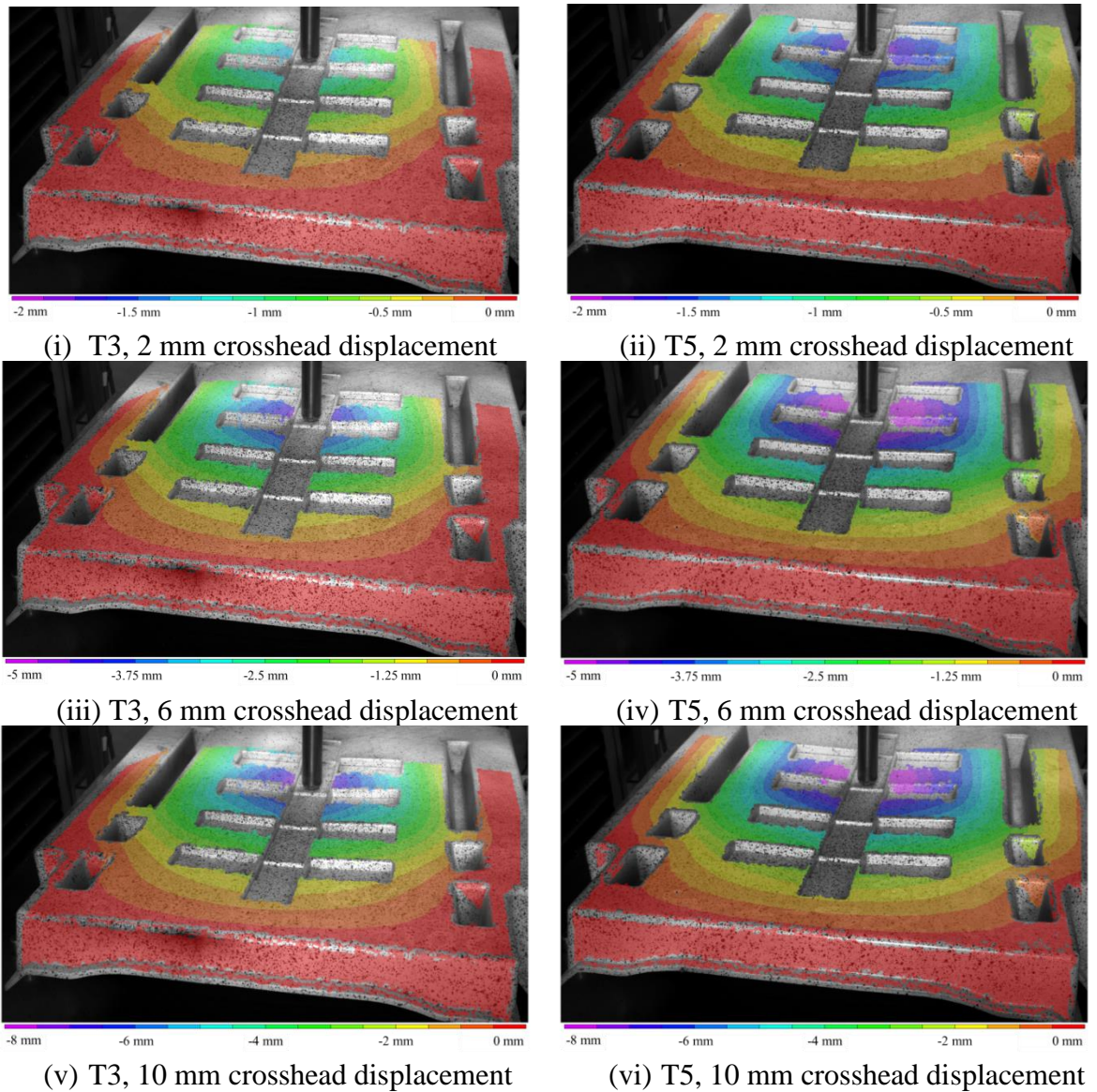
Figure 6.16: Contour plots of z-deflection for transverse charge automotive seatback specimens T3 and T5

No significant differences between longitudinal and transverse charge seatbacks were observed for quasi-static loading either in terms of force-deflection response or z-deflection contours. Variability (in terms of z-displacement contours) between specimens with the same charge orientation is approximately equal to the differences between any non-outlier longitudinal and transverse specimens under quasi-static loading.

6.3.3 Low Velocity Impact Loading of Seatbacks

A pair of unfiltered force-deflection responses for low velocity impact are shown in Figure 6.17. Only two responses were selected for presentation as any further plots added to these graphs resulted in a cumbersome illustration of specific observed data. Filtered force-deflection responses for impact loading are shown in Figure 6.18. A Butterworth filter with a channel frequency class (CFC) of 1000 (default in J211) was applied consistent with SAE standard J211 [13]. Repeatability was observed in the force-deflection responses for the first 5 mm of deflection. The transverse charge specimens exhibit a more uniform force over the deflection domain with respect to the longitudinal charge specimens which have a distinct peak load just prior to catastrophic failure. The initial stiffness, deflection at which the onset of failure occurs, and the deflection at which catastrophic failure occurs are similar for both charge placements. The longitudinal charge specimens have a local maxima in the force deflection response at approximately 15 – 20 mm of deflection. However, comparing average maximum force for longitudinal and transverse charge seatbacks (2634 N and 2383 N, respectively) with standard deviations of 197 N and 138 N, it is not possible to make strong conclusions regarding this behaviour. Energy-deflection responses are shown in Figure 6.19. Summaries of low velocity puncture properties are given in Table 6.6 and Table 6.7.
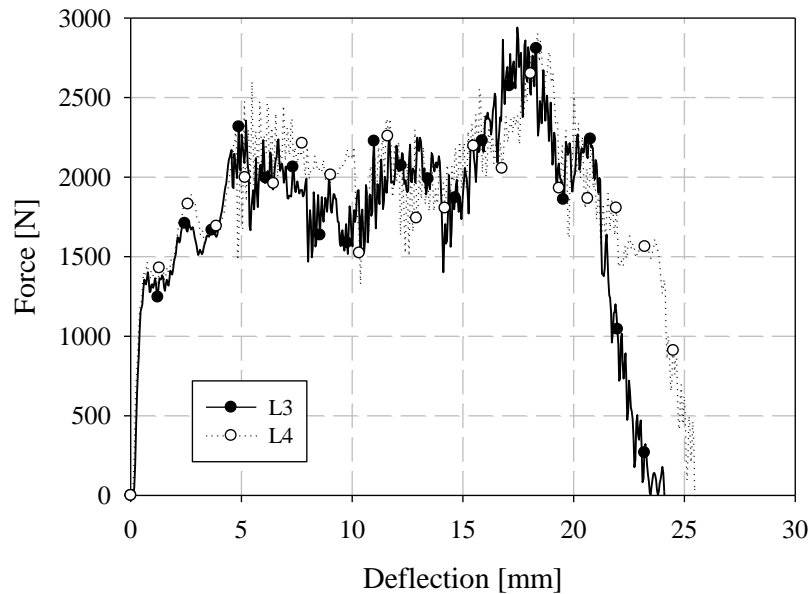
(a)
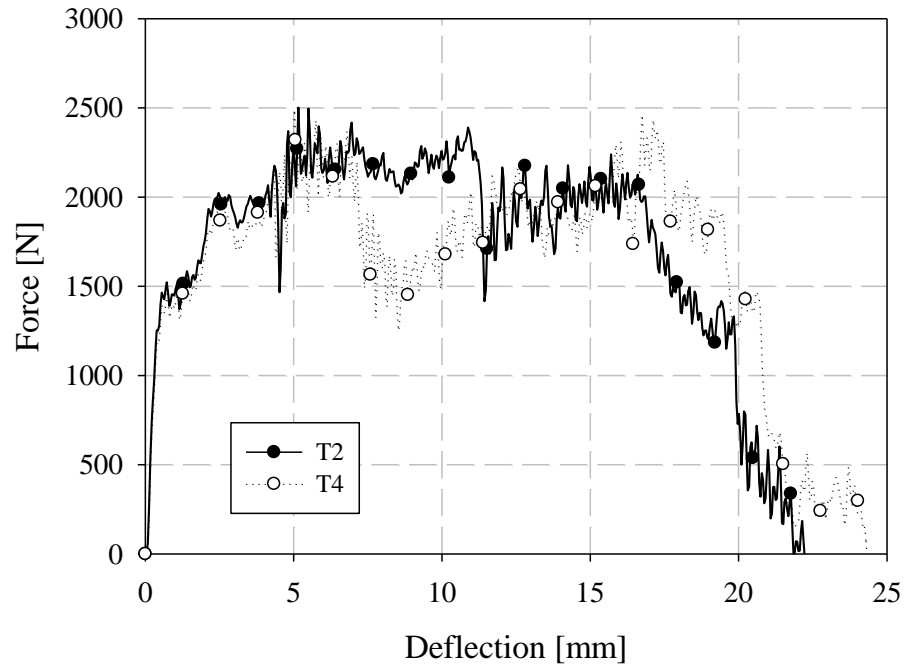
(b)

Figure 6.17: Unfiltered force-deflection responses for low velocity impact loading of (a) longitudinal and (b) transverse charge placement automotive seatbacks
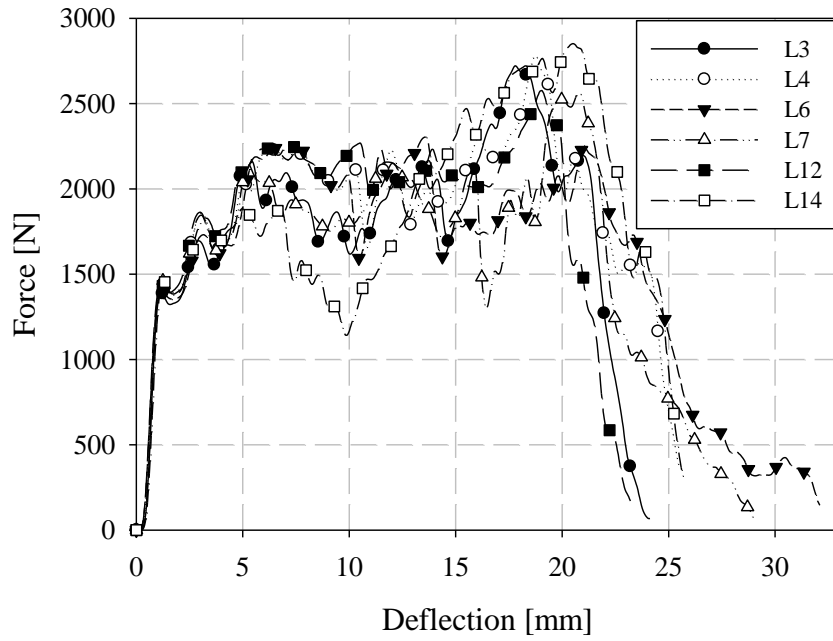
(a)
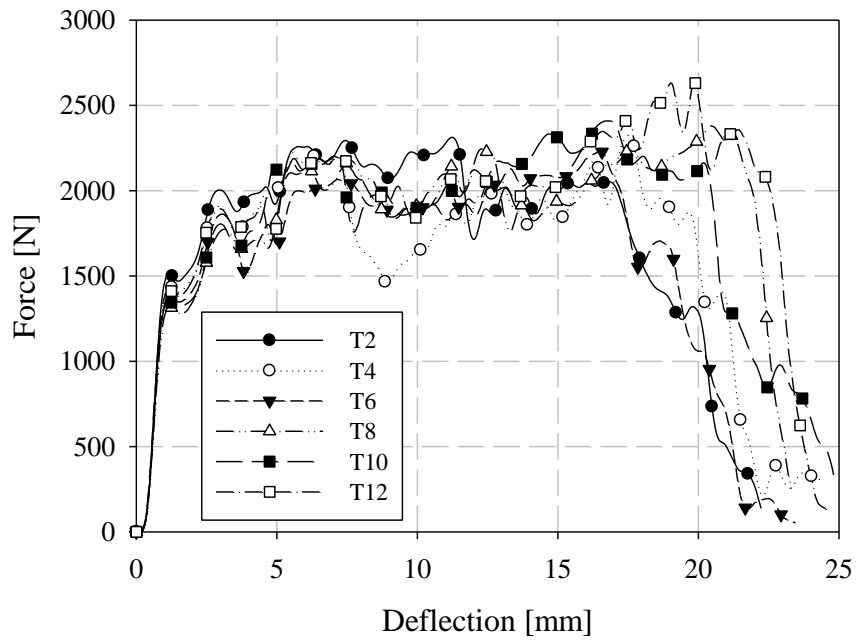
(b)

Figure 6.18: Low velocity impact force-deflection responses (filtered) for automotive seatbacks: (a) longitudinal and (b) transverse charge placement
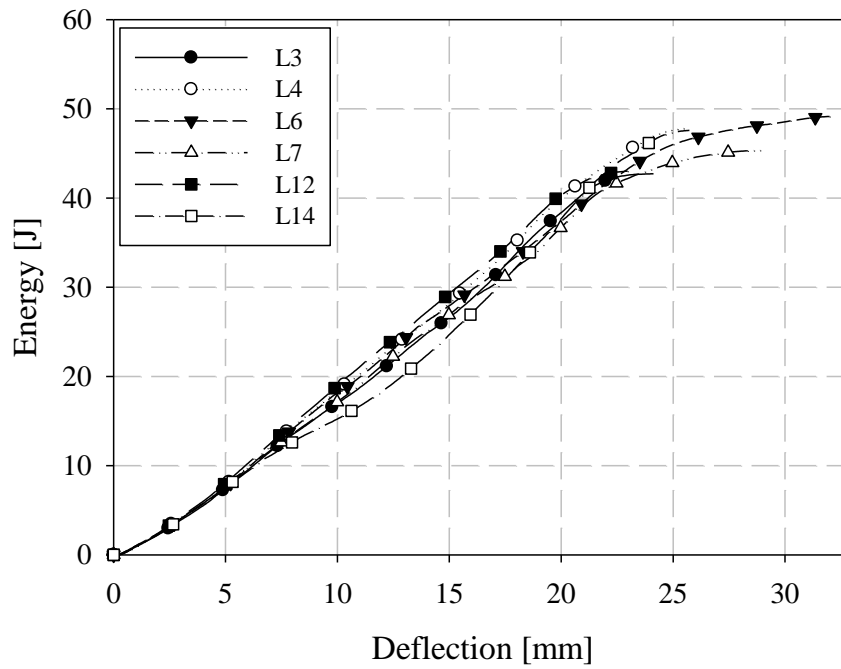
(a)
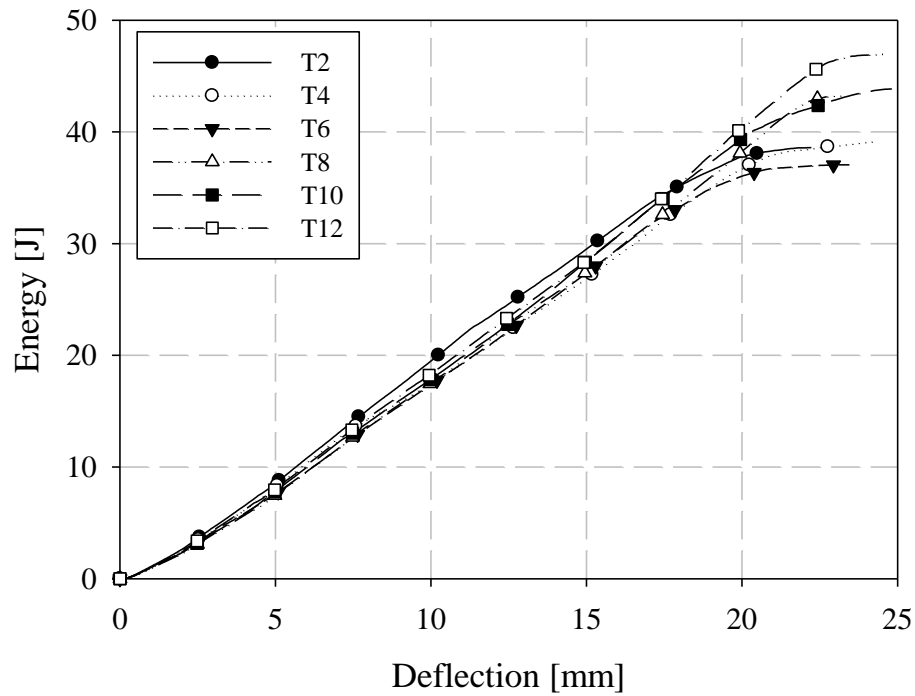
(b)

Figure 6.19: Energy deflection response for low velocity impact loading of automotive seatbacks: (a) longitudinal and (b) transverse charge seatbacks

Table 6.6: Summary of low velocity impact characteristics of longitudinal charge automotive seatbacks

	Stiffness [N/mm]	Maximum Force [N]	Deflection at Maximum Force [mm]	Energy [J]	Deflection Fracture Onset [mm]	Deflection Catastrophic Failure [mm]
L3	1256	2721	17.78	42.72	1.18	24.2
L4	1320	2785	18.74	47.79	1.21	25.8
L6	1331	2304	13.59	49.15	1.18	32.1
L7	1225	2567	20.80	45.34	1.21	29
L12	1375	2576	19.01	43.02	1.15	23.3
L14	1096	2851	20.50	47.58	1.28	25.8
Average	1267 (7.9%)	2634 (7.5%)	18.40 (14.2%)	45.93 (5.8%)	1.20 (3.7%)	26.7 (12.3%)

Table 6.7: Summary of low velocity impact puncture characteristics of transverse charge automotive seatbacks

	Stiffness [N/mm]	Maximum Force [N]	Deflection at Maximum Force [mm]	Energy [J]	Deflection Fracture Onset [mm]	Deflection Catastrophic Failure [mm]
T2	1417	2313	11.22	38.60	1.15	22.2
T4	1374	2326	17.49	39.13	1.18	24.3
T6	1388	2231	16.49	37.06	1.19	23.5
T8	1348	2380	20.47	43.27	1.2	23.2
T10	1358	2409	16.83	43.84	1.17	24.8
T12	1363	2634	19.84	46.95	1.16	23.8
Average	1375 (1.8%)	2382 (5.8%)	17.06 (19.3%)	41.48 (9.2%)	1.18 (1.6%)	23.6 (3.8%)

A pair of longitudinal charge seatbacks are compared in terms of low velocity impact filtered force-deflection and energy-deflection responses in Figure 6.20 and z-deflection contours in Figure 6.21. Specimen L4 was unique in terms of camera position and captured the greatest extent of the part. Force-deflection responses are essentially identical to just under 5 mm deflection. Camera position was altered between the testing of these two specimens resulting in different fields of view for the z-deflection contour plots. For the overlapping regions, there is little variability in terms of z-deflection contours, even at large deflections. This is particularly interesting given the significant differences in the force-deflection responses for deflections greater than 5 mm. For specimen L14, a significant drop in the indenter force suggests the onset of failure and propagation of associated fractures with damage propagation limited sufficiently to allow the load to again increase. However, there is no significant evidence of a reduction in overall deflection associated with strain energy release.
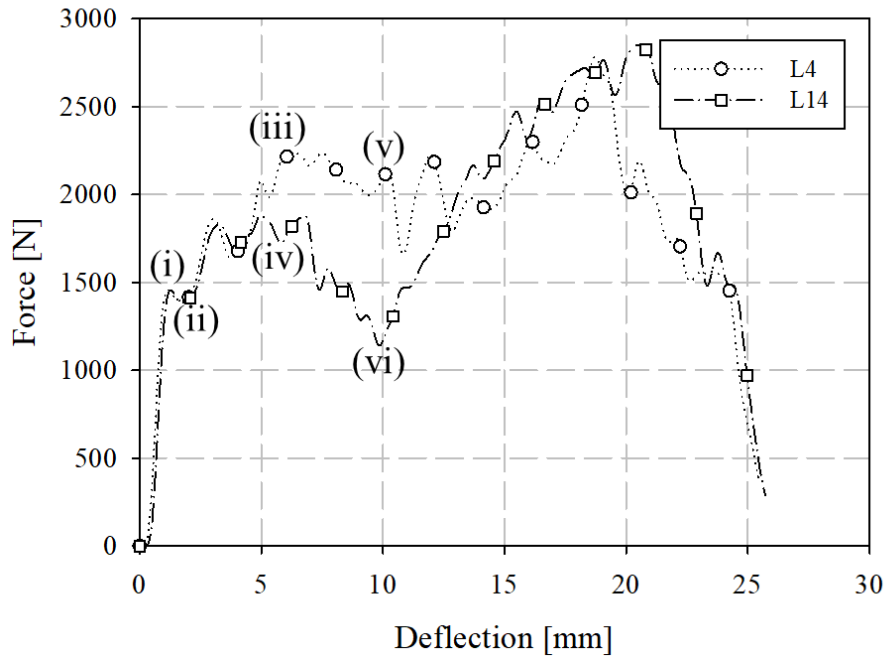
(a)
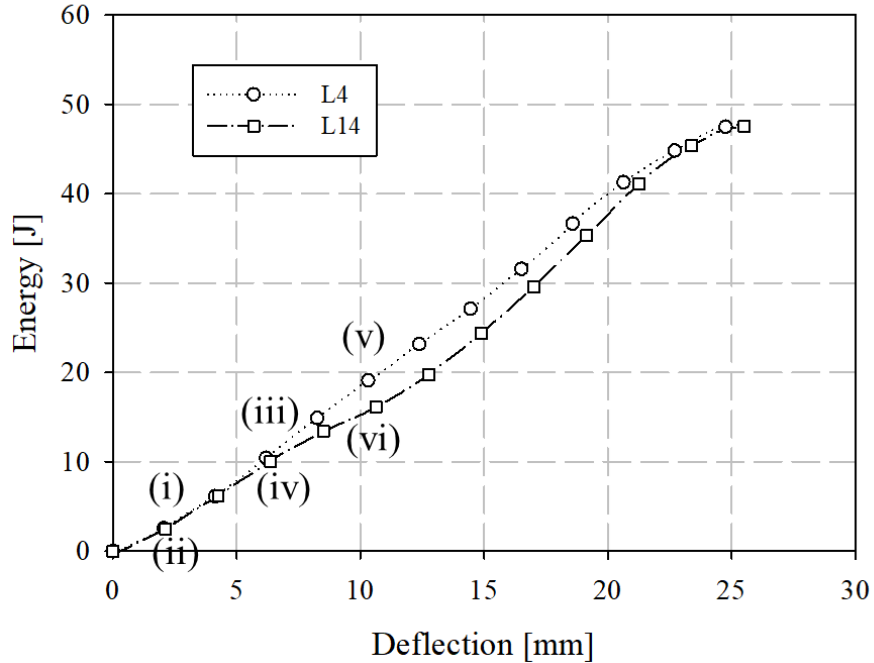
(b)

Figure 6.20: Comparison of longitudinal charge (a) force-deflection and (b) energy-deflection responses for low-velocity impact of automotive seatbacks with a hemispherical indenter

(i) L4, 2 mm crosshead displacement
(ii) L14, 2 mm crosshead displacement

(iii) L4, 6 mm crosshead displacement
(iv) L14, 6 mm crosshead displacement

(v) L4, 10 mm crosshead displacement
(vi) L14, 10 mm crosshead displacement
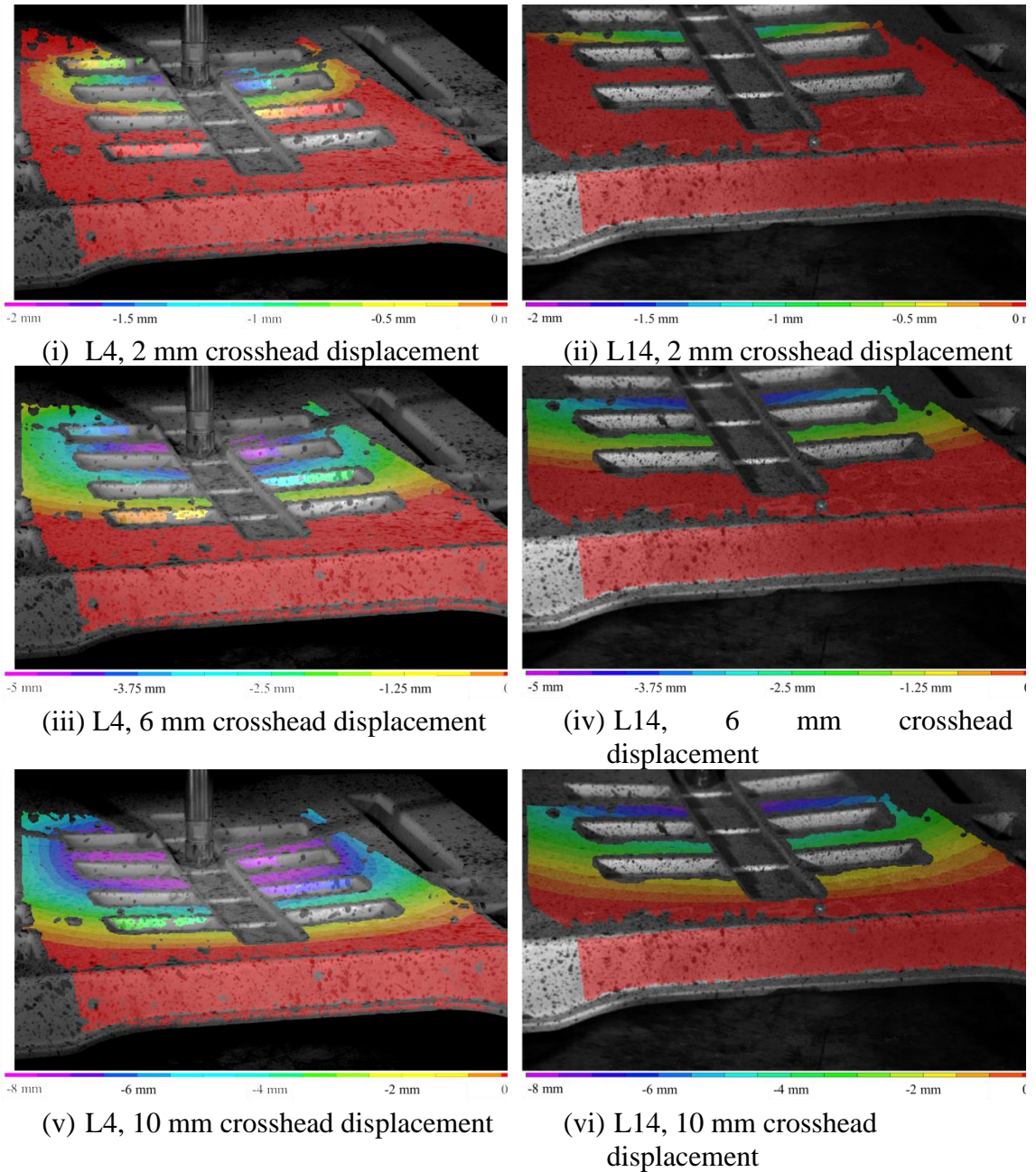
Figure 6.21: Contour plots of z-deflection for transverse charge automotive seatback specimens L4 and L14, low velocity impact

Two transverse charge seatbacks are compared under low velocity impact in terms of force-deflection in Figure 6.22 and z-deflection contours in Figure 6.23. The force-deflection responses are essentially identical up to 1 mm. These responses are also generally consistent in terms of overall behaviour through the full domain. Contour plots

of z-deflection are also generally consistent at each crosshead position assessed where the fields of view are overlapping. As noted in the previous section comparing low velocity impact longitudinal z-deflection contours, the camera was repositioned between these two tests.

(a)

(b)
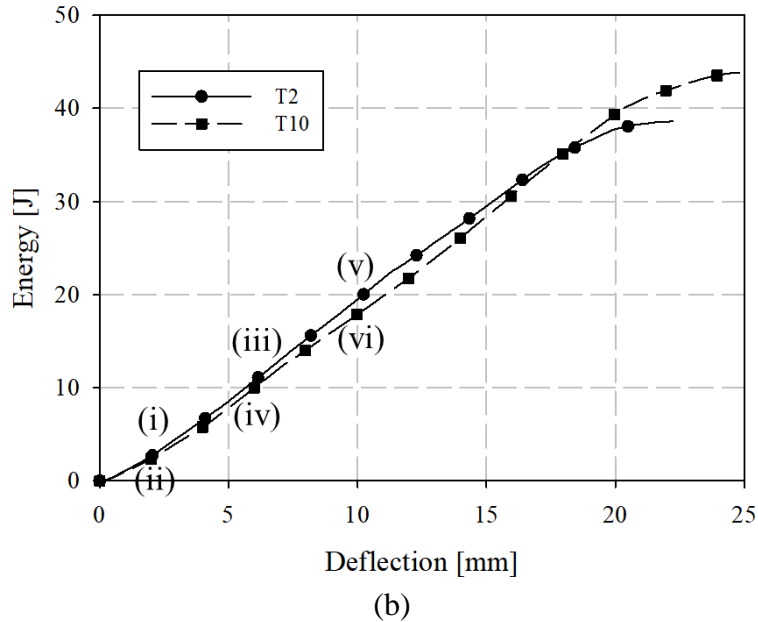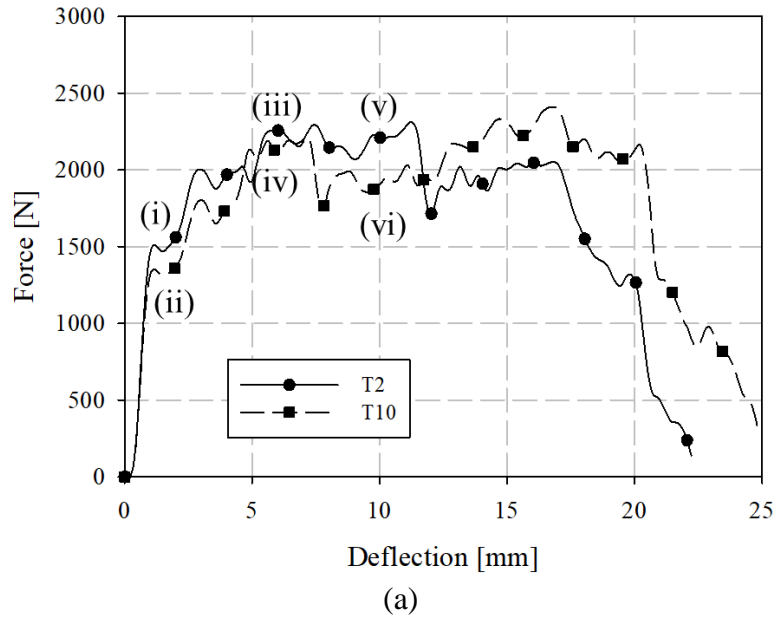
Figure 6.22: (a) Force-deflection and (b) energy-deflection responses for low velocity impact loading of two transverse charge automotive seatbacks

(i) T2, 2mm crosshead displacement

(ii) T10, 2 mm crosshead displacement

(iii) T2, 6 mm crosshead displacement

(iv) T10, 6 mm crosshead displacement

(v) T2, 10 mm crosshead displacement

(vi) T10, 10 mm crosshead displacement
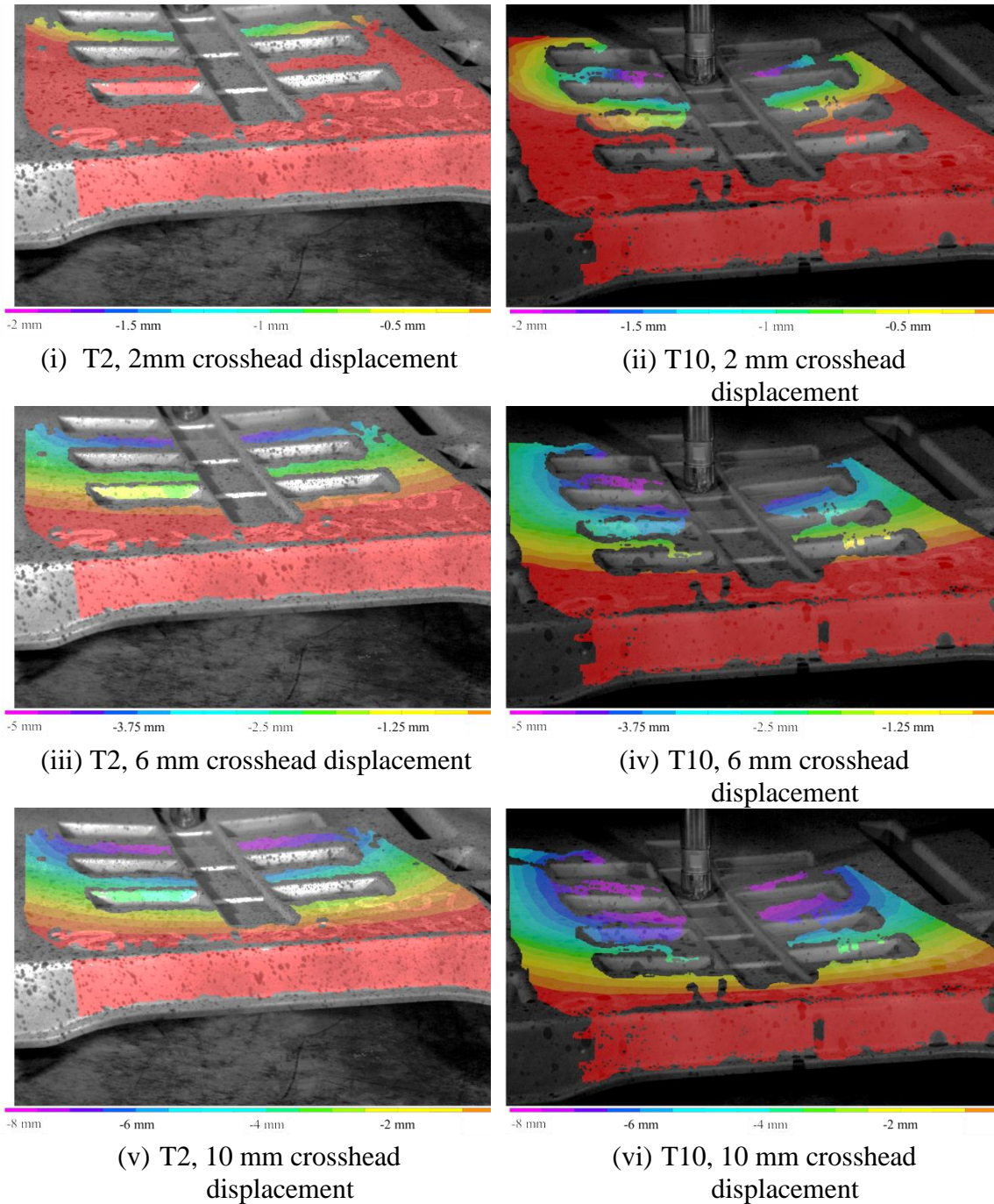
Figure 6.23: z-deflection contours for transverse charge automotive seatbacks T2 and T10, low velocity impact

Longitudinal and transverse charge seatbacks are compared in terms of force-deflection responses in Figure 6.24 and low velocity impact z-deflection contours in Figure 6.25. As noted previously, under low velocity impact longitudinal charge placement

seatbacks exhibit a peak load just prior to catastrophic failure. Transverse seatbacks have a more uniform force-deflection response. Prior to this peak load (for longitudinal seatbacks), the force-deflection responses are generally consistent (loads within approximately 25% for a given displacement) regardless of charge orientation. This increase in force with longitudinal charge placement results in an increase in energy absorption. This may be observable indirectly in terms of z-deflection contours: increased deformation across the full part (more significant away from the indenter) is observed with a longitudinal charge (approximately 3 mm, where the maximum deflection measured is approximately 12 mm). However, this increase in z-deflection away from the indenter with longitudinal charge seatbacks is asymmetric and is hypothesized to potentially be the result of part warpage and irregular contact between the seatback and the flat supporting plate of the fixture.
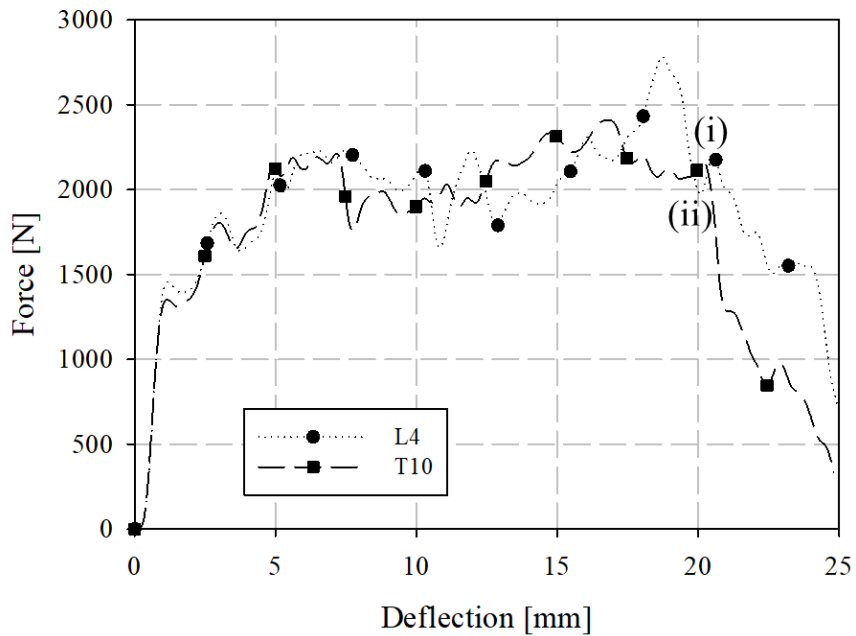
(a)
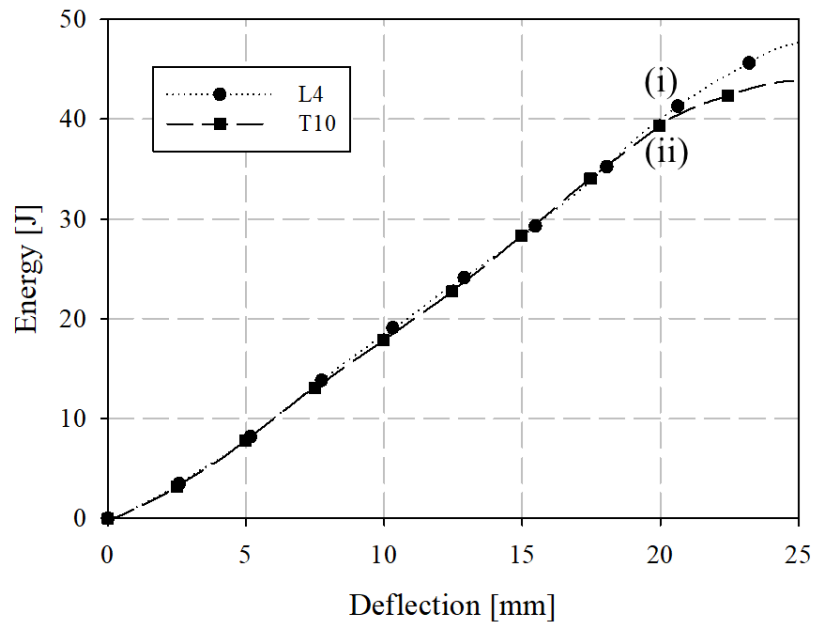
(b)

Figure 6.24: (a) Force-deflection and (b) energy-deflection response comparisons between longitudinal and transverse charge automotive seatbacks, low velocity impact

(i) L4, 20 mm crosshead displacement

(ii) T10, 20 mm crosshead displacement
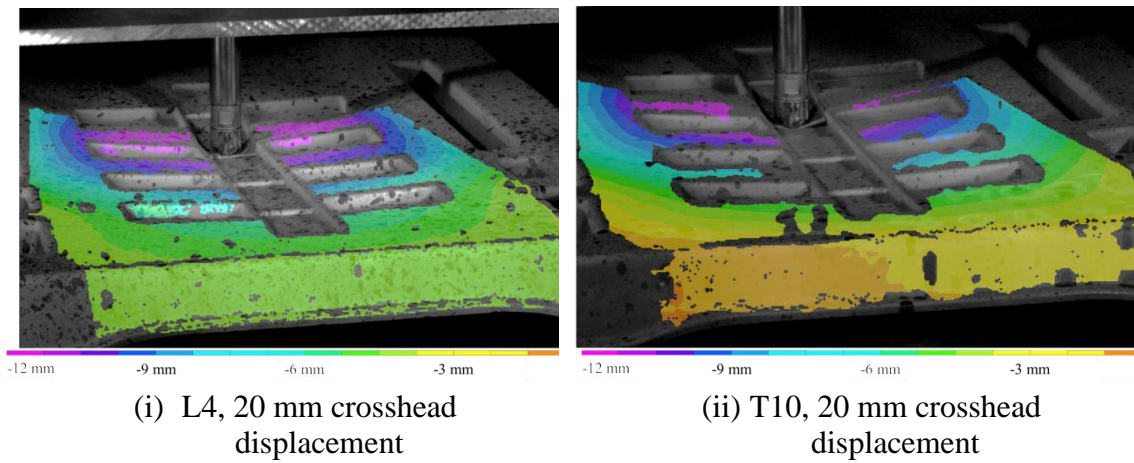
Figure 6.25: z-deflection contour comparison of longitudinal and transverse seatbacks, low velocity impact

6.3.4 Comparison of Quasi-Static and Low Velocity Impact Loading

A comparison of all longitudinal and transverse seatbacks at both quasi-static and low velocity loading rates is presented in terms of mechanical puncture parameters in Table 6.8. Initial stiffness increases from approximately 200 N/mm to approximately 1300 N/mm with no significant dependence on charge orientation. Catastrophic failure occurs much earlier in the domain for quasi-static loading (approximately 18 mm deflection), compared to approximately 25 mm for impact. This difference in behaviour at catastrophic failure is opposite to that observed in a previous study of PA6/carbon fibre (with lower fibre content ranging from 9% to 25% by weight) [14]. However, earlier onset of fracture/failure initialization under impact (approximately 1 mm for impact, 11 mm for quasi-static loading) was observed consistent to [14].

Table 6.8: Summary of quasi-static and impact mechanical puncture characteristics

	Stiffness [N/mm]	Maximum Force [N]	Deflection at Maximum Force [mm]	Energy [J]	Deflection Fracture Onset [mm]	Deflection Catastrophic Failure [mm]
Longitudinal Quasi-Static	196 (14.0%)	2419 (8.4%)	16.9 (16.7%)	30.4 (22.4%)	10.9 (6.4%)	19.3 (16.1%)
Longitudinal Impact	1267 (7.9%)	2634 (7.5%)	18.4 (14.2%)	45.9 (5.8%)	1.2 (3.7%)	26.7 (12.3%)
Transverse Quasi-Static	210 (3.1%)	2366 (7.1%)	12.7 (15.8%)	27.2 (13.0%)	11.1 (10.6%)	17.4 (9.6%)
Transverse Impact	1375 (1.8%)	2382 (5.8%)	17.1 (19.3%)	41.5 (9.2%)	1.2 (1.6%)	23.6 (3.8%)

Quasi-static and low-velocity impact loading of longitudinal charge seatbacks are compared in terms of force-deflection and energy-deflection in Figure 6.26 and z-deflection contours in Figure 6.27. In terms of force-deflection and energy-deflection, evidence of significant strain rate sensitivity of this material and/or inertial effects is observed prior to the onset of failure. Since these two particular seatbacks were previously examined in terms of z-deflection over a 2 mm to 10 mm range, this quasi-static to impact analysis focused on smaller deflections (1-5 mm) where the majority of the part is undergoing elastic deformation or the very onset of localized failure. Deformation, in terms of z-deflection, is much more localized for impact loading which may be associated with

the inertial forces. For impact loading no deformation away from the indenter was observed initially. In comparison, for quasi-static loading deflections as large as 0.25 mm are observed well away from the indenter (where localized deformation near the indenter is approximately 1 mm for both quasi-static and impact loading). As deflection increases, this localization is reduced until the responses are nearly identical (less than 0.5 mm deflection difference with a maximum deflection measurement near the indenter of 4 mm).

(a)
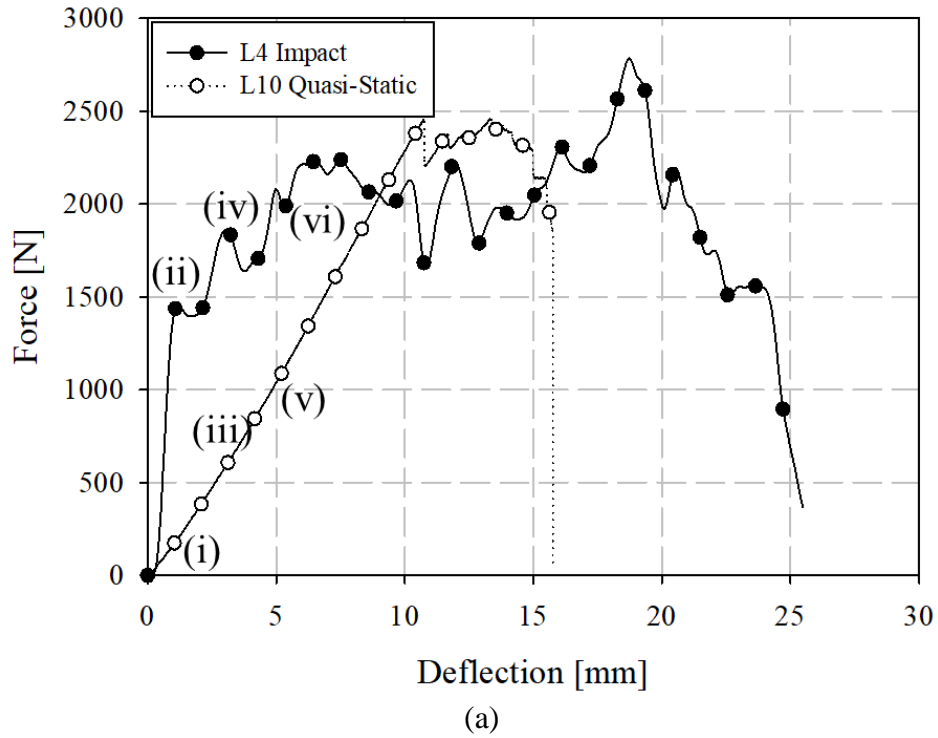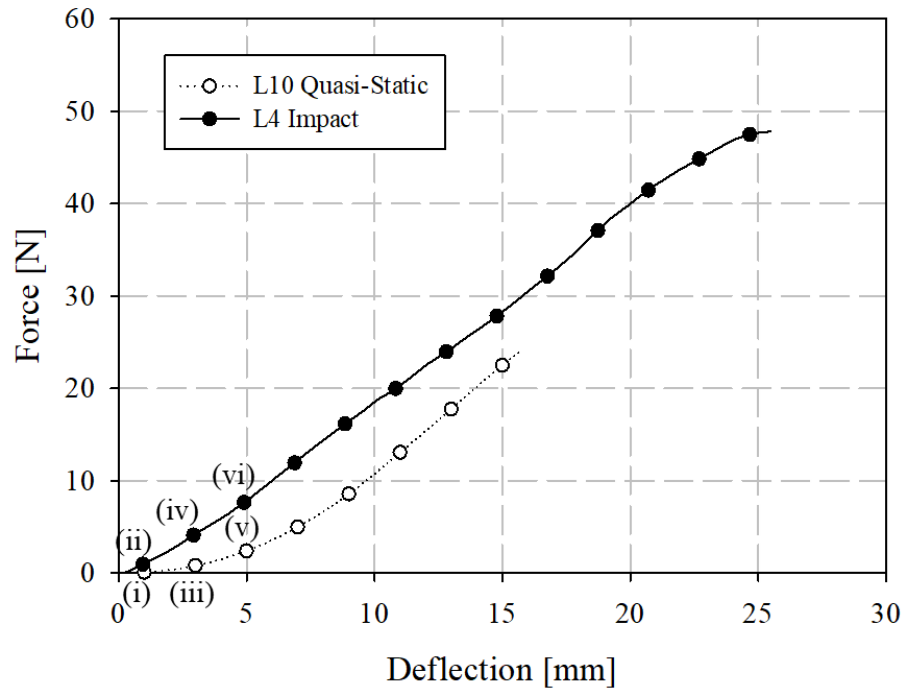
(b)

Figure 6.26: Quasi-static and low velocity impact loading comparison for longitudinal charge automotive seatbacks: (a) force-deflection and (b) energy-deflection

(i) L10, 1 mm crosshead displacement

(ii) L4, 1 mm crosshead displacement

(iii) L10, 3 mm crosshead displacement

(iv) L4, 3 mm crosshead displacement

(v) L10, 5 mm crosshead displacement

(vi) L4 5 mm crosshead displacement
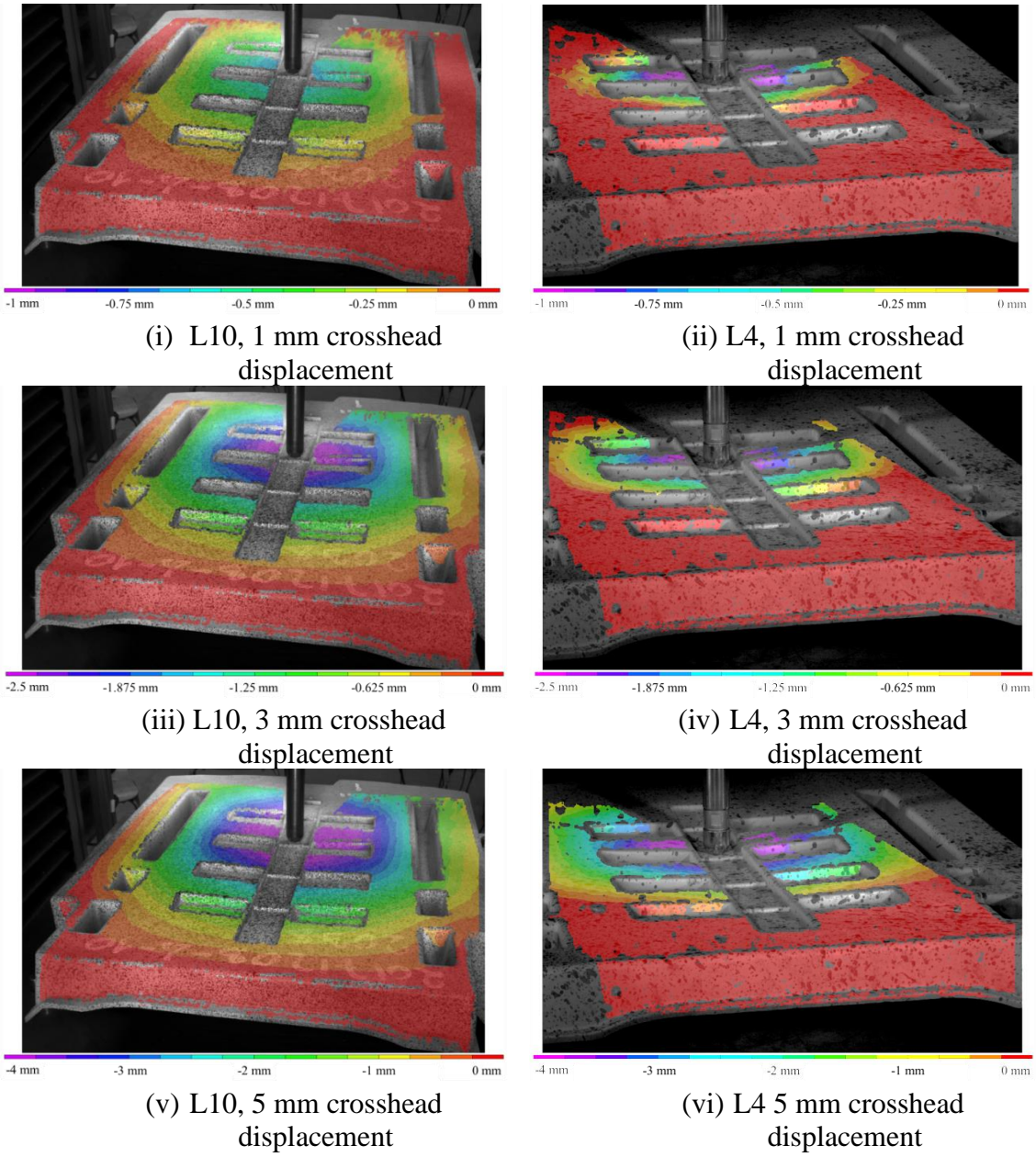
Figure 6.27: Quasi-static (L10) and low velocity (L4) impact loading comparison for longitudinal charge automotive seatbacks: z-deflection contours

Quasi-static and low-velocity impact loading of transverse charge seatbacks are compared in terms of force-deflection and energy-deflection in Figure 6.28 and z-deflection contours in Figure 6.29. In terms of force-deflection, the general findings are unchanged from comparing two longitudinal charge components. The onset of failure occurs at a reduced deflection under impact loading; catastrophic failure occurs at an increased deflection. In terms of energy-deflection, once failure has initiated the rate of energy absorption is very similar regardless of loading rate. The representative specimen selected here for quasi-static loading is unique in terms of force-deflection and energy deflection response approaching catastrophic failure. However, the brittle nature of this material is associated with poor consistency between specimens at the upper end of the deflection range. Specimen selection was limited by the small number of specimens and apparatus configuration to these two specimens to allow for comparisons of the most complete deflection contours. In terms of z-deflection, within the vicinity of the indenter, the contours are similar. Away from the indenter a greater level of deformation is observed under quasi-static loading, possibly as high as 50% (0.5 mm difference in deflection where the maximum deflection is 1 mm, at the indenter).

(a)

174
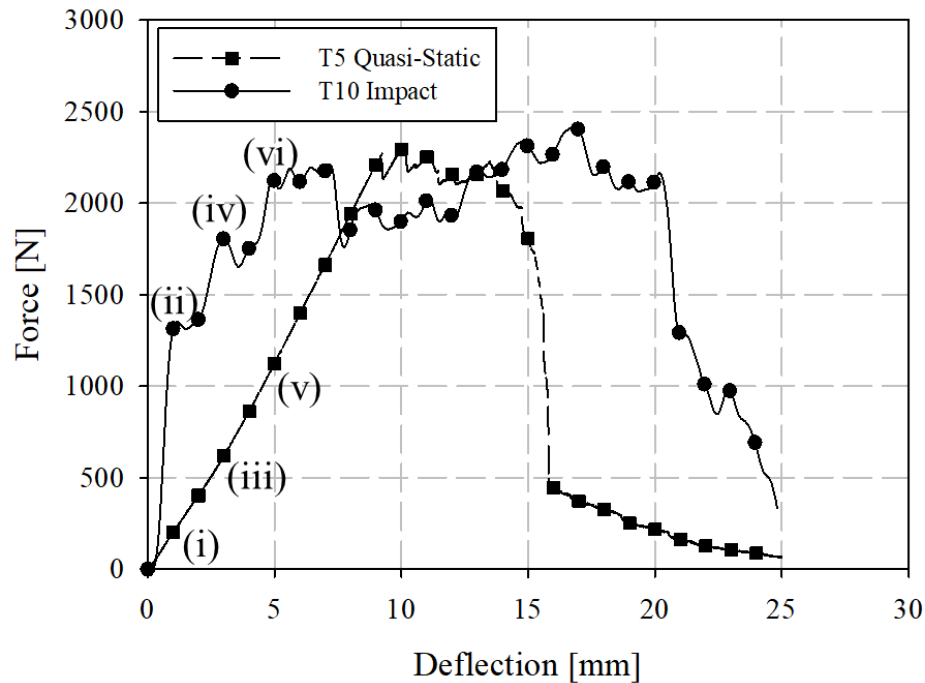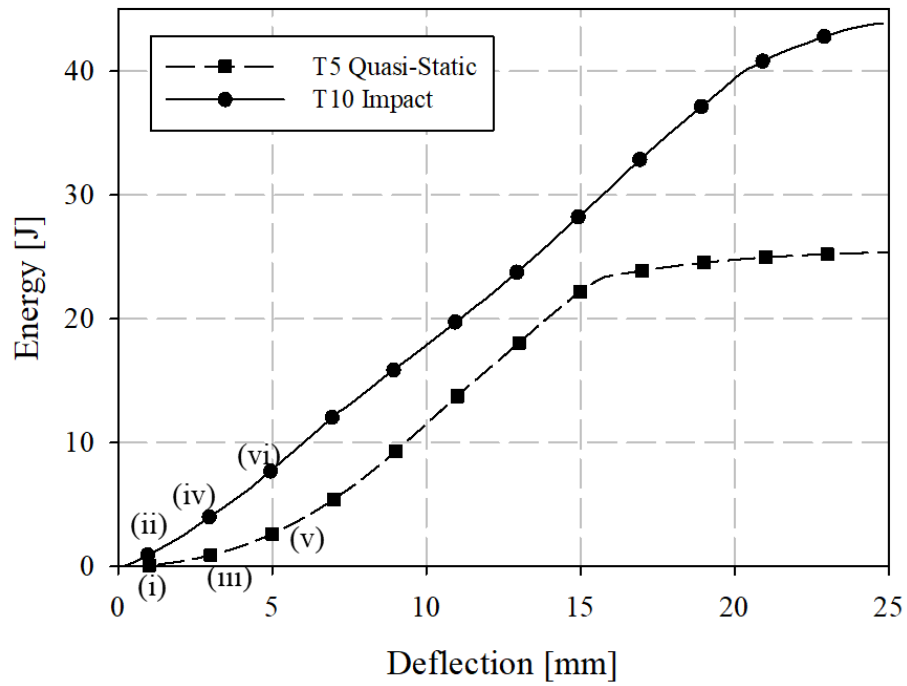
(b)

Figure 6.28: Quasi-static and low velocity impact loading comparison for transverse charge automotive seatbacks: (a) force-deflection and (b) energy-deflection
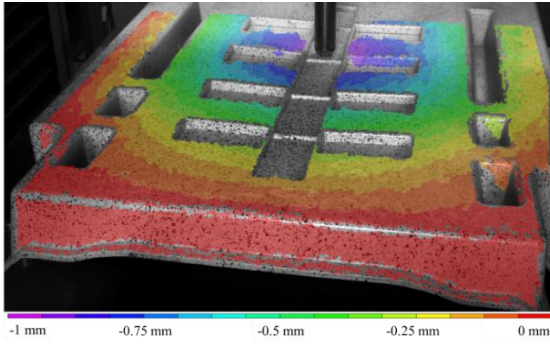
(i) T5, 1 mm crosshead displacement
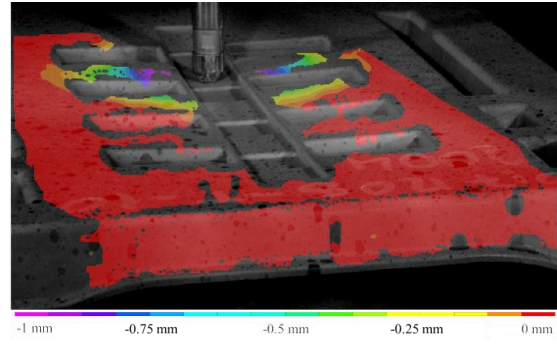
(ii) T10, 1 mm crosshead displacement
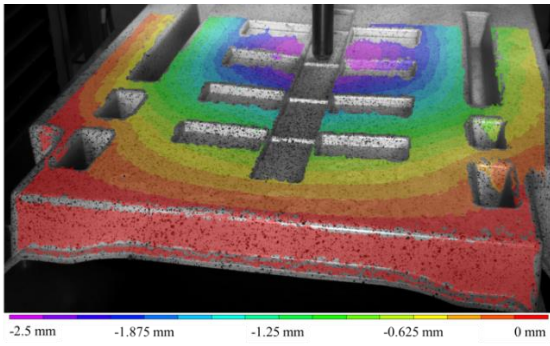
(iii) T5, 3 mm crosshead displacement
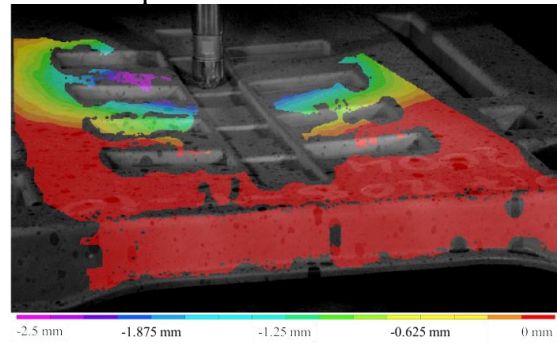
(iv) T10, 3 mm crosshead displacement
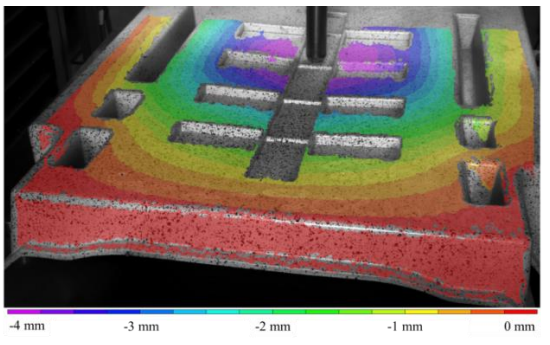
(v) T5, 5 mm crosshead displacement
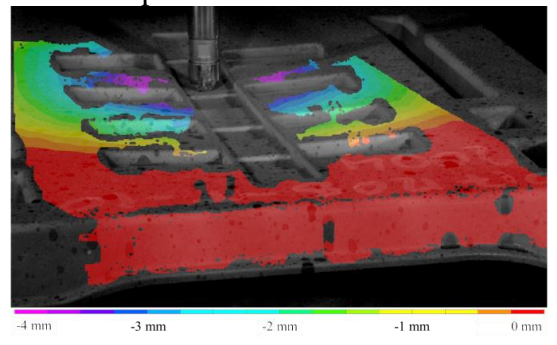
(vi) T10, 5 mm crosshead displacement

Figure 6.29: Quasi-static (T5) and low velocity impact (T10) loading comparison for transverse charge automotive seatbacks: z-deflection contours

6.4 Conclusions

An automotive seatback was compression molded from carbon fibre/PA66 direct/inline compounded long fibre thermoplastic. Fundamental material characterization (tensile tests) and component level testing, at quasi-static and elevated loading rates, was completed. The findings are as follows:

1. Tensile specimens extracted from molded seatbacks did not allow for a rigorous identification of charge and flow regions. Even with the assumed charge region, distinct and repeatable mechanical properties were observed for some specimen groups. This is particularly interesting given the random/anisotropic/ inhomogeneous nature of a compression molding charge. Flow induced orientation would result in significant anisotropy which was not observed for the top of the part.

2. Charge region tensile specimens from both longitudinal and transverse seatbacks exhibited significant scatter and were not clearly identifiable as distinct populations either in terms of local part direction or charge placement position/orientation. Only for the flow region of longitudinal seatbacks do the elastic modulus measurements differ by direction (0-degree: 9.79 GPa, 90-degree: 21.6 GPa) with sufficiently low coefficients of variation (15.6% and 23%, respectively) to indicate that these may not be measurements from the same population.

3. No significant difference was observed between longitudinal and transverse charge placements for quasi-static loading with a hemispherical indenter in terms of force-deflection, energy deflection, and z-deflection contours with a hemispherical indenter.

4. Under low velocity impact loading, a local force maxima was observed for seatbacks produced with a longitudinal charge orientation at deflections of approximately 15 – 20 mm. No local maxima were consistently observed for transverse charge seatbacks.

5. Peak loads for longitudinal and transverse charge seatbacks were 2634 N and 2382 N, the difference is not significant with respect to standard deviations (197 N and 138 N).

6. Strain rate sensitivity and/or inertial effects were observed in terms of force-deflection characteristics for full seatback components loaded centrally with a hemispherical indenter. Stiffness was 550% higher for low velocity impact with respect to quasi-static loading.

7. Digital image correlation identified a greater level of deformation in terms of z-deflection, particularly away from the indenter, for quasi-static loading (as high as 50%).

8. Catastrophic failure occurs much earlier in the domain for quasi-static loading (approximately 18 mm deflection), compared to approximately 25 mm for impact.

9. Fracture/failure initialization under impact occurred at a smaller deflection (approximately 1 mm for impact, 11 mm for quasi-static loading).

There are two primary contributions of this study to the understanding of direct/inline compounded carbon fibre long fibre thermoplastic. First, this study comprehensively documents the variables associated with manufacture, particularly extruder RPMs, temperatures, and compression molding press profiles. The manufacturing process, being of the direct/inline compounding LFT variant, is not particularly common in industry. Use of carbon fibre with this LFT variant is one element of this study that is absolutely unique at this time. Second, extensive data on impact loading of carbon fibre LFT materials is uncommon in the open literature. Data on a practical geometry (not simply a flat panel) is particularly difficult to find. The combination of this industry relevant manufacturing exercise with exhaustive quantification of deformation behaviour is not found elsewhere.

6.5 References

1.   ISO. 6603–2-2000 Determination of Puncture Impact Behavior of Rigid Plastics - Part 2: Instrumented Puncture.
2.   Thomason J. The influence of fibre length, diameter and concentration on the impact performance of long glass-fibre reinforced polyamide 6, 6. Composites Part A: applied science and manufacturing. 2009;40(2):114-124.
3.   Bartus S, Vaidya U. Performance of long fiber reinforced thermoplastics subjected to transverse intermediate velocity blunt object impact. Composite structures. 2005;67(3):263-277.
4.   Zhang Y JA, Guan J, Simard B. Low-speed Impact Characterization of Two Types of Fiber Reinforced Polymer Composites. 2015 Aerospace Structural Impact Dynamics International Conference; Seville, Spain2015. p. 1-25.
5.   Thattaiparthasarathy KB, Pillay S, Ning H, et al. Process simulation, design and manufacturing of a long fiber thermoplastic composite for mass transit application. Composites Part A: Applied Science and Manufacturing. 2008;39(9):1512-1521.
6.   Bartus S, Vaidya U, Ulven C. Design and development of a long fiber thermoplastic bus seat. Journal of Thermoplastic Composite Materials. 2006;19(2):131-154.
7.   J826 S. Devices for use in defining and measuring vehicle seating accommodation. Society of Automotive Engineers Warrendale, PA; 2008.
8.   Ning H, Pillay S, Thattaiparthasarathy KB, et al. Design and manufacturing of long fiber thermoplastic composite helmet insert. Composite Structures. 2017;168:792-797.
9.   Vaidya UK, Serrano JC, Villalobos A, et al. Design and analysis of a long fiber thermoplastic composite tailcone for a tank gun training round. Materials & Design. 2008;29(2):305-318.
10.   Tsai SW, Wu EM. A general theory of strength for anisotropic materials. Journal of composite materials. 1971;5(1):58-80.
11.   Rohan K, McDonough T, Ugresic V, et al. Mechanical Study of Direct Long Fiber Thermoplastic Carbon/Polyamide 6 and its Relations to Processing Parameters. University of Western Ontario/Zoltek Corporation; 2015. p. 1-24.
12.   Bondy M, Pinter P, Altenhof W. Experimental characterization and modelling of the elastic properties of direct compounded compression molded carbon fibre/polyamide 6 long fibre thermoplastic. Materials & Design. 2017;122:184-196.
13.   SAE. J211-1 Instrumentation for Impact Test—Part 1—Electronic Instrumentation. Warrendale, PA: SAE.
14.   Bondy M, Altenhof W. Low velocity impact testing of direct/inline compounded carbon fibre/polyamide-6 long fibre thermoplastic. International Journal of Impact Engineering. 2018;111:66-76.

CHAPTER 7

ELEVATED STRAIN RATE CHARACTERIZATION OF COMPRESSION

MOLDED DIRECT/IN-LINE COMPOUNDED CARBON FIBRE / POLYAMID 66

LONG FIBRE THERMOPLASTIC

7.1 Introduction

The two preceding chapters discuss characterization of carbon fibre/polyamide compression molded LFT-D under impact. In chapter 5, characterization strictly follows the ISO 6603-2 standard [1]. In chapter 6, an automotive seatback component is characterized with the ISO 6603-2 [1] hemispherical indenter. Significant rate effects are observed in these studies but the mechanism for this rate sensitivity is not comprehensively determined. In this chapter, intermediate strain rate uniaxial tension tests are completed on a novel apparatus to identify any material strain-rate sensitivity.

Carbon fibre reinforced engineering thermoplastics are increasingly considered for automotive applications [2-4], however, there are few publications in the open literature which characterize their mechanical properties. Several studies focusing on polyamide matrix/LFT composites are summarized in Table 7.1. One particularly active area of research for carbon fibre-reinforced thermoplastics is surface modification to improve interfacial strength between non-polar carbon fibre and highly polar thermoplastics; a review paper on this topic is included in the table [5].

Table 7.1: Carbon fibre reinforced thermoplastic literature review

Material	Summary	Reference
PA6/CF **(2-20%)**	Modulus and tensile strength increased with fibre content. Failure strain decreased. Glass transition temperature did not change significantly with fibre content.	[6]
PA66/CF **(20-30%)**	Short fibre and LFT materials compared with improved tensile modulus and strength with increased fibre length.	[7]
PA6/clay/CF **(10–30%)**	Nanoscale clay increased tensile/flexural strength and modulus without reducing impact strength.	[8]

Material	Summary	Reference
PA6/PP Blends 20% CF	PA6/PP blend to reduce the sensitivity of PA6 tensile strength and elastic modulus to moisture content.	[9]
PP/CF (LFT)	Increasing tensile/flexural and impact strength up to 25% fibre. Hypothesized that at higher fibre contents increasing void content degrades properties.	[10]
Various polymers/CF	Review paper on surface modification of carbon fibre for polar thermoplastic matrix materials.	[5]

High quality, comprehensive data on direct/in-line compounded carbon fibre reinforced thermoplastics are particularly scarce. This research is part of an international collaboration between Canadian and German researchers in partnership with Fraunhofer. Table 7.2 summarizes select publications on fundamental characterization of carbon fibre D-LFT material resulting from this research network. Fundamental characterization of this D-LFT material is presented in [11] including, but not limited to fibre length characterization, fibre orientation distribution characterization by µCT, elastic modulus, and tensile strength. No significant differences between materials of the same fibre content but with different process parameters were observed suggesting an insensitivity to any thermal/mechanical polymer degradation within the range of process parameters considered.

Table 7.2: Carbon-reinforced long fibre thermoplastic research by the International Composites Research Group

Material	Summary	Reference
PA6/CF (9-25%)	Fundamental mechanical characterization including elastic and flexural moduli, tensile strength, and strain to failure. µCT characterization of fibre orientation. Fibre length characterization.	[11]
PA6/CF (9-25%)	ISO 6603-2 instrumented puncture impact testing.	[12]
PA66/CF (40%)	Tension-tension (R = 0.1) stress-life fatigue characterization and SEM studies of fracture surfaces.	[13]
PA66/GF PA66/CF	TGA, DSC, and GPC characterization.	[14]

ISO 6603-2 [1] instrumented puncture tests provide evidence of a rate sensitivity in terms of stiffness and deflection at failure. Similar thermoset materials with carbon fibre reinforcement characterized with the same methodology and apparatus showed no sign of inertial effects in terms of the stiffness [15]. Carbon fibre alone has been shown to be strain rate insensitive [16] and numerous studies documented the strain rate insensitivity of many carbon fibre composites for fibre dominated properties. A few examples are discussed herein. Modulus, fracture strength, and the failure mode of unidirectional reinforcement carbon fibre reinforced polymer (epoxy) specimens were independent of strain rate (range between 10^{-4} s^{-1} to 1000 s^{-1}) [17]. Melin and Asp [18] assessed the transverse, matrix-dominated mechanical properties of carbon fibre/epoxy composites, the average modulus showed no dependence on strain rate while strain/stress to failure were found to increase slightly with strain rate. Considering only the thermoplastic matrix, polyamide 6 was characterized at strain rates between 10^{-2} and 10^3 s^{-1} [19]. Flow stress was highly sensitive to strain rate but elastic modulus did not significantly depend on strain rate.

Direct/in-line compounded PA6/CF long fibre thermoplastic was characterized under low velocity impact consistent with ISO standard 6603-2 [12]; a quasi-static variant of the ISO method was also employed to indirectly assess rate sensitivity. Flow region specimens were notably more brittle considering the force-deflection response at quasi-static loading rates. Puncture energy under low velocity impacts decreased by 18%, on average, with respect to quasi-static loading. This study prioritized energy absorption and did not compare the force-deflection responses directly between quasi-static loading and low-velocity impact. With respect to the current work, it is important to note that the matrix in [12] was PA6 versus PA66 for the current study. The carbon fibre supplier in [12] was Toho Tenax with sizing for an epoxy matrix while the current study sourced a thermoplastic sized carbon fibre from Zoltek (Panex 35-62).

A lightweight concept for an automotive seatback was evaluated under similar testing conditions to those of the current study (quasi-static and low velocity puncture consistent to ISO 6603-2) [20]. Digital image correlation (DIC) acquired the three-dimensional displacement fields for a large region spanning the impact surface and regions of the seatback supported by a stiff fixture for both quasi-static and impact loading. Force-deflection responses were compared between quasi-static and low velocity impact

loading with significant differences noted. For small deflections the force-deflection response was linear for both loading rates, but the stiffness was approximately 550% higher for specimens subjected to low velocity impacts. Digital image correlation showed deflection of the seatback to be more localized within the vicinity of the hemispherical striker for low velocity impact indicating that even though the impact speed is low [21,22], inertial effects are significant. However, a possible contribution of strain rate sensitivity of the material to the significant increase in stiffness at small deflections could not be conclusively ruled out, and thus this was one of the main driving factors for the current study.

7.1.1 Motivation

The motivation of the current study was to further develop the observations and findings of a previous study of the ISO 6603-2 [1] puncture test applied to this LFT material [12] and impact loading of an LFT automotive seatback [20] to advance the understanding of the rate sensitivity observed in these studies. One advantage of the direct compounding process is the customization of the resulting fibre reinforced thermoplastic through independent selection of many process parameters including but not limited to thermoplastic resin, carbon fibre content, and tow count/roving number. A robust understanding of the relationship between the material and its constituent components is a necessary preliminary step in optimizing the material for, in this case, applications with impact loading requirements. Therefore, a more fundamental characterization of the strain rate sensitivity of the unreinforced PA66 thermoplastic and the carbon fibre / PA66 composite was carried out under uniaxial tension.

As a precursor to this strain rate dependency, a uniaxial tension size effect study was completed at a quasi-static strain rate (10^{-5} to 10^{-4} s^{-1}). The seatback study demonstrated, with the assistance of DIC measurements, the presence of a significant inertial effect. However, it was unknown if this carries over from the seatback resting on a flat plate to the much smaller, clamped specimen of the ISO 6603-2 [1] method of impact characterization. The inertia effects observed with the automotive seatback may be highly dependent on material properties and specimen geometry. An improved understanding of these dependencies for the ISO 6603-2 [1] puncture loading methodology is a significant

contribution to the engineering community considering the novel and growing field of impact loading of composite materials.

7.2 Methodology

7.2.1 Specimen Preparation

The direct/inline compounded long fiber thermoplastic (LFT-D) specimens for this study were fabricated on a Dieffenbacher LFT-D manufacturing line at the Fraunhofer Innovation Platform for Composites Research at Western University in London, Ontario. A schematic drawing and a flowchart for this manufacturing process is provided in Figure 7.1 (a) and (b), respectively. A Motan granule dosing system (item (1) within Figure 7.1) feeds (2) a Leistritz ZSE-60HP-28D co-rotating twin screw extruder. This extruder introduces molten polymer via a waterfall die (a fully open film die) to (3) a ZSG Leistritz ZSG-75 P-17D co-rotating twin screw extruder (L/D = 17, 75 mm diameter). The carbon fibre roving feed zone (3a) was simplified to remove sharp metallic edges and include the ability to feed the carbon fiber roving directly from center pull bobbins.

Charges (approximately 160 mm by 400 by 40 mm) exited this extruder, travelled along a heated conveyor (4), and were manually placed in a Dieffenbacher DCP-U 2500/2200 press (5) fitted with a 460 mm by 460 mm flat plaque tool, the corresponding temperature set points and measurements for the flat plaque tool are given in Table 1. The press was then closed with a speed of 800 mm/s until a 30 mm offset from fully closed was achieved, followed by 80 mm/s until 5 mm from fully closed, and finally 20 mm/s to fully closed. Once fully closed, the press was held closed for 40 seconds to allow the polymer to solidify. The polymer was BASF Ultramid® A3W polyamide 66. The carbon fiber was Zoltek Panex 35-62 and the target fiber weight content was 40%. In a previous study of lower fibre content material, fibre lengths ranged from 20 to 5000 µm with an average length of approximately 300 µm [23]. Specimens were extracted by water jet cutting and dried in a vacuum oven at 100°C (measured with thermocouples on the specimens) at a vacuum of 70 kPa for one week until a steady state mass reduction of approximately 0.75% was recorded.
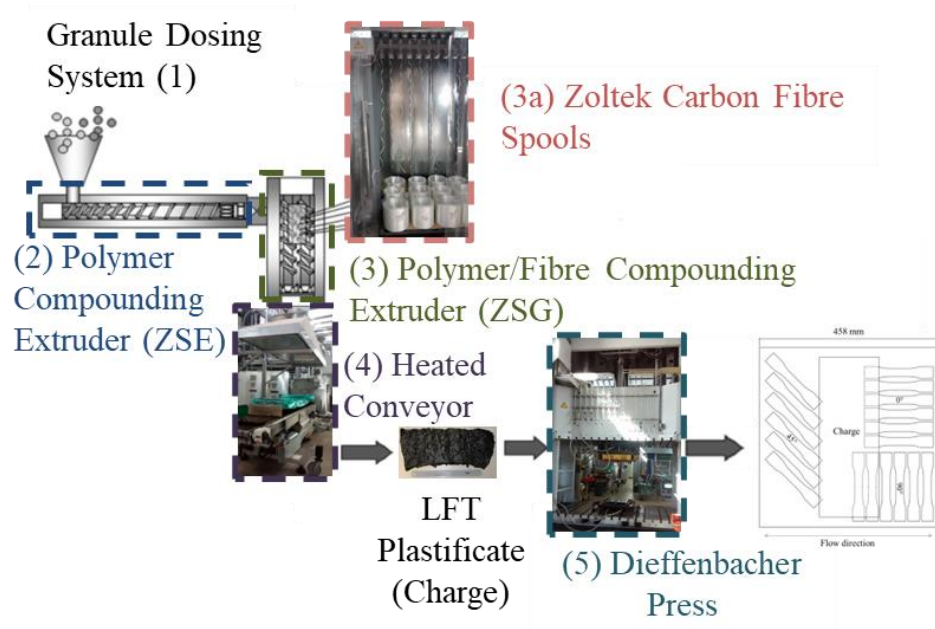
(a)
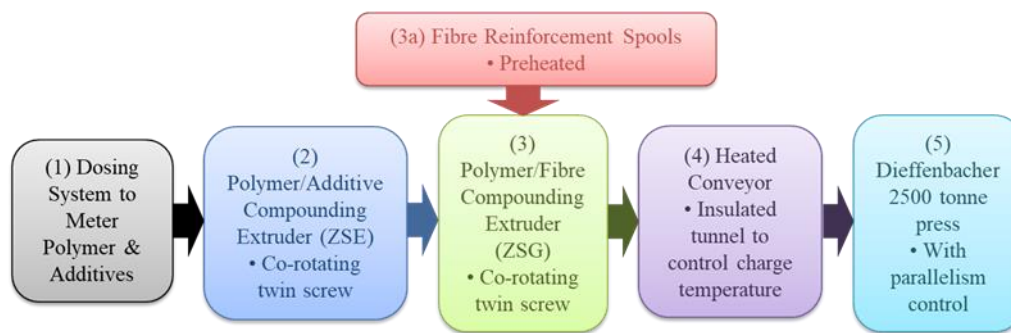
(b)

Figure 7.1: (a) Schematic and (b) Flowchart of Dieffenbacher LFT-D line at the Fraunhofer Innovation Platform for Composites Research at Western University [10]

Table 7.3: Tool temperature set points and measurements for compression molding of material for intermediate strain rate characterization

Cavity	Core	Notes
135°C	140°C	Set point at beginning of trial
110°C	112°C	Initial surface temperature readings
119°C	127°C	Surface temperature after 25 charges
120°C	126°C	Surface temperature after 50 charges
120°C	128°C	Surface temperature after 75 charges
145°C	150°C	Set point after lunch break
124°C	126°C	Initial surface temperature readings
130°C	136°C	Surface temperature after end of trials

7.2.2 Quasi-static Uniaxial Tension Characterization

Baseline quasi-static tensile tests at orientations of 0° and 90° with respect to the flow direction (see Figure 7.2), conducted at strain rates between 10^{-5} s^{-1} and 10^{-4} s^{-1}, were completed on an MTS electromechanical load frame with a 25 mm mechanical extensometer and MTS video extensometer employing a 1.3 MP Allied Vision monochrome camera. The crosshead speed was maintained at 1 mm/min, resulting in a strain rate between 10^{-5} s^{-1} and 10^{-4} s^{-1} in the gauge region. The specimen geometry was Type III from standard D638 [24]; Type III specimens possess a 19 mm gauge width and a 57 mm gauge length. Additional specimens with reduced gauge lengths were evaluated at quasi-static strain rates of 10^{-5} s^{-1} to 10^{-4} s^{-1} (note: average strain rates and coefficients of variation are given in the Results section for each specimen geometry) prior to intermediate strain rate testing to quantify the influence of specimen size on the material properties. As the gauge length and width approach the maximum fibre length, reduced gauge dimensions may capture the general response of a material with a modified fibre length distribution compared to that of a significantly larger part. Thus, a specimen size study was performed to determine whether minimizing gauge length is a feasible option to experimentally obtain higher strain rates.

SAE standard J2749 [25] provides some guidance on specimen geometry from existing ISO and ASTM standards. Grip-to-gauge transitions remained unchanged from the ASTM D638 Type III specimen; however, the gauge length was progressively reduced from 57 mm to 6.25 mm (with intermediate gauge lengths of 25.4 mm and 12.7 mm). All specimen layouts were consistent with only the gauge length reduced to preserve consistency, as shown in Figure 7.2. Quasi-static tensile testing of reduced gauge length specimens inherently limited mechanical strain measurements due to the gauge length of the extensometer. Therefore, the strain was measured optically for all specimens while the mechanical extensometer was only used for validation purposes with specimen geometries where the gauge length was greater than 25 mm.
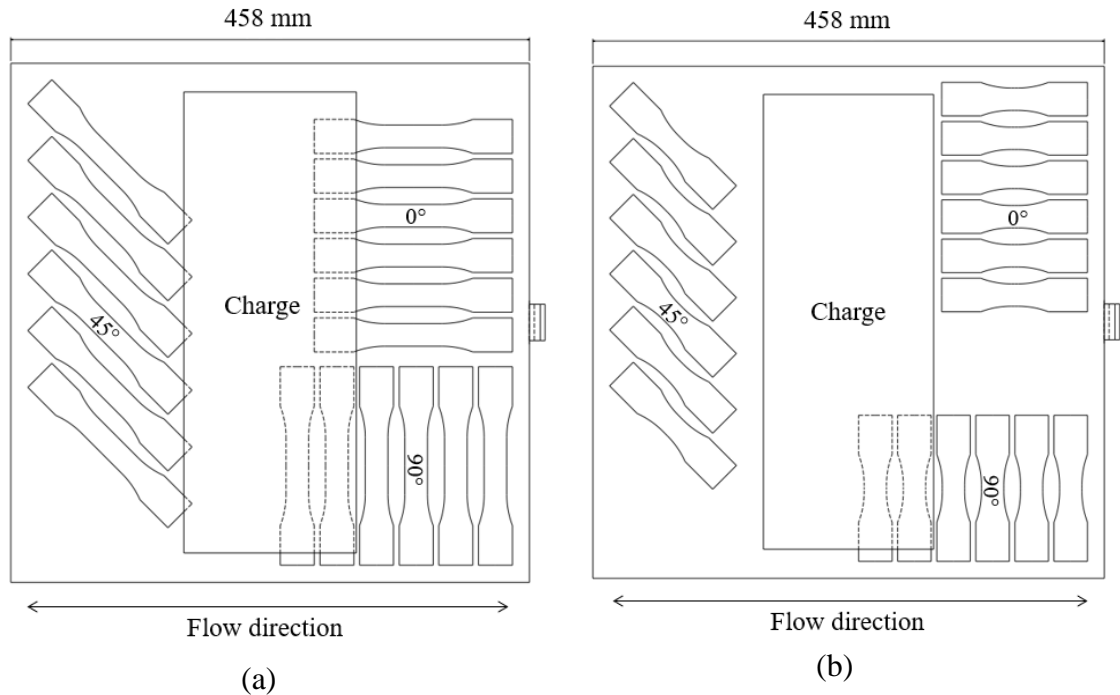
Figure 7.2: Uniaxial tension size effect specimen layout: (a) ASTM D638 Type III, (b) ASTM D638 Type III with reduced gauge length (6.25 mm shown)

7.2.3 Intermediate Strain Rate Uniaxial Tension Characterization

Elevated, intermediate strain rate (approximately 10 s^{-1} to 200 s^{-1}) tensile tests were completed on a custom designed and engineered apparatus shown in Figure 7.3 and Figure 7.4. A 101.6 mm by 101.6 mm hollow structural section (HSS) of steel tubing

formed the barrel of the impactor and connected to a pressure vessel which was utilized to accelerate an 8 kg aluminum projectile, this set of components is identified as the pneumatic accelerator in Figure 7.3. The projectile passed over an aperture in the barrel near the muzzle to disrupt the signal obtained from a laser displacement transducer for triggering of a high-speed camera and data acquisition from the load cell. The projectile impacted an assembly (Figure 7.4) with one translational degree of freedom (through constraints imposed by seven ceramic linear bearings), connected to a 7000 series aluminum grip assembly which constrained one end of a tensile specimen. The other end of the specimen was held by an identical grip assembly connected to an IEPE load cell (PCB 224C) mounted to a fixed assembly ultimately supported by a large rigid barrier fastened to a concrete floor. The grip design went through multiple iterations to minimize mass (at approximately 50 grams per grip, not including the fasteners). For the stiffer and higher strength 0-degree specimens, a small piece of vinyl rubber (approximately 10 mm by 10 mm by 10 mm) with an adhesive pre-applied on one side was attached to the surface of the apparatus impacted by the projectile to reduce vibration in the apparatus resulting from this impact.

The IEPE load cell was powered by a PCB 484B06 signal conditioner (AC coupled), allowing for high-speed data acquisition since the highest possible sampling rate for CompactDAQ modules with IEPE signals as direct inputs are otherwise limited to 102.4 kHz. The force/time data was acquired with a NI 9223 module in a CompactDAQ chassis at 1 MHz. Strain was acquired by post-processing (images (128 pixels by 64 pixels) from a Photron Fastcam SA4 high speed camera with Correlated Solutions ® VIC-2D DIC software. The camera frame rate was 225000 frames per second triggered with a transistor-to-transistor logic (TTL) signal from a National Instruments 9401 digital input/output module. A custom LabVIEW program was developed to trigger and synchronize data acquisition from the load cell/signal conditioner and trigger the acquisition of high-speed imagery from the camera when the laser displacement transducer registers the passage of the projectile over the aperture in the wall of the barrel of the pneumatic accelerator.
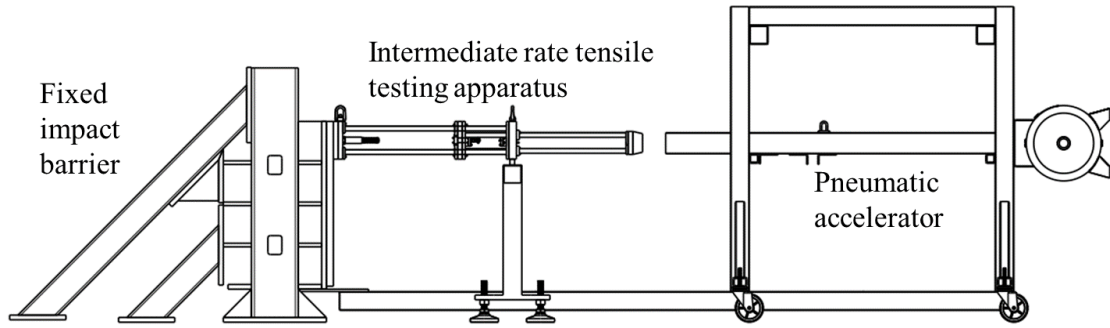
Figure 7.3: Intermediate strain rate tensile test apparatus integrated with fixed impact barrier and pneumatic accelerator
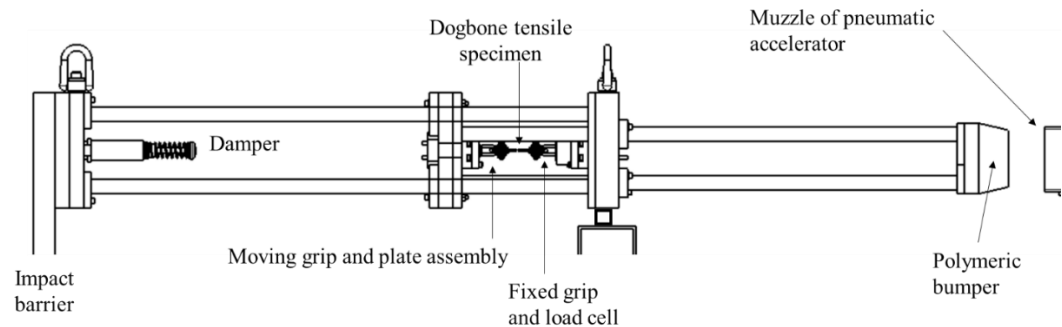
Figure 7.4: Focused view of the intermediate strain rate tensile apparatus

The tensile specimen geometry for the intermediate strain rate tests was a modified ASTM D638 [24] Type V geometry (modified to allow a fastener to pass through the gripping regions both to pin the specimen and apply a clamping load through serrated surfaces of the grip). This geometry was utilized in previous studies of similar LFT materials at quasi-static strain rates [20,23]. The gauge length was also reduced from the 9.53 mm length in ASTM D638 [24] to 5 mm to maximize the achievable strain rate. The specimen layout is shown in Figure 7.5 (a), note that material availability was limited for these intermediate strain rate tests and the available plaques did not permit every specimen shown to be extracted from each plaque. Multiple plaques were needed to extract the specimens for intermediate strain rate testing.
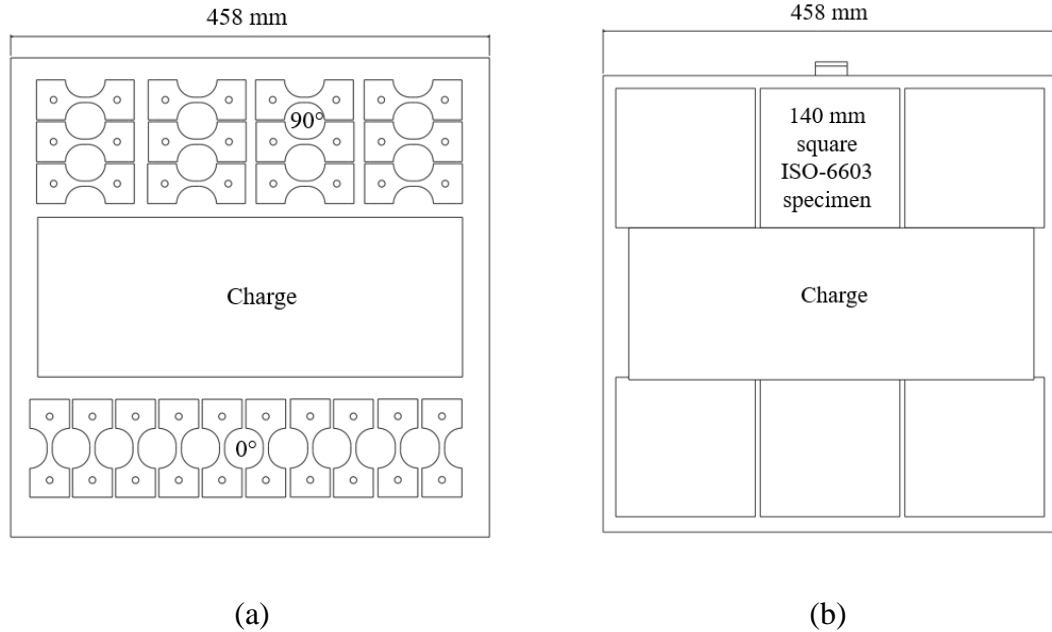
Figure 7.5: (a) Intermediate strain rate specimen layout, (b) ISO 6603 specimen layout

7.2.4 ISO 6603-2 Low Velocity Instrumented Puncture

Instrumented low-velocity puncture tests were completed consistent with ISO standard 6603-2 on a custom drop tower shown in Figure 7.6 (a); per the ISO standard, the impact velocity was 4.4 ± 0.2 m/s. The 140 mm by 140 mm specimen size (specimen layout shown in Figure 7.5 (b)) was selected following the guideline of the ISO 6603-2 standard [1] for brittle materials. Force at the 20 mm diameter hemispherical indenter was measured with a Dytran 1050V6 integrated electronics piezo-electric (IEPE) load cell connected to a National Instruments 9250 IEPE capable analog input module with a data acquisition rate of 102.4 kHz. A Photron Fastcam SA4 high speed camera observed the specimen surface opposite the indenter through a mirror at 72000 frames per second with a shutter speed of 118000 s^{-1} at a resolution of 192 pixels by 192 pixels. Camera to load cell data synchronization was implemented with a custom LabView program and a TTL signal from a National Instruments 9401 digital input/output module to the highspeed camera. A dual camera configuration to allow digital image correlation (DIC) was not attempted due to constraints imposed by the drop tower design and fixture.

190

7.2.5 Quasi-static Instrumented Puncture

Quasi-static puncture tests were completed on an electromechanical MTS load frame with a crosshead speed of 0.22 mm/s (0.005% of 4400 mm/s) as shown in Figure 7.6 (b). Displacement and strain fields on the specimen surface (100 mm diameter region inside of the clamping ring) opposite the 20 mm hemispherical indenter were acquired with a Correlated Solutions digital image correlation (DIC) system running VIC 3D software. Two Point Grey Grasshopper GRAS-50S5M cameras were triggered with a transistor-to-transistor logic (TTL) signal from the load frame to a NI USB-6221BNC data acquisition device which activated/deactivated the DIC system at the beginning/end of the prescribed crosshead displacement.

(a)   (b)
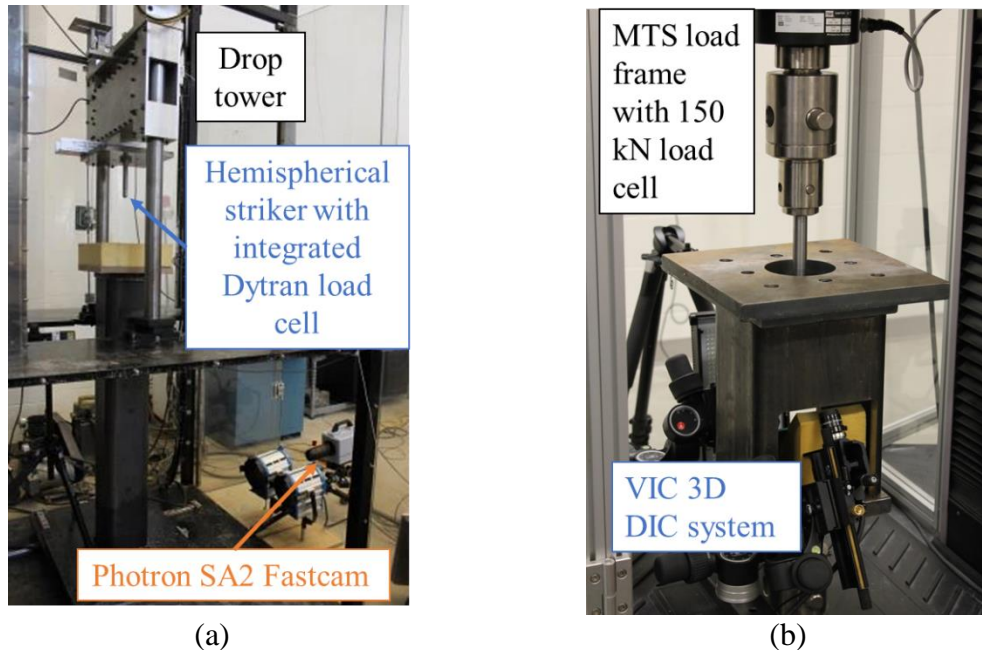
Figure 7.6: (a) Low velocity ISO 6603-2 apparatus and (b) quasi-static puncture apparatus

7.3 Results and Discussion

7.3.1 Quasi-Static Uniaxial Tensile Tests

Several specimen geometries were utilized to ensure that error was effectively mitigated for measured material properties through modified fibre length distributions. Intermediate to high rate testing inherently required a short gage section both to achieve the strain rate magnitude objective of this study and a state of dynamic stress equilibrium. An SAE draft standard recommends 10 to 15 elastic wave reflection propagations through the gage between the start of loading and yielding [26]. With LFT-D PA66/carbon fibre specimens, the wave speed (v_{ws}) in the 90-degree direction is approximately 2200 m/s. For a strain rate of 50 s^{-1} ($\dot{\varepsilon}$), a yield strain of 1% (ε_{yeld}), and a gage length of 50 mm (L_{gauge}), less than 5 stress wave reflections ($N_{reflect}$) across the gage are expected (from Equation 7.1). The only parameter which can be controlled for a desired strain rate and a given material is the gauge length, this necessitates a shorter gauge to achieve higher strain rates. The gauge length should be less than 10 mm to achieve the recommended 15 reflections and a nominal strain rate of 100 s^{-1}. Note that the presence of a grip between the load cell and specimen requires that this length be further reduced to achieve the recommended stress wave propagation condition.

$$N_{reflect} = \frac{\varepsilon_{yield} v_{ws}}{2 L_{gauge} \dot{\varepsilon}}$$
<div align="right">Equation 7.1</div>

Quasi-static engineering stress-strain responses for the 0-degree direction are provided in Figure 7.7 for ASTM D638 [24] Type III and reduced gauge length (6.25 mm) specimens. Specimens are labeled with the format XDYSZQS where X is the gauge length in mm, Y is the orientation with respect to the flow direction (0- or 90-degrees), SZ is the specimen ID (generally starting at S1), and QS indicates a quasi-static loading rate. Stress-strain responses are generally consistent for these two specimen geometries. Quasi-static engineering stress-strain responses for the 90-degree direction are shown in Figure 7.8. Less consistency between the two specimen geometries was observed with respect to the 0-degree reference direction. However, except for 57D90S1QS, 6.25D90S6QS, and 6.25D90S3QS, the responses were reasonably consistent. The 90-degree specimen layout

includes two specimens with proximity to the charge region, which may have correspondingly reduced development of flow-induced fibre orientation.
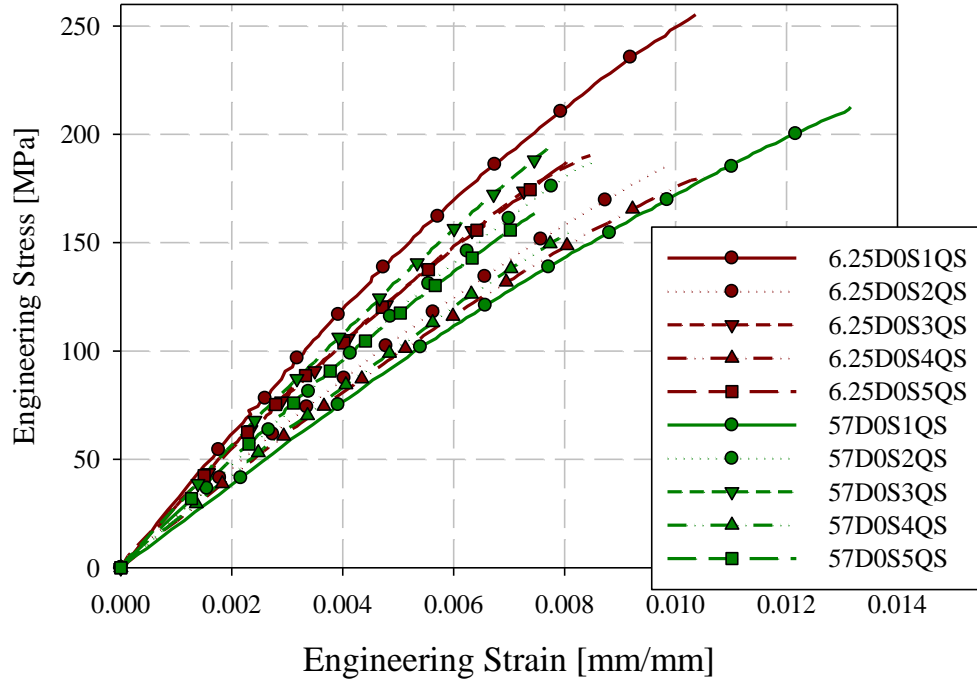
Figure 7.7: PA66/40% carbon fibre LFT-D 0-degree quasi-static engineering stress-strain responses ASTM D638 type III and reduced gauge length (6.25 mm) specimens
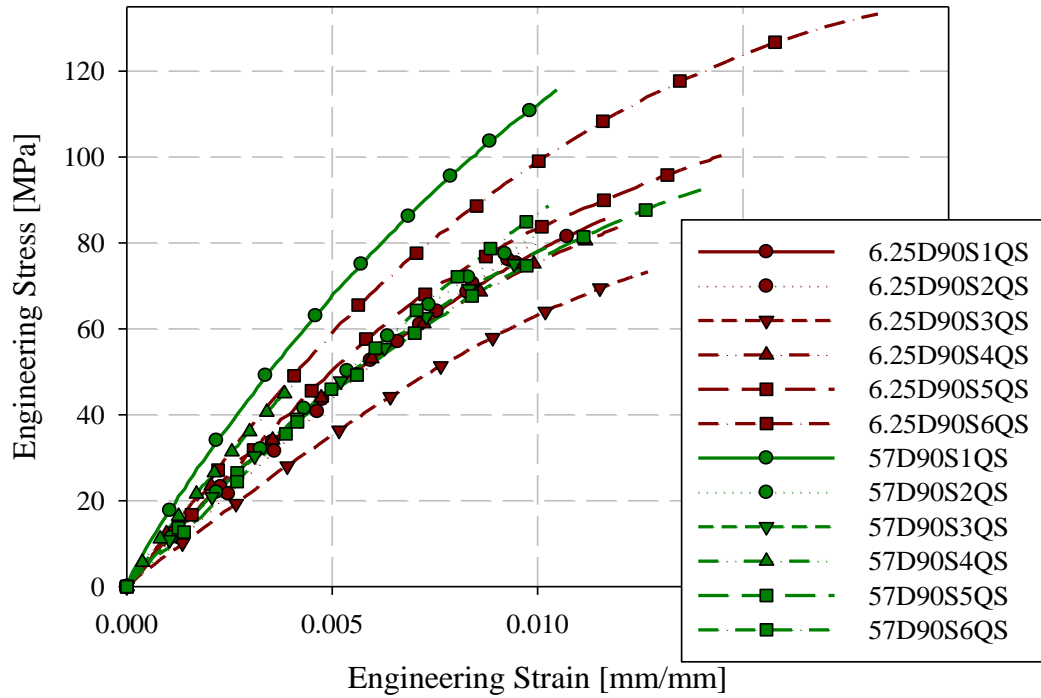
Figure 7.8: PA66/40% carbon fibre LFT-D 90-degree quasi-static engineering stress-strain responses ASTM D638 type III and reduced gauge length (6.25 mm) specimens

Summaries of quasi-static mechanical properties for all specimens are given in Table 7.4. For each mean value, the coefficient of variation (expressed in percent) is given in brackets. Considering all mechanical properties summarized in Table 7.4, no mechanical properties exhibited a high sensitivity to gauge length. Strain to failure with reduced gauge lengths may be slightly reduced with respect to the ASTM D638 [24] Type III standard specimen geometry due to the effect of testing small material volumes, which limits the probability of encountering significant structural defects [27]. However, the change in elastic modulus and tensile strength with respect to specimen size is generally lower than the variation in each mechanical property for any one specimen size, for example, the tensile strength in the 90-degree direction decreased by 0.2% for each additional millimeter of gauge length. Therefore, for the full range of gauge lengths studied (6.25 mm to 57 mm), the average tensile strength decreased by 11.1%. However, the minimum coefficient of variation for 90-degree tensile strength was 13.8% (25 mm gauge length). Failure strain measurements displayed a moderate sensitivity to gauge length. As shown in Table 7.4, the

sensitivity (percent change over the full range of gauge lengths) was generally larger than the coefficient of variation, however, the margin is not intolerably large and the scatter for some individual specimen sizes can still exceed the percent change across the full range of gauge length studied.

Table 7.4: Summary of PA66/40% carbon fibre LFT-D quasi-static uniaxial tension size effect results (coefficient of variation in parentheses)

Specimen Group	Strain Rate [s^{-1}]	Elastic Modulus [GPa]	Tensile Strength [MPa]	Engineering Strain at Failure [%]	Poisson's Ratio
6.25D0	4.9E-5 (15.1%)	24.6 (15.0%)	201.2 (15.8%)	1.34 (21.2%)	0.358 (10.7%)
12.7D0	6.6E-5 (8.5%)	24.0 (8.5%)	206.8 (6.5%)	1.06 (15.3%)	0.426 (15.4%)
25D0	6.2E-5 (20.8%)	20.6 (5.7%)	182.9 (9.4%)	1.01 (14.7%)	0.506 (17.8%)
57D0	5.8E-5 (20.2%)	23.1 (13.1%)	186.3 (12.1%)	0.90 (25.6%)	0.401 (24.7%)
0° Sensitivity to Gauge Length	2.3%	-5.8%	-9.6%	-27.5%	3.5%
6.25D90	1.6E-4 (18.5%)	9.45 (18.4%)	93.3 (23.4%)	1.33 (23.4%)	0.155 (33.9%)
12.7D90	1.3E-4 (16.2%)	9.42 (17.0%)	96.9 (13.9%)	1.34 (21.2%)	0.206 (37.6%)
25D90	1.3E-4 (16.6%)	8.34 (8.3%)	89.4 (13.8%)	1.18 (14.7%)	0.207 (34.8%)
57D90	1.0E-4 (11.5%)	10.3 (18.2%)	85.1 (25.9%)	0.99 (31.2%)	0.190 (30.3%)
90° Sensitivity to Gauge Length	-35.9%	10%	-11.1%	-29.9%	8.1%

7.3.2 Intermediate Strain Rate Uniaxial Tensile Tests

Uniaxial tension tests stress-strain results from the intermediate strain rate tension testing apparatus, obtained for the 0-degree direction, are shown in Figure 7.9. Specimens were labeled with the format D0SXIRZ where SX is the specimen ID (generally starting at S1), IR indicates an intermediate strain rate (10 s^{-1} to 200 s^{-1}), and Z is the strain rate (s^{-1}). The intermediate strain rate results skewed towards the upper limit observed for the quasi-static

response, also presented in Figure 7.9. The stress-strain responses are significantly more linear than the complementary quasi-static results which may be indicative of minimal positive strain rate sensitivity. The stress-time (obtained from load-time with the initial specimen gauge cross section) and strain-time (from DIC) were cross-plotted by fitting spline segments to the strain-time data and increasing the time domain resolution to equal that of the load-time data. The load data was not manipulated in any way; no filters or smoothing were applied when post-processing the data.
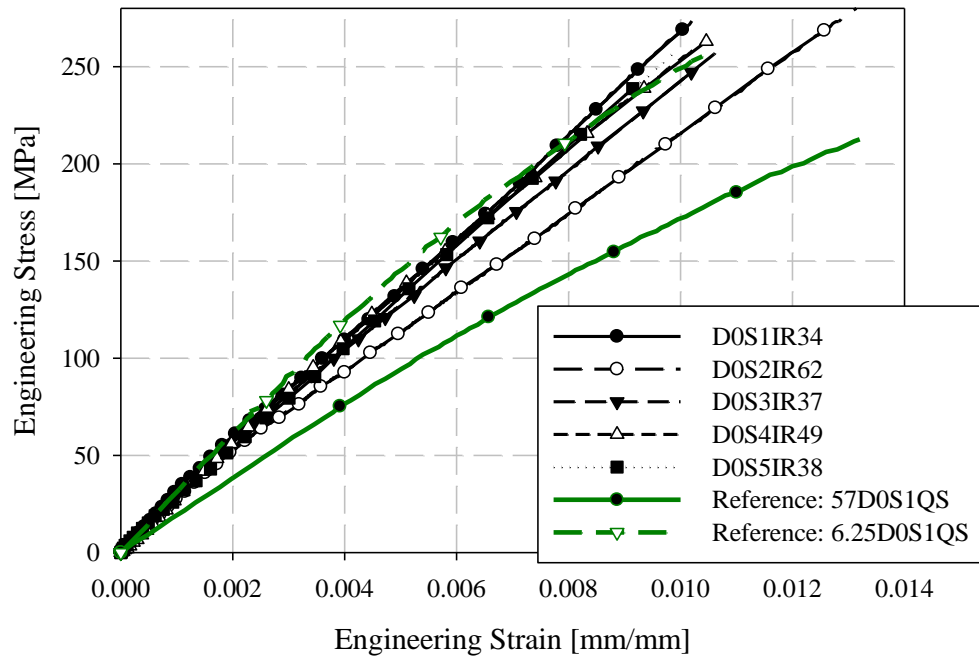
Figure 7.9: PA66/40% carbon fibre LFT-D 0-degree intermediate strain rate engineering stress-strain responses with upper and lower bound quasi-static reference responses

Intermediate strain rate results for 90-degree specimens are shown in Figure 7.10. There is a wide corridor for these results but this is consistent with previous studies [20,23]. The 90-degree direction is perpendicular to the flow direction towards which the fibre will orientate. However, depending upon the specific position of each specimen in the plaque and randomness in the fibre orientation of the charge, the small fraction of fibres reinforcing the 90-degree direction will vary significantly. These tests did not employ the vinyl rubber impact attenuator which, through pilot testing did provide a level of mechanically filtering the impact load. Only the matrix is expected to influence any

observed strain rate sensitivity due to the expected lack of rate sensitivity associated with the carbon fibre reinforcement [16]. Therefore, it may be that any positive strain rate sensitivity of the matrix in the 0-degree direction only counteracts the stiffness reduction observed at quasi-static strain rates but at 90-degrees, which will be far more sensitive to matrix properties, any positive strain rate sensitivity of the matrix is observed as a slight stiffening. Since the vinyl rubber attenuator was not used, the strain rates are higher than the 0-degree intermediate strain rate tests. This is another factor to be considered in understanding the 90-degree responses compared to the 0-degree responses in terms of stiffness.
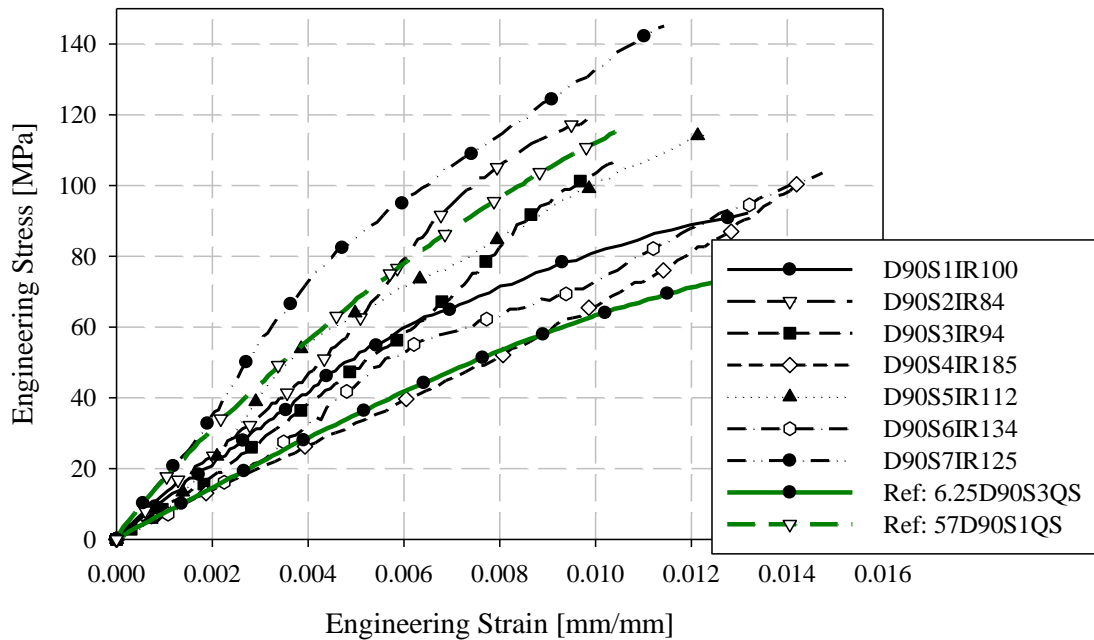
Figure 7.10: PA66/40% carbon fibre LFT-D 90-degree intermediate strain rate engineering stress-strain responses with upper and lower bound quasi-static reference responses

7.3.3 Quasi-Static Puncture Tests

Quasi-static puncture testing was conducted consistent with ISO standard 6603-2 [1], but with the velocity reduced to 0.22 mm/s or 0.005% of the ISO 6630 impact speed of 4.4 m/s. Specimens were labelled with the format ISOSXQS where X is the specimen ID (starting at 1). Force-deflection from this series of tests are shown in Figure 7.11. This

drastic reduction in loading rate allowed for the use of high-resolution cameras with the digital image correlation (DIC) system while acquiring high resolution data in the deflection domain. Table 7.5 presents the consistency in general force-deflection responses in terms of initial stiffness and peak load and the corresponding deflection at peak load. Energy-deflection responses are shown in Figure 7.12. Force-deflection and energy-deflection responses are generally consistent for all six quasi-static specimens until the onset of catastrophic failure. Energy-deflection responses up to approximately 10 mm of deflection were very consistent. Force-deflection responses, even at deflections as low as 2.5 mm, exhibit variation associated with the initiation and propagation of fracture.
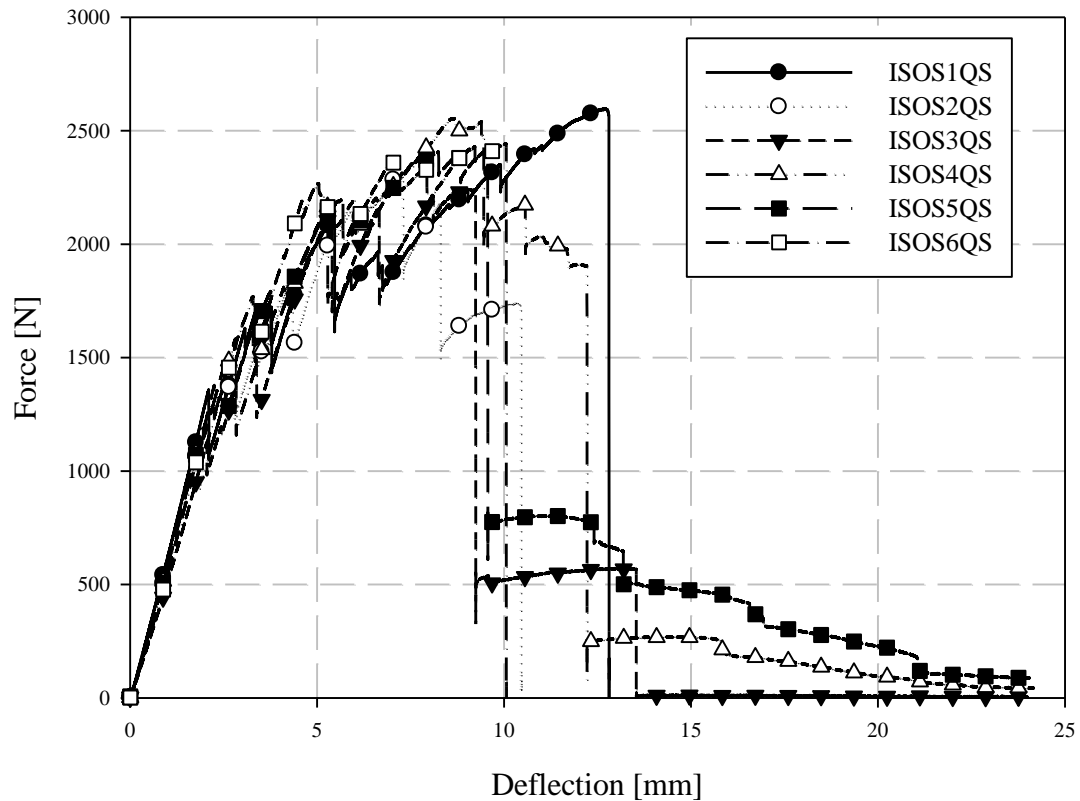
Figure 7.11 PA66/40% carbon fibre LFT-D quasi-static puncture force-deflection responses
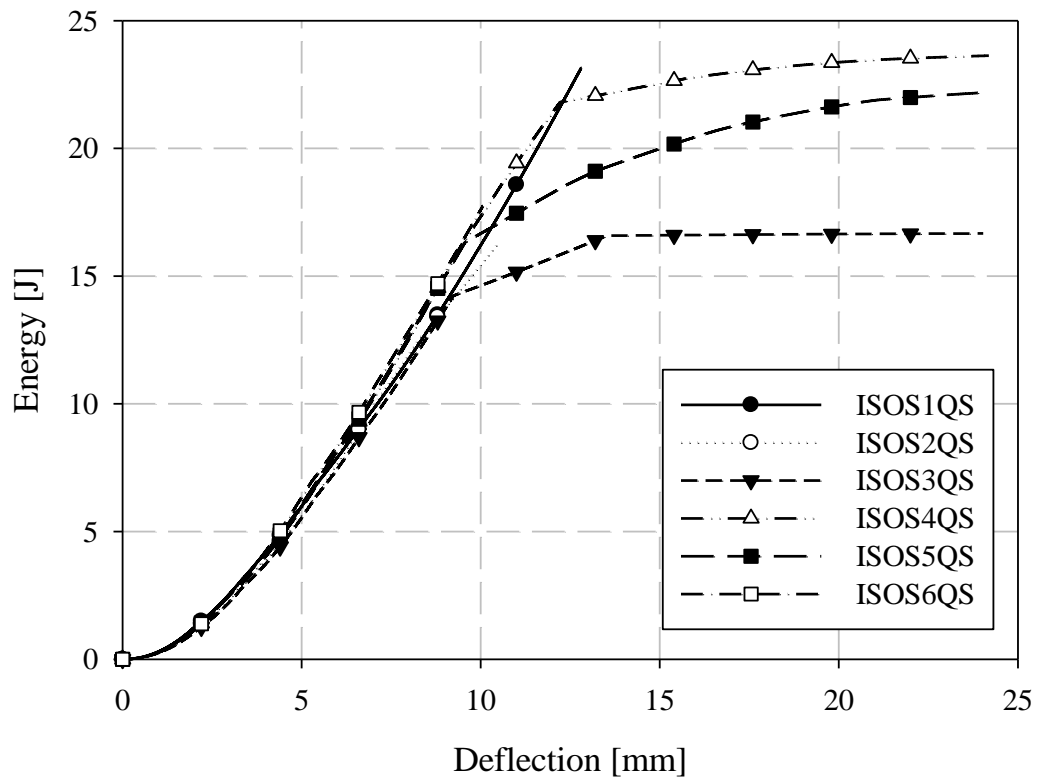
Figure 7.12: PA66/40% carbon fibre LFT-D quasi-static puncture energy-deflection responses

A tabular summary of the results of quasi-static puncture testing is presented in Table 7.5. The elastic stiffness was computed by fitting a straight line to the force-deflection response from 0 mm of deflection up to the maximum deflection at which a linear fit was appropriate. For quasi-static loading this was the deflection at which fracture initiated, which was approximately 2 mm. Energy is the total energy absorbed up to the maximum displacement in Figure 7.12 for each specimen. The deflection and first principal strain at the onset of fracture were identified from DIC images.

Table 7.5: Summary of PA66/40% carbon fibre LFT-D quasi-static puncture mechanical responses

Specimen Identifier	Elastic Stiffness [N/mm]	Maximum Force [N]	Deflection at Maximum Force [mm]	Absorbed Energy [J]	Deflection at Onset of Fracture [mm]	Principal Strain at Onset of Fracture [%]
ISOS1QS	650	2596	12.7	23.1	2.2	2.5
ISOS2QS	609	2297	7.2	16.2	2.3	2.7
ISOS3QS	550	2250	8.9	16.7	2.1	3.3
ISOS4QS	620	2554	8.7	23.6	2.4	5.7
ISOS5QS	618	2415	9.5	22.2	2.2	3.8
ISOS6QS	605	2444	10.0	17.7	2.4	3.4
Average	609 N/mm	2426 N	9.5 mm	19.9 J	2.3 mm	3.6%
Coefficient of variation	5.4%	5.6%	19.3%	17.1%	5.3%	32.2%

A single DIC image of the contours of the first principal engineering strain immediately prior to the onset of fracture for quasi-static puncture of specimen ISOS1QS is shown in Figure 7.13. The maximum principal engineering strain under loading with a hemispherical indenter was higher than observed for uniaxial tensile tests, being an average of 3.6% for quasi-static puncture versus 1.1% for uniaxial tension tests. The specimen underwent biaxial tension and bending when subjected to puncture loading at the midspan. However, another key difference between these tests is the source of this strain data. The engineering strain at failure for quasi-static puncture is a localized measurement of peak strain while the strain at failure for uniaxial tension is distributed over the gauge region within the contact areas of the clips of the extensometer. To better understand the difference between maximum local engineering strain and the average engineering strain over a large region, two dimensional DIC was employed to obtain localized maximum strain for select tensile tests. Tensile specimen failure was observed to occur outside the small region of the gauge in most tensile tests, for which images were collected for DIC. For specimens where failure occurred in the region analyzed with DIC, the maximum strain was similar to the extensometer value being within 0.1% strain.
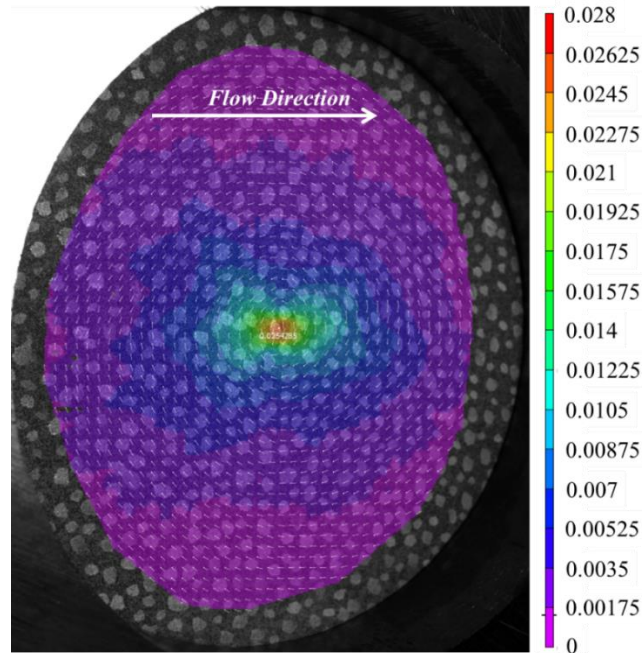
Figure 7.13: 1st principal (engineering) strain from DIC for PA66/40% carbon fibre LFT-D quasi-static specimen #1

7.3.4 Low Velocity ISO 6603-2 Puncture Tests

Low-velocity ISO 6603-2 puncture specimens were labelled with the format ISOSXLV where X is the specimen ID (starting at 1). Filtered force-deflection responses for low velocity puncture testing, completed in accordance with the ISO 6603-2 standard [1], are shown in Figure 7.14 for all six specimens tested and a single force-deflection response is shown for specimen ISOS1LV in Figure 7.15 (both filtered and unfiltered). A 2-pole Butterworth filter with forward and reverse passes (effectively a 4-pole filter) with a channel frequency class (CFC) of 1000 was applied. This is the highest frequency cut-off low-pass filter specification in SAE J211 [28]. Compared to the quasi-static results, the change in force associated with initiation and propagation of fractures were not captured well in either the filtered or unfiltered responses. Energy-deflection responses are shown in Figure 7.16. In terms of energy-deflection, all six specimens show very similar responses with only some variation in the displacement to failure and the peak energy dissipated through the puncture testing.
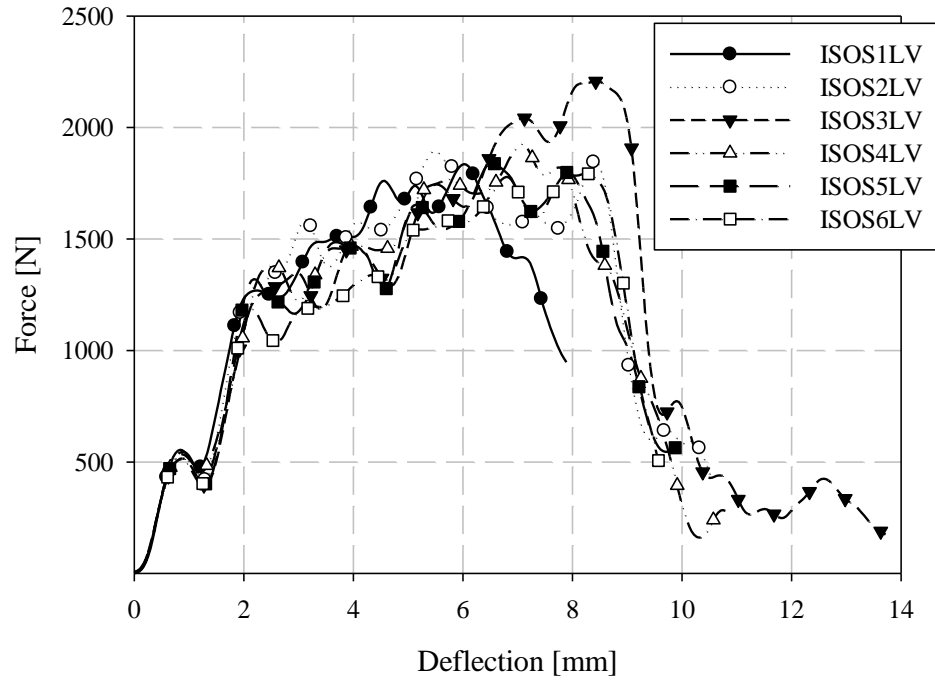
Figure 7.14: PA66/40% carbon fibre LFT-D filtered low velocity impact puncture force-deflection responses
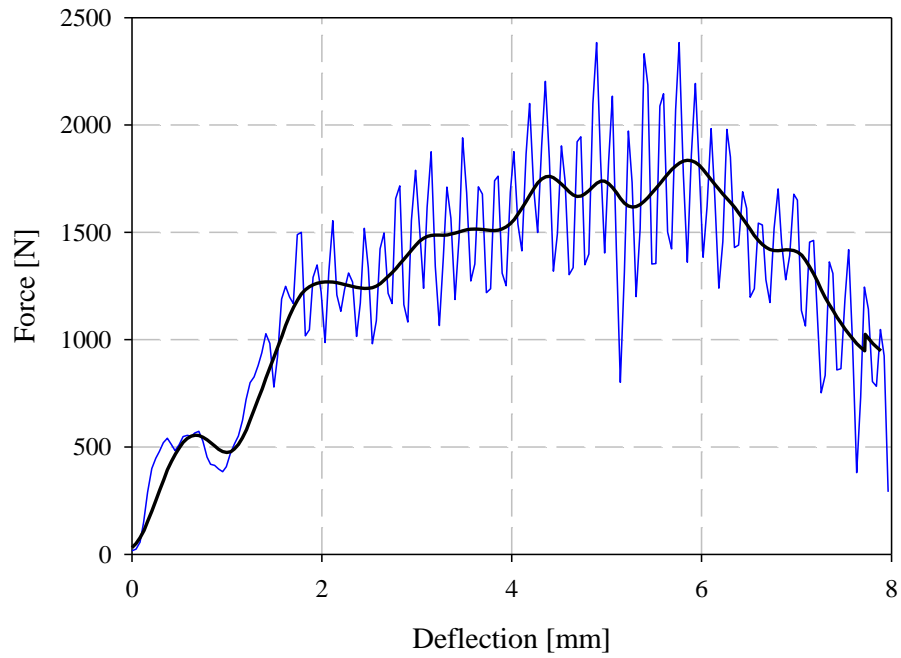
Figure 7.15: PA66/40% carbon fibre LFT-D filtered and unfiltered force deflection response for low velocity impact specimen ISOS1LV
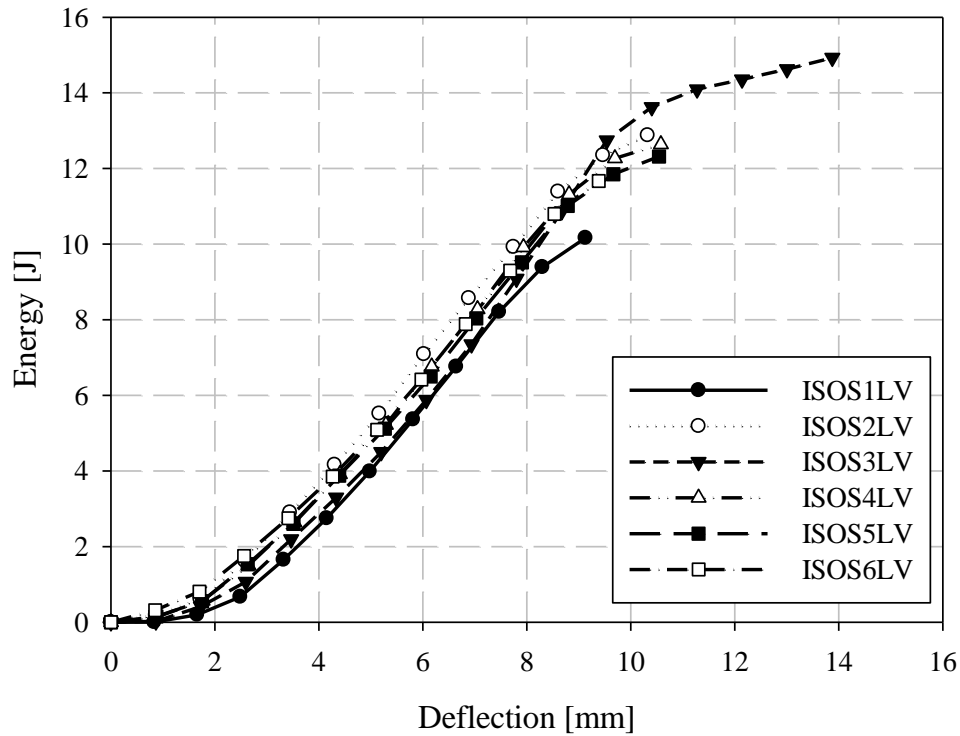
Figure 7.16: PA66/40% carbon fibre LFT-D low velocity impact puncture energy-deflection responses

A tabular summary of the results of low velocity puncture is presented in Table 7.6. The elastic stiffness was computed by fitting a straight line to the force-deflection response from 0 mm of deflection up to a deflection where a linear fit was appropriate; the deflection domain for this linear fit was approximately 0.5 mm. The maximum force and coinciding deflection were based on filtered data. Energy represents the total energy absorbed up to the maximum displacement in Figure 7.16 for each specimen. The deflection at the onset of fracture was identified from high-speed imagery, best attempts were made to assess given the camera acquisition rate and resolution.

Table 7.6: Summary of PA66/40% carbon fibre LFT-D low velocity puncture mechanical responses

Specimen Identifier	Elastic Stiffness [N/mm]	Maximum Force [N] (Filtered)	Deflection at Maximum Force [mm]	Absorbed Energy [J]	Deflection Fracture Onset [mm]
ISOS1LV	983	1836	7.3	10.2	< 0.1
ISOS2LV	963	1895	6.0	13.2	< 0.1
ISOS3LV	958	2207	9.3	15.0	0.1
ISOS4LV	967	1927	7.7	12.8	< 0.1
ISOS5LV	1016	1842	7.1	12.3	< 0.1
ISOS6LV	989	1793	8.4	11.8	< 0.1
Average	979 N/mm	1917 N	7.6 mm	12.6 J	< 0.1 mm
Coefficient of variation	2.2%	7.8%	14.9%	12.7%	-

7.3.5 ISO 6603-2 Puncture Test: Comparison of Quasi-static and Low Velocity Responses

Representative samples from quasi-static and low velocity puncture tests are compared in terms of force-deflection response in Figure 7.17 and for energy-deflection responses in Figure 7.18. At small deflections, the force-deflection responses are similar, though not identical, at the two loading rates considered. In previous ISO 6603-2 puncture tests [12] and similar tests of an automotive seating components loaded with the same hemispherical indenter [20], polyamide/carbon fibre LFT exhibited significant rate effects (due to inertial and/or strain rate phenomena) at small deflections. The material was not identical, but in the case of the automotive seatback, the matrix and fibre were from the same supplier and the compounding process was identical. Flow induced fibre orientation in the mold is the only differentiating factor between the material in the current study and the automotive

seatback study. This indicates geometric and material dependency on rate effects, and that there is little to no strain rate effect in terms of the observed elastic modulus. In terms of rate effects, this earlier onset of failure is significant. This earliest onset of failure has a significant effect on damage propagation and the ultimate failure and energy absorption due to the brittle nature of carbon fibre reinforced materials.
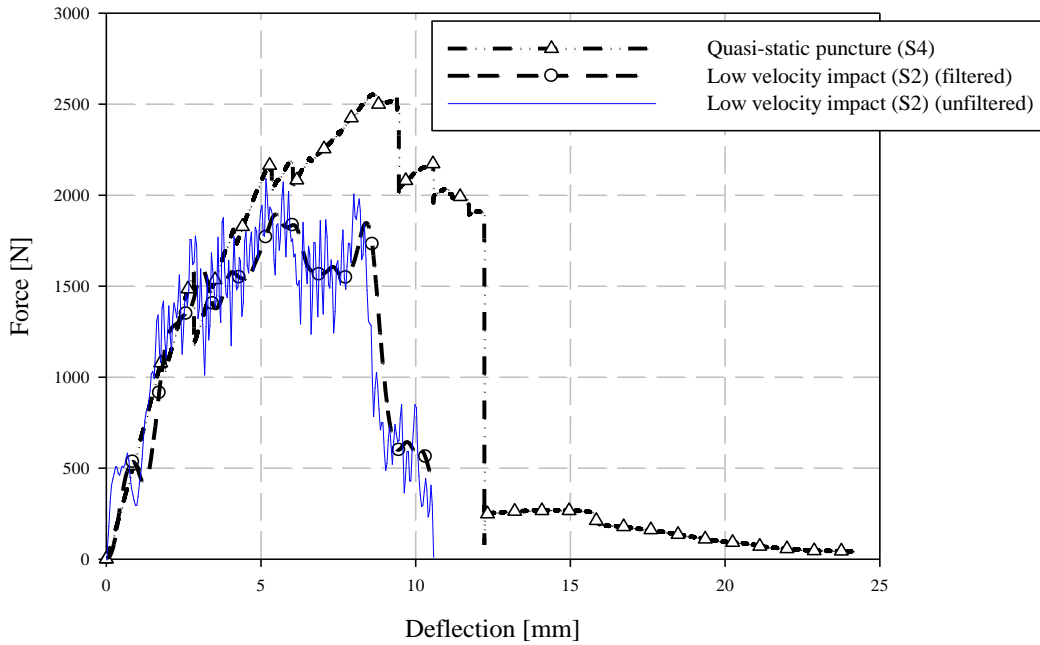
Figure 7.17: Comparison of PA66/40% carbon fibre LFT-D quasi-static and low velocity puncture force-deflection responses
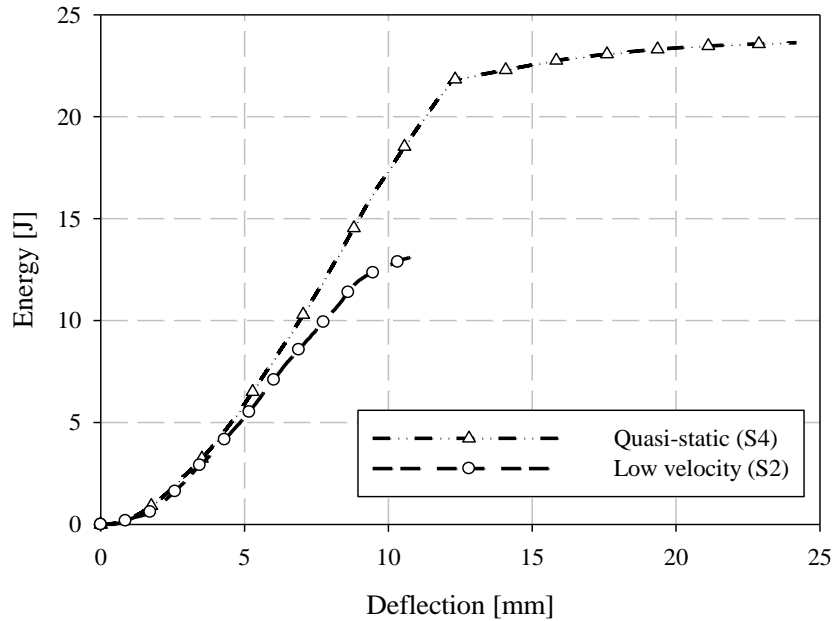
Figure 7.18: Comparison of PA66/40% carbon fibre LFT-D quasi-static and low velocity puncture energy-deflection responses

Imagery of the specimen faces opposite to the indenter is compared between loading rates in Figure 7.19. Note that the quasi-static images are not perpendicular to the face of the undeformed specimen since the images are acquired from one of the two cameras of a DIC system with an angle between the cameras sufficient to resolve out-of-plane displacements. A crack is visible at approximately 2 mm of quasi-static crosshead displacement. Under low velocity impact loading, a crack appears at a dramatically lower magnitude of deflection, that being approximately 0.1 mm. This observation may be a further indication of the dynamic nature of the ISO puncture test, particularly, there may be localized deformations with much higher strains for equal striker displacements between quasi-static and low velocity tests. The flow direction is shown on the impact test specimens with a large arrow and also applies to the neighbouring quasi-static specimen image. In both cases the crack initially forms parallel to the flow direction (approximately parallel to the nominal fibre direction). At displacements in the range of 8.5 mm to 10 mm, circumferential cracks are generally present under low velocity loading that are not visible in quasi-static tests. These circumferential cracks cause large segments of the specimen to break off which drastically reduces the load carrying capacity of the specimen. Comparing

206

data within Table 7.5 and Table 7.6, the initial stiffness was approximately 50% higher for low velocity puncture testing compared to the complementary quasi-static value. This indication of inertial effects presents challenges for understanding material behavior from this puncture test.

(i)
Quasi-static
Deflection = 0.1 mm

(i) Time = 0.023 ms
Low velocity
Deflection = 0.1 mm

(ii)
Quasi-static
Deflection = 2.4 mm

(ii) Time = 0.55 ms
Low velocity
Deflection = 2.4 mm

(iii)
Quasi-static
Deflection = 8.5 mm

(iii) Time = 1.93 ms
Low velocity
Deflection = 8.5 mm
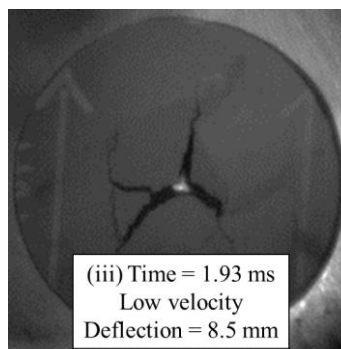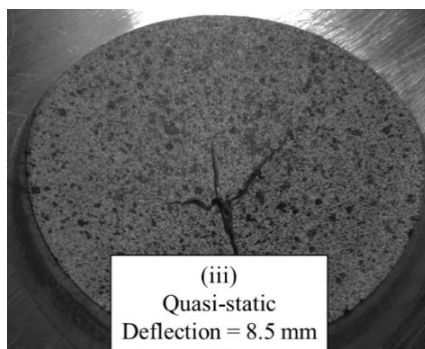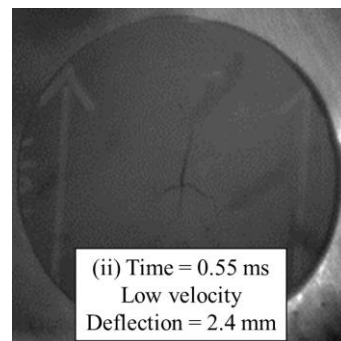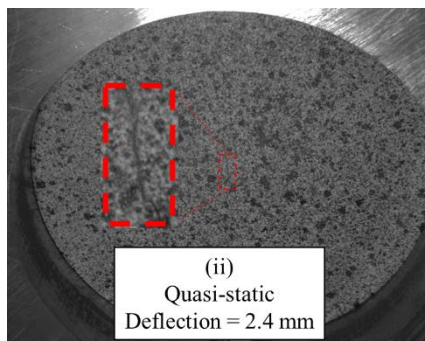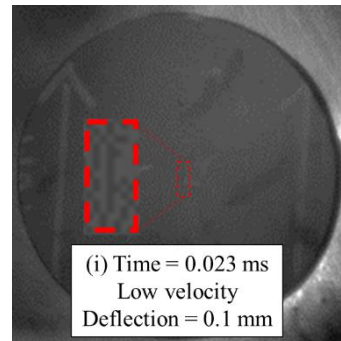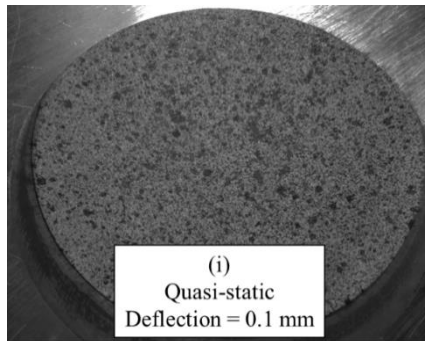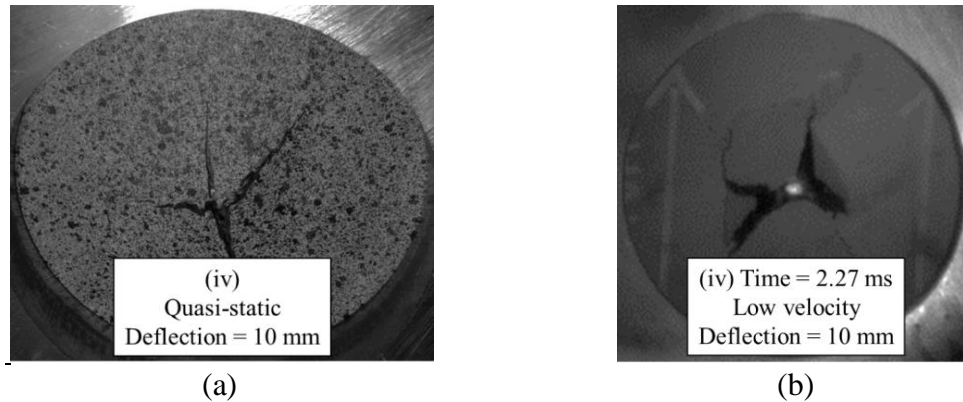
Figure 7.19: PA66/40% carbon fibre LFT-D images of specimen face opposite indenter: (a) quasi-static, (b) low velocity

7.3.6 Quasi-static and Low Velocity Impact Loading of an LFT-D Automotive Seatback

A previously published study, summarized in the introduction, documented rate sensitivity of a PA66/carbon fibre LFT-D automotive seatback subjected to similar loading with a hemispherical indenter [20]. The seatback, shown in Figure 7.20 (the seatback is dark green), was comprised of the same fibre and matrix material in unchanged proportions processed with the same extruders as the tensile and ISO puncture specimens previously discussed. However, since the fibre orientation is the result of transient material flow in the mold, due to the geometry of the seatback the fibre orientation is therefore expected to differ significantly. As previously noted, the puncture tests strictly following the ISO standard showed an average initial stiffness 50% greater than quasi-static tests. Previous work on lower carbon fibre content specimens similarly showed a significant difference between quasi-static and low velocity impact loading following the ISO 6603-2 standard [12].

This is much lower than the increased stiffness with increasing loading rate observed with the automotive seatback at 550% (Figure 7.21). Comparing the displacement fields from DIC (Figure 6.27) in conjunction with the force-deflection responses show that at displacements less than 10 mm there is a large difference in the force for a given deflection. Correspondingly, the displacement fields show that deformation is much more localized to the region around the hemispherical indenter under impact providing strong evidence of an inertia effect. When the displacement reaches approximately 10 mm, the

208

forces for quasi-static and low-velocity impact loading have nearly equalized. DIC shows that at this level of deflection there is no longer significant localization of deflection around the indenter for low velocity impact.

<div align="center">(a)   (b)</div>
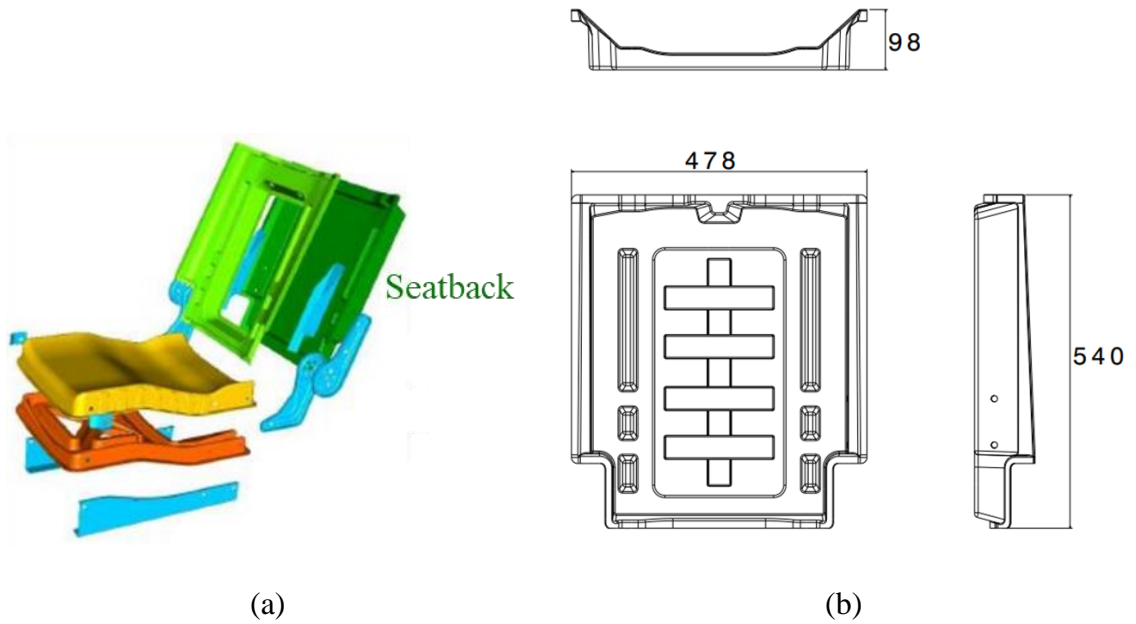
Figure 7.20: LFT-D Automotive Seatback: (a) as part of assembly, (b) overall dimensions [mm]
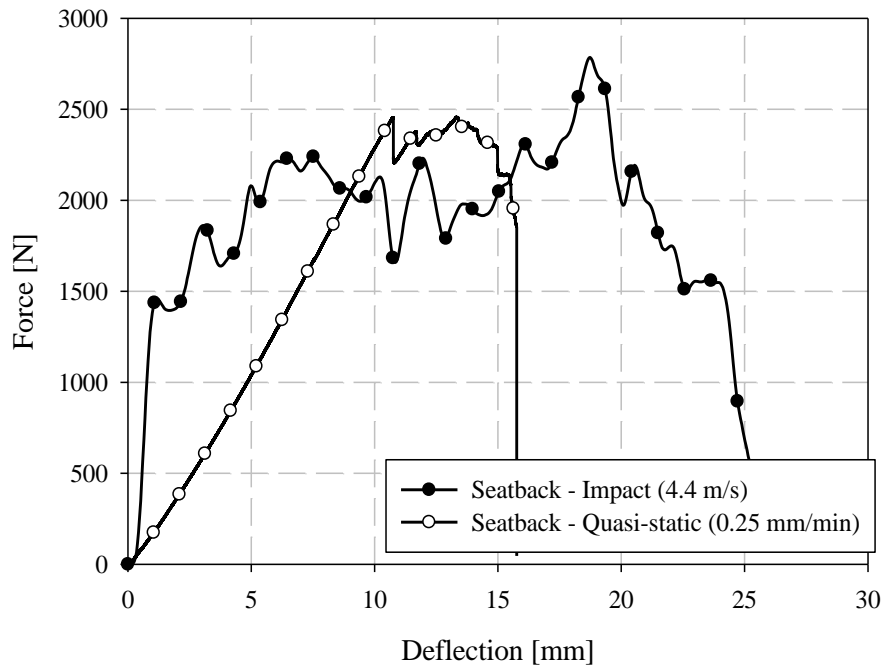
Figure 7.21: Comparison of quasi-static and low velocity impact test force-deflection responses of carbon fibre LFT seatback components.
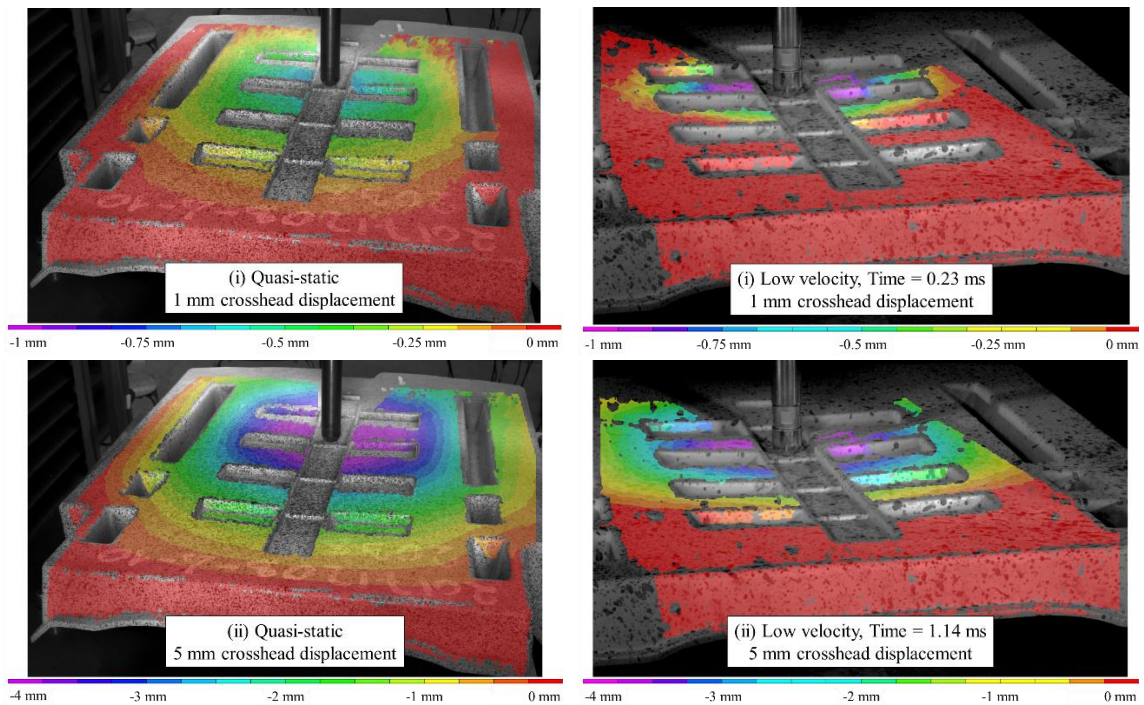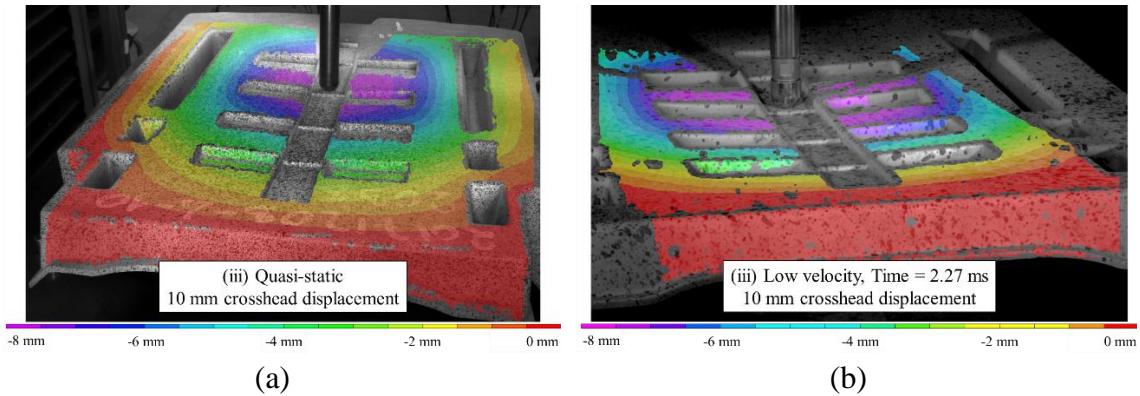
Figure 7.22: (a) Quasi-static and (b) low velocity impact loading comparison for longitudinal charge seatbacks: z-deflection contours

Considering this prior work on similar carbon fibre LFT materials and the results of the current study, the ISO puncture test should be employed with caution for brittle materials, particularly where quantifying energy absorption is a primary objective. The ISO 6603-2 standard specifically includes guidelines for testing such materials but does not include any discussion on the challenges and limitations of testing such materials for energy absorption. Energy absorption, as computed in ISO 6603-2 [1] from the indenter force and displacement, quantifies a notably different energy transfer process for ductile materials versus brittle materials. In a ductile material, the work done by the indenter has a significant component dissipated through plastic deformation. Additionally, for a ductile material the specimen is essentially stationary shortly after the indenter punctures the specimen, therefore, the specimen has no significant kinetic energy in this final state.

With a brittle material, shortly after puncture there will likely be large fragments of the specimen which are moving with velocities that are not negligible and therefore possess significant kinetic energies. The entire specimen will also vibrate after any catastrophic failure as the elastic internal energy is suddenly converted to kinetic energy. Compared to a ductile material, much less energy is absorbed by plastic deformation while more energy is absorbed through crack propagation in the brittle specimen. For a composite material consisting of a large strain to failure matrix and relatively brittle reinforcing fibre (as is the case here), the volume fraction of the matrix undergoing large plastic deformations will also be significantly lower than for an unreinforced polymer. Under impact loading, energy

absorptions of multiple materials with similar constituents (i.e., different fibre contents) may have different contributions from kinetic energy. Any such results obtained with the standard ISO puncture specimen are likely not applicable to offer guidance in the design of complex geometries, e.g., commercial products.

7.4 Conclusions

The mechanical response of compression molded direct/in-line compounded carbon fibre LFT was evaluated at quasi-static strain rates through uniaxial tension tests and puncture testing as well as at intermediate strain rates (10-100 s^{-1}) through uniaxial tension testing with a novel apparatus and ISO instrumented puncture tests. The quasi-static uniaxial tension tests included a study of specimen size effects. The key findings of this investigation are as follows:

1. Quasi-static uniaxial tension tests with 4 specimen gauge lengths ranging from 6.25 mm to 57 mm did not exhibit evidence of a significant size effect for elastic modulus or tensile strength. Failure strain was moderately sensitive to specimen gauge length. For the 0-degree direction, the failure strain decreased 27.5% across the full range of gauge length studied (coefficient of variation for 0-degree specimens: 19.2%). For the 90-degree direction, the failure strain decreased 29.9% across the full range of gauge length studied (coefficient of variation for 90-degree specimens: 22.6%).

2. Intermediate strain rate tensile tests showed little to no strain rate sensitivity for both the 0-degree and 90-directions. This is expected since carbon fibre has little to no rate sensitivity and PA66 is not highly strain rate sensitive.

3. Compared to quasi-static tensile tests, the 0-degree intermediate strain rate tests possess a more linear response compared to the decreasing stiffness (with increasing strain) of the quasi-static tests. This was indicative of a slightly positive strain rate sensitivity of the PA66 matrix since the strain rate is ramping up throughout the test, particularly for 0-degree tests where an impact attenuator was utilized to reduce the vibration of the system.

4. The 90-degree intermediate strain rate tests were characterized by a nonlinear response. This was likely caused by positive strain rate sensitivity of the PA66 matrix, to which the 90-degree tests are more sensitive. However, another factor to consider is that the 90-degree tests did not employ a vinyl rubber impact attenuator (which was present for the 0-degree tests) and thus the strain rate ramped up more rapidly and more vibration was present in the system for the apparatus used within this investigation.

213

5. Low velocity ISO 6603-2 instrumented puncture tests were completed. A quasi-static variation of this material characterization methodology was also conducted on a consistent load frame. The initial stiffness was approximately 50% higher for low velocity impact tests compared to the quasi-static tests and the displacement at the onset of fracture was much lower, approximately 95% lower, for low velocity impact tests. Correspondingly, the displacement at the peak force and the peak force were reduced for low velocity impact tests, 20% and 21%, respectively.

6. A seatback comprised of a consistent material to the current study loaded in a similar condition had a 550% increase in initial stiffness under low velocity impact conditions compared to quasi-static tests. DIC analysis revealed the deformation to be more localized to the indenter for low velocity impact tests at small displacements. The dynamic effect may also be significant well before failure of the specimen.

7. The ISO 6603-2 low velocity impact test methodology should be employed with caution for brittle materials since the kinetic energy of the specimen (and fragments thereof) as the specimen fails is large relative to the internal energy. Significant dynamic effects were present in the considered testing, additionally, this dynamic effect was highly sensitive to material properties and specimen geometry.

7.5 References

1.   ISO. 6603–2-2000 Determination of Puncture Impact Behavior of Rigid Plastics - Part 2: Instrumented Puncture.
2.   Milberg E. GMC Reveals Carbon Fiber Truck Bed in New 2019 Sierra Denali: Composites Manufacturing; 2018 [cited 2018 2018-11-21]. Available from: http://compositesmanufacturingmagazine.com/2018/03/gm-carbon-fiber-truck-bed-2019-sierra-denali/
3.   Caliendo H. Clemson developing composite vehicle front-door: Composites World; 2015 [cited 2018 2018-11-22]. Available from: https://www.compositesworld.com/news/clemson-developing-composite-vehicle-front-door-
4.   Chouinard T. SPE Automotive Plastics News: Society of Plastics Engineers; 2017 [cited 2018 2018-11-22]. Available from: http://speautomotive.com/wp-content/uploads/2017/12/SPEADNews_DecFULL_LR_12_1.pdf
5.   Alshammari BA, Alsuhybani MS, Almushaikeh AM, et al. Comprehensive review of the properties and modifications of carbon fiber-reinforced thermoplastic composites. Polymers. 2021;13(15):2474.
6.   Karsli NG, Aytac A. Tensile and thermomechanical properties of short carbon fiber reinforced polyamide 6 composites. Composites Part B: Engineering. 2013;51:270-275.
7.   Hassan A, Hornsby P, Folkes M. Structure–property relationship of injection-molded carbon fibre-reinforced polyamide 6, 6 composites: the effect of compounding routes. Polymer testing. 2003;22(2):185-189.
8.   Wu S-H, Wang F-Y, Ma C-CM, et al. Mechanical, thermal and morphological properties of glass fiber and carbon fiber reinforced polyamide-6 and polyamide-6/clay nanocomposites. Materials Letters. 2001;49(6):327-333.
9.   Do V-T, Nguyen-Tran H-D, Chun D-M. Effect of polypropylene on the mechanical properties and water absorption of carbon-fiber-reinforced-polyamide-6/polypropylene composite. Composite structures. 2016;150:240-245.
10.   Harper L, Burn D, Johnson MS, et al. Long discontinuous carbon fibre/polypropylene composites for high volume structural applications. Journal of Composite Materials. 2018;52(9):1155-1170.
11.   Bondy M, Pinter, P., Altenhof, W. Experimental Characterization and Modelling of the Elastic Properties of Direct Compounded Compression Molded Carbon Fibre/Polyamide 6 Long Fibre Thermoplastic. Submitted to Materials & Design. 2016 12/16/2016:1-25.
12.   Bondy M, Altenhof W. Low velocity impact testing of direct/inline compounded carbon fibre/polyamide-6 long fibre thermoplastic. International Journal of Impact Engineering. 2018;111:66-76.
13.   Bondy M, Rodgers W, Altenhof W. Tensile fatigue characterization of polyamide 66/carbon fiber direct/in-line compounded long fiber thermoplastic composites. Composites Part B: Engineering. 2019:106984.
14.   Yang M. Molecular Weight and Thermal Properties of Fiber Reinforced Polyamide-Based Composites Throughout the Direct Long-Fiber Reinforced Thermoplastic Process: Western; 2019.

15. Trauth A, Bondy M, Weidenmann K, et al. Mechanical properties and damage evolution of a structural sheet molding compound based on a novel two step curing resin system. Materials & Design. 2018;143:224-237.
16. Zhou Y, Wang Y, Jeelani S, et al. Experimental study on tensile behavior of carbon fiber and carbon fiber reinforced aluminum at different strain rate. Applied Composite Materials. 2007;14(1):17-31.
17. Harding J, Welsh LM. A tensile testing technique for fibre-reinforced composites at impact rates of strain. Journal of Materials Science. 1983;18(6):1810-1826.
18. Melin LG, Asp L. Effects of strain rate on transverse tension properties of a carbon/epoxy composite: studied by moiré photography. Composites Part A: Applied Science and Manufacturing. 1999;30(3):305-316.
19. Tsuda T, Hayashi H, Yamamoto T, et al. Dynamic Tensile Properties of Engineering Plastics over a Wide Range of Strain Rates. Journal of Solid Mechanics and Materials Engineering. 2012;6(6):711-720.
20. Bondy M, Altenhof W. Experimental characterisation of the mechanical properties of a carbon fibre/PA66 LFT automotive seatback under quasi-static and impact loading. International Journal of Crashworthiness. 2019:1-20.
21. Bartus S, Vaidya U. Performance of long fiber reinforced thermoplastics subjected to transverse intermediate velocity blunt object impact. Composite structures. 2005;67(3):263-277.
22. Abrate S. Impact on composite structures. Cambridge university press; 2005.
23. Bondy M, Pinter P, Altenhof W. Experimental characterization and modelling of the elastic properties of direct compounded compression molded carbon fibre/polyamide 6 long fibre thermoplastic. Materials & Design. 2017;122:184-196.
24. International A. D638. Standard Test Method for Tensile Properties of Plastics. West Conshohocken, PA: ASTM International.
25. International S. J2749 High Strain rate Tensile Testing of Polymers. SAE.
26. Xiao X. Dynamic tensile testing of plastic materials. Polymer Testing. 2008;27(2):164-178.
27. Bondy M, Rodgers W, Altenhof W. Tensile fatigue characterization of polyamide 66/carbon fiber direct/in-line compounded long fiber thermoplastic composites. Composites Part B: Engineering. 2019;173:106984.
28. SAE. J211-1 Instrumentation for Impact Test—Part 1—Electronic Instrumentation. Warrendale, PA: SAE.

CHAPTER 8

CONCLUSIONS AND FUTURE WORK

8.1 Executive Summary

The objective of this research was to comprehensively mechanically characterize carbon fibre/polyamide compression molded, direct compounded long fibre thermoplastic. A holistic approach spanned fundamental mechanical characterization to impact characterization for both standardized specimens and a complex automotive application. This mechanical characterization consisted of standard quasi-static uniaxial tension and three-point bending tests, tensile fatigue characterization (R = 0.1), ISO 6603-2 instrumented puncture impact testing [1], and intermediate strain rate uniaxial tension tests. An automotive seating component was also mechanically characterized (quasi-static loading and low velocity impact) with the ISO 6603-2 hemispherical indenter. This dissertation provides the comprehensive material characterization data set necessary to advance commercial application of direct compounded long carbon fibre thermoplastic.

For the material formulations from which quasi-static tensile and three-point bending specimens were extracted, the fibre orientation distribution was assessed by micro-computed tomography. The fibre length distribution was also characterized by an industrial partner. Mechanical characterization demonstrated a +45°/-45° asymmetry that was supported by the fibre orientation distribution measurement. This is hypothesized to be the result of the initial fibre orientation in the compression molding charge due to the pitch of the extruder screw. Combining fibre length data with the fibre orientation data as inputs to micromechanics models did not accurately predict the experimentally measured mechanical properties. The mean fibre length measured by the industrial partner was very low. Increasing the fibre length significantly improved correlation between micromechanics models and experimental data.

Fatigue characterization was completed at General Motors Warren Technical Center. Failure surfaces were studied by SEM at the University of Windsor. The stress-life fatigue properties exhibited significant variation. For specimens with poor fatigue characteristics, significant structural defects (in the form of poor fibre dispersion/wet-out) were observed at the failure surface. Optimization of the compounding process is

warranted, particularly increasing the number of rovings and reducing the tow count. Reducing the fibre content may also be necessary.

Impact characterization, in the form of low velocity impact with a hemispherical indenter, was completed as per ISO standard 6603-2. Quasi-static characterization following this methodology was also completed to assess rate effects. Additionally, an automotive seatback was similarly characterized with the ISO 6603-2 hemispherical indenter under low velocity impact and quasi-static loading. Significant rate effects were observed, particularly for the seatback where the initial stiffness increased 550% for low velocity impact with respect to quasi-static loading. Digital image correlation for both loading rates identified localization of the deformation to the seatback in the vicinity of the hemispherical indenter under low velocity impact.

A final study primarily focused on intermediate strain rate uniaxial tension testing, a novel apparatus to complete this testing, and a discussion of the ISO 6603-2 methodology. No significant strain rate sensitivity was expected or observed. This provided further evidence that the rate effects observed when loading the hemispherical indenter of the ISO 6603-2 standard are mainly due to inertia. Other carbon fibre reinforced sheet moulding compound materials show no such inertia effects. The sensitivity of this ISO material characterization methodology, in terms of inertia effects, to specimen geometry and material presents challenges for comparing similar materials or applying the findings of such testing with the standard sample to a more complex geometry of a typical engineering application.

8.2 Conclusions

The conclusions of this study of compression molded direct compounded carbon fibre/polyamide long fibre thermoplastic can be summarized as follows:

1. Fundamental material characterization consisting of uniaxial tension and three-point bending tests were completed for carbon fibre LFT-D material with fibre weight fractions between 8 and 25%. Asymmetry was observed between the +45° and -45° directions for uniaxial tension and flexure. Tensile modulus was, on average, 20% higher in the +45° direction. Tensile strength was 10% higher. Flexural modulus was 8% higher. Direct measurement of fibre orientation confirmed this asymmetry. This asymmetry of mechanical properties and microstructure is hypothesized to be the result of the initial fibre orientation in the compression molding charge. It may be a function of the pitch of the fibre compounding extruder screw.

2. Fibre length distribution measurements identified a small fraction of long (approximately 5 mm) fibers, but the average fibre length was only 300 µm. Using micromechanics models to compute elastic properties with the experimental fibre orientation and length distributions underpredicted the experimental mechanical properties. Increasing the fibre length improved this correlation suggesting that the fibre length measurements have significant bias/systemic error.

3. For fatigue specimens, the average runout stress (10^6 cycles) was 50% of the mean quasi-static tensile strength, regardless of specimen orientation. For the 0-degree direction, the average runout stress was approximately 200% higher than the runout stress for unreinforced PA66. For the 45-degree and 90-degree directions, the runout stress was 130% and 45% higher than unreinforced PA66, respectively.

4. One of the most significant findings of this investigation is the wide range of fatigue properties. Bundles of poorly wet-out fibres were found at many fracture surfaces of specimens with fatigue properties at the lower bound stress-life response. One path to improving fatigue performance is reducing the fibre weight/volume fraction. Another potential solution, which should not degrade material performance (at a higher financial cost), would be to use a larger number of rovings each with a lower

219

tow count. However, this may require significant alterations to the compounding process.

5. Assessing impact by following the ISO 6603-2 instrumented puncture impact testing standard [1] demonstrated that the onset of fracture occurred at a much small indenter displacement for low-velocity impact (2 mm indenter displacement) with respect to quasi-static loading (8 mm indenter displacement). Catastrophic failure (the formation of large fragments as circumferential cracks connect radial cracks) also occurred at smaller indenter displacements for low-velocity impact (14 mm versus 20 mm average indenter displacement).

6. Quasi-static energy absorption did not differ significantly between charge and flow region specimens loaded with a hemispherical indenter; no consistent trend for the mean energy absorption (comparing flow region versus charge region) was identified for the eight material formulations evaluated.

7. Under low-velocity impact, the average energy absorbed was consistently higher for charge region specimens compared to the flow region. However, the difference was small and may not be statistically significant.

8. For an automotive seatback component, the initial stiffness when loaded with the hemispherical indenter of ISO 6603-2 was 550% higher for low-velocity impact with respect to quasi-static loading of the seatback.

9. Comparing DIC acquired displacement fields for quasi-static and low-velocity loading with a hemispherical indenter, displacement is much more localized to the indenter for low-velocity impact indicating a significant inertial component in the previously noted stiffness increase.

10. As was observed for the characterization strictly following the ISO 6603-2 standard with a 140 mm by 140 mm specimen, fracture initiates at a much smaller displacement for hemispherical loading of the seatback under low velocity impact (1 mm indenter displacement) with respect to quasi-static loading (11 mm). This is consistent with the observation of deformation localized to the indenter from DIC. Since the displacement gradient increases, strain will be higher for low-velocity impact.

11. No significant differences in mechanical properties between seatbacks produced with longitudinal charge placement compared to transverse charge placement were observed. The difference in average peak loads was only slightly larger than the standard deviation.

12. Intermediate strain rate uniaxial tension characterization of LFT-D specimens did not identify significant strain rate sensitivity providing further evidence that the rate effects observed under loading with a hemispherical indenter (for both standard ISO specimens and the automotive seatback) are primarily inertial effects.

13. The significant inertial effects observed when loading with a hemispherical indenter are not consistent in their effect on the force-deflection response for two very different specimen geometries with common fibre/matrix and common weight fraction of fibre. Carbon fibre reinforced sheet moulding compound ISO 6603-2 specimens show no inertia effect. This variable inertia effect with dependence on material properties and geometry presents significant challenges for utilizing the ISO 6603-2 methodology for comparative studies of different materials or for applying data from ISO standard specimens to a more complex geometry of an engineering application.

Polyamide (nylon) / carbon fibre LFT-D is a potential candidate material in applications where light-weighting has sufficient economic incentives to justify the relatively high cost of carbon fibre. As shown in Chapter 4, with 40% carbon fibre (by weight) the elastic modulus of LFT-D can approach that of magnesium with a density 30% lower. Tensile strength of 40% carbon fibre LFT-D is 45% lower than SAE 1010 steel but the density is reduced 80% with 40% carbon fibre LFT-D. Carbon fibre LFT-D may also be competitive with high strength aluminum alloys. The elastic modulus of aluminum is 2.3X that of 40% carbon fibre LFT-D (0°) with a density only 2.1X that the composite. For 2024 T-4 aluminum, the tensile strength is 2.4X that of 40% carbon fibre LFT-D (0°). However, in terms of fatigue, the fatigue stress at 10^6 cycles for 2024 T4 aluminum is 95 MPa (standard deviation of 17 MPa, coefficient of variation: 18%) compared to 51/72/105 MPa (90°/45°/0°) for 40% carbon fibre LFT-D. For the 0° direction, the standard deviation is only 4 MPa (coefficient of variation 4%). Even for the 90% direction the coefficient of variation for the fatigue stress at 10^6 cycles is only 10%.

For engineering applications where there will be significant flow induced orientation of fibre in the molding process and this direction can be aligned with loading (ruling out applications with multiaxial fatigue), 40% carbon fibre LFT-D may be an advantageous material purely in terms of mechanical properties. With further development of the manufacturing process, the fatigue properties may even improve. Since the specific stiffness of aluminum and 40% carbon fibre LFT-D are similar (0°), dynamic response (not considering damping) will be approximately equivalent. The polymeric matrix may have more internal damping. Fatigue applications where the frequency response of the structure is aligned to the frequency of excitation may be particularly promising for carbon fibre LFT-D materials.

8.3 Originality of the Work

This dissertation includes the first published research on the mechanical properties of compression molded carbon fibre PA66 direct/in-line compounded long fibre thermoplastic. While some of these properties can be estimated analytically, the low-velocity impact and fatigue characterization would be challenging, if not impossible, to evaluate without experimental testing. The fatigue characterization in particular showed that while quasi-static and impact properties may be acceptable, defects in the material present challenges for fatigue performance and clearly demonstrate avenues for future work.

Though the quasi-static characterization consisted mainly of standard uniaxial tension and three-point bending, significant novel findings were identified. The +45°/-45° asymmetry was not previously published and presents opportunities for future work in process modelling and simulation of the resulting mechanical properties. Fibre length measurements demonstrated that current industrial techniques for acquiring this data are deficient. In addition to the documented fibre length characterization by BASF, overtures to the Fraunhofer Institute for Chemical Technology were made to provide additional fibre length data but they were unable to sufficiently separate the fibres.

Impact characterization identified significant inertia effects are possible for the ISO 6603-2 apparatus employing a hemispherical indenter. Previous work with carbon fibre SMC did not identify inertia effects. Additionally, if inertia effects were present, the contribution of inertia effects to the measured response varied with the geometry of the specimen. It is challenging, if not impossible, to separate inertia effects and strain rate sensitivity. Therefore, the ISO 6603-2 methodology for low-velocity impact characterization [1] has significant deficiencies for a study comparing similar materials or in applications of ISO 6603-2 data from ISO standard specimens to more complex geometries, i.e., a real-world engineering application.

To understand the observed rate effects of the ISO 6603-2 low-velocity impact characterization, a novel device was developed to assess strain rate sensitivity under uniaxial tension. The fundamental aspects of the mechanical design and data acquisition were published in the open literature. This apparatus, particularly without the data

acquisition hardware (which it may be possible to rent) is extremely economical to fabricate. The apparatus has seen use with other research groups at the University of Windsor for materials with significant strain rate sensitivity. The data acquired compares favourably with lower and higher strain rate data from other apparatuses.

8.4 Recommendations for Future Work

There are a number of potential avenues for future investigations based upon the findings of the research documented in this dissertation. The wide scope of this work naturally leads to a wide scope of future work. Though there may be challenges in organizing/funding further studies of carbon fibre materials, the international and cross-Canada partnerships for composites research should allow for the pursuit of extending and improving upon this body of work. A number of specific suggestions for areas of future work, based upon the conclusions previously documented, are included below:

1. Previous research with glass fibre has taken the more rigorous approach of developing a process model and mapping the fibre orientation to a structural model. There are significant challenges in doing so, particularly for direct/in-line compounding since the fibre content can be optimized. Glass fibre LFT research has relied on commercial data for rheological properties of the charge. This may be reasonable when there are many rheological data sets, as there may be for glass fibre since it is much more common in industrial applications. For carbon fibre, there are few such data sets which may not provide data for a carbon fibre content of interest. An approach where the rheological properties are computed may be warranted. This is a large scale endeavour which would require the coordination of a large research team that likely spans institutions.

2. The +45°/-45° asymmetry presents an opportunity for correlation of numerical models of the compression molding process, particularly in terms of the initial orientation of the compression molding charge. However, the flow induced fibre orientation modelling will of course also play a role in predicting this disparity in mechanical properties across the geometric plane of symmetry of the plaque mold used in this investigation. A simple experimental trial where the compression molding charge is rotated 180° and the mechanical properties are compared to a plaque molded without rotating the charge may also be considered.

3. Further studies of carbon fibre length distribution are clearly needed. The Fraunhofer Institute for Chemical Technologies was briefly engaged in discussions to engage in further fibre length studies but it was found that separating the carbon fibres presented a significant hurdle. There have been several intervening years and

they may have made progress in this area. One approach could be painstaking optical microscopy with many sections offset by approximately one fibre diameter (or less). Fibre length degradation in the molding process is another active area of research. Fibre length measurements are critical for validation in this area of research.

4. Further fatigue studies of carbon fibre reinforced long fibre thermoplastic are clearly needed. Lower carbon fibre content and/or lower tow count rovings are the simplest changes that can be made to improve fatigue property consistency/reduce fibre wet-out defects.

5. The length scale of the defects observed in the evaluation of fatigue/fracture surfaces in this dissertation was such that there are inspection technologies that can be used to have immediate data after a plaque is produced. Thermal and acoustic inspection technologies could be used with opaque polymers. Visual inspection would be possible with transparent/translucent polymers. For preliminary investigations of process optimization to improve fibre dispersion, such inspection technologies would be much more practical and have a dramatically lower cost (financial and the investment of time) with respect to mechanical fatigue testing.

6. Impact characterization conducted as per the ISO 6603-2 standard [1] identified significant inertia effects dependent on material properties and geometry. The ISO 6603-2 standard includes multiple specimen geometries but recommends a 140 mm diameter, or 140 mm by 140 mm square, specimen for brittle materials. A specimen geometry with minimal inertia effects regardless of the material may be beneficial to allow comparison of different materials with this methodology. A study, which may be experimental, numerical, or a combination of the two, may be able to identify a suitable specimen or identify materials for which inertia effects will be significant with the current specimen geometries of the ISO standard.

7. Digital image correlation was used to acquire the displacement field for quasi-statically loaded ISO 6603-2 specimens as well as the automotive seatback. The currently available high-speed cameras are well suited to the load rate of these tests. However, the ISO 6603-2 low velocity impact fixture does not easily allow two high speed cameras to be used. An alternative fixture design, that would likely

require features to protect the cameras, would allow digital image correlation for low-velocity impact following the ISO 6603-2 standard.

8. The intermediate strain rate uniaxial tension characterization apparatus developed to support this research has seen limited use with a small number of materials. In preliminary investigations it has performed well for ductile materials where the elastic response is not of primary interest and allows for the ramp-up of strain rate. The vinyl rubber impact attenuator can be used while maintaining a moderate strain rate in the range of interest for automotive crashworthiness applications. For brittle materials, challenges remain with achieving these intermediate strain rates while obtaining high quality data. There may be alternative countermeasures to the vinyl rubber impact attenuator to reduce vibration in the apparatus resulting from the impact of the projectile launched by the pneumatic accelerator. Additionally, alternative instrumentation may improve the data acquired. A higher frame rate/higher resolution high speed camera and a load cell with a range/sensitivity better suited to the specimens of interest are two options that immediately come to mind.

8.5 References

1. ISO. 6603–2-2000 Determination of Puncture Impact Behavior of Rigid Plastics - Part 2: Instrumented Puncture.
2. DuPont. DuPont Minlon and Zytel nylon resins Design Information - Module II. 2018.
3. Budynas, R. G., & Nisbett, J. K. (2011). Shigley's mechanical engineering design (Vol. 9). New York: McGraw-hill.

APPENDICES

Appendix A – Generalized Self-Consistent Micromechanics Model

$$\frac{E_{11}}{E_{matrix}} = \frac{E_{fibre}}{E_{matrix}}V_{fibre} + 1 - V_{fibre}$$
$$+ \frac{4V_{fibre}(1 - V_{fibre})(\nu_{fibre} - \nu_{matrix})^2}{E_{matrix}\left(\dfrac{V_{fibre}}{k_{matrix}} + \dfrac{1 - V_{fibre}}{k_{fibre}} + \dfrac{1}{G_{matrix}}\right)}$$

Equation A.1

$$\frac{G_{12}}{G_{matrix}} = \frac{G_{fibre}(1 + V_{fibre}) + G_{matrix}(1 - V_{fibre})}{G_{fibre}(1 - V_{fibre}) + G_{matrix}(1 + V_{fibre})}$$

Equation A.2

$$\frac{\nu_{12}}{\nu_{matrix}} = \frac{\nu_{fibre}}{\nu_{matrix}}V_{fibre} + 1 - V_{fibre}$$
$$+ \frac{V_{fibre}(1 - V_{fibre})(\nu_{fibre} - \nu_{matrix})\left(\dfrac{1}{k_{matrix}} - \dfrac{1}{k_{fibre}}\right)}{\nu_{matrix}\left(\dfrac{V_{fibre}}{k_{matrix}} + \dfrac{1 - V_{fibre}}{k_{fibre}} + \dfrac{1}{G_{matrix}}\right)}$$

Equation A.3

$$\frac{k}{k_{matrix}} = 1 + \frac{V_{fibre}}{k_{matrix}\left(\dfrac{1}{k_{fibre} - k_{matrix}} + \dfrac{1 - V_{fibre}}{k_{matrix} + G_{matrix}}\right)}$$

Equation A.4

$$\frac{G_{23}}{G_{matrix}} = \frac{-B_{GSC} \pm \sqrt{B_{GSC}^2 - A_{GSC}C_{GSC}}}{A_{GSC}}$$

Equation A.5

$$A_{GSC} = 3V_{fibre}\left(1 - V_{fibre}\right)^2 \left(\frac{G_{fibre}}{G_{matrix}} - 1\right)\left(\frac{G_{fibre}}{G_{matrix}} + \eta_{fibre}\right)$$
$$+ \left[\frac{G_{fibre}}{G_{matrix}}\eta_{matrix} + \eta_{fibre}\eta_{matrix}\right.$$
$$- \left(\frac{G_{fibre}}{G_{matrix}}\eta_{matrix}\right.$$
$$\left.\left. - \eta_{fibre}\right)V_{fibre}^3\right]\left[V_{fibre}\eta_{matrix}\left(\frac{G_{fibre}}{G_{matrix}} - 1\right)\right.$$
$$\left. - \left(\frac{G_{fibre}}{G_{matrix}}\eta_{matrix} + 1\right)\right]$$

$$B_{GSC} = -3V_{fibre}\left(1 - V_{fibre}\right)^2 \left(\frac{G_{fibre}}{G_{matrix}} - 1\right)\left(\frac{G_{fibre}}{G_{matrix}} + \eta_{fibre}\right)$$
$$+ \frac{1}{2}\left[\frac{G_{fibre}}{G_{matrix}}\eta_{matrix} + \left(\frac{G_{fibre}}{G_{matrix}} - 1\right)V_{fibre}\right.$$
$$\left. + 1\right]\left[(\eta_{matrix} - 1)\left(\frac{G_{fibre}}{G_{matrix}} + \eta_{fibre}\right)\right.$$
$$\left. - 2\left(\frac{G_{fibre}}{G_{matrix}}\eta_{matrix} - \eta_{fibre}\right)V_{fibre}^3\right]$$
$$+ \frac{V_{fibre}}{2}(\eta_{matrix} + 1)\left(\frac{G_{fibre}}{G_{matrix}} - 1\right)\left[\frac{G_{fibre}}{G_{matrix}} + \eta_{fibre}\right.$$
$$\left. + \left(\frac{G_{fibre}}{G_{matrix}}\eta_{matrix} - \eta_{fibre}\right)V_{fibre}^3\right]$$

$$C_{GSC} = 3V_{fibre}\left(1 - V_{fibre}\right)^2 \left(\frac{G_{fibre}}{G_{matrix}} - 1\right)\left(\frac{G_{fibre}}{G_{matrix}} + \eta_{fibre}\right)$$
$$+ \left[\frac{G_{fibre}}{G_{matrix}}\eta_{matrix} + \left(\frac{G_{fibre}}{G_{matrix}} - 1\right)V_{fibre}\right.$$
$$\left. + 1\right]\left[\frac{G_{fibre}}{G_{matrix}} + \eta_{fibre}\right.$$
$$\left. + \left(\frac{G_{fibre}}{G_{matrix}}\eta_{matrix} - \eta_{fibre}\right)V_{fibre}^3\right]$$

$$\eta_{matrix} = 3 - 4v_{matrix}$$

$$\eta_{fibre} = 3 - 4v_{fibre}$$

Appendix B – Mori Tanaka Micromechanics Model

$$\frac{E_{11}}{E_{matrix}} = \frac{1}{1 + \dfrac{V_{fibre}(\alpha_1 + 2v_{matrix}\alpha_2)}{\alpha_6}}$$

<div align="right">Equation B.1</div>

$$\frac{G_{12}}{G_{matrix}} = 1 + \frac{V_{fibre}}{\dfrac{G_{matrix}}{G_{fibre} - G_{matrix}} + 2V_{matrix}S_{1212}}$$

<div align="right">Equation B.2</div>

$$\frac{G_{23}}{G_{matrix}} = 1 + \frac{V_{fibre}}{\dfrac{G_{matrix}}{G_{fibre} - G_{matrix}} + 2V_{matrix}S_{2323}}$$

<div align="right">Equation B.3</div>

$$\frac{v_{12}}{v_{matrix}} = 1 - V_{fibre}\frac{v_{matrix}(\alpha_1 + 2v_{matrix}\alpha_2) + \alpha_3 - v_{matrix}\alpha_4}{v_{matrix}[\alpha_6 + V_{fibre}(\alpha_1 + 2v_{matrix}\alpha_2)]}$$

<div align="right">Equation B.4</div>

$$\frac{k}{k_{matrix}} = \frac{(1 + v_{matrix})(1 - 2v_{matrix})}{1 - v_{matrix}(1 + 2v_{12}) + \dfrac{V_{fibre}[2\alpha_3(v_{12} - v_{matrix}) + \alpha_4(1 - v_{matrix}(1 + 2v_{12}))]}{\alpha_6}}$$

<div align="right">Equation B.5</div>

$$\alpha_1 = F_1(\beta_4 + \beta_5) - 2\beta_2$$

<div align="right">Equation B.6</div>

$$\alpha_2 = \beta_2(1 + F_1) - \beta_4 - \beta_5$$

<div align="right">Equation B.7</div>

$$\alpha_3 = \beta_1 - F_1\beta_3$$

<div align="right">Equation B.8</div>

$$\alpha_4 = \beta_1(1 + F_1) - 2\beta_3$$

<div align="right">Equation B.9</div>

$$\alpha_5 = \frac{1 - F_1}{\beta_4 - \beta_5}$$

<div align="right">Equation B.10</div>

$$\alpha_6 = 2\beta_2\beta_3 - \beta_1(\beta_4 + \beta_5)$$

<div align="right">Equation B.11</div>

$$\beta_1 = V_{fibre}F_1 + F_2 + V_{matrix}(F_1 S_{1111} + 2S_{2211})$$

<div align="right">Equation B.12</div>

$$\beta_2 = V_{fibre} + F_3 + V_{matrix}(F_1 S_{1122} + S_{2222} + S_{2233})$$

<div align="right">Equation B.13</div>

$$\beta_3 = V_{fibre} + F_3 + V_{matrix}(S_{1111} + S_{2211} + F_1 S_{2211})$$

<div align="right">Equation B.14</div>

$$\beta_4 = V_{fibre}F_1 + F_2 + V_{matrix}(S_{1122} + F_1 S_{2222} + S_{2233})$$

<div align="right">Equation B.15</div>

$$\beta_5 = V_{fibre} + F_3 + V_{matrix}(S_{1122} + S_{2222} + F_1 S_{2233})$$

<div align="right">Equation B.16</div>

$$F_1 = 1 + 2\frac{G_{fibre} - G_{matrix}}{\lambda_{fibre} - \lambda_{matrix}}$$

<div align="right">Equation B.17</div>

$$F_2 = \frac{\lambda_{matrix} + 2G_{matrix}}{\lambda_{fibre} - \lambda_{matrix}}$$

<div align="right">Equation B.18</div>

$$F_3 = \frac{\lambda_{matrix}}{\lambda_{fibre} - \lambda_{matrix}}$$

<div align="right">Equation B.19</div>

$$\lambda = \frac{E\nu}{(1 + \nu)(1 - 2\nu)}$$

<div align="right">Equation B.20</div>

Eshelby Tensor

$$S_{1111} = \frac{1}{2(1 - v_{matrix})}\left[1 - 2v_{matrix} + \frac{3a^2 - 1}{a^2 - 1} - \left(1 - 2v_{matrix} + \frac{3a^2}{a^2 - 1}\right)g\right]$$
Equation B.21

$$S_{2222} = \frac{3a^2}{8(1 - v_{matrix})(a^2 - 1)} + \frac{1}{4(1 - v_{matrix})}\left[1 - 2v_{matrix} - \frac{9}{4(a^2 - 1)}\right]g$$
Equation B.22

$$S_{2233} = \frac{1}{4(1 - v_{matrix})}\left[\frac{a^2}{2(a^2 - 1)} - \left(1 - 2v_{matrix} + \frac{3}{4(a^2 - 1)}\right)g\right]$$
Equation B.23

$$S_{2211} = -\frac{a^2}{2(1 - v_{matrix})(a^2 - 1)} + \frac{1}{4(1 - v_{matrix})}\left[\frac{3a^2}{a^2 - 1} - 1 + 2v_{matrix}\right]g$$
Equation B.24

$$S_{1122} = -\frac{1}{2(1 - v_{matrix})}\left[1 - 2v_{matrix} + \frac{1}{a^2 - 1}\right] + \frac{1}{2(1 - v_{matrix})}\left[1 - 2v_{matrix} + \frac{3}{2(a^2 - 1)}\right]g$$
Equation B.25

$$S_{2323} = \frac{1}{4(1 - v_{matrix})}\left[\frac{a^2}{2(a^2 - 1)} + \left(1 - 2v_{matrix} - \frac{3}{4(a^2 - 1)}\right)g\right]$$
Equation B.26

$$S_{1212} = \frac{1}{4(1 - v_{matrix})}\left[1 - 2v_{matrix} - \frac{a^2 + 1}{a^2 - 1} - \frac{1}{2}\left(1 - 2v_{matrix} - \frac{3(a^2 + 1)}{a^2 - 1}\right)g\right]$$
Equation B.27

$$g = \frac{a}{(a^2 - 1)^{\frac{3}{2}}}\left[a(a^2 - 1)^{\frac{1}{2}} - cosh^{-1}(a)\right] \ for \ a > 1$$
Equation B.28

$$g = \frac{a}{(1 - a^2)^{\frac{3}{2}}}\left[cos^{-1}(a) - a(a^2 - 1)^{\frac{1}{2}}\right] \ for \ a < 1$$
Equation B.29

$$S_{3322} = S_{2222}$$

$$S_{3322} = S_{2233}$$

$$S_{3311} = S_{2233}$$

$$S_{1133} = S_{1122}$$

$$S_{1313} = S_{1212}$$

$$a = \frac{l}{d}$$

Appendix C – MATLAB code to compute fibre orientation from a micrograph

```matlab
% Subroutine (save in a separate file)
function [ outkD ] = kroneckerDelta( i,j )

if i==j
    outkD=1;
else
    outkD=0;
end

end


% MATLAB code to compute fibre orientation from a micrograph

clear all
close all
clc
format long

% Number of regions through the thickness in which to find 2nd order
% orientation tensor diagonal
Number_sections_thickness=10;

% Error tolerance for fibre cross sections (check that they are
% elliptical)
err_tol=0.8;

% Find image files
img_files=glob('*.jpg');

img1=imread(img_files{1});

% cropping
cropping_pixels=[200 1000 400 400]; %top bottom left right
img1=img1(cropping_pixels(1):end-
cropping_pixels(2),cropping_pixels(3):end-cropping_pixels(4));

figure(1)
imshow(img1)

% convert to black and white
level1=graythresh(img1);
imgbw1=im2bw(img1,1.6*level1);
figure(2)
imshow(imgbw1)

imgbw1=bwareaopen(imgbw1,500);
figure(3)
imshow(imgbw1)

% identify fibre cross sections
cc1=bwconncomp(imgbw1);
```

```matlab
% visualize fibre cross sections
labeled1=labelmatrix(cc1);
RGB_label1=label2rgb(labeled1,@spring,'c','shuffle');
figure(4)
imshow(RGB_label1)


% compute cross sectional area, find the centroid, major axis length,
minor
% axis length, and in-plane orientation of cross section
fibre_data1=regionprops(cc1,'Area','Centroid','MajorAxisLength','MinorA
xisLength','Orientation');

% save each characteristic in each cross section separately
area1=[fibre_data1.Area];
centroid1=[fibre_data1.Centroid];
major1=[fibre_data1.MajorAxisLength];
minor1=[fibre_data1.MinorAxisLength];
orientation1=[fibre_data1.Orientation]*pi/180; % convert from degrees
to radians

% check that each cross section is roughly elliptical using the cross
% sectional area and major/minor diameters
j=1;
for i=1:length(area1)
    abs((area1(i)-pi*major1(i)*minor1(i))/(pi*major1(i)*minor1(i))); %
remove suppression semicolon to see the relative area for elliptical
shape printed to the command window, useful for setting the error
tolerance above (line 17)
    if abs((area1(i)-
pi*major1(i)*minor1(i))/(pi*major1(i)*minor1(i)))<err_tol
        good_fibre_data1(j,:)=[area1(i) centroid1(:,2*i-1)
centroid1(:,2*i) major1(i) minor1(i) orientation1(i)
acos(minor1(i)/major1(i))];
        good_fibre_data1_indices(j)=i;
        j=j+1;
    end
end

% Redraw figure 4 showing only fibres that have cross sections that are
% approximately elliptical
cc1B.Connectivity=cc1.Connectivity;
cc1B.ImageSize=cc1.ImageSize;
cc1B.NumObjects=length(good_fibre_data1_indices);
for index_cc1=1:length(good_fibre_data1_indices)

cc1B.PixelIdxList{index_cc1}=cc1.PixelIdxList{good_fibre_data1_indices(
index_cc1)};
end
labeled1B=labelmatrix(cc1B);
RGB_label1B=label2rgb(labeled1B,@spring,'c','shuffle');
figure(5)
imshow(RGB_label1B)


% orientation tensor diagonal for image 1 (only need one cross section)
```

```matlab
% generate plot of tensor components through the thickness
% this really needs to be parameterized...
size_img1=size(img1);
for thickness_index=1:Number_sections_thickness
    k{thickness_index}=1;
    for i=1:length(good_fibre_data1)
        if
good_fibre_data1(i,3)<=size_img1(1)*thickness_index/Number_sections_thi
ckness && good_fibre_data1(i,3)>=size_img1(1)*(thickness_index-
1)/Number_sections_thickness

in_plane{thickness_index}(k{thickness_index},1)=good_fibre_data1(i,6);

out_plane{thickness_index}(k{thickness_index},1)=good_fibre_data1(i,7);
            k{thickness_index}=k{thickness_index}+1;
        end
    end

p{thickness_index}=[sin(out_plane{thickness_index}).*cos(in_plane{thick
ness_index})
sin(out_plane{thickness_index}).*sin(in_plane{thickness_index})
cos(out_plane{thickness_index})];

% second order orientation tensor for each region through the thickness
    for i=1:3
        for j=1:3

a2{thickness_index}(i,j)=sum(1./sin(abs(out_plane{thickness_index})).*p
{thickness_index}(:,i).*p{thickness_index}(:,j))./sum(1./sin(abs(out_pl
ane{thickness_index})));
        end
    end
end

for thickness_index=1:Number_sections_thickness
    a2_11(thickness_index)=a2{thickness_index}(1,1);
    a2_22(thickness_index)=a2{thickness_index}(2,2);
    a2_33(thickness_index)=a2{thickness_index}(3,3);
end

% Plot 2nd order orientation tensor diagonal through the thickness
figure(6)
plot(linspace(1,Number_sections_thickness,Number_sections_thickness)/Nu
mber_sections_thickness,a2_11,...

linspace(1,Number_sections_thickness,Number_sections_thickness)/Number_
sections_thickness,a2_22,...

linspace(1,Number_sections_thickness,Number_sections_thickness)/Number_
sections_thickness,a2_33)
title('Fibre orientation tensor components through the thickness')
xlabel('z/thickness')
ylabel('Tensor component')
legend('x-component','y-component','z-component')
grid on
```

Appendix D – MATLAB code to compute elastic properties of a composite material given the fibre length and orientation distributions

```matlab
% Subroutines (save in separate files)


%%%%%%%%%%%%%%%%%%%%%%%%%%%%%%%%%%%%%%%%%%%%%%%%%%%%%%%%%%%%%%%%%%%%%%%%%%%

function [ C ] = GSC(
E_matrix,PR_matrix,E_fiber,PR_fiber,vf_fiber,G_matrix,G_fiber_AB )
% GSC Generalized Self Consistent micromechanics model
% Generalized Self Consistent micromechanics model for unidirectional
% fibre reinforced material. Cannot account for the effect of fibre
%   aspect ratio.
    % Bulk modulus of the matrix under plane strain
    km=E_matrix/2/(1-2*PR_matrix)/(1+PR_matrix);
    % Bulk modulus of the fiber under plane strain (longitudinal
direction)
    kf=E_fiber/2/(1-2*PR_fiber)/(1+PR_fiber);
    % Composite modulus in longitudinal direction
    E_1=E_fiber*vf_fiber+(1-vf_fiber)*E_matrix+4*vf_fiber*(1-
vf_fiber)*(PR_fiber-PR_matrix)^2/(vf_fiber/km+(1-
vf_fiber)/kf+1/G_matrix);
    % Composite shear modulus 12
    G_12=G_matrix*(G_fiber_AB*(1+vf_fiber)+G_matrix*(1-
vf_fiber))/(G_fiber_AB*(1-vf_fiber)+G_matrix*(1+vf_fiber));
    % Poissons ratio 12
    PR_12=PR_fiber*vf_fiber+(1-vf_fiber)*PR_matrix+vf_fiber*(1-
vf_fiber)*(PR_fiber-PR_matrix)*(1/km-1/kf)/(vf_fiber/km+(1-
vf_fiber)/kf+1/G_matrix);
    % Composite bulk modulus
    k=km+vf_fiber/(1/(kf-km)+(1-vf_fiber)/(km+G_matrix));
    % composite shear modulus 23
    nf=3-4*PR_fiber;
    nm=3-4*PR_matrix;
    A=3*vf_fiber*(1-vf_fiber)^2*(G_fiber_AB/G_matrix-
1)*(G_fiber_AB/G_matrix+nf)+(G_fiber_AB/G_matrix*nm+nf*nm-
(G_fiber_AB/G_matrix*nm-
nf)*vf_fiber^3)*(vf_fiber*nm*(G_fiber_AB/G_matrix-1)-
(G_fiber_AB/G_matrix*nm+1));
    B=-3*vf_fiber*(1-vf_fiber)^2*(G_fiber_AB/G_matrix-
1)*(G_fiber_AB/G_matrix+nf)+0.5*(G_fiber_AB/G_matrix*nm+(G_fiber_AB/G_m
atrix-1)*vf_fiber+1)*((nm-1)*(G_fiber_AB/G_matrix+nf)-
2*(G_fiber_AB/G_matrix*nm-
nf)*vf_fiber^3)+vf_fiber/2*(nm+1)*(G_fiber_AB/G_matrix-
1)*(G_fiber_AB/G_matrix+nf+(G_fiber_AB/G_matrix*nm-nf)*vf_fiber^3);
    C=3*vf_fiber*(1-vf_fiber)^2*(G_fiber_AB/G_matrix-
1)*(G_fiber_AB/G_matrix+nf)+(G_fiber_AB/G_matrix*nm+(G_fiber_AB/G_matri
x-1)*vf_fiber+1)*(G_fiber_AB/G_matrix+nf+(G_fiber_AB/G_matrix*nm-
nf)*vf_fiber^3);
    G_23=G_matrix*(-B+sqrt(B^2-A*C))/A;
    if G_23<0
        G_23=G_matrix*(-B-sqrt(B^2-A*C))/A;
    end
    % Stiffness tensor
```

```matlab
    Q(1,1)=E_1+4*PR_12^2*k;
    Q(1,2)=2*k*PR_12;
    Q(2,2)=G_23+k;
    Q(2,3)=-G_23+k;
    Q(6,6)=G_12;
    C=[Q(1,1) Q(1,2) Q(1,2) 0 0 0; Q(1,2) Q(2,2) Q(2,3) 0 0 0; Q(1,2)
Q(2,3) Q(2,2) 0 0 0; 0 0 0 (Q(2,2)-Q(2,3))/2 0 0; 0 0 0 0 Q(6,6) 0; 0 0
0 0 0 Q(6,6)];
end


%%%%%%%%%%%%%%%%%%%%%%%%%%%%%%%%%%%%%%%%%%%%%%%%%%%%%%%%%%%%%%%%%%%%%%%%%%%


function [ C ] =
HalpinTsai(AR,E_matrix,PR_matrix,E_fiber,PR_fiber,vf_fiber,vf_fiber_max
,G_matrix,G_fiber_AB,flag_fld,fld,fibre_diameter)
% HalpinTsai Halpin Tsai micromechanics model
% Halpin Tsai micromechanics model for unidirectional fibre composite
    if flag_fld==1
        for i=1:length(fld)
            A_1=2*fld(i,1)/fibre_diameter;
            psi=1+(1-vf_fiber_max)/vf_fiber_max^2*vf_fiber;
            B_1=(E_fiber/E_matrix-1)/(E_fiber/E_matrix+A_1);
            E_1=E_matrix*(1+A_1*B_1*vf_fiber)/(1-B_1*psi*vf_fiber);
            A_12=1;
            B_12=(G_fiber_AB/G_matrix-1)/(G_fiber_AB/G_matrix+A_12);
            G_12=G_matrix*(1+A_12*B_12*vf_fiber)/(1-B_12*psi*vf_fiber);
            PR_12=vf_fiber*PR_fiber+(1-vf_fiber)*PR_matrix;
            A_G_23=1;
            B_G_23=(G_fiber_AB*0.7/1.3/G_matrix-
1)/(G_fiber_AB*0.7/1.3/G_matrix+A_G_23);
            G_23=G_matrix*(1+A_G_23*B_G_23*vf_fiber)/(1-
B_G_23*psi*vf_fiber);
            % Bulk modulus of the matrix under plane strain
            km=E_matrix/2/(1-2*PR_matrix)/(1+PR_matrix);
            % Bulk modulus of the fiber under plane strain
(longitudinal direction)
            kf=E_fiber/2/(1-2*PR_fiber)/(1+PR_fiber);
            k=km+vf_fiber/(1/(kf-km)+(1-vf_fiber)/(km+G_matrix));
            % Stiffness tensor
            Q(1,1)=E_1+4*PR_12^2*k;
            Q(1,2)=2*k*PR_12;
            Q(2,2)=G_23+k;
            Q(2,3)=-G_23+k;
            Q(6,6)=G_12;
            Cfld(:,:,i)=[Q(1,1) Q(1,2) Q(1,2) 0 0 0; Q(1,2) Q(2,2)
Q(2,3) 0 0 0; Q(1,2) Q(2,3) Q(2,2) 0 0 0; 0 0 0 (Q(2,2)-Q(2,3))/2 0 0;
0 0 0 0 Q(6,6) 0; 0 0 0 0 0 Q(6,6)];
        end
        for j=1:6
            for k=1:6
                for l=1:length(fld)
                    Cfld_temp(l)=Cfld(j,k,l);
                end

C(j,k)=trapz(fld(:,1),Cfld_temp'.*fld(:,2))/trapz(fld(:,1),fld(:,2));
            end
        end
```

239

```matlab
    else
        A_1=2*AR;
        psi=1+(1-vf_fiber_max)/vf_fiber_max^2*vf_fiber;
        B_1=(E_fiber/E_matrix-1)/(E_fiber/E_matrix+A_1);
        E_1=E_matrix*(1+A_1*B_1*vf_fiber)/(1-B_1*psi*vf_fiber);
        A_12=1;
        B_12=(G_fiber_AB/G_matrix-1)/(G_fiber_AB/G_matrix+A_12);
        G_12=G_matrix*(1+A_12*B_12*vf_fiber)/(1-B_12*psi*vf_fiber);
        PR_12=vf_fiber*PR_fiber+(1-vf_fiber)*PR_matrix;
        A_G_23=1;
        B_G_23=(G_fiber_AB*0.7/1.3/G_matrix-
1)/(G_fiber_AB*0.7/1.3/G_matrix+A_G_23);
        G_23=G_matrix*(1+A_G_23*B_G_23*vf_fiber)/(1-
B_G_23*psi*vf_fiber);
        % Bulk modulus of the matrix under plane strain
        km=E_matrix/2/(1-2*PR_matrix)/(1+PR_matrix);
        % Bulk modulus of the fiber under plane strain (longitudinal
direction)
        kf=E_fiber/2/(1-2*PR_fiber)/(1+PR_fiber);
        k=km+vf_fiber/(1/(kf-km)+(1-vf_fiber)/(km+G_matrix));
        % Stiffness tensor
        Q(1,1)=E_1+4*PR_12^2*k;
        Q(1,2)=2*k*PR_12;
        Q(2,2)=G_23+k;
        Q(2,3)=-G_23+k;
        Q(6,6)=G_12;
        C=[Q(1,1) Q(1,2) Q(1,2) 0 0 0; Q(1,2) Q(2,2) Q(2,3) 0 0 0;
Q(1,2) Q(2,3) Q(2,2) 0 0 0; 0 0 0 (Q(2,2)-Q(2,3))/2 0 0; 0 0 0 0 Q(6,6)
0; 0 0 0 0 0 Q(6,6)];
    end
end


%%%%%%%%%%%%%%%%%%%%%%%%%%%%%%%%%%%%%%%%%%%%%%%%%%%%%%%%%%%%%%%%%%%%%%%%%

function [ C ] =
MoriTanaka(AR,E_matrix,PR_matrix,E_fiber,PR_fiber,vf_fiber,G_matrix,G_f
iber_AB,flag_fld,fld,fibre_diameter)
%MoriTanaka Mori Tanaka micromechanics model
%   Mori-Tanaka unidirectional fibre reinforced material micromechanics
%   model
    if flag_fld==0
        % Mori-Tanaka micromechanics model
        a=AR; % fiber aspect ratio
        if a<1
            g=a/(1-a^2)^1.5*(acos(a)-a*sqrt(a^2-1));
        elseif a>1
            g=a/(a^2-1)^1.5*(a*sqrt(a^2-1)-acosh(a));
        end
        % Eshelby tensor components
        S1111=1/2/(1-PR_matrix)*(1-2*PR_matrix+(3*a^2-1)/(a^2-1)-(1-
2*PR_matrix+3*a^2/(a^2-1))*g);
        S2222=3*a^2/8/(1-PR_matrix)/(a^2-1)+1/4/(1-PR_matrix)*(1-
2*PR_matrix-9/4/(a^2-1))*g;
        S2233=1/4/(1-PR_matrix)*(a^2/2/(a^2-1)-(1-2*PR_matrix+3/4/(a^2-
1))*g);
        S2211=-a^2/2/(1-PR_matrix)/(a^2-1)+1/4/(1-
PR_matrix)*(3*a^2/(a^2-1)-(1-2*PR_matrix))*g;
```

```matlab
        S1122=-1/2/(1-PR_matrix)*(1-2*PR_matrix+1/(a^2-1))+1/2/(1-
PR_matrix)*(1-2*PR_matrix+3/2/(a^2-1))*g;
        S2323=1/4/(1-PR_matrix)*(a^2/2/(a^2-1)+(1-2*PR_matrix-3/4/(a^2-
1))*g);
        S1212=1/4/(1-PR_matrix)*(1-2*PR_matrix-(a^2+1)/(a^2-1)-0.5*(1-
2*PR_matrix-3*(a^2+1)/(a^2-1))*g);
        S3333=S2222;
        S3322=S2233;
        S3311=S2211;
        S1133=S1122;
        S1313=S1212;
        % Lame constants
        muf=E_fiber/2/(1+PR_fiber);
        mum=E_matrix/2/(1+PR_matrix);
        lf=E_fiber*PR_fiber/(1+PR_fiber)/(1-2*PR_fiber);
        lm=E_matrix*PR_matrix/(1+PR_matrix)/(1-2*PR_matrix);
        D1=1+2*(muf-mum)/(lf-lm);
        D2=(lm+2*mum)/(lf-lm);
        D3=lm/(lf-lm);
        B1=vf_fiber*D1+D2+(1-vf_fiber)*(D1*S1111+2*S2211);
        B2=vf_fiber+D3+(1-vf_fiber)*(D1*S1122+S2222+S2233);
        B3=vf_fiber+D3+(1-vf_fiber)*(S1111+(1+D1)*S2211);
        B4=vf_fiber*D1+D2+(1-vf_fiber)*(S1122+D1*S2222+S2233);
        B5=vf_fiber+D3+(1-vf_fiber)*(S1122+S2222+D1*S2233);
        A1=D1*(B4+B5)-2*B2;
        A2=(1+D1)*B2-(B4+B5);
        A3=B1-D1*B3;
        A4=(1+D1)*B1-2*B3;
        A5=(1-D1)/(B4-B5);
        A=2*B2*B3-B1*(B4+B5);
        % Composite properties
        E_1=E_matrix/(1+vf_fiber*(A1+2*PR_matrix*A2)/A);
        G_12=G_matrix+G_matrix*vf_fiber/(G_matrix/(G_fiber_AB-
G_matrix)+2*(1-vf_fiber)*S1212);
        G_23=G_matrix+G_matrix*vf_fiber/(G_matrix/(G_fiber_AB-
G_matrix)+2*(1-vf_fiber)*S2323);
        PR_12=PR_matrix-
PR_matrix*vf_fiber*(PR_matrix*(A1+2*PR_matrix*A2)+(A3-
PR_matrix*A4))/PR_matrix/(A+vf_fiber*(A1+2*PR_matrix*A2));
        % Bulk modulus of the matrix under plane strain
        km=E_matrix/2/(1-2*PR_matrix)/(1+PR_matrix);
        k=km*(1+PR_matrix)*(1-2*PR_matrix)/(1-
PR_matrix*(1+2*PR_12)+(vf_fiber*(2*(PR_12-PR_matrix)*A3+(1-
PR_matrix*(1+2*PR_12))*A4))/A);
        % Stiffness tensor
        Q(1,1)=E_1+4*PR_12^2*k;
        Q(1,2)=2*k*PR_12;
        Q(2,2)=G_23+k;
        Q(2,3)=-G_23+k;
        Q(6,6)=G_12;
        C=[Q(1,1) Q(1,2) Q(1,2) 0 0 0; Q(1,2) Q(2,2) Q(2,3) 0 0 0;
Q(1,2) Q(2,3) Q(2,2) 0 0 0; 0 0 0 (Q(2,2)-Q(2,3))/2 0 0; 0 0 0 0 Q(6,6)
0; 0 0 0 0 0 Q(6,6)];
    else
        for i=1:length(fld)
            a=fld(i,1)/fibre_diameter;
            if a<1
```

```matlab
                g=a/(1-a^2)^1.5*(acos(a)-a*sqrt(a^2-1));
                if isreal(g)
                    g=g;
                else
                    g=abs(g);
                end
            elseif a>1
                g=a/(a^2-1)^1.5*(a*sqrt(a^2-1)-acosh(a));
                if isreal(g)
                    g=g;
                else
                    g=abs(g);
                end
            end
            % Eshelby tensor components
            S1111=1/2/(1-PR_matrix)*(1-2*PR_matrix+(3*a^2-1)/(a^2-1)-
(1-2*PR_matrix+3*a^2/(a^2-1))*g);
            S2222=3*a^2/8/(1-PR_matrix)/(a^2-1)+1/4/(1-PR_matrix)*(1-
2*PR_matrix-9/4/(a^2-1))*g;
            S2233=1/4/(1-PR_matrix)*(a^2/2/(a^2-1)-(1-
2*PR_matrix+3/4/(a^2-1))*g);
            S2211=-a^2/2/(1-PR_matrix)/(a^2-1)+1/4/(1-
PR_matrix)*(3*a^2/(a^2-1)-(1-2*PR_matrix))*g;
            S1122=-1/2/(1-PR_matrix)*(1-2*PR_matrix+1/(a^2-1))+1/2/(1-
PR_matrix)*(1-2*PR_matrix+3/2/(a^2-1))*g;
            S2323=1/4/(1-PR_matrix)*(a^2/2/(a^2-1)+(1-2*PR_matrix-
3/4/(a^2-1))*g);
            S1212=1/4/(1-PR_matrix)*(1-2*PR_matrix-(a^2+1)/(a^2-1)-
0.5*(1-2*PR_matrix-3*(a^2+1)/(a^2-1))*g);
            S3333=S2222;
            S3322=S2233;
            S3311=S2211;
            S1133=S1122;
            S1313=S1212;
            % Lame constants
            muf=E_fiber/2/(1+PR_fiber);
            mum=E_matrix/2/(1+PR_matrix);
            lf=E_fiber*PR_fiber/(1+PR_fiber)/(1-2*PR_fiber);
            lm=E_matrix*PR_matrix/(1+PR_matrix)/(1-2*PR_matrix);
            D1=1+2*(muf-mum)/(lf-lm);
            D2=(lm+2*mum)/(lf-lm);
            D3=lm/(lf-lm);
            B1=vf_fiber*D1+D2+(1-vf_fiber)*(D1*S1111+2*S2211);
            B2=vf_fiber+D3+(1-vf_fiber)*(D1*S1122+S2222+S2233);
            B3=vf_fiber+D3+(1-vf_fiber)*(S1111+(1+D1)*S2211);
            B4=vf_fiber*D1+D2+(1-vf_fiber)*(S1122+D1*S2222+S2233);
            B5=vf_fiber+D3+(1-vf_fiber)*(S1122+S2222+D1*S2233);
            A1=D1*(B4+B5)-2*B2;
            A2=(1+D1)*B2-(B4+B5);
            A3=B1-D1*B3;
            A4=(1+D1)*B1-2*B3;
            A5=(1-D1)/(B4-B5);
            A=2*B2*B3-B1*(B4+B5);
            % Composite properties
            E_1=E_matrix/(1+vf_fiber*(A1+2*PR_matrix*A2)/A);
            G_12=G_matrix+G_matrix*vf_fiber/(G_matrix/(G_fiber_AB-
G_matrix)+2*(1-vf_fiber)*S1212);
```

```matlab
            G_23=G_matrix+G_matrix*vf_fiber/(G_matrix/(G_fiber_AB-
G_matrix)+2*(1-vf_fiber)*S2323);
            PR_12=PR_matrix-
PR_matrix*vf_fiber*(PR_matrix*(A1+2*PR_matrix*A2)+(A3-
PR_matrix*A4))/PR_matrix/(A+vf_fiber*(A1+2*PR_matrix*A2));
            % Bulk modulus of the matrix under plane strain
            km=E_matrix/2/(1-2*PR_matrix)/(1+PR_matrix);
            k=km*(1+PR_matrix)*(1-2*PR_matrix)/(1-
PR_matrix*(1+2*PR_12)+(vf_fiber*(2*(PR_12-PR_matrix)*A3+(1-
PR_matrix*(1+2*PR_12))*A4))/A);
            % Stiffness tensor
            Q(1,1)=E_1+4*PR_12^2*k;
            Q(1,2)=2*k*PR_12;
            Q(2,2)=G_23+k;
            Q(2,3)=-G_23+k;
            Q(6,6)=G_12;
            Cfld(:,:,i)=[Q(1,1) Q(1,2) Q(1,2) 0 0 0; Q(1,2) Q(2,2)
Q(2,3) 0 0 0; Q(1,2) Q(2,3) Q(2,2) 0 0 0; 0 0 0 (Q(2,2)-Q(2,3))/2 0 0;
0 0 0 0 Q(6,6) 0; 0 0 0 0 0 Q(6,6)];
        end
        for j=1:6
            for k=1:6
                for l=1:length(fld)
                    Cfld_temp(l)=Cfld(j,k,l);
                end

C(j,k)=trapz(fld(:,1),Cfld_temp'.*fld(:,2))/trapz(fld(:,1),fld(:,2));
            end
        end
    end
end


%%%%%%%%%%%%%%%%%%%%%%%%%%%%%%%%%%%%%%%%%%%%%%%%%%%%%%%%%%%%%%%%%%%%%%%%

function [ a4 ] = Linear2D( a2 )
%Linear2D Linear closure approximation
% Linear closure approximation to obtain fourth order orientation
% tensor from 2nd order tensor for 2D fibre orientation
    for i=1:3
        for j=1:3
            for k=1:3
                for l=1:3
                    a4(i,j,k,l)=-
1/24*(kroneckerDelta(i,j)*kroneckerDelta(k,l)+kroneckerDelta(i,k)*krone
ckerDelta(j,l)+kroneckerDelta(i,l)*kroneckerDelta(j,k))+1/6*(a2(i,j)*kr
oneckerDelta(k,l)+a2(i,k)*kroneckerDelta(j,l)+a2(i,l)*kroneckerDelta(j,
k)+a2(k,l)*kroneckerDelta(i,j)+a2(j,l)*kroneckerDelta(i,k)+a2(j,k)*kron
eckerDelta(i,l));
                end
            end
        end
    end
end


%%%%%%%%%%%%%%%%%%%%%%%%%%%%%%%%%%%%%%%%%%%%%%%%%%%%%%%%%%%%%%%%%%%%%%%%
```

```matlab
function [ a4 ] = Linear3D( a2 )
%Linear3D Linear closure approximation
%   Linear closure approximation to obtain fourth order orientation
% tensor from 2nd order tensor for 3D fibre orientation
    for i=1:3
        for j=1:3
            for k=1:3
                for l=1:3
                    a4(i,j,k,l)=-
1/35*(kroneckerDelta(i,j)*kroneckerDelta(k,l)+kroneckerDelta(i,k)*krone
ckerDelta(j,l)+kroneckerDelta(i,l)*kroneckerDelta(j,k))+1/7*(a2(i,j)*kr
oneckerDelta(k,l)+a2(i,k)*kroneckerDelta(j,l)+a2(i,l)*kroneckerDelta(j,
k)+a2(k,l)*kroneckerDelta(i,j)+a2(j,l)*kroneckerDelta(i,k)+a2(j,k)*kron
eckerDelta(i,l));
                end
            end
        end
    end
end


%%%%%%%%%%%%%%%%%%%%%%%%%%%%%%%%%%%%%%%%%%%%%%%%%%%%%%%%%%%%%%%%%%%%%%%%%

function [ a4 ] = Quadratic( a2 )
%Quadratic Quadratic closure approximation
% Quadratic closure approximation to find 4th order orientation tensor
% from 2nd order tensor
    for i=1:3
        for j=1:3
            for k=1:3
                for l=1:3
                    a4(i,j,k,l)=a2(i,j)*a2(k,l);
                end
            end
        end
    end
end


%%%%%%%%%%%%%%%%%%%%%%%%%%%%%%%%%%%%%%%%%%%%%%%%%%%%%%%%%%%%%%%%%%%%%%%%%

function [ a4 ] = Hybrid2D( a2 )
%Hybrid2D Hybrid closure approximation
% Hybrid closure approximation to obtain 4th order orientation tensor
% from 2nd order tensor using quadratic and 2D linear closures
    % linear (planar) closure model
    a4_lin=Linear2D(a2);
    % quadratic closure
    a4_quad=Quadratic(a2);
    for i=1:3
        for j=1:3
            if i==1 && j==1
                f=2*a2(i,j)*a2(j,i)-1;
            else
                f=f+2*a2(i,j)*a2(j,i);
            end
        end
    end
```

244

```matlab
    % f=1-27*det(a2);
    a4=(1-f)*a4_lin+f*a4_quad;
end


%%%%%%%%%%%%%%%%%%%%%%%%%%%%%%%%%%%%%%%%%%%%%%%%%%%%%%%%%%%%%%%%%%%%%%%%%%%

function [ a4 ] = Hybrid3D( a2 )
%Hybrid3D Hybrid closure approximation
% Hybrid closure approximation to obtain 4th order orientation tensor
% from 2nd order tensor using quadratic and 3D linear closures
    % linear (planar) closure model
    a4_lin=Linear3D(a2);
    % quadratic closure
    a4_quad=Quadratic(a2);
    for i=1:3
        for j=1:3
            if i==1 && j==1
                f=3/2*a2(i,j)*a2(j,i)-1/2;
            else
                f=f+3/2*a2(i,j)*a2(j,i);
            end
        end
    end
    % f=1-27*det(a2);
    a4=(1-f)*a4_lin+f*a4_quad;
end


%%%%%%%%%%%%%%%%%%%%%%%%%%%%%%%%%%%%%%%%%%%%%%%%%%%%%%%%%%%%%%%%%%%%%%%%%%%

function [ a4 ] = Natural( a2 )
%Natural Natural closure approximation
%   Natural closure approximation to obtain the 4th order orientation
%   tensor from the 2nd order tensor
    for i=1:3
        for j=1:3
            for k=1:3
                for l=1:3

a4(i,j,k,l)=1/6*det(a2)*(kroneckerDelta(i,j)*kroneckerDelta(k,l)+kronec
kerDelta(i,k)*kroneckerDelta(j,l)+kroneckerDelta(i,l)*kroneckerDelta(j,
k))+1/3*(a2(i,j)*a2(k,l)+a2(i,k)*a2(j,l)+a2(i,l)+a2(j,k));
                end
            end
        end
    end
end
%%%%%%%%%%%%%%%%%%%%%%%%%%%%%%%%%%%%%%%%%%%%%%%%%%%%%%%%%%%%%%%%%%%%%%%%%%%
function [ a4 ] = OrthoFitted( a2 )
%OrthoFitted Orthotropic fitted closure approximation
%   Orthotropic fitted closure approximation to obtain 4th order
%   orientation tensor from 2nd order tensor.
    [eig_vec_a2, eig_val_a2]=eig(a2);
    eig_val_a2=diag(eig_val_a2);
    [max_eig_val, max_eig_val_ind]=max(eig_val_a2);
    [min_eig_val, min_eig_val_ind]=min(eig_val_a2);
```

```matlab
    if (max_eig_val_ind==1 && min_eig_val_ind==2) ||
(max_eig_val_ind==2 && min_eig_val_ind==1)
        mid_eig_val_ind=3;
    elseif (max_eig_val_ind==1 && min_eig_val_ind==3) ||
(max_eig_val_ind==3 && min_eig_val_ind==1)
        mid_eig_val_ind=2;
    else
        mid_eig_val_ind=1;
    end
    mid_eig_val=eig_val_a2(mid_eig_val_ind);
    A_bar_diag_123=[0.060964 0.371243 0.555301 -0.36916 0.318266
0.371218;
        0.124711 -0.389402 0.258844 0.086169 0.796080 0.544992;
        1.228982 -2.054116 0.821548 -2.260574 1.053907 1.819756]*[1;
max_eig_val; max_eig_val^2; mid_eig_val; mid_eig_val^2;
max_eig_val*mid_eig_val];
    A_bar_diag_456=[0 1 1; 1 0 1; 1 1 0]\[max_eig_val-
A_bar_diag_123(1); mid_eig_val-A_bar_diag_123(2); min_eig_val-
A_bar_diag_123(3)];
    A_bar=[A_bar_diag_123(1) A_bar_diag_456(3) A_bar_diag_456(2) 0 0 0;
        A_bar_diag_456(3) A_bar_diag_123(2) A_bar_diag_456(1) 0 0 0;
        A_bar_diag_456(2) A_bar_diag_456(1) A_bar_diag_123(3) 0 0 0;
        0 0 0 A_bar_diag_456(1) 0 0;
        0 0 0 0 A_bar_diag_456(2) 0;
        0 0 0 0 0 A_bar_diag_456(3);];
    a4_bar=ContractedNotation(A_bar);
    % Transform from principal axis system of 2nd order tensor back to
    % axis system of user input 2nd order tensor
    a4=a4transformation(a4_bar,a2);
end

%%%%%%%%%%%%%%%%%%%%%%%%%%%%%%%%%%%%%%%%%%%%%%%%%%%%%%%%%%%%%%%%%%%%%%%%

function [ a4 ] = OrthoFittedWide( a2 )
%OrthoFitted Orthotropic fitted wide closure approximation
%   Orthotropic fitted (wide interaction coefficient values) closure
approximation to obtain 4th order
%   orientation tensor from 2nd order tensor.
    [eig_vec_a2, eig_val_a2]=eig(a2);
    eig_val_a2=diag(eig_val_a2);
    [max_eig_val, max_eig_val_ind]=max(eig_val_a2);
    [min_eig_val, min_eig_val_ind]=min(eig_val_a2);
    if (max_eig_val_ind==1 && min_eig_val_ind==2) ||
(max_eig_val_ind==2 && min_eig_val_ind==1)
        mid_eig_val_ind=3;
    elseif (max_eig_val_ind==1 && min_eig_val_ind==3) ||
(max_eig_val_ind==3 && min_eig_val_ind==1)
        mid_eig_val_ind=2;
    else
        mid_eig_val_ind=1;
    end
    mid_eig_val=eig_val_a2(mid_eig_val_ind);
    A_bar_diag_123=[0.070055 0.339376 0.590331 -0.396796 0.333693
0.411944;
        0.115177 -0.368267 0.252880 0.094820 0.800181 0.535224;
```

```matlab
        1.249811 -2.148297 0.898521 -2.290157 1.044147 1.934914]*[1;
max_eig_val; max_eig_val^2; mid_eig_val; mid_eig_val^2;
max_eig_val*mid_eig_val];
    A_bar_diag_456=[0 1 1; 1 0 1; 1 1 0]\[max_eig_val-
A_bar_diag_123(1); mid_eig_val-A_bar_diag_123(2); min_eig_val-
A_bar_diag_123(3)];
    A_bar=[A_bar_diag_123(1) A_bar_diag_456(3) A_bar_diag_456(2) 0 0 0;
        A_bar_diag_456(3) A_bar_diag_123(2) A_bar_diag_456(1) 0 0 0;
        A_bar_diag_456(2) A_bar_diag_456(1) A_bar_diag_123(3) 0 0 0;
        0 0 0 A_bar_diag_456(1) 0 0;
        0 0 0 0 A_bar_diag_456(2) 0;
        0 0 0 0 0 A_bar_diag_456(3);];
    a4_bar=ContractedNotation(A_bar);
    % Transform from principal axis system of 2nd order tensor back to
    % axis system of user input 2nd order tensor
    a4=a4transformation(a4_bar,a2);
end

%%%%%%%%%%%%%%%%%%%%%%%%%%%%%%%%%%%%%%%%%%%%%%%%%%%%%%%%%%%%%%%%%%%%%%%%%

function [ a4 ] = OrthoSmooth( a2 )
    % OrthoSmooth Orthotropic smooth closure approximation
    % Orthotropic smooth closure approximation to obtain 4th order
orientation
    % tensor from 2nd order tensor.
    [eig_vec_a2, eig_val_a2]=eig(a2);
    eig_val_a2=diag(eig_val_a2);
    [max_eig_val, max_eig_val_ind]=max(eig_val_a2);
    [min_eig_val, min_eig_val_ind]=min(eig_val_a2);
    if (max_eig_val_ind==1 && min_eig_val_ind==2) ||
(max_eig_val_ind==2 && min_eig_val_ind==1)
        mid_eig_val_ind=3;
    elseif (max_eig_val_ind==1 && min_eig_val_ind==3) ||
(max_eig_val_ind==3 && min_eig_val_ind==1)
        mid_eig_val_ind=2;
    else
        mid_eig_val_ind=1;
    end
    mid_eig_val=eig_val_a2(mid_eig_val_ind);
    A_bar_diag_123=[-0.15+1.15*max_eig_val-0.10*mid_eig_val
        -0.15+0.15*max_eig_val+0.90*mid_eig_val
        0.60-0.60*max_eig_val-0.60*mid_eig_val];
    A_bar_diag_456=[0 1 1; 1 0 1; 1 1 0]\[max_eig_val-
A_bar_diag_123(1); mid_eig_val-A_bar_diag_123(2); min_eig_val-
A_bar_diag_123(3)];
    A_bar=[A_bar_diag_123(1) A_bar_diag_456(3) A_bar_diag_456(2) 0 0 0
        A_bar_diag_456(3) A_bar_diag_123(2) A_bar_diag_456(1) 0 0 0
        A_bar_diag_456(2) A_bar_diag_456(1) A_bar_diag_123(3) 0 0 0
        0 0 0 A_bar_diag_456(1) 0 0
        0 0 0 0 A_bar_diag_456(2) 0
        0 0 0 0 0 A_bar_diag_456(3)];
    a4_bar=ContractedNotation(A_bar);
    % Transform from principal axis system of 2nd order tensor back to
    % axis system of user input 2nd order tensor
    a4=a4transformation(a4_bar,a2);
end
```

```matlab
%%%%%%%%%%%%%%%%%%%%%%%%%%%%%%%%%%%%%%%%%%%%%%%%%%%%%%%%%%%%%%%%%%%%%%%%%

function [ C2 ] = OrientationAveraging(
a2,a4,B1inv,B2inv,B3inv,B4inv,B5inv )
%OrientationAveraging Given the orientation tensors and unidirectional
%fibre stiffness tensor invariants, compute the stiffness tensor
    for i=1:3
        for j=1:3
            for k=1:3
                for l=1:3

C2(i,j,k,l)=B1inv*a4(i,j,k,l)+B2inv*(a2(i,j)*kroneckerDelta(k,l)+a2(k,l
)*kroneckerDelta(i,j))+B3inv*(a2(i,k)*kroneckerDelta(j,l)+a2(i,l)*krone
ckerDelta(j,k)+a2(j,l)*kroneckerDelta(i,k)+a2(j,k)*kroneckerDelta(i,l))
+B4inv*kroneckerDelta(i,j)*kroneckerDelta(k,l)+B5inv*(kroneckerDelta(i,
k)*kroneckerDelta(j,l)+kroneckerDelta(i,l)*kroneckerDelta(j,k));
                end
            end
        end
    end
end

%%%%%%%%%%%%%%%%%%%%%%%%%%%%%%%%%%%%%%%%%%%%%%%%%%%%%%%%%%%%%%%%%%%%%%%%%


function [ C2matrix, C2 ] =
mat_anisotropic(a2in,closure_approximation,micromechanics_model,AR,vf_f
iber_max,flag_orientation,E_matrix,PR_matrix,E_fiber,PR_fiber,vf_fiber,
a4,flag_fld,fld,fibre_diameter)
%mat_anisotropic Find the stiffness tensor (C2) for an anisotropic
material
%given fibre and matrix properties, 2nd order orientation tensor,
closure approximation,
% fibre aspect ratio and micromechanics model

% find modulus of rigidity (shear) from elastic modulus
G_matrix=E_matrix/2/(1+PR_matrix);
G_fiber_AB=E_fiber/2/(1+PR_fiber); % fibre is anisotropic, this
equation may not yield a very accurate value

% Reformat the input 2nd order orientation tensor
a2=[a2in(1) a2in(4) a2in(5); a2in(4) a2in(2) a2in(6); a2in(5) a2in(6)
a2in(3)];

% micromechanics model
if micromechanics_model==1 % Generalized Self Consistent

C=GSC(E_matrix,PR_matrix,E_fiber,PR_fiber,vf_fiber,G_matrix,G_fiber_AB)
;
elseif micromechanics_model==2 % Mori Tanaka

C=MoriTanaka(AR,E_matrix,PR_matrix,E_fiber,PR_fiber,vf_fiber,G_matrix,G
_fiber_AB,flag_fld,fld,fibre_diameter);
elseif micromechanics_model==3 % Halpin_Tsai
```

```matlab
C=HalpinTsai(AR,E_matrix,PR_matrix,E_fiber,PR_fiber,vf_fiber,vf_fiber_m
ax,G_matrix,G_fiber_AB,flag_fld,fld,fibre_diameter);
end

% Unidirectional fibre composite stiffness matrix invariants
B1inv=C(1,1)+C(2,2)-2*C(1,2)-4*C(6,6);
B2inv=C(1,2)-C(2,3);
B3inv=C(6,6)+0.5*(C(2,3)-C(2,2));
B4inv=C(2,3);
B5inv=0.5*(C(2,2)-C(2,3));

% Estimate the 4th order orientation tensor with a closure
approximation,
% if necessary
if flag_orientation == 1 || flag_orientation==3 || flag_orientation==5
|| flag_orientation==6
    if closure_approximation==1
        % Linear 3D closure approximation
        a4=Linear3D(a2);
    elseif closure_approximation==2
        % Linear 2D closure approximation
        a4=Linear2D(a2);
    elseif closure_approximation==3
        % Quadratic closure approximation
        a4=Quadratic(a2);
    elseif closure_approximation==4
        % Hybrid 3D closure approximation
        a4=Hybrid3D(a2);
    elseif closure_approximation==5
        % Hybrid 2D closure approximation
        a4=Hybrid2D(a2);
    elseif closure_approximation==6
        % Orthotropic smooth closure
        a4=OrthoSmooth(a2);
    elseif closure_approximation==7
        % orthotropic fitted
        a4=OrthoFitted(a2);
    elseif closure_approximation==8
        % natural closure
        a4=Natural(a2);
    elseif closure_approximation==9
        % Orthotropic closure for wide (range of?) interaction
coefficients
        a4=OrthoFittedWide(a2);
    end
end

% Orientation averaging
C2=OrientationAveraging(a2,a4,B1inv,B2inv,B3inv,B4inv,B5inv);

% Reformat 4th order stiffness tensor into 6 x 6 stiffness matrix
C2matrix=[C2(1,1,1,1) C2(1,1,2,2) C2(1,1,3,3) C2(1,1,2,3) C2(1,1,1,3)
C2(1,1,1,2);
        C2(2,2,1,1) C2(2,2,2,2) C2(2,2,3,3) C2(2,2,2,3) C2(2,2,1,3)
C2(2,2,1,2);
```

```matlab
        C2(3,3,1,1) C2(3,3,2,2) C2(3,3,3,3) C2(3,3,2,3) C2(3,3,1,3)
C2(3,3,1,2);
        C2(2,3,1,1) C2(2,3,2,2) C2(2,3,3,3) C2(2,3,2,3) C2(2,3,1,3)
C2(2,3,1,2);
        C2(1,3,1,1) C2(1,3,2,2) C2(1,3,3,3) C2(1,3,2,3) C2(1,3,1,3)
C2(1,3,1,2);
        C2(1,2,1,1) C2(1,2,2,2) C2(1,2,3,3) C2(1,2,2,3) C2(1,2,1,3)
C2(1,2,1,2)];


end % end function



%%%%%%%%%%%%%%%%%%%%%%%%%%%%%%%%%%%%%%%%%%%%%%%%%%%%%%%%%%%%%%%%%%%%%%%%%


function [ a4 ] = a4transformation( a4_bar,a2 )
%a4transformation Transform orthotropic 4th order orientation tensor
%    Transform orthotropic 4th order orientation tensor from principal
axis
%    system of 2nd order tensor to global reference frame.
    [eig_vec_a2, eig_val_a2]=eig(a2);
    eig_val_a2=diag(eig_val_a2);
    [max_eig_val, max_eig_val_ind]=max(eig_val_a2);
    [min_eig_val, min_eig_val_ind]=min(eig_val_a2);
    if (max_eig_val_ind==1 && min_eig_val_ind==2) ||
(max_eig_val_ind==2 && min_eig_val_ind==1)
        mid_eig_val_ind=3;
    elseif (max_eig_val_ind==1 && min_eig_val_ind==3) ||
(max_eig_val_ind==3 && min_eig_val_ind==1)
        mid_eig_val_ind=2;
    else
        mid_eig_val_ind=1;
    end

    e{1}=eig_vec_a2(:,max_eig_val_ind);
    e [1]=eig_vec_a2(:,mid_eig_val_ind);
    e{3}=eig_vec_a2(:,min_eig_val_ind);
    ep{1}=[1; 0; 0];
    ep [1]=[0; 1; 0];
    ep{3}=[0; 0; 1];
    if (dot(cross(e{1},e [1]),e{3}))<0
%         e3_old=e{3};
%         e{3}=e [1];
%         e [1]=e3_old;
        e{3}=-e{3};
        %disp('LH coordinate system changed to RH.')
        %disp(dot(cross(e{1},e [1]),e{3}))
    end
%     tmx=[e{1} e [1] e{3}];
%     a4=transform(a4_bar,tmx);
    for i=1:3
        for j=1:3
            for k=1:3
                for l=1:3
                    for m=1:3
                        for n=1:3
```

250

```matlab
                                for o=1:3
                                    for p=1:3
                                        if m==1 && n==1 && o==1 && p==1

a4(i,j,k,l)=dot(e{m},ep{i})*dot(e{n},ep{j})*dot(e{o},ep{k})*dot(e{p},ep
{l})*a4_bar(m,n,o,p);
                                        else

a4(i,j,k,l)=a4(i,j,k,l)+dot(e{m},ep{i})*dot(e{n},ep{j})*dot(e{o},ep{k})
*dot(e{p},ep{l})*a4_bar(m,n,o,p);
                                        end
                                    end
                                end
                            end
                        end
                    end
                end
            end
        end
    end
end


%%%%%%%%%%%%%%%%%%%%%%%%%%%%%%%%%%%%%%%%%%%%%%%%%%%%%%%%%%%%%%%%%%%%%%%%%

function [ a4_bar ] = ContractedNotation( A_bar )
%ContractedNotation Convert 4th order tensor to contracted notation
%   Convert 4th order tensor to contracted notation
    for m=1:6
        for n=1:6
            if (m==1 || m==2 || m==3) && (n==1 || n==2 || n==3)
                a4_bar(m,m,n,n)=A_bar(m,n);
            elseif (m==1 || m==2 || m==3) && n==4
                a4_bar(m,m,2,3)=A_bar(m,n);
                a4_bar(m,m,3,2)=A_bar(m,n);
            elseif (m==1 || m==2 || m==3) && n==5
                a4_bar(m,m,1,3)=A_bar(m,n);
                a4_bar(m,m,3,1)=A_bar(m,n);
            elseif (m==1 || m==2 || m==3) && n==6
                a4_bar(m,m,1,2)=A_bar(m,n);
                a4_bar(m,m,2,1)=A_bar(m,n);
            elseif (n==1 || n==2 || n==3) && m==4
                a4_bar(2,3,n,n)=A_bar(m,n);
                a4_bar(3,2,n,n)=A_bar(m,n);
            elseif (n==1 || n==2 || n==3) && m==5
                a4_bar(1,3,n,n)=A_bar(m,n);
                a4_bar(3,1,n,n)=A_bar(m,n);
            elseif (n==1 || n==2 || n==3) && m==6
                a4_bar(1,2,n,n)=A_bar(m,n);
                a4_bar(2,1,n,n)=A_bar(m,n);
            elseif m==4 && n==4
                a4_bar(2,3,2,3)=A_bar(m,n);
                a4_bar(3,2,3,2)=A_bar(m,n);
                a4_bar(2,3,3,2)=A_bar(m,n);
                a4_bar(3,2,2,3)=A_bar(m,n);
            elseif m==5 && n==5
                a4_bar(1,3,1,3)=A_bar(m,n);
                a4_bar(3,1,3,1)=A_bar(m,n);
```

251

```matlab
                a4_bar(1,3,3,1)=A_bar(m,n);
                a4_bar(3,1,1,3)=A_bar(m,n);
            elseif m==6 && n==6
                a4_bar(1,2,1,2)=A_bar(m,n);
                a4_bar(2,1,2,1)=A_bar(m,n);
                a4_bar(1,2,2,1)=A_bar(m,n);
                a4_bar(2,1,1,2)=A_bar(m,n);
            elseif m==4 && n==5
                a4_bar(2,3,1,3)=A_bar(m,n);
                a4_bar(3,2,3,1)=A_bar(m,n);
                a4_bar(2,3,3,1)=A_bar(m,n);
                a4_bar(3,2,1,3)=A_bar(m,n);
            elseif m==4 && n==6
                a4_bar(2,3,1,2)=A_bar(m,n);
                a4_bar(3,2,2,1)=A_bar(m,n);
                a4_bar(2,3,2,1)=A_bar(m,n);
                a4_bar(3,2,1,2)=A_bar(m,n);
            elseif m==5 && n==6
                a4_bar(1,3,1,2)=A_bar(m,n);
                a4_bar(3,1,2,1)=A_bar(m,n);
                a4_bar(1,3,2,1)=A_bar(m,n);
                a4_bar(3,1,1,2)=A_bar(m,n);
            elseif m==5 && n==4
                a4_bar(1,3,3,2)=A_bar(m,n);
                a4_bar(3,1,2,3)=A_bar(m,n);
                a4_bar(1,3,2,3)=A_bar(m,n);
                a4_bar(3,1,3,2)=A_bar(m,n);
            elseif m==6 && n==5
                a4_bar(2,1,1,3)=A_bar(m,n);
                a4_bar(1,2,3,1)=A_bar(m,n);
                a4_bar(2,1,3,1)=A_bar(m,n);
                a4_bar(1,2,1,3)=A_bar(m,n);
            elseif m==6 && n==4
                a4_bar(1,2,3,2)=A_bar(m,n);
                a4_bar(2,1,2,3)=A_bar(m,n);
                a4_bar(1,2,2,3)=A_bar(m,n);
                a4_bar(2,1,3,2)=A_bar(m,n);
            end
        end
    end
end

%%%%%%%%%%%%%%%%%%%%%%%%%%%%%%%%%%%%%%%%%%%%%%%%%%%%%%%%%%%%%%%%%%%%%%%%%%

function [ Stiffness_tensor_rotated ] = Tensor_rotation( S2,theta )
    %Tensor_rotation Tensor rotational transformation
    %   Rotate stiffness (or any other) tensor with the given input
    %   transformation.
    % original reference frame
    e{1}=[1; 0; 0];
    e [1]=[0; 1; 0];
    e{3}=[0; 0; 1];
    % local reference frame
    ep{1}=[cos(theta); sin(theta); 0];
    ep [1]=[cos(theta+pi/2); sin(theta+pi/2); 0];
    ep{3}=e{3};
```

```matlab
        if (dot(cross(ep{1},ep [1]),ep{3}))<0
            ep{3}=-ep{3};
            disp(dot(cross(ep{1},ep [1]),ep{3}))
        end
        for i=1:3
            for j=1:3
                for k=1:3
                    for l=1:3
                        for m=1:3
                            for n=1:3
                                for o=1:3
                                    for p=1:3
                                        if m==1 && n==1 && o==1 && p==1

S2_rotated(i,j,k,l)=dot(e{m},ep{i})*dot(e{n},ep{j})*dot(e{o},ep{k})*dot
(e{p},ep{l})*S2(m,n,o,p);
                                        else

S2_rotated(i,j,k,l)=S2_rotated(i,j,k,l)+dot(e{m},ep{i})*dot(e{n},ep{j})
*dot(e{o},ep{k})*dot(e{p},ep{l})*S2(m,n,o,p);
                                        end
                                    end
                                end
                            end
                        end
                    end
                end
            end
        end
    Stiffness_tensor_rotated=[S2_rotated(1,1,1,1) S2_rotated(1,1,2,2)
S2_rotated(1,1,3,3) S2_rotated(1,1,2,3) S2_rotated(1,1,1,3)
S2_rotated(1,1,1,2);
    S2_rotated(2,2,1,1) S2_rotated(2,2,2,2) S2_rotated(2,2,3,3)
S2_rotated(2,2,2,3) S2_rotated(2,2,1,3) S2_rotated(2,2,1,2);
    S2_rotated(3,3,1,1) S2_rotated(3,3,2,2) S2_rotated(3,3,3,3)
S2_rotated(3,3,2,3) S2_rotated(3,3,1,3) S2_rotated(3,3,1,2);
    S2_rotated(2,3,1,1) S2_rotated(2,3,2,2) S2_rotated(2,3,3,3)
S2_rotated(2,3,2,3) S2_rotated(2,3,1,3) S2_rotated(2,3,1,2);
    S2_rotated(1,3,1,1) S2_rotated(1,3,2,2) S2_rotated(1,3,3,3)
S2_rotated(1,3,2,3) S2_rotated(1,3,1,3) S2_rotated(1,3,1,2);
    S2_rotated(1,2,1,1) S2_rotated(1,2,2,2) S2_rotated(1,2,3,3)
S2_rotated(1,2,2,3) S2_rotated(1,2,1,3) S2_rotated(1,2,1,2)];
end


%%%%%%%%%%%%%%%%%%%%%%%%%%%%%%%%%%%%%%%%%%%%%%%%%%%%%%%%%%%%%%%%%%%%%%%%%%%

% MATLAB code to map fibre orientation from a Moldflow process model to
an LS-DYNA structural model

clear all
close all
clc
format long

% 1) Use the same coordinate system (not necessarily the same
% geometry) for the process and structural models.
```

```matlab
% 2) This script can create one material model per element of the LS-
% DYNA model.
% 3) Highly recommended to simplify the LS-DYNA model to only a mesh of
% just the part (or region of a part) of interest for this application.
% A mixture of shell and solid elements in the part used with this
% script will likely cause problems.
% 4) Linear elastic only.
% 5) V1 features:
% Micromechanics models: Halpin-Tsai, GSC, Mori-Tanaka
% Closure approximations: 1) Linear, 2) Quadratic, 3) Hybrid, 4)
% Orthotropic Smooth, 5) Orthotropic Fitted, 6) Natural
% LS-DYNA elements: Hexahedrons only (no collapsed hexahedrons =
% pentahedrons)
% Moldflow: Tetrahedrons only (no other option, as of the time this
% script was written, for a Moldflow model employing solid elements)
% 6) Features to be added:
% Non-linear stress-strain characteristics and/or failure
% Support for tetrahedron and shell elements in LS-DYNA
% Support for orientation prediction of Moldex
% The material reference frame in the LS-DYNA model is currently fixed.
% Ideally, the solver would automatically convert the material
% properties currently computed in the global reference frame to the
% local material reference frame (defined using the nodes of each
% element). If an element undergoes significant rotations, V1 of this
% script will not accurately predict material characteristics.
%%%%%%%%%%%%%%%%%%%%%%%%%%%%%%%%%%%%%%%%%%%%%%%%%%%%%%%%%%%%%%%%%%%%%%%%
% User inputs
flag_orientation=2; % 1) 2nd order orientation tensor given and closure
% approximation specified below, 2) 2nd and 4th order orientation
% tensors given, 3) several 2nd order orientation tensors and locations
% given, 4) several 2nd and 4th order orientation tensors and locations
% given, 5) Moldflow model, 6) Moldex model (not implemented)
%%%%%%%%%%%%%%%%%%%%%%%%%%%%%%%%%%%%%%%%%%%%%%%%%%%%%%%%%%%%%%%%%%%%%%%%
if flag_orientation==1 % 2nd order tensor
    a2=load('a2.mat');
    a2=a2.a2;
    a2=[a2(1,1) a2(2,2) a2(3,3) a2(1,2) a2(1,3) a2(2,3)];
    a2=[0.77084 0.17931 0.029907    0.019882    0.0083573];
    a2=[a2(1) a2(2) 1-a2(1)-a2(2) a2(3) a2(4) a2(5)];
elseif flag_orientation==2 % 2nd and 4th order tensors
    a2=load('a2.mat');
    a2=a2.a2;
    a2=[a2(1,1) a2(2,2) a2(3,3) a2(1,2) a2(1,3) a2(2,3)];
    a4=load('a4.mat');
    a4=a4.a4;
elseif flag_orientation==3 % 2nd order tensors with positions
    x_coord=[-300 -200 -100 0 100 200 300]'; % x coordinates of a2
tensors
    y_coord=[-300 -200 -100 0 100 200 300]'; % y coordinates of a2
tensors
    z_coord=[-300 -200 -100 0 100 200 300]'; % z coordinates of a2
tensors
    A2xx=[1 1 1 1 1 1 1]'; % xx components of a2 tensors
    A2yy=[0 0 0 0 0 0 0]'; % yy components of a2 tensors
    A2zz=[0 0 0 0 0 0 0]'; % zz components of a2 tensors
    A2xy=[0 0 0 0 0 0 0]'; % xy components of a2 tensors
    A2xz=[0 0 0 0 0 0 0]'; % xz components of a2 tensors
```

254

```matlab
    A2yz=[0 0 0 0 0 0 0]'; % yz components of a2 tensors
    Axx=scatteredInterpolant(x_coord,y_coord,z_coord,A2xx);
    Ayy=scatteredInterpolant(x_coord,y_coord,z_coord,A2yy);
    Azz=scatteredInterpolant(x_coord,y_coord,z_coord,A2zz);
    Axy=scatteredInterpolant(x_coord,y_coord,z_coord,A2xy);
    Axz=scatteredInterpolant(x_coord,y_coord,z_coord,A2xz);
    Ayz=scatteredInterpolant(x_coord,y_coord,z_coord,A2yz);
elseif flag_orientation==4
    disp('Not implemented.')
end
%%%%%%%%%%%%%%%%%%%%%%%%%%%%%%%%%%%%%%%%%%%%%%%%%%%%%%%%%%%%%%%%%%%%%
% Fibre length distribution
flag_fld=0; % activated if flag = 1, de-activated if flag = 0
fld=load('fld6.mat');
fld=fld.fld; % probability density function (fibre length)
fibre_diameter=7; % microns - units should be consistent with fld data
fld(:,2)=fld(:,2)/trapz(fld(:,1),fld(:,2)); % scale fld such that
integral = 1 (PDF)
% test case, normal distribution, mean length 2 mm, standard deviation
0.1 mm
%     fld2(:,1)=linspace(0,3)*1000;
%     fld2(:,2)=normpdf(fld2(:,1),2*1000,0.1*1000);
%     fld=fld2;
%%%%%%%%%%%%%%%%%%%%%%%%%%%%%%%%%%%%%%%%%%%%%%%%%%%%%%%%%%%%%%%%%%%%%
% Coordinate transformation
% Not currently implemented in LS-DYNA model
% A version of this may eventually be used to transform material
properties
% for each element and use element coordinate system
% V1_03: only rotation about z-axis
flag_rotation=0; % set to 1 to perform a rotational transformation, 0
for no transformation
theta=45*pi/180; % radians
%%%%%%%%%%%%%%%%%%%%%%%%%%%%%%%%%%%%%%%%%%%%%%%%%%%%%%%%%%%%%%%%%%%%%
element_type='hexahedron'; % LSDYNA model (Moldflow elements are always
tetrahedrons for compression molding)
% Other Moldflow elements ('shell' elements for injection molding for
% example) have not been tested. The sections to read the Moldflow
model
% are unlikely to interpret such a model correctly.
% IMPORTANT: LS-DYNA element types other than hexahedron, including
collapsed hexahedrons
% (pentahedrons) are NOT currently implemented
scatteredInterpolant_method='nearest'; % scatteredInterpolant method to
extract orientation tensor from Moldflow results by position
flag_moldflow_elements=0; % If this flag is set to 1, element data is
extracted from Moldflow model, not currently used
flag_unique_material=1; % If this flag is set to 1, generate a unique
material model for each element of the LS-DYNA model
% Unique material models for each element requires one part for each
element which may result in a very large and computationally expensive
model
material_accuracy=0.1; % If the unique material flag is 0, this
parameter will be used to determine if fibre orientation
% is significantly different from the orientation of the previous
element (sum of relative errors for each orientation tensor entry)
secid=1; % LSDYNA element formulation ID
```

```
material_model=1; % LS-DYNA material model, 1) mat_anisotropic
closure_approximation=3; % 1) 'linear 3D', 2) 'linear 2D', 3)
'quadratic', 4) 'hybrid 3D', 5) 'hybrid 2D',
% 6) 'orthotropic smooth', 7) 'orthotropic fitted', 8) 'natural', and
9) Orthotropic Wide (ORW) currently implemented
% Natural closure is implemented but probably just a planar FOD version
and no assessment of whether it has been implemented correctly has been
run in any way.
micromechanics_model=3; % 1) 'GSC' (Generalized Self Consistent), 2)
'Mori-Tanaka', 3) 'Halpin-Tsai' currently implemented
AOPT=0; % Method by which local coordinate system is defined in LS-DYNA
% Only AOPT = 2 is currently implemented.
unit_system=2; % LS-DYNA model unit system 1) m, s, kg, N, Pa, 2) mm,
s, tonne, N, MPa, 3) mm, ms, kg, kN, GPa
% Note that length unit is already defined in LS-DYNA and Moldflow
models and should be consistent with the unit system selected here
% This is also addressed elsewhere, but the coordinate systems of the
% structural and process models must also be consistent for correct
mapping of fibre orientation.
%%%%%%%%%%%%%%%%%%%%%%%%%%%%%%%%%%%%%%%%%%%%%%%%%%%%%%%%%%%%%%%%%%%%%%%%%
% Material properties
% Do not change the units if using one of the LS-DYNA unit systems
above
% Conversions are completed automatically within this script.
wf_fiber=0.09; % weight fraction of fibre (in the range of 0 to 1)
%%%%%%%%%%%%%%%%%%%%%%%%%%%%%%%%%%%%%%%%%%%%%%%%%%%%%%%%%%%%%%%%%%%%%%%%%
E_matrix=2500; % MPa, elastic modulus of the matrix
PR_matrix=0.39; % potentially unreliable data (found online)
E_fiber=240000; % MPa, longitudinal fiber modulus, from TohoTenax test
report
% E_fiber=E_fiber*a2(1)+E_fiber/16*(1-a2(1)); % fiber modulus
adjustment for anisotropy, based on properties on pg 80 of Principles
of Composite Material Mechanics by Gibson
% E_fiber=240000/16;
PR_fiber=0.2; % Poisson's ratio of carbon fiber, from pg 80 of
Principles of Composite Material Mechanics by Gibson
rho_matrix=1.13; % g/cc, density of matrix (BASF Ultramid B22 NE 01),
from BASF datasheet (available by request from BASF)
rho_fiber=1.81; % g/cc, data in report from TohoTenax (sent by Vanja at
the FPC)
vf_fiber=rho_matrix*wf_fiber/(rho_fiber*(1-
wf_fiber)+rho_matrix*wf_fiber); % volume fraction of fiber
rho_composite=rho_fiber*vf_fiber+rho_matrix*(1-vf_fiber); % composite
density
AR=133.22; % Fibre aspect ratio, define this even if FLD is used to
avoid errors
Cmin=4; % minimum for random 3D fibre orientation
Cmax=30; % maximum for in plane random fibre orientation
vf_fiber_max=Cmax/AR; % maximum fibre volume fraction, used only for
Halpin-Tsai micromechanics model
% can be as high as 0.8-0.9 for well aligned fibre which is not
expected here
% can be as low as 0.1 for high aspect ratio fibres with a random FOD
%%%%%%%%%%%%%%%%%%%%%%%%%%%%%%%%%%%%%%%%%%%%%%%%%%%%%%%%%%%%%%%%%%%%%%%%%%%
%%%%%%%%%%%%%%%%%%%%%%%%%%%%%%%%%%%%%%%%%%%%%%%%%%%%%%%%%%%%%%%%%%%%%%%%%%%
% End of user inputs
```

```matlab
% It should not be necessary to modify any code past this point.
%%%%%%%%%%%%%%%%%%%%%%%%%%%%%%%%%%%%%%%%%%%%%%%%%%%%%%%%%%%%%%%%%%%%%%%%%
%%%%%%%%%%%%%%%%%%%%%%%%%%%%%%%%%%%%%%%%%%%%%%%%%%%%%%%%%%%%%%%%%%%%%%%%%
% LS-DYNA unit system conversion
if unit_system==1
    E_matrix=E_matrix*1E6;
    E_fiber=E_fiber*1E6;
    rho_composite=rho_composite*1E3;
elseif unit_system==2
    rho_composite=rho_composite*1E-9;
elseif unit_system==3
    E_matrix=E_matrix/1E3;
    E_fiber=E_fiber/1E3;
    rho_composite=rho_composite*1E-6;
end
%%%%%%%%%%%%%%%%%%%%%%%%%%%%%%%%%%%%%%%%%%%%%%%%%%%%%%%%%%%%%%%%%%%%%%%%%
%%%%%%%%%%%%%%%%%%%%%%%%%%%%%%%%%%%%%%%%%%%%%%%%%%%%%%%%%%%%%%%%%%%%%%%%%
if flag_orientation==4
    % Load Moldflow data
    %% Initialize variables.
    Moldflow_model=glob('*.udm');
    filename = Moldflow_model{1};
    delimiter = ' ';

    %% Format string for each line of text:
    % For more information, see the TEXTSCAN documentation.
    formatSpec = '%s%s%s%s%s%s%s%s%s%s%s%s%s%[^\n\r]';

    %% Open the Moldflow model.
    fileID = fopen(filename,'r');

    %% Read columns of data according to format string.
    dataArray = textscan(fileID, formatSpec, 'Delimiter', delimiter,
'MultipleDelimsAsOne', true, 'EmptyValue' ,NaN, 'ReturnOnError',
false);

    %% Close the text file.
    fclose(fileID);

    %% Allocate imported array to column variable names
    Column_A = dataArray{:, 1};
    Column_B = dataArray{:, 2};
    Column_C = dataArray{:, 3};
    Column_D = dataArray{:, 4};
    Column_E = dataArray{:, 5};
    Column_F = dataArray{:, 6};
    Column_G = dataArray{:, 7};
    Column_H = dataArray{:, 8};
    Column_I = dataArray{:, 9};
    Column_J = dataArray{:, 10};
    Column_K = dataArray{:, 11};
    Column_L = dataArray{:, 12};

    %% Clear temporary variables
    clear filename delimiter formatSpec fileID dataArray ans;
```

```matlab
    flag_nodal_data=0;
    counter_nodal_data=1;
    counter_element_data=1;

    % find first and last rows with nodal and element data
    for i=1:length(Column_A)
        if flag_nodal_data~=2 && strcmp(Column_B(i),'NODE{LABEL')
            first_nodal_data_line=i+1;
            flag_nodal_data=1;
        elseif flag_nodal_data==1 && strcmp(Column_B(i),'Beginning')
            last_nodal_data_line=i-1;
            first_element_data_line=i+4;
            flag_nodal_data=2;
        end

    end

    % Define size of nodal data matrix for efficiency
    % Otherwise MATLAB will re-evaluate how to store this data on each
loop iteration
    nodal_data_moldflow=zeros(last_nodal_data_line-
first_nodal_data_line+1,4);

    % Extract Moldflow nodal data
    for i=first_nodal_data_line:last_nodal_data_line

nodal_data_moldflow(counter_nodal_data,:)=[sscanf(char(Column_A(i)),'NO
DE{%u') str2num(char(Column_F(i))) str2num(char(Column_G(i)))
sscanf(char(Column_H(i)),'%f}')];
        counter_nodal_data=counter_nodal_data+1;
    end

    % Extract Moldflow element data
    if flag_moldflow_elements==1
        element_data_moldflow=zeros(length(Column_A)-
first_element_data_line,5);
        for i=first_element_data_line:(length(Column_A)-1)

element_data_moldflow(counter_element_data,:)=[sscanf(char(Column_A(i))
,'TET4{%u') str2double(char(Column_I(i))) str2double(char(Column_J(i)))
str2double(char(Column_K(i))) sscanf(char(Column_L(i)),'%u}')];
            counter_element_data=counter_element_data+1;
        end
    end

    clear Column_A Column_B Column_C Column_D Column_E Column_F
Column_G Column_H Column_I Column_J Column_K Column_L;
    disp('Moldflow nodal and/or element data processed.')


%%%%%%%%%%%%%%%%%%%%%%%%%%%%%%%%%%%%%%%%%%%%%%%%%%%%%%%%%%%%%%%%%%%%%%%%%
%%%%%%%%%%%%%%%%%%%%%%%%%%%%%%%%%%%%%%%%%%%%%%%%%%%%%%%%%%%%%%%%%%%%%%%%%
    % load Moldflow orientation tensor data
    orientation_tensor_file=glob('*.nod');
```

258

```matlab
    orientation_tensors=dlmread(orientation_tensor_file{1},' ',3,0);
    orientation_tensors=orientation_tensors(:,3:9);

    %%%%%%%%%%%%%%%%%%%%%%%%%%%%%%%%%%%%%%%%%%%%%%%%%%%%%%%%%%%%%%%%%%%%%%%
    % Add orientation tensors to Moldflow nodal data matrix

temp_orientation=array2table(orientation_tensors,'VariableNames',{'Node
ID','Axx','Ayy','Azz','Axy','Axz','Ayz'});

temp_moldflow_nodes=array2table(nodal_data_moldflow,'VariableNames',{'N
odeID','X','Y','Z'});

nodal_data_moldflow=table2array(innerjoin(temp_moldflow_nodes,temp_orie
ntation));
    clear temp_orientation temp_moldflow_nodes orientation_tensors

    % Use scattered interpolant to obtain the relationship between
location and
    % each component of the orientation tensor

Axx=scatteredInterpolant(nodal_data_moldflow(:,2),nodal_data_moldflow(:
,3),nodal_data_moldflow(:,4),nodal_data_moldflow(:,5));

Ayy=scatteredInterpolant(nodal_data_moldflow(:,2),nodal_data_moldflow(:
,3),nodal_data_moldflow(:,4),nodal_data_moldflow(:,6));

Azz=scatteredInterpolant(nodal_data_moldflow(:,2),nodal_data_moldflow(:
,3),nodal_data_moldflow(:,4),nodal_data_moldflow(:,7));

Axy=scatteredInterpolant(nodal_data_moldflow(:,2),nodal_data_moldflow(:
,3),nodal_data_moldflow(:,4),nodal_data_moldflow(:,8));

Axz=scatteredInterpolant(nodal_data_moldflow(:,2),nodal_data_moldflow(:
,3),nodal_data_moldflow(:,4),nodal_data_moldflow(:,9));

Ayz=scatteredInterpolant(nodal_data_moldflow(:,2),nodal_data_moldflow(:
,3),nodal_data_moldflow(:,4),nodal_data_moldflow(:,10));
    disp('Moldflow orientation data processed.')
end

    %%%%%%%%%%%%%%%%%%%%%%%%%%%%%%%%%%%%%%%%%%%%%%%%%%%%%%%%%%%%%%%%%%%%%%%
% Each element has a unique material model
if flag_orientation==3 || flag_orientation==4 || flag_orientation==5 ||
flag_orientation==6

    %%%%%%%%%%%%%%%%%%%%%%%%%%%%%%%%%%%%%%%%%%%%%%%%%%%%%%%%%%%%%%%%%%%%%%%
    %%%%%%%%%%%%%%%%%%%%%%%%%%%%%%%%%%%%%%%%%%%%%%%%%%%%%%%%%%%%%%%%%%%%%%%
    % Load LS-DYNA model data
    %%%%%%%%%%%%%%%%%%%%%%%%%%%%%%%%%%%%%%%%%%%%%%%%%%%%%%%%%%%%%%%%%%%%%%%
    % load nodal data from LS-DYNA model
    DYNA_files=glob('*.dyn');
    filename_nodes = DYNA_files{1};
    fileID_LSDYNA = fopen(filename_nodes,'r');
    formatSpec_nodes = '%8s%16s%16s%16s%[^\n\r]';
    dataArrayNodes = textscan(fileID_LSDYNA, formatSpec_nodes);
    NodeID=dataArrayNodes{1};
```

```matlab
    NodeX=dataArrayNodes [1];
    NodeY=dataArrayNodes{3};
    NodeZ=dataArrayNodes{4};

    clear dataArrayNodes

    for i=1:length(NodeID)
        if strcmp(NodeID{i},'*NODE')
            line_1_nodes=i+2; % the integer added to i (currently 1)
may need to be adjusted in some cases (Hypermesh inserts a few lines of
text for example)
        elseif strcmp(NodeID{i},'*ELEMENT')
            line_1_elements=i+2;
        end
    end

    if line_1_nodes<line_1_elements % nodal data is before element data
        line_last_nodes=line_1_elements-1;
        for i=1:length(NodeID)
            if strcmp(NodeID{i},'*END')
                line_last_elements=i-1;
            end
        end
    else % nodal data is after element data
        line_last_elements=line_1_nodes-1;
        for i=1:length(NodeID)
            if strcmp(NodeID{i},'*END')
                line_last_nodes=i-1;
            end
        end
    end

    NodeID=NodeID(line_1_nodes:line_last_nodes);
    NodeID=str2double(NodeID);
    NodeX=NodeX(line_1_nodes:line_last_nodes);
    NodeX=str2double(NodeX);
    NodeY=NodeY(line_1_nodes:line_last_nodes);
    NodeY=str2double(NodeY);
    NodeZ=NodeZ(line_1_nodes:line_last_nodes);
    NodeZ=str2double(NodeZ);
    Node_data_LSDYNA=[NodeID NodeX NodeY NodeZ];
    clear NodeID NodeX NodeY NodeZ;


    %%%%%%%%%%%%%%%%%%%%%%%%%%%%%%%%%%%%%%%%%%%%%%%%%%%%%%%%%%%%%%%%%%%%%%%%
    % load element data from LS-DYNA model
    fileID_LSDYNA2 = fopen(filename_nodes,'r');
    if strcmp(element_type,'hexahedron')
        formatSpec_elements = '%8s%8s%8s%8s%8s%8s%8s%8s%8s%8s%[^\n\r]';
        dataArrayElements = textscan(fileID_LSDYNA2,
formatSpec_elements);
        ElementID=dataArrayElements{1};
        PartID=dataArrayElements [1];
        ElementNode1=dataArrayElements{3};
        ElementNode2=dataArrayElements{4};
        ElementNode3=dataArrayElements{5};
```

```matlab
        ElementNode4=dataArrayElements [1];
        ElementNode5=dataArrayElements{7};
        ElementNode6=dataArrayElements [1];
        ElementNode7=dataArrayElements{9};
        ElementNode8=dataArrayElements{10};
    end

    ElementID=ElementID(line_1_elements:line_last_elements);
    ElementID=str2double(ElementID);
    PartID=PartID(line_1_elements:line_last_elements);
    PartID=str2double(PartID);
    ElementNode1=ElementNode1(line_1_elements:line_last_elements);
    ElementNode1=str2double(ElementNode1);
    ElementNode2=ElementNode2(line_1_elements:line_last_elements);
    ElementNode2=str2double(ElementNode2);
    ElementNode3=ElementNode3(line_1_elements:line_last_elements);
    ElementNode3=str2double(ElementNode3);
    ElementNode4=ElementNode4(line_1_elements:line_last_elements);
    ElementNode4=str2double(ElementNode4);
    if strcmp(element_type,'hexahedron')
        ElementNode5=ElementNode5(line_1_elements:line_last_elements);
        ElementNode5=str2double(ElementNode5);
        ElementNode6=ElementNode6(line_1_elements:line_last_elements);
        ElementNode6=str2double(ElementNode6);
        ElementNode7=ElementNode7(line_1_elements:line_last_elements);
        ElementNode7=str2double(ElementNode7);
        ElementNode8=ElementNode8(line_1_elements:line_last_elements);
        ElementNode8=str2double(ElementNode8);
        Element_data_LSDYNA=[ElementID PartID ElementNode1 ElementNode2
ElementNode3 ElementNode4 ElementNode5 ElementNode6 ElementNode7
ElementNode8];
        clear dataArrayElements ElementID PartID ElementNode1
ElementNode2 ElementNode3 ElementNode4 ElementNode5 ElementNode6
ElementNode7 ElementNode8;
    end

    disp('Nodal and/or element data from LS-DYNA model processed.')




%%%%%%%%%%%%%%%%%%%%%%%%%%%%%%%%%%%%%%%%%%%%%%%%%%%%%%%%%%%%%%%%%%%%%%%%%%
    % Add nodal positions to LS-DYNA element data
    if strcmp(element_type,'hexahedron')
        LSDYNA_nodes_per_element=8;

temp_Element_data_LSDYNA=array2table(Element_data_LSDYNA,'VariableNames
',{'ElementID','PartID','Node1','Node2','Node3','Node4','Node5','Node6'
,'Node7','Node8'});
    end

    for i=1:LSDYNA_nodes_per_element

temp_nodes_LSDYNA=array2table(Node_data_LSDYNA,'VariableNames',{['Node'
num2str(i)],'X','Y','Z'});
```

```matlab
temp_Element_data_LSDYNA2=innerjoin(temp_Element_data_LSDYNA,temp_nodes
_LSDYNA);
    end

    Element_data_LSDYNA=table2array(temp_Element_data_LSDYNA2);
    clear temp_nodes_LSDYNA temp_Element_data_LSDYNA;

    disp('LSDYNA nodal positions added to element data.')


%%%%%%%%%%%%%%%%%%%%%%%%%%%%%%%%%%%%%%%%%%%%%%%%%%%%%%%%%%%%%%%%%%%%%%%%
    % Add approximate centroid of each element
    % This position will be used to identify the corresponding fibre
    % orientation from the Moldflow model
    size_Element_data_LSDYNA=size(Element_data_LSDYNA);
    width_Element_data_LSDYNA=size_Element_data_LSDYNA(2);
    for i=1:length(Element_data_LSDYNA)
        if strcmp(element_type,'hexahedron')

Element_data_LSDYNA(i,1:width_Element_data_LSDYNA+3)=[Element_data_LSDY
NA(i,1:width_Element_data_LSDYNA) sum(Element_data_LSDYNA(i,11:3:end-
2))/8 sum(Element_data_LSDYNA(i,12:3:end-1))/8
sum(Element_data_LSDYNA(i,13:3:end))/8];
        end
    end
    disp('Centroids of LS-DYNA elements added to element data.')


%%%%%%%%%%%%%%%%%%%%%%%%%%%%%%%%%%%%%%%%%%%%%%%%%%%%%%%%%%%%%%%%%%%%%%%%
    % Find orientation tensor from Moldflow for each element in LSDYNA
    Element_orientation=[Axx(Element_data_LSDYNA(:,end-
2),Element_data_LSDYNA(:,end-1),Element_data_LSDYNA(:,end))...
        Ayy(Element_data_LSDYNA(:,end-2),Element_data_LSDYNA(:,end-
1),Element_data_LSDYNA(:,end))...
        Azz(Element_data_LSDYNA(:,end-2),Element_data_LSDYNA(:,end-
1),Element_data_LSDYNA(:,end))...
        Axy(Element_data_LSDYNA(:,end-2),Element_data_LSDYNA(:,end-
1),Element_data_LSDYNA(:,end))...
        Axz(Element_data_LSDYNA(:,end-2),Element_data_LSDYNA(:,end-
1),Element_data_LSDYNA(:,end))...
        Ayz(Element_data_LSDYNA(:,end-2),Element_data_LSDYNA(:,end-
1),Element_data_LSDYNA(:,end))];
    % Append this data to the LSDYNA element data matrix
    Element_data_LSDYNA=[Element_data_LSDYNA Element_orientation];
    disp('Orientation tensor added to element data.')

    clear Axx Ayy Azz Axy Axz Ayz



%%%%%%%%%%%%%%%%%%%%%%%%%%%%%%%%%%%%%%%%%%%%%%%%%%%%%%%%%%%%%%%%%%%%%%%%
%%%%%%%%%%%%%%%%%%%%%%%%%%%%%%%%%%%%%%%%%%%%%%%%%%%%%%%%%%%%%%%%%%%%%%%%
    % Modify LS-DYNA model to incorporate fibre orientation data
```

```matlab
    % For each element compute mechanical properties and create
material model
    if flag_unique_material==1
        for i=1:length(Element_data_LSDYNA)
            Element_data_LSDYNA(i,2)=i; % Create a new part number for
each element
            if i==1 % Only print '*PART' once
                string_part='*PART\n';
                string_mat='*MAT_ANISOTROPIC_ELASTIC\n';
            else
                string_mat=[string_mat '*MAT_ANISOTROPIC_ELASTIC\n'];
            end
            if material_model==1 % mat_anisotropic_elastic
                if flag_orientation~=4 % use closure approximation
                    if flag_fld==0
                        [Stiffness_matrix
S2]=mat_anisotropic(Element_data_LSDYNA(i,11:16),closure_approximation,
micromechanics_model,AR,vf_fiber_max,flag_orientation,E_matrix,PR_matri
x,E_fiber,PR_fiber,vf_fiber,zeros(3,3,3,3),flag_fld,fld,fibre_diameter)
;
                    else
                        [Stiffness_matrix
S2]=mat_anisotropic(Element_data_LSDYNA(i,11:16),closure_approximation,
micromechanics_model,AR,vf_fiber_max,flag_orientation,E_matrix,PR_matri
x,E_fiber,PR_fiber,vf_fiber,zeros(3,3,3,3),flag_fld,fld,fibre_diameter)
;
                    end
                else % use interpolated 4th order orientation tensor
                    if flag_fld==0
                        [Stiffness_matrix
S2]=mat_anisotropic(Element_data_LSDYNA(i,11:16),closure_approximation,
micromechanics_model,AR,vf_fiber_max,flag_orientation,E_matrix,PR_matri
x,E_fiber,PR_fiber,vf_fiber,a4,flag_fld,fld,fibre_diameter);
                    else
                        [Stiffness_matrix
S2]=mat_anisotropic(Element_data_LSDYNA(i,11:16),closure_approximation,
micromechanics_model,AR,vf_fiber_max,flag_orientation,E_matrix,PR_matri
x,E_fiber,PR_fiber,vf_fiber,a4,flag_fld,fld,fibre_diameter);
                    end
                end
            end
            string_part=[string_part sprintf('%10d%10d%10d',i,secid,i)
'\n'];
            string_mat=[string_mat
sprintf('%10d%10g%10g%10g%10g%10g%10g%10g',i,rho_composite*1000,Stiffne
ss_matrix(1,1),Stiffness_matrix(1,2),Stiffness_matrix(2,2),Stiffness_ma
trix(1,3),Stiffness_matrix(2,3),Stiffness_matrix(3,3)) '\n'];
            string_mat=[string_mat
sprintf('%10g%10g%10g%10g%10g%10g%10g%10g',Stiffness_matrix(1,4),Stiffn
ess_matrix(2,4),Stiffness_matrix(3,4),Stiffness_matrix(4,4),Stiffness_m
atrix(1,5),Stiffness_matrix(2,5),Stiffness_matrix(3,5),Stiffness_matrix
(4,5)) '\n'];
            string_mat=[string_mat
sprintf('%10g%10g%10g%10g%10g%10g%10g%10d',Stiffness_matrix(5,5),Stiffn
ess_matrix(1,6),Stiffness_matrix(2,6),Stiffness_matrix(3,6),Stiffness_m
atrix(4,6),Stiffness_matrix(5,6),Stiffness_matrix(6,6),AOPT) '\n'];
        end % end creating a material card for each element
```

```matlab
    end % end if statement for one material card per element
end % end if statement checking source of fibre orientation data

%%%%%%%%%%%%%%%%%%%%%%%%%%%%%%%%%%%%%%%%%%%%%%%%%%%%%%%%%%%%%%%%%%%%%%%%
% Create strings for material model/nodes/elements

if flag_orientation==1 || flag_orientation==2 % One material model -
2nd order tensor and/or 4th order tensor given
    if flag_orientation==1 % 2nd order tensor given
        if flag_fld==0
            [Stiffness_matrix,
S2]=mat_anisotropic(a2,closure_approximation,micromechanics_model,AR,vf
_fiber_max,flag_orientation,E_matrix,PR_matrix,E_fiber,PR_fiber,vf_fibe
r,zeros(3,3,3,3),flag_fld,fld,fibre_diameter);
        else
            [Stiffness_matrix,
S2]=mat_anisotropic(a2,closure_approximation,micromechanics_model,AR,vf
_fiber_max,flag_orientation,E_matrix,PR_matrix,E_fiber,PR_fiber,vf_fibe
r,zeros(3,3,3,3),flag_fld,fld,fibre_diameter);
        end
    elseif flag_orientation==2 % 2nd order and 4th order tensor given
        if flag_fld==0
            [Stiffness_matrix,
S2]=mat_anisotropic(a2,closure_approximation,micromechanics_model,AR,vf
_fiber_max,flag_orientation,E_matrix,PR_matrix,E_fiber,PR_fiber,vf_fibe
r,a4,flag_fld,fld,fibre_diameter);
        else
            [Stiffness_matrix,
S2]=mat_anisotropic(a2,closure_approximation,micromechanics_model,AR,vf
_fiber_max,flag_orientation,E_matrix,PR_matrix,E_fiber,PR_fiber,vf_fibe
r,a4,flag_fld,fld,fibre_diameter);
        end
    end

    if flag_rotation==1
        Stiffness_matrix_rotated = Tensor_rotation( S2,theta );
        Compliance_matrix_rotated=inv(Stiffness_matrix_rotated);
        E1_rotated=1/Compliance_matrix_rotated(1,1)
        E2_rotated=1/Compliance_matrix_rotated(2,2)
        E3_rotated=1/Compliance_matrix_rotated(3,3)
    end

    Compliance_matrix=inv(Stiffness_matrix);
    E1=1/Compliance_matrix(1,1)
    E2=1/Compliance_matrix(2,2)
    E3=1/Compliance_matrix(3,3)
    string_mat='*MAT_ANISOTROPIC_ELASTIC\n';
    string_mat=[string_mat
sprintf('%10d%10.5g%10g%10g%10g%10g%10g%10g',1,rho_composite,Stiffness_
matrix(1,1),Stiffness_matrix(1,2),Stiffness_matrix(2,2),Stiffness_matri
x(1,3),Stiffness_matrix(2,3),Stiffness_matrix(3,3)) '\n'];
    string_mat=[string_mat
sprintf('%10g%10g%10g%10g%10g%10g%10g%10g',Stiffness_matrix(1,4),Stiffn
ess_matrix(2,4),Stiffness_matrix(3,4),Stiffness_matrix(4,4),Stiffness_m
atrix(1,5),Stiffness_matrix(2,5),Stiffness_matrix(3,5),Stiffness_matrix
(4,5)) '\n'];
```

```matlab
    string_mat=[string_mat
sprintf('%10g%10g%10g%10g%10g%10g%10g%10d',Stiffness_matrix(5,5),Stiffn
ess_matrix(1,6),Stiffness_matrix(2,6),Stiffness_matrix(3,6),Stiffness_m
atrix(4,6),Stiffness_matrix(5,6),Stiffness_matrix(6,6),AOPT) '\n'];
    file_mat_model=fopen('mat_model.txt','w');
    fprintf(file_mat_model,string_mat);
    fclose(file_mat_model);
else % One material model per element
    string_nodes='*NODE\n';
    for i=1:length(Node_data_LSDYNA)
        string_nodes=[string_nodes
sprintf('%8d%16g%16g%16g',Node_data_LSDYNA(i,1:4)) '\n'];
    end
    string_elements='*ELEMENT_SOLID\n';
    for i=1:length(Element_data_LSDYNA)
        string_elements=[string_elements
sprintf('%8d%8d%8d%8d%8d%8d%8d%8d%8d%8d',Element_data_LSDYNA(i,1:10))
'\n'];
    end
    string_section=['*SECTION_SOLID\n' sprintf('%10d%10d',1,secid)
'\n'];
    string_model=['*KEYWORD\n' string_section string_part string_mat
string_elements string_nodes '*END'];
    file_FE_model=fopen('Finite_element_model.k','w');
    fprintf(file_FE_model,string_model);
    fclose(file_FE_model);
end
```

Appendix E – ISO 6603-2 Force-Deflection Responses
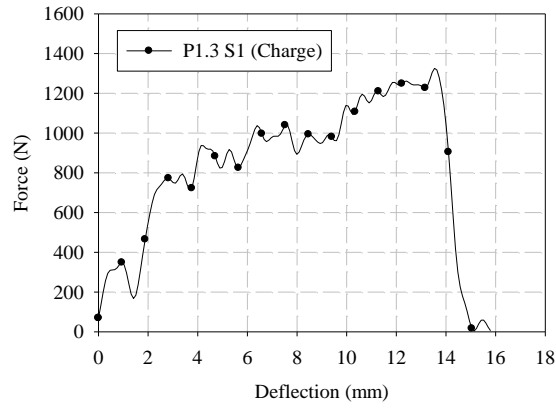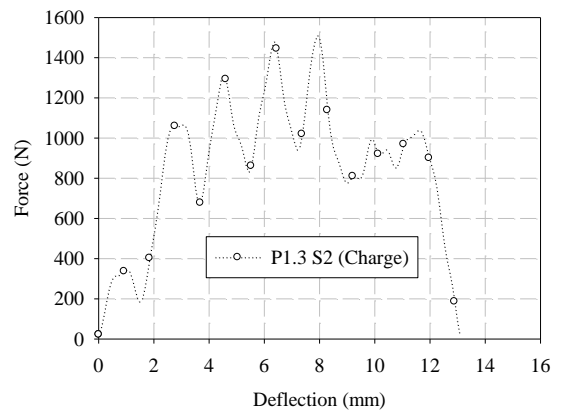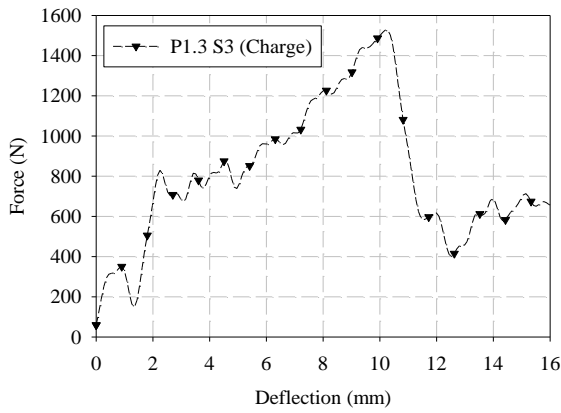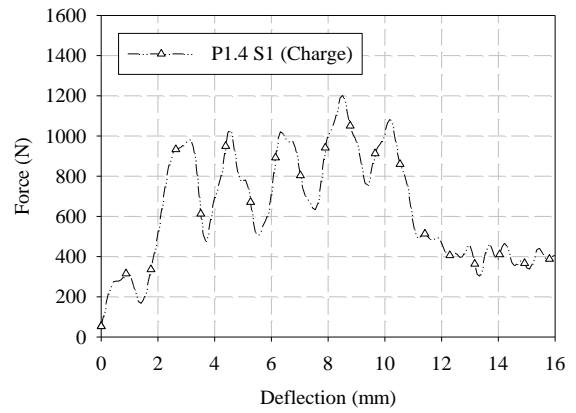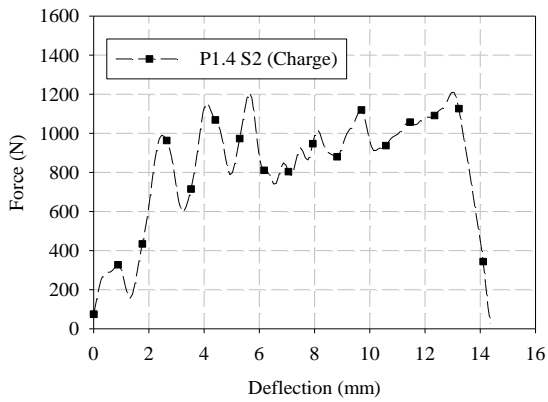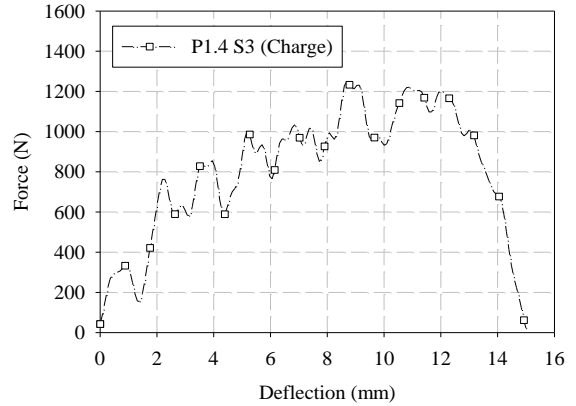
Figure E.1: Charge region force-deflection responses for process configuration V1
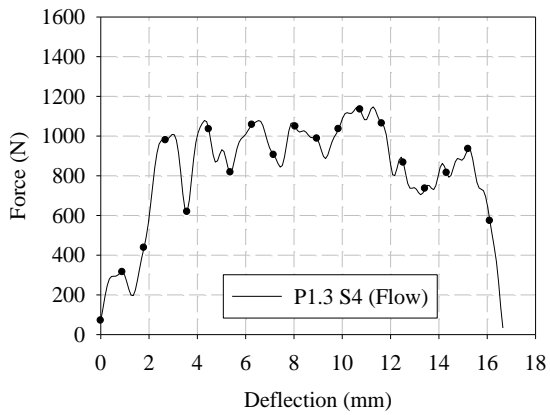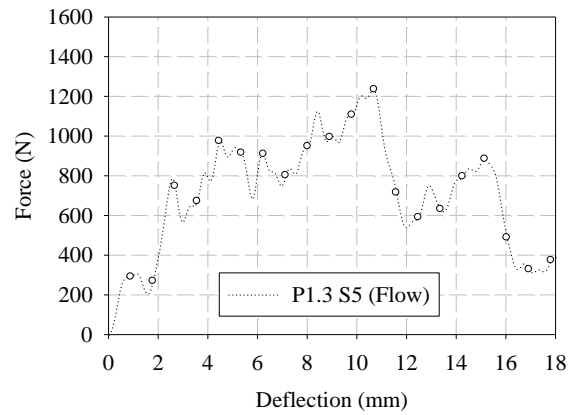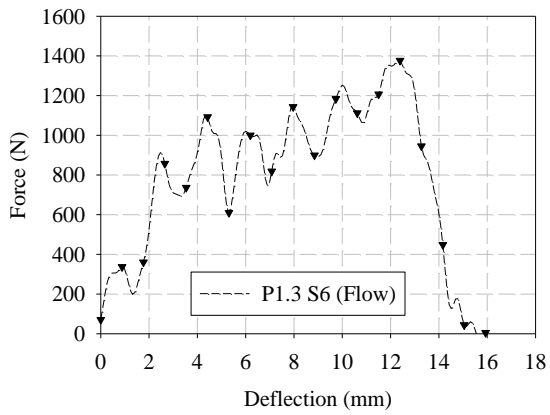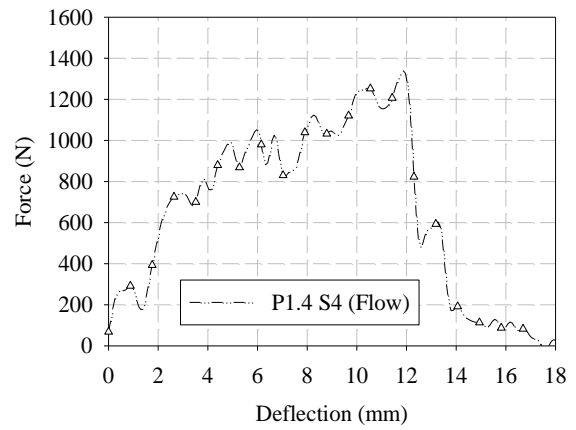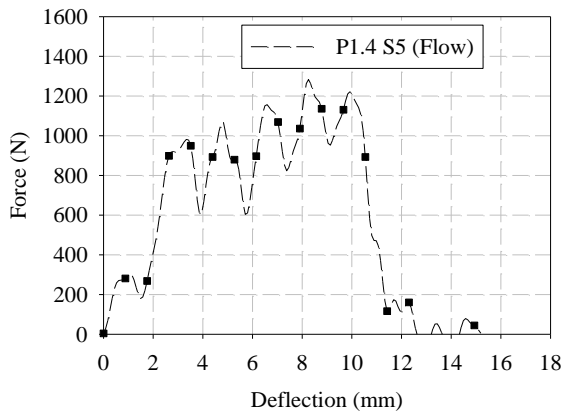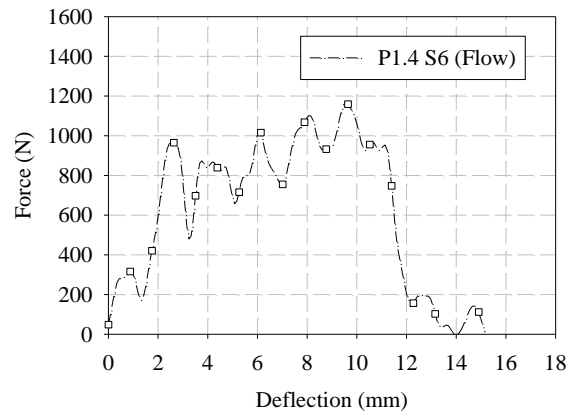
Figure E.2: Flow region force-deflection responses for process configuration V1

Appendix F – Copyright Permissions

The following are the copyright permissions for the published articles adapted to develop the main body of this dissertation:

Chapter 3:

Experimental characterization and modelling of the elastic properties of direct compounded compression molded carbon fibre/polyamide 6 long fibre thermoplastic

Author: Matthew Bondy,Pascal Pinter,William Altenhof
Publication: Materials & Design
Publisher: Elsevier
Date: 15 May 2017

Journal Author Rights

BACK   CLOSE WINDOW

Chapter 4:

Tensile fatigue characterization of polyamide 66/carbon fiber direct/in-line compounded long fiber thermoplastic composites

Author: M. Bondy,W. Rodgers,W. Altenhof
Publication: Composites Part B: Engineering
Publisher: Elsevier
Date: 15 September 2019

Journal Author Rights

BACK   CLOSE WINDOW

Chapter 5:

Low velocity impact testing of direct/inline compounded carbon fibre/polyamide-6 long fibre thermoplastic

Author: Matthew Bondy,William Altenhof
Publication: International Journal of Impact Engineering
Publisher: Elsevier
Date: January 2018

Journal Author Rights

BACK   CLOSE WINDOW

Chapter 6:

Chapter 7:

MDPI Open Access Information and Policy

VITA AUCTORIS

NAME: Matthew Bondy

PLACE OF BIRTH: Windsor, ON

YEAR OF BIRTH: 1986

EDUCATION: St. Anne High School, Tecumseh, ON, 2004

                    St. Clair College, Windsor, ON, 2007

                    University of Windsor, B.A.Sc., Windsor, ON,
                    2009

                    University of Windsor, M.A.Sc., Windsor, ON,
                    2012

                    Politecnico di Torino, Laurea Magistrale,
                    Torino, Piemonte, Italia, MMXII